Improvements to the discrete generalized multigroup method based on proper orthogonal decomposition and SPH factors

by

Richard Reed

B.S., Kansas State University, 2011

M.S., Kansas State University, 2015

AN ABSTRACT OF A DISSERTATION

submitted in partial fulfillment of the
requirements for the degree

DOCTOR OF PHILOSOPHY

Department of Mechanical and Nuclear Engineering
Carl R. Ice College of Engineering

KANSAS STATE UNIVERSITY
Manhattan, Kansas

2019

Abstract

The deterministic transport methods that drive much of nuclear reactor design are invariably based on the multigroup method, in which fluxes and cross sections are treated as constant within small intervals of the energy domain called groups. The discrete generalized multigroup (DGM) method provides an alternative way to represent and solve the multigroup neutron transport equation by dividing the group structure into a smaller number of coarse groups and expanding the energy variable within each coarse group in an orthogonal basis. However, the original form of the DGM equations leads to higher memory costs and a larger computational burden than the equivalent multigroup formulation of a given problem. This work presented herein aimed to improve the efficiency of the DGM method while preserving its accuracy (1) by incorporating a basis from proper orthogonal decomposition (POD) that yields highly-accurate, low-order representations of fine-group fluxes and (2) by introducing specialized superhomogénéisation (SPH) factors to mitigate errors related to averaging (i.e., "homogenizing") cross sections over space and energy.

By truncating the flux-moment expansions, computational savings are gained, but accuracy is somewhat reduced. POD-driven bases were generated using spectral information extracted from small, representative models, and, therefore, perform well under truncation, i.e., the leading terms capture the majority of the variation in energy. This is in stark contrast to the discrete Legendre polynomials, which incorporate no physics and, therefore, require complete expansions in the basis to preserve the underlying, multigroup physics. A key observation made is that the number of degrees of freedom per coarse group required to obtain a desired accuracy is nearly independent of the total number of energy groups. For example, a POD basis truncated to three degrees of freedom per coarse group resulted in approximately 0.1% error in the fission density for all 1-D problems and group structures tested.

The second set of improvements explored the use of spatial homogenization and angular approximation to reduce the memory requirements of DGM. These improvements are again at the cost of some accuracy, but the impact is on the same order of magnitude as that of the truncated basis. Approximating the angular dependence of the total cross section using a linear Legendre expansion introduces approximately 0.5% error into the solution, and homogenizing the cross section moments over coarse-mesh regions increases the error by approximately 2%. These two approximations used in conjunction with a POD basis truncated to three degrees of freedom per coarse group results in a total error of around 2% in the fission densities.

The final improvement is the use of superhomogénéisation or SPH factors, which are used to correct homogenized cross sections for use in larger, downstream problems. SPH factors were used to correct spatial homogenization of the cross section moments to preserve the reaction rates. Although traditional SPH factors performed better than the corrected moments for specific problems, the DGM method with SPH factors produced cross section moments with a smaller error for general problems. In other words, correcting the DGM moments provided a way to create cross section moments that were more problem agnostic as compared to the traditional method. In particular, the DGM-SPH cross section moments achieved an error of around 1% in the pincell fission densities using just three degrees of freedom per coarse group which was consistent over several different problems. This can be compared to traditional SPH correction of spatial homogenization that resulted in as large as 10% error for a comparable number of energy degrees of freedom.

Improvements to the discrete generalized multigroup method based on proper orthogonal decomposition and SPH factors

by

Richard Reed

B.S., Kansas State University, 2011

M.S., Kansas State University, 2015

A DISSERTATION

submitted in partial fulfillment of the
requirements for the degree

DOCTOR OF PHILOSOPHY

Department of Mechanical and Nuclear Engineering
Carl R. Ice College of Engineering

KANSAS STATE UNIVERSITY
Manhattan, Kansas

2019

Approved by:

Major Professor
Jeremy Roberts

Copyright

Abstract

The deterministic transport methods that drive much of nuclear reactor design are invariably based on the multigroup method, in which fluxes and cross sections are treated as constant within small intervals of the energy domain called groups. The discrete generalized multigroup (DGM) method provides an alternative way to represent and solve the multigroup neutron transport equation by dividing the group structure into a smaller number of coarse groups and expanding the energy variable within each coarse group in an orthogonal basis. However, the original form of the DGM equations leads to higher memory costs and a larger computational burden than the equivalent multigroup formulation of a given problem. This work presented herein aimed to improve the efficiency of the DGM method while preserving its accuracy (1) by incorporating a basis from proper orthogonal decomposition (POD) that yields highly-accurate, low-order representations of fine-group fluxes and (2) by introducing specialized superhomogénéisation (SPH) factors to mitigate errors related to averaging (i.e., "homogenizing") cross sections over space and energy.

By truncating the flux-moment expansions, computational savings are gained, but accuracy is somewhat reduced. POD-driven bases were generated using spectral information extracted from small, representative models, and, therefore, perform well under truncation, i.e., the leading terms capture the majority of the variation in energy. This is in stark contrast to the discrete Legendre polynomials, which incorporate no physics and, therefore, require complete expansions in the basis to preserve the underlying, multigroup physics. A key observation made is that the number of degrees of freedom per coarse group required to obtain a desired accuracy is nearly independent of the total number of energy groups. For example, a POD basis truncated to three degrees of freedom per coarse group resulted in approximately 0.1% error in the fission density for all 1-D problems and group structures tested.

The second set of improvements explored the use of spatial homogenization and angular approximation to reduce the memory requirements of DGM. These improvements are again at the cost of some accuracy, but the impact is on the same order of magnitude as that of the truncated basis. Approximating the angular dependence of the total cross section using a linear Legendre expansion introduces approximately 0.5% error into the solution, and homogenizing the cross section moments over coarse-mesh regions increases the error by approximately 2%. These two approximations used in conjunction with a POD basis truncated to three degrees of freedom per coarse group results in a total error of around 2% in the fission densities.

The final improvement is the use of superhomogénéisation or SPH factors, which are used to correct homogenized cross sections for use in larger, downstream problems. SPH factors were used to correct spatial homogenization of the cross section moments to preserve the reaction rates. Although traditional SPH factors performed better than the corrected moments for specific problems, the DGM method with SPH factors produced cross section moments with a smaller error for general problems. In other words, correcting the DGM moments provided a way to create cross section moments that were more problem agnostic as compared to the traditional method. In particular, the DGM-SPH cross section moments achieved an error of around 1% in the pincell fission densities using just three degrees of freedom per coarse group which was consistent over several different problems. This can be compared to traditional SPH correction of spatial homogenization that resulted in as large as 10% error for a comparable number of energy degrees of freedom.

Table of Contents

List of Figures

List of Tables

List of Symbols

Symbol	Description	Units
$\mathbf{\Omega}$	solid angle vector	sr
∇	del operator	
ψ	angular flux	$\mathrm{cm}^{-1}\mathrm{s}^{-1}\mathrm{sr}^{-1}$
$\boldsymbol{r}$	spatial vector	cm
E	energy	MeV
Σ	macroscopic cross section	cm^{-1}
χ	PDF for fission emission energy	
k_{eff}	effective multiplication value or eigenvalue	
ν	neutrons produced per fission	
ϕ	scalar flux	$\mathrm{cm}^{-1}\mathrm{s}^{-1}$
P	orthogonal basis set	
g	energy group for fine-group structure	
R	reaction rate	$\mathrm{cm}^{-1}\mathrm{s}^{-1}$
N_g	number of energy groups	
G	energy group for a coarse-group structure	
b	energy band	
μ	cosine of the discrete scattering angle	
a	discrete angle index	
c	spatial cell index	
l	Legendre order	
N_l	maximum order of the Legendre expansion	

Continued on next page

– continued from previous page

Symbol	Description	Unit
N_a	number of discrete angles	
w	weight corresponding to a discrete angle	
N_G	number of coarse groups	
N_g^G	number of fine groups within the coarse group	
δ	angular correction for the total cross section	$\mathrm{cm}^{-1}\mathrm{sr}^{-1}$
λ	relaxation factor for Krasnoselskii iteration	
Σ^*	mass matrix	
V	volume of a cell or region (length in 1-D)	cm
$\bar{\Sigma}$	averaged cross section	cm^{-1}
$\bar{\phi}$	averaged scalar flux	$\mathrm{cm}^{-1}\mathrm{s}^{-1}$
$\bar{R}$	averaged reaction rate	$\mathrm{cm}^{-1}\mathrm{s}^{-1}$
ω	SPH factor	
$\bar{\chi}$	averaged PDF for fission emission energy	

List of Abbreviations

Abbreviation	Description
SPH	**s**u**p**er**h**omogénéisation
GM	**G**eneralized **M**ultigroup
DGM	**D**iscrete **G**eneralized **M**ultigroup
SD	**S**tep **D**ifference
DCT	**D**iscrete **C**osine **T**ransform of type II
SEAM	**S**ource **E**quivalence **A**cceleration **M**ethod
POD	**P**roper **O**rthogonal **D**ecomposition
GET	**G**eneralized **E**quivalence **T**heory
DLPs	**D**iscrete **L**egendre **P**olynomials
DOF	**D**egrees **O**f **F**reedom
KLT	**K**arhunen-**L**oève **T**ransform
PCA	**P**rincipal **C**omponent **A**nalysis
SVD	**S**ingular **V**alue **D**ecomposition
1-D	**O**ne-**D**imensional
2-D	**T**wo-**D**imensional
DD	**D**iamond **D**ifference
CG	**C**oarse **G**roup
MOX	**M**ixed **Ox**ide
UO_2	**U**ranium Di**o**xide
BWR	**B**oiling **W**ater **R**eactor

Acknowledgments

This work would not have been possible without the contributions from several groups and individuals. Firstly, this work was funded in part by the United States nuclear regulatory commission (NRC) under grant NRC-HQ-84-14-G-0033. Secondly, the computational resources and staff of Beocat have been extensively used to test the methods described in this manuscript. My major professor, Jeremy Roberts, has been pivotal in providing guidance as well as a sounding board for each of my research endeavors, and this work has been enriched by his vision. Finally, this work would have been impossible without the support and encouragement of my office cohort including Kevin, Rabab, Ye, John, and Leidong as well as that of my family and friends.

Dedication

"Mostly, when you see programmers, they aren't doing anything. One of the attractive things about programmers is that you cannot tell whether or not they are working simply by looking at them. Very often they're sitting there seemingly drinking coffee and gossiping, or just staring into space. What the programmer is trying to do is get a handle on all the individual and unrelated ideas that are scampering around in his head."

— Charles M. Strauss

Chapter 1

Introduction

As designs for the cores of nuclear reactors become more complex, increasing fidelity is needed for computational core models. Historically, reactor cores were designed with few heterogeneities, and thus, small spatial models (e.g. pincells or assemblies) with reflective boundary conditions provided sufficient accuracy for neutronic analysis. However, improving the fidelity of a simulation is not as simple as merely increasing the number of unknowns in the problem. Modern core designs incorporate new materials and geometries, which are not well approximated by simple homogeneous models alone. This work explores ways to improve the existing framework, which extends its use to new core designs.

In deterministic methods, the core model is based on the neutron transport equation, which is a formidable relationship in up to seven phase-space variables (three spatial, two angular, energy, and time). Creating a model with high fidelity in each variable quickly leads to an intractably large system because the total number of unknowns scales with the product of the number of unknowns for each phase-space variable. At the current level of computation, it is impossible to model all variables directly with high fidelity. Even as computers improve, it will be unreasonable to model such a problem even if the model can fit in the memory space of the computer.

The goal of this chapter is to outline the current and historical processes for modeling a reactor core. We begin by presenting the continuous-energy, neutron transport equation

in Section 1.1. As will be discussed in Section 1.2, solving the continuous energy equation directly is currently infeasible. We must make approximations for each of the phase-space variables in order to reduce the complexity, and we continue this chapter by first considering approximations for the energy variable.

Typically, continuous energy regions are divided into several energy bins, and the most straightforward method for this is the multigroup approximation introduced in Section 1.2. A generalization to the multigroup method, on which the bulk of this manuscript builds, is discussed in Section 1.3. The chapter continues with a brief discussion of methods related to the traditional multigroup method in Section 1.4.

In Section 1.5, we discuss a way to reduce the spatial complexity of the problem using factors designed to preserve reaction rates during homogenization. This chapter then concludes with the primary objective of the present work as well as the organization of remainder of this manuscript in Section 1.6.

1.1 Continuous Energy Neutron Transport

The continuous-energy, eigenvalue form of the steady-state neutron transport equation is

$$\begin{aligned} \boldsymbol{\Omega}\cdot\nabla\psi(\boldsymbol{r},E,\boldsymbol{\Omega}) + \Sigma_t(\boldsymbol{r},E)\psi(\boldsymbol{r},E,\boldsymbol{\Omega}) & \\ = \int_{4\pi}\int_0^\infty \Sigma_s(\boldsymbol{r},E\leftarrow E',\boldsymbol{\Omega}\cdot\boldsymbol{\Omega}')\psi(\boldsymbol{r},E',\boldsymbol{\Omega}')dE'd\boldsymbol{\Omega}' & \\ + \frac{\chi(\boldsymbol{r},E)}{4\pi k_{\text{eff}}}\int_0^\infty \nu\Sigma_f(\boldsymbol{r},E')\phi(\boldsymbol{r},E')dE'\,, & \end{aligned} \tag{1.1}$$

where

$$\phi(\boldsymbol{r},E) = \int_{4\pi}\psi(\boldsymbol{r},E,\boldsymbol{\Omega})d\Omega\,, \tag{1.2}$$

and $\boldsymbol{r}$ is the spatial coordinate, $\boldsymbol{\Omega}$ is the direction of travel, and E is the neutron energy. Further, $\psi(\boldsymbol{r},E,\boldsymbol{\Omega})$ is the angular flux, and the Σ terms represent the various cross sections. As written, this equation is a function of six phase-space variables (three spatial, two angular, and one energy).

As an example, let us attempt to solve Eq. (1.1) for a reactor core directly. To begin, we divide each spatial variable into 1 cm regions, which is on the order of the diameter of a pincell. This leads to on the order of 200 spatial cells in each of the three spatial variables assuming an active region of 8m^3. Assume that the angular dependence is represented by an expansion in spherical harmonics. If an expansion of degree 3 is used, 16 moments are produced for each spatial cell, which leads to 1.28×10^8 phase-space cells before accounting for energy dependence. Using double precision and assuming only one unknown per phase-space cell means that each energy point requires approximately 250 MB of memory.

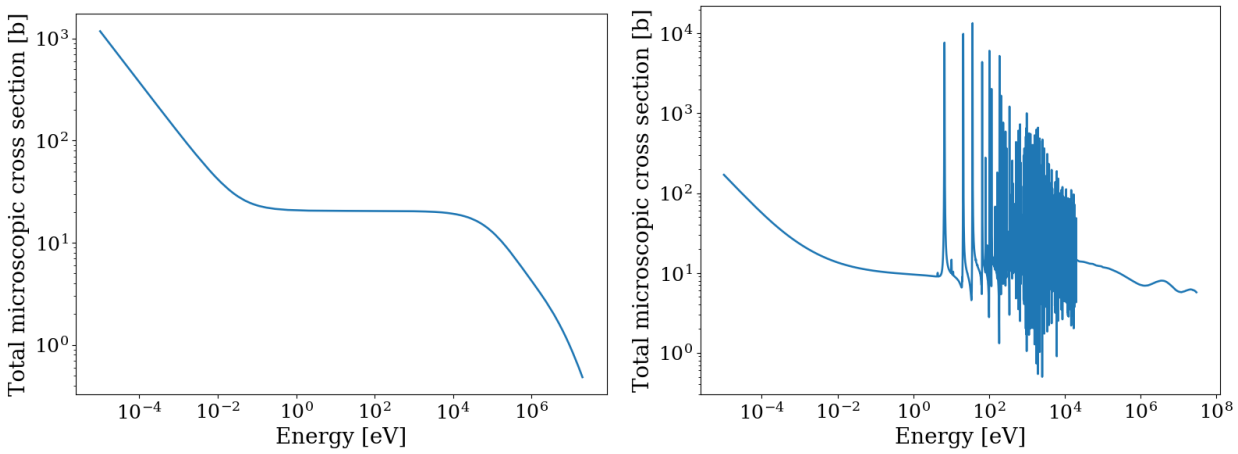

Figure 1.1: Total cross sections of H-1 and U-238

The energy dependence is heavily dependent on the materials in the problem. As an example, Fig. 1.1 shows the total microscopic cross section as a function of energy for both hydrogen-1 and uranium-238, both of which are common elements in nuclear reactor cores. While the energy dependence of hydrogen is rather simple, the resonances (sharp changes in the cross section over a small energy range) of uranium are difficult to capture accurately. As no simple functional dependence exists for the energy dependence, it is common to divide the energy space into a number of points between which the cross sections may be linearly interpolated at high accuracy. For hydrogen, this requires relatively few points as compared to uranium.

Accounting for the energy dependence fully requires on the order of 1×10^5 energy unknowns

leading to a requirement of over 23 TB of memory space for a relatively small problem. This number excludes any accounting of thermal hydraulic feedback or burnup of the fuel using a time-dependent model. Further, note that a pincell has a diameter of approximately 1 cm; thus, even more spatial cells are required to account for spatial self-shielding effects accurately. Direct solution of the continuous form of the transport equation is impossible at our current computational level, and thus, we seek ways to approximate its solution by combining the solution of several small, but similar problems to the core model.

1.2 Approximate Continuous Energy Dependence

We first look for a way to reduce the complexity of the energy dependence. Traditionally, this is done by dividing the energy space into several discrete energy bins. Consider the function

$$P_g(E) = \begin{cases} 1 & \text{if } E_g < E \leq E_{g-1} \\ 0 & \text{otherwise} \end{cases}, \tag{1.3}$$

where E_g and E_{g-1} are selected as the lower and upper bounds, respectively, on an energy bin, and g represents the bin number. These functions are depicted in Fig. 1.2.

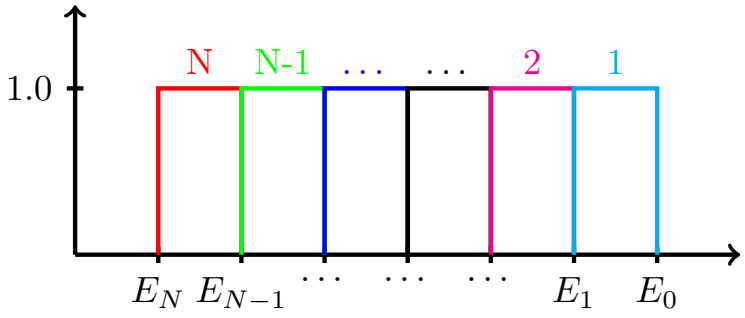

Figure 1.2: Membership functions used for the multigroup method. The number above each rectangle is the group number.

Multiplication of Eq. (1.1) by the functions in Eq. (1.3) and integrating over energy from

E_g to E_{g-1} yields

$$\begin{aligned}
&\boldsymbol{\Omega}\cdot\nabla\int_{E_g}^{E_{g-1}} P_g(E)\psi(\boldsymbol{r},E,\boldsymbol{\Omega})dE+\int_{E_g}^{E_{g-1}} P_g(E)\Sigma_t(\boldsymbol{r},E)\psi(\boldsymbol{r},E,\boldsymbol{\Omega})dE\\
&\quad=\int_{E_g}^{E_{g-1}} P_g(E)\int_{4\pi}\int_0^{\infty}\Sigma_s(\boldsymbol{r},E\leftarrow E',\boldsymbol{\Omega}\cdot\boldsymbol{\Omega}')\psi(\boldsymbol{r},E',\boldsymbol{\Omega}')dE'd\boldsymbol{\Omega}'dE \qquad (1.4)\\
&\quad+\int_{E_g}^{E_{g-1}} P_g(E)\frac{\chi(\boldsymbol{r},E)}{4\pi k_{\text{eff}}}\int_0^{\infty}\nu\Sigma_f(\boldsymbol{r},E')\phi(\boldsymbol{r},E')dE'dE\,.
\end{aligned}$$

We now define

$$\psi_g(\boldsymbol{r},\boldsymbol{\Omega})=\frac{\int_{E_g}^{E_{g-1}} P_g(E)\psi(\boldsymbol{r},E,\boldsymbol{\Omega})dE}{\int_{E_g}^{E_{g-1}} P_g(E)dE}\,, \qquad (1.5)$$

and correspondingly

$$\phi_g(\boldsymbol{r})=\int_{4\pi}\psi_g(\boldsymbol{r},\boldsymbol{\Omega})d\Omega\,. \qquad (1.6)$$

Now, the reaction rate for a general cross section is defined as

$$R(\boldsymbol{r},E,\boldsymbol{\Omega})=\Sigma(\boldsymbol{r},E,\boldsymbol{\Omega})\psi(\boldsymbol{r},E,\boldsymbol{\Omega})\,, \qquad (1.7)$$

which is averaged over an energy range as

$$\frac{\int_{E_g}^{E_{g-1}} P_g(E)R(\boldsymbol{r},E,\boldsymbol{\Omega})dE}{\int_{E_g}^{E_{g-1}} P_g(E)dE}=\frac{\int_{E_g}^{E_{g-1}} P_g(E)\Sigma(\boldsymbol{r},E,\boldsymbol{\Omega})\psi(\boldsymbol{r},E,\boldsymbol{\Omega})dE}{\int_{E_g}^{E_{g-1}} P_g(E)dE}\,, \qquad (1.8)$$

where we define

$$R_g(\boldsymbol{r},\boldsymbol{\Omega})=\frac{\int_{E_g}^{E_{g-1}} P_g(E)R(\boldsymbol{r},E,\boldsymbol{\Omega})dE}{\int_{E_g}^{E_{g-1}} P_g(E)dE}=\Sigma_g(\boldsymbol{r},\boldsymbol{\Omega})\psi_g(\boldsymbol{r},\boldsymbol{\Omega})\,, \qquad (1.9)$$

leading to the definition for an averaged cross section as

$$\Sigma_g(\boldsymbol{r},\boldsymbol{\Omega})=\frac{\int_{E_g}^{E_{g-1}} P_g(E)\Sigma(\boldsymbol{r},E,\boldsymbol{\Omega})\psi(\boldsymbol{r},E,\boldsymbol{\Omega})dE}{\int_{E_g}^{E_{g-1}} P_g(E)\psi(\boldsymbol{r},E,\boldsymbol{\Omega})dE}\,. \qquad (1.10)$$

Following this pattern, each of the cross sections from Eq. (1.4) may be averaged over the

energy group by dividing the equation by the denominator of Eq. (1.5) resulting in

$$\begin{aligned}\boldsymbol{\Omega}\cdot\nabla\psi_g(\boldsymbol{r},\boldsymbol{\Omega})+\Sigma_{t,g}(\boldsymbol{r})\psi_g(\boldsymbol{r},\boldsymbol{\Omega})&\\ =\int_{4\pi}\sum_{g'=1}^{N_g}\Sigma_{s,g\leftarrow g'}(\boldsymbol{r},\boldsymbol{\Omega}\cdot\boldsymbol{\Omega}')\psi_{g'}(\boldsymbol{r},\boldsymbol{\Omega}')d\boldsymbol{\Omega}'&\\ +\frac{\chi_g(\boldsymbol{r})}{4\pi k_{\text{eff}}}\sum_{g'=1}^{N_g}\nu\Sigma_{f,g'}(\boldsymbol{r})\phi_{g'}(\boldsymbol{r})\,,&\end{aligned}\tag{1.11}$$

where the integrals over energy have become sums over all groups, and N_g is the number of energy groups. Equation (1.11) is the multigroup form of the transport equation, where reaction rates have been preserved over each of the energy groups. The astute observer would notice that preserving the reaction rates required the solution to Eq. (1.1), which was previously deemed impossible to obtain. As such, the flux used to homogenize the cross section is approximated by solving small problems, which are related to the full-core solution we desire.

Traditionally, this leads to a multi-step process[1]. The transition from Eq. (1.1) to Eq. (1.11) commonly uses an analytical flux spectrum obtained from modeling each material with continuous energy in simple geometry, e.g., infinite media or pincell. Resonance effects are typically approximated assuming that either the resonance is narrow (i.e., a scattering neutron is likely to avoid the resonance), wide (i.e., a scattering neutron is likely to scatter into the resonance), or somewhere in between[2;3]. While a full discussion of this treatment is outside the scope of the present discussion, a continuous-energy flux spectrum is the result, which is used to average each material over the energy groups. As an alternative, continuous-energy Monte Carlo methods may be used to find a flux spectrum for the infinite medium or spatially small problem (e.g., a pincell subject to reflective conditions). At this stage, the continuous energy range is typically divided into an ultrafine-group structure (1×10^5 groups or more) based on regions of equal lethargy.

Several codes have been created to process the continuous-energy cross sections to a multigroup structure including (but not limited to) AMPX[4] and NJOY[5]. Additionally,

modern treatments based on Monte Carlo methods (e.g., SERPENT[6]) are also available to produce multigroup cross sections. Resolving the energy dependence at this stage still requires too many degrees of freedom for use in full-core models, thus we must further collapse the group structures.

We now introduce the discrete form of the collapse from Eq. (1.1) to Eq. (1.11), i.e., we introduce the function

$$P_G(g) = \begin{cases} 1 & \text{if } g \in G \\ 0 & \text{otherwise} \end{cases}, \tag{1.12}$$

where G is a coarse group comprised of a number of fine groups g. We further define the coarse-group reaction rate as

$$R_G(\boldsymbol{r}, \boldsymbol{\Omega}) = \Sigma_G(\boldsymbol{r}, \boldsymbol{\Omega})\psi_G(\boldsymbol{r}, \boldsymbol{\Omega}) = \frac{\sum\limits_{g \in G} P_G(g) R_g(\boldsymbol{r}, \boldsymbol{\Omega})}{\sum\limits_{g \in G} P_G(E)} = \frac{\sum\limits_{g \in G} P_G(g)\Sigma_g(\boldsymbol{r}, \boldsymbol{\Omega})\psi_g(\boldsymbol{r}, \boldsymbol{\Omega})}{\sum\limits_{g \in G} P_G(E)}, \tag{1.13}$$

where

$$\psi_G(\boldsymbol{r}, \boldsymbol{\Omega}) = \frac{\sum\limits_{g \in G} P_G(g)\psi_g(\boldsymbol{r}, \boldsymbol{\Omega})}{\sum\limits_{g \in G} P_G(E)}, \tag{1.14}$$

and

$$\Sigma_G(\boldsymbol{r}, \boldsymbol{\Omega}) = \frac{\sum\limits_{g \in G} P_G(g)\Sigma_g(\boldsymbol{r}, \boldsymbol{\Omega})\psi_g(\boldsymbol{r}, \boldsymbol{\Omega})}{\sum\limits_{g \in G} P_G(g)\psi_g(\boldsymbol{r}, \boldsymbol{\Omega})}. \tag{1.15}$$

This process suffers from the same problem as before, i.e., the reaction rates are only preserved if the flux spectrum is already known for the full-core problem. A common solution method is to perform a series of computations using the neutron transport equation with increasing fidelity in space and angle while decreasing fidelity in energy. Using the ultrafine-group structure, a small pincell problem subject to reflective conditions is typically solved. This calculation leads to a flux spectrum used to collapse to a structure with between several tens and thousands of energy groups henceforth called the fine-group structure. Over the years, several fine-group structures have been defined for various uses. The structures used in this work are discussed in Chapter 3. The energy group structures are decided based on

the application, e.g., uranium-oxide fuel requires a different energy detail than mixed-oxide fuels[7].

The next step in the process is commonly called the lattice physics calculation, wherein typically an assembly of fuel pins is modeled with the fine-group structure subject to reflective conditions. In this calculation, spatial and angular effects are captured as the neutron flux and reaction rates are computed. A review of these lattice methods and various production implementations of them was published by Hébert[8]. It is common at this stage to employ methods such as the collision probability method[9] or the method of characteristics[10] to solve for the angular flux. With a new flux, the fine-group cross sections are further collapsed to a coarse-group structure which typically contains fewer than ten energy groups. The cross sections are averaged (i.e., homogenized) over energy and space to preserve the reaction rate for the entire assembly. At this stage, typically spatial homogenization methods such as superhomogénéisation (SPH)[11] factors are employed to better preserve reaction rates over the assembly. These spatial homogenization methods are discussed later in Section 1.5. At this point, multigroup cross sections for each assembly have been computed, which are ready for full 3-D core simulations.

Though the multigroup approximation is commonly used, it is not perfect. At each stage of cross section processing, a loss of fidelity occurs directly resulting from smoothing the spectrum by reducing the number of energy groups. As previously mentioned, the full-core flux would be needed at the beginning of the process to correctly preserve the reaction rates. The infinite medium calculations fail to perfectly capture self-shielding or resonance interference effects[7]. Lattice physics calculations often approximate or ignore the junction between different assemblies, which can lead to large errors for heterogeneous cores. This work will not correct all of these sources of error but does seek to lessen the impact of coarsening the group structure.

1.3 Generalize the Multigroup Approximation

The functions presented in Eqs. (1.3) and (1.12) are traditionally used to provide one degree of freedom per coarse group, i.e., the flux is assumed to be flat over the coarse group, and may thus be represented by a single value. The multigroup method may be generalized by expanding Eqs. (1.3) and (1.12) using complete basis sets over each coarse group instead of single vectors. When the fine groups are collapsed to a coarse-group structure, information is lost, but using a complete basis would provide a way to retain the group information. This idea forms the foundation for the generalized multigroup (GM) method (when collapsing from continuous energy) and the discrete generalized multigroup (DGM) method (when further collapsing fine-group structures). The bulk of the present work extends the discrete generalized multigroup method, and thus, the presentation will focus on collapsing a fine-group structure into coarse-group moments.

The process of collapsing the continuous-energy space with a complete basis was first presented in 2007, where Forget and Rahnema[12] introduced a method to extract a fine-group solution from a coarse-group calculation. This method was the beginning of the generalized multigroup (GM) method, upon which the present work builds. The work of Forget and Rahnema[12] relied on collapsing the energy dependence of the transport equation into moments using a set of orthogonal polynomials, specifically the Legendre polynomials. This leads to a series of moment-based equations and, when solved, corresponding flux moments. The flux moments could then be recombined using the orthogonal basis to reproduce the fine-group solution.

The zeroth-moment equation was equivalent to the standard multigroup approximation discussed in Section 1.2, whereas the higher terms corrected the zeroth equation to fine-group accuracy. Essentially, the method provided a way to use a non-flat flux for coarse-group regions. In particular, Forget and Rahnema[12] applied the method to the discrete ordinates method, which is a simple way to treat the angular dependence of the transport equation. While the GM and DGM methods could be applied to other solution methods (e.g. method of characteristics), much of the development of the method has used discrete ordinates. Unless

otherwise specified, all developments presented in this section used the discrete ordinates method to solve the transport equation.

Rahnema et al.[13] expanded on the work of Forget and Rahnema[12] by generalizing the method to an arbitrary, continuous basis set. By ensuring that all basis functions other than the zeroth integrate to zero, the higher-order equations are decoupled from each other. The decoupling means that the higher-order equations are nearly trivial to solve, as they depend only upon the solution to the zeroth-order equation. As the zeroth-order equation is equivalent to the standard multigroup collapse, the problem is solved using approximately the same work as is typical for a coarse-group computation. Thus, this expansion suggests that a fine-group solution may be recovered from a solution with coarse-group work. However, since the method relies on the continuous, Legendre polynomials, the reconstructed fine-group solution could have negative flux values. A continuous basis requires an infinite number of moments for exact preservation; thus, the method required truncation after a number of moments. Truncated Legendre polynomials lead to oscillations near the group boundaries, which could be large enough for negative fluxes particularly in energy-groups with a low flux.

Zhu and Forget[14] further improved the method in 2010 by using the discrete Legendre polynomials and renamed the method to the discrete generalized multigroup (DGM) method. This change eliminated the oscillations and was a more natural fit for the discrete nature of the multigroup approximation. The discrete Legendre polynomials retained the property of decoupling the higher-order moment equations from all but the zeroth equation. Zhu and Forget[14] also introduced flux updates to the method which were used to improve the accuracy of the reconstructed flux spectrum. The flux updates were essentially a single application of the fine-group transport operator, which was used to improve the stability of the method as well as correct any negative flux values. It was suggested to use the resulting fine-group DGM solution as the input to a traditional, fine-group, multigroup solution. In other words, they suggested that the DGM equations could be used as an acceleration method for traditional deterministic methods, which was confirmed in later work by the same authors[15]. While the method did save some computation time, larger storage requirements were needed to hold the additional cross sections and angular flux as compared to other acceleration methods.

Also in 2010, Forget and Zhu[16] applied the DGM method to the diffusion equation. In that work, the derived equation was applied to problems using different energy-group structures in neighboring cells. In simulations with relatively low energy dependence, a coarser-group structure may be used as compared to regions with high energy dependence. The work demonstrated that the DGM method could use neighboring regions with different group structures, which could provide significant computational savings by selecting coarser-group structures in regions with low energy dependence.

Zhu and Forget[17] further improved the DGM method by adding the idea of recondensation in 2011. Shortly thereafter, Douglass and Rahnema[18] added recondensation to their generalized energy condensation theory, which is closely related to the DGM method but instead uses a continuous basis. The DGM method assumes an initial flux spectrum, which typically comes from fine-group lattice calculations, for the initial collapse of the cross sections. The output of the method is an improved estimate of the fine-group flux spectrum. The updated spectrum thus could be used as the initial spectrum to another iteration of the DGM method. This iterative process was called recondensation and lead to improved reaction rates by better incorporating model heterogeneities into the cross sections. Due to iteration, the solution is dependent on the initial flux estimate only for convergence speed. It was shown that two or three iterations on the coarse-group solution were sufficient for significant improvement.

Using this approach, Zhu and Forget[17] suggested that assembly level calculations are unnecessary within the DGM framework with recondensation. However, their method required the use of fine-group flux updates to prevent possible negative fluxes, which could cause the recondensation procedure to diverge. A flux update was essentially one transport iteration (sweep) using the fine-group solution, which was performed between each iteration of the DGM method with recondensation.

Furthermore, Zhu and Forget[17] showed that the DGM method is most accurate relative to the fine-group solution when implemented with the flat-flux approximation, e.g., using step difference (SD). Since the zeroth-order equation of DGM is claimed to be identical to the standard multigroup collapse from fine-group to coarse-group structures, the reaction rates should be identical. It was shown mathematically that a systemic bias exists in DGM if SD

is not used. In other words, the reaction rates for the zeroth DGM and standard multigroup are not equal. The work did not attempt to quantify the bias.

In 2012, Douglass and Rahnema[19] updated their generalized energy condensation theory to account for the angular dependence of the total cross section. This was accomplished by splitting the total cross section into an average term (dependent on the scalar flux) and a perturbation (dependent on the angular flux). However, this feature was already present in the DGM method as presented by Zhu and Forget[14] several years earlier.

In 2012, Gibson and Forget[20] applied the DGM method to the infinite medium problem with a group structure of more than 10,000 energy groups to avoid self-shielding methodologies. The authors suggested that DGM would substantially reduce the computational cost for solving an ultrafine-group problem as compared to traditional methods once spatial dependence was included. Their method required the fine-group flux updates to ensure the stability of the method. Furthermore, the coarse-group structure was also found to impact the rate of convergence.

Gibson and Forget[21] then explored the stability of the DGM method, and sought to eliminate the computationally expensive fine-group flux updates. The authors introduced the idea of Krasnoselskii iteration, which improved the stability at the cost of additional computational expense. Essentially, a relaxation term was introduced to the DGM recondensation iteration, which leads to slower convergence for the flux and corresponding eigenvalue. Gibson and Forget[21] further showed that the ratio of cross sections within a coarse group can lead directly to instabilities, which Krasnoselskii iteration could correct. However, the best relaxation coefficient cannot be known *a priori*, selection of which balances stability and computational time.

In 2013, Gibson and Forget[22] expanded on previous efforts to further explore the stability of the DGM method. From their work, varying the group structure was found to greatly impact the stability of the recondensation iteration scheme. A proper group structure was shown to favorably impact stability, and thus, allowed for larger values for the relaxation coefficient in Krasnoselskii iteration. They suggested a set of criteria for selecting a coarse-group structure based on the fine-group total cross sections. Specifically, a proper group

structure limits the ratio of largest to smallest cross sections within a coarse group to about 2.0, as well as the number of fine groups allowed within a coarse group to about 60. Further, the ratio requirement was removed for coarse groups containing only small cross sections (i.e., less than 1.5 cm^{-1}). Additionally, Gibson and Forget [22] implemented a method where different relaxation values were assigned for each coarse group, which allowed the groups to converge independently. A troublesome group, i.e. in the resonance region, could be assigned a small value for the relaxation coefficient, which reduced stability concerns from that coarse group.

At about the same time, Everson and Forget [23] explored the spatial dependence of the DGM method. Specifically, the authors were seeking a formulation of the DGM equations that provided an exact recreation of the fine-group solution without being limited to the flat flux approximation as discussed previously [17]. In that work, the DGM method was tested with a basis created using the discrete cosign transforms of type II (DCT). Additionally, the method was derived specifically for implementation in methods of characteristics, which uses 1-D step characteristics for a spatial approximation. Finally, a method of redefining the cross sections moments for memory and computational savings was presented, which will be discussed in more detail in Section 2.3.

One of the more recent efforts related to DGM returned to continuous polynomials. Everson and Forget [24] introduced the source equivalence acceleration method (SEAM), which combined the lessons learned from previous work [23] with the subgroup decomposition method introduced previously by Douglass and Rahnema [25]. The subgroup decomposition method is essentially a simplification of the DGM formulation, which uses continuous basis functions to perform cross section collapses on only the incoming energy group side of the scattering and fission cross sections. The method of characteristics code OpenMOC was the platform for testing SEAM, where it was compared against CMFD and found to outperform CMFD for some complex problems. SEAM was formulated to remove the dependence of DGM on the flat flux approximation, and thus provides full consistency between coarse-group and fine-group problems for higher-order spatial approximations.

Recently, Gamarino et al. [26] presented an implementation of a recondensation method

as applied to core-level simulation. The work explored the ability to generate corrected, homogeneous cross sections on the fly, which have been synthesized from infinite medium and environmental spectra. The presentation used an orthogonal basis, which incorporated physical insight into the basis (as opposed to purely analytical functions) by using the proper orthogonal decomposition (POD), which will be discussed in detail in Chapter 3. Fundamentally, the method is similar to the DGM method discussed in this chapter and derived in Chapter 2. The POD basis allowed the method to account for the errors caused by taking homogenized cross sections from an infinite media and creating a heterogeneous core design. The authors showed that the POD basis, created using the method of snapshots, performed better than pure analytical functions (e.g., Chebyshev polynomials).

Gamarino et al.[27] then applied their previous method to several example core configurations typically encountered in modern reactor cores. Their method worked well when the reference leakage spectrum was used, which means the method did not introduce significant additional error. However, the method failed to correct spatial homogenization errors, thus the authors suggested that effective spatial rehomogenization methods must be used in conjunction with the presented spectral rehomogenization.

1.4 Methods Similar to Multigroup

By changing the membership function defined in Eq. (1.3), a plethora of multigroup like methods may be developed. While not considered further in this work, these methods attempt a similar goal to the generalized multigroup method presented in Section 1.3. In this section, we briefly discuss the family of multiband methods and the linear multigroup method.

1.4.1 Multiband Methods

The most naive formulation of a multigroup structure would divide the energy range into a series of contiguous ranges. Each range would thus become an energy group, and the number of groups would be dependent on the range of energies spanned. Multiband methods result

by allowing a discontinuous energy range to comprise an energy group.

Multiband methods use a set of member functions to select the energy groups that have similar cross section values. To accomplish this, Eq. (1.3) is modified to allow discontinuous energy ranges, i.e.

$$P_b(E) = \begin{cases} 1 & \text{if } \Sigma_b < \Sigma(E) \leq \Sigma_{b-1} \\ 0 & \text{otherwise} \end{cases}, \tag{1.16}$$

where the subscript b refers to the energy band. Equation (1.16) is equivalent to

$$P_b(E) = \sum_{g \in b} P_g(E)\,, \tag{1.17}$$

where the energy bounds for each group g are selected such that the cross sections meet the selection criteria for the energy band b.

The family of multiband methods began in 1994, where Shilkov[28] discussed a departure from the naive approach and allowed discontinuous energy ranges to be combined to form a single group. In his work, two methods were presented including the generalized multigroup approximation and the Lebesgue averaging method. These methods lead to the family of multiband methods. Typically in these methods, a group is no longer comprised of cross sections at similar energies, but rather a group contains the energy ranges which have similar cross sections.

This change in group structure minimally affects the form of the transport equations but instead has a substantial impact on the scattering matrix. High energy particles lose energy via scattering, thus transitioning from group to group. In the traditional multigroup formulation, the scattering matrix is almost lower triangular, which signifies that high energy particles cannot gain energy via scattering. In the multiband approach, group to group transfer is not directly correlated to energy, thus the scattering matrix is no longer lower triangular. Most methods of solving the transport equation are less efficient and slower to converge with this apparent upscattering.

Considerable effort has been devoted to developing various multiband methods. An

excellent history of the various forms and developments of multiband methods was produced by Till[29] in 2015. A method in the multiband family was developed by Till et al.[30], which uses finite-elements and trial functions to partition the energy space into discrete regions. His method extended a previous, similar method[31] to use discontinuous energy groupings. The method used modified Heaviside functions to select the group and band membership and promised to treat self-shielding effects better than the standard multigroup approximation. Furthermore, the method was less dependent on the initial weighting spectrum as compared to the multigroup approximation.

1.4.2 Linear Multigroup Method

The linear multigroup method[32] is another variation on the multigroup method, where the membership functions presented in Eq. (1.3) are modified to allow partial membership in multiple groups by use of so-called hat functions. The membership functions are modified to

$$P_g(E) = \begin{cases} \frac{E-E_{g-1}}{E_g-E_{g-1}} & \text{if } E_{g-1} < E \leq E_g \\ \frac{E-E_{g+1}}{E_g-E_{g+1}} & \text{if } E_g < E \leq E_{g+1} \\ 0 & \text{otherwise} \end{cases}, \tag{1.18}$$

which produces functions similar to those shown in Fig. 1.3.

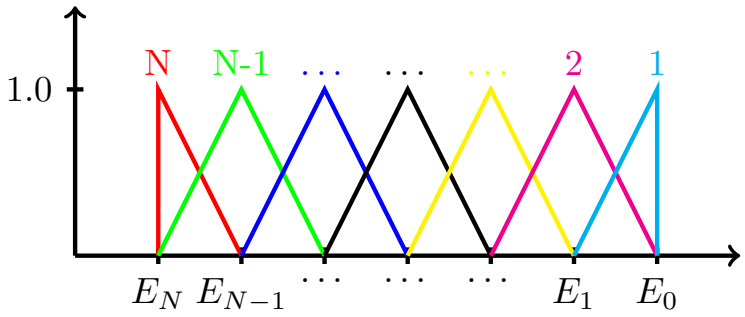

Figure 1.3: Hat functions used in the linear multigroup method. The number above each hat is the group number.

This approach was developed by Attieh and Pevey[33] in 2002, which allowed a fine-energy

group to have partial membership in more than one coarse group. Although the method was shown to work better than the standard multigroup method for some applications, the method suffered from several drawbacks.

First, due to partial membership in multiple coarse groups, the scattering matrix was no longer almost lower triangular, and instead contained so-called "fictitious upscattering" similar to multiband methods. Furthermore, the method introduced a group-to-group dependence to the total cross section, which was non-physical. Finally, the method was only tested for infinite homogeneous media and would be difficult to extend to full-core simulation.

1.5 Approximate Spatial Dependence

We now turn our focus to methods designed to lessen the impact of errors due to spatial (and spectral) homogenization. As mentioned previously, the standard multigroup framework necessarily homogenizes over spatial regions on the march to prepare few-group, nodal cross sections for core simulations. Smearing the information over a spatial region means that important quantities such as the leakage from that region are not automatically preserved through naive averaging. Two main ideas exist for spatial homogenization including discontinuity factors (computed using general equivalence theory) and superhomogénéisation (SPH) factors.

Both methods seek to define homogenized cross sections such that the reaction rates for an entire region are preserved. Without these factors, a problem using homogenized cross sections in place of the non-homogenized cross sections can produce different reaction rates. This section will focus primarily on SPH factors, as they are used in the present work. Discontinuity factors[34–36] are closely related to SPH factors, but require storage of the factors. Conversely, the SPH factors are used to modify the homogenized cross sections directly, which eliminates the storage requirements.

The beginnings of the SPH technique are outlined in 1981 by Hébert and Kavenoky[37]. The method seeks to ensure reaction rates are equivalent between the spatially fine and spatially coarse solutions by producing a set of factors. These factors are computed by a

ratio of the homogenized to non-homogenized flux in the homogenized region and are used to directly adjust the values for the homogenized cross sections. In other words, these correction factors would force equivalence between the low-order and high-order methods by adjusting the cross sections iteratively.

Note that SPH factors are incorporated directly into the homogenized cross sections as opposed to discontinuity factors, which are stored separately. Therefore, SPH corrected cross sections may be used directly for nodal calculations for core models without changing existing algorithms. In particular, the SPH method is typically used in so-called Pin-by-Pin homogenization calculations, wherein nuclear properties are homogenized over each pincell in the core/assembly model. The method typically produces a single SPH equivalence factor per pincell per energy group, and many similar formulations of SPH factors exist. Hebert [38] discusses the history of the SPH methods through the early 1990s, which includes developments for SPH factors applicable to transport calculations instead of merely diffusion.

Each SPH algorithm contains two distinct steps. First, a spatially heterogeneous calculation is performed, which determines the values for the reaction rates and the eigenvalue for a region. Secondly, the region is spatially homogenized, which produces a set of homogenized cross sections. The problem is solved again but replaces the heterogeneous region with the homogenized material, which could result in different reaction rates as compared to the heterogeneous problem. The ratio of the reference (heterogeneous) reaction rates and the newly calculated (homogeneous) rates leads to an equivalence factor, which is multiplied into each cross section to force equivalence of the reaction rates. The adjusted cross sections are used for another solution using the homogenized mesh resulting in updated reaction rates. This process continues iteratively until convergence between the heterogeneous and homogeneous reaction rates.

In 2004, Yamamoto et al. [39] proposed an improvement to the SPH method, which more accurately accounts for heterogeneous boundaries in the model. SPH factors and discontinuity factors attempt to perform a similar role, and the suggested improvement brings the two methods into closer parity. With a small modification to the normalization of SPH factors, flux discontinuity information stemming from adjacent assemblies can be incorporated into

the SPH framework. This modification leads to an equivalence between SPH factors and those of generalized equivalence theory (GET), which relies on discontinuity factors. Before that improvement, SPH factors were less accurate for pin-by-pin calculations (i.e., preserving the pincell reaction rates) as compared to GET. With that work, the accuracy of discontinuity factors can be achieved without storing a separate factor for each cell as is required for traditional discontinuity factors.

Hébert[40] presented a change in the definition of the SPH factors, which corrected for inconsistencies in the higher-order angular moments. In particular, the traditional SPH method was only accurate for P_1 transport calculations or diffusion calculations. The reformulation did not change the definition of the factors themselves but rather defined how the factors were to be applied to the transport equation, specifically the parity form.

More recently, Zhang et al.[41] evaluated both GET (discontinuity factors) and the SPH method for preparing cross sections for use in pin-by-pin calculations involving mixed fuel. They found that both methods were sufficiently accurate for spatial homogenization. These methods were compared using group structures containing 2 and 7 coarse groups and found that 2 coarse groups were not sufficient to capture the energy dependence for the SP_3 method.

Similar work was presented by Ortensi et al.[42], where the SPH method was explored for use at Idaho National Lab in regards to the MOOSE framework. In that work, the authors presented two equivalent ways of applying SPH factors to the even/odd parity form of the transport equation. The methods differ by which terms are multiplied, i.e., which cross sections are adjusted, while still preserving the reaction rates. They coupled the traditional SPH iteration into a preconditioned Jacobian free Newton Krylov solver, which they creatively called the PJFNK-SPH method. By comparing the solution at each iteration to a reference calculation (provided by SERPENT), the new method quickly converged, and in the process, preserved the reaction rates of the reference solution.

1.6 Objective and Organization

As mentioned previously, the bulk of this manuscript focuses on improving the discrete generalized multigroup (DGM) method. As used in this work, the DGM method is most useful for modeling assemblies using 100s to 10000s of energy groups in preparation for full-core modeling, i.e., in the area of lattice physics. The end goal is to produce a method that can produce more accurate cross sections for downstream use as compared to traditional flux weighting described in Section 1.2. The improvements can be grouped into three sections, which correspond to the organization of this manuscript.

Chapter 2 provides a detailed derivation of the baseline discrete generalized multigroup method. Chapter 3 introduces a new basis set into the DGM method, which is more apt to truncation. Chapter 4 encompasses the first set of improvements, which is the use of a truncated basis set for the method. Chapter 5 focuses on ways to reduce the computational requirements of the DGM method. Two approximations are provided, which seek to reduce memory requirements. Chapter 6 combines the DGM method with the SPH method to lead to homogenized, downstream cross sections. Finally, Chapter 7 provides some concluding remarks.

This work also includes three appendices. Appendix A details how the fine-group cross sections were created for this work. Appendix B describes how the coarse-group structures were chosen for the DGM method. Appendix C explores different types of snapshots for use with the POD basis creation.

Chapter 2

The Discrete Generalized Multigroup Method

Historically, the use of the discrete generalized multigroup (DGM) method has been to recover the full, fine-group flux values. Previous efforts[14;23] have sought ways to ensure that the recovered fine-group flux from DGM is identical to that found by solving the transport equation without DGM. The DGM method as presented in this chapter can recover the fine-group solution using a complete basis set outside of some numerical differences in the spatial discretization as discussed in Section 1.3.

In this chapter, we explore the DGM method in more detail. We begin by first deriving the DGM equations in Section 2.1. A method of solving the DGM equation is presented in Section 2.2. A more efficient formulation and solution method for DGM equations are derived in Section 2.3. The chapter concludes with Section 2.4, wherein basis sets suitable for DGM are discussed.

2.1 Derivation of the DGM Equations

Fundamentally, DGM is a way to represent the energy-space of a problem and is compatible with any deterministic transport approximation (e.g., discrete ordinates, method of charac-

teristics) in theory. However, the present work was implemented using discrete ordinates, and thus the derivation, which has been adapted from a previous presentation[22], is focused on that method.

We begin with the k-eigenvalue form of the 1-D, S_n equations[1] with the multigroup approximation and with anisotropic scattering approximated using spherical harmonics (Legendre polynomials in 1-D) written as

$$\begin{aligned}\mu_a \frac{\partial}{\partial x}\psi_{c,a,g} + \Sigma^t_{c,g}\psi_{c,a,g} = &\sum_{l=0}^{N_l} \frac{2l+1}{2} P_l(\mu_a) \sum_{g'=1}^{N_g} \Sigma^s_{c,g\leftarrow g',l}\phi_{c,g',l} \\ &+ \frac{\chi_{c,g}}{2k} \sum_{g'=1}^{N_g} \nu\Sigma^f_{c,g'}\phi_{c,g',0}\,,\end{aligned} \tag{2.1}$$

where $\psi_{c,a,g}$ is the angular flux in cell c for group g in the direction of angle a, μ_a is the cosine of the angle a, $\Sigma^t_{c,g}$ is the total cross section for group g in cell c, $\Sigma^s_{c,g\leftarrow g',l}$ is the lth order Legendre moment of the scattering cross section from group g' to g in cell c, k is the eigenvalue, $\chi_{c,g}$ is the fission spectrum in cell c for group g, $\Sigma^f_{c,g'}$ is the fission cross section in cell c for group g', $P_l(\mu_a)$ is the Legendre polynomial of lth order evaluated at μ_a, N_l is the order of the Legendre expansion, N_g is the number of energy-groups, and

$$\phi_{c,g,l} = \sum_{a=1}^{N_a} w_a P_l(\mu_a)\psi_{c,a,g}\,, \tag{2.2}$$

where N_a is the number of discrete angles, and w_a is the weight corresponding to the discrete angle μ_a for the chosen angular quadrature scheme (e.g. Gauss Legendre).

Now, we divide the energy-groups g into a number of coarse groups N_G such that each fine group belongs to one, and only one coarse group G, which leads to

$$\begin{aligned}\mu_a \frac{\partial}{\partial x}\psi_{c,a,g} + \Sigma^t_{c,g}\psi_{c,a,g} = &\sum_{l=0}^{N_l} \frac{2l+1}{2} P_l(\mu_a) \sum_{G'=1}^{N_G} \sum_{g'=1}^{N_g^{G'}} \Sigma^s_{c,g\leftarrow g',l}\phi_{c,g',l} \\ &+ \frac{\chi_{c,g}}{2k} \sum_{G'=1}^{N_G} \sum_{g'=1}^{N_g^{G'}} \nu\Sigma^f_{c,g'}\phi_{c,g',0}\,,\end{aligned} \tag{2.3}$$

where N_g^G is the number of fine groups within coarse group G.

We introduce a set of energy-dependent, orthonormal basis vectors $P_{i,g}^G$, where the subscript i is the order of the basis function, the subscript g is the fine-group index, and the superscript G is the coarse group for the expansion. A given basis has vectors that are orthogonal within the coarse group, and hence, a different choice of basis may be used within each coarse group. While not a requirement of the method, the basis was assumed to be normalized with unity weights to simplify the notation. The choice of energy basis is the subject of Section 2.4. Multiplication by the orthogonal basis set and summation over the fine groups within a coarse group G yields

$$\begin{aligned}\mu_a \frac{\partial}{\partial x} \sum_{g=1}^{N_g^G} P_{i,g}^G \psi_{c,a,g} + \sum_{g=1}^{N_g^G} P_{i,g}^G \Sigma_{c,g}^t \psi_{c,a,g} = & \sum_{l=0}^{N_l} \frac{2l+1}{2} P_l(\mu_a) \sum_{g=1}^{N_g^G} P_{i,g}^G \sum_{G'=1}^{N_G} \sum_{g'=1}^{N_g^{G'}} \Sigma_{c,g\leftarrow g',l}^s \phi_{c,g',l} \\ & + \sum_{g=1}^{N_g^G} P_{i,g}^G \frac{\chi_{c,g}}{2k} \sum_{G'=1}^{N_G} \sum_{g'=1}^{N_g^{G'}} \nu \Sigma_{c,g'}^f \phi_{c,g',0} \,.\end{aligned} \tag{2.4}$$

We now define the flux moments as

$$\phi_{c,G,l,i} = \sum_{g=1}^{N_g^G} P_{i,g}^G \phi_{c,g,l} \,, \tag{2.5}$$

and

$$\psi_{c,a,G,i} = \sum_{g=1}^{N_g^G} P_{i,g}^G \psi_{c,a,g} \,. \tag{2.6}$$

Thus, the flux may be reconstructed by

$$\phi_{c,g,l} = \sum_{i=1}^{N_i} P_{i,g}^G \phi_{c,G,l,i} \quad \text{and} \quad \psi_{c,a,g} = \sum_{i=1}^{N_i} P_{i,g}^G \psi_{c,a,G,i} \,. \tag{2.7}$$

Equation (2.4) may be simplified to

$$\mu_a \frac{\partial}{\partial x}\psi_{c,a,G,i} + \sum_{g=1}^{N_g^G} P_{i,g}^G \Sigma_{c,g}^t \psi_{c,a,g} = \sum_{l=0}^{N_l} \frac{2l+1}{2} P_l(\mu_a) \sum_{g=1}^{N_g^G} P_{i,g}^G \sum_{G'=1}^{N_G} \sum_{g'=1}^{N_g^{G'}} \Sigma_{c,g\leftarrow g',l}^s \phi_{c,g',l} + \frac{\chi_{c,G,i}}{2k} \sum_{G'=1}^{N_G} \sum_{g'=1}^{N_g^{G'}} \nu \Sigma_{c,g'}^f \phi_{c,g',0} \,, \tag{2.8}$$

by defining and using

$$\chi_{c,G,i} = \sum_{g=1}^{N_g^G} P_{i,g}^G \chi_{c,g} \,, \tag{2.9}$$

as well as Eq. (2.6).

2.1.1 Treating the total interaction term

From here, we turn our attention to the total cross section and the associated reaction rate. We first assume that the total cross section may be split into a scalar and angular part as

$$\Sigma_{c,g}^t = \Sigma_{c,G}^t + \delta_{c,a,g} \,, \tag{2.10}$$

where in the traditional multigroup method, the δ term is assumed to be zero, and

$$\Sigma_{c,G}^t = \frac{\sum_{g=1}^{N_g^G} P_{0,g}^G \Sigma_{c,g}^t \phi_{c,g,0}}{\phi_{c,G',0,0}} \,. \tag{2.11}$$

With the use of Eq. (2.10), the total reaction rate can be preserved as

$$R_{c,G,i}^t = \sum_{g=1}^{N_g^G} P_{i,g}^G \Sigma_{c,g}^t \phi_{c,g,0} = \Sigma_{c,G}^t \phi_{c,G,0,i} + \sum_a \delta_{c,a,G,i} \psi_{c,a,G,0} \,, \tag{2.12}$$

into which Eq. (2.6) is inserted to yield an expression for $\delta_{c,a,G,i}$, i.e.,

$$\begin{aligned}\delta_{c,a,G,i} &= \frac{\sum_{g=1}^{N_g^G} P_{i,g}^G \Sigma_{c,g}^t \psi_{c,a,g} - \Sigma_{c,G}^t \psi_{c,a,G,i}}{\psi_{c,a,G,0}} \\ &= \frac{\sum_{g=1}^{N_g^G} P_{i,g}^G \Sigma_{c,g}^t \psi_{c,a,g} - \Sigma_{c,G}^t \sum_{g=1}^{N_g^G} P_{i,g}^G \psi_{c,a,g}}{\psi_{c,a,G,0}} \\ &= \frac{\sum_{g=1}^{N_g^G} P_{i,g}^G \left(\Sigma_{c,g}^t - \Sigma_{c,G}^t\right) \psi_{c,a,g}}{\psi_{c,a,G,0}} .\end{aligned} \tag{2.13}$$

The term δ represents a correction for the assumption that the total cross section is isotropic upon condensation from the fine-group to the coarse-group structure. Inserting Eq. (2.12) into Eq. (2.8) yields

$$\begin{aligned}&\mu_a \frac{\partial}{\partial x}\psi_{c,a,G,i} + \Sigma_{c,G}^t \psi_{c,a,G,i} + \delta_{c,a,G,i}\psi_{c,a,G,0} \\ &\quad = \sum_{l=0}^{N_l} \frac{2l+1}{2} P_l(\mu_a) \sum_{g=1}^{N_g^G} P_{i,g}^G \sum_{G'=1}^{N_G} \sum_{g'=1}^{N_g^{G'}} \Sigma_{c,g\leftarrow g',l}^s \phi_{c,g',l} \\ &\quad + \frac{\chi_{c,G,i}}{2k} \sum_{G'=1}^{N_G} \sum_{g'=1}^{N_g^{G'}} \nu\Sigma_{c,g'}^f \phi_{c,g',0} .\end{aligned} \tag{2.14}$$

2.1.2 Treating the scattering term

We now treat the scattering term by expanding the reaction rate as

$$R_{c,g\leftarrow g',l}^s = \Sigma_{c,g\leftarrow g',l}^s \phi_{c,g',l} = \sum_{j=0}^{N_j} P_{j,g'}^{G'} R_{c,g\leftarrow G',l,j}^s , \tag{2.15}$$

where

$$R_{c,g\leftarrow G',l,j}^s = \sum_{g'=1}^{N_g^{G'}} P_{j,g'}^{G'} R_{c,g\leftarrow g',l}^s . \tag{2.16}$$

Substituting this relationship into the scattering term of Eq. (2.14) yields

$$\begin{aligned}
&\sum_{l=0}^{N_l} \frac{2l+1}{2} P_l(\mu_a) \sum_{g=1}^{N_g^G} P_{i,g}^G \sum_{G'=1}^{N_G} \sum_{g'=1}^{N_g^{G'}} \Sigma_{c,g\leftarrow g',l}^s \phi_{c,g',l} \\
&\qquad = \sum_{l=0}^{N_l} \frac{2l+1}{2} P_l(\mu_a) \sum_{g=1}^{N_g^G} P_{i,g}^G \sum_{G'=1}^{N_G} \sum_{g'=1}^{N_g^{G'}} \sum_{j=0}^{N_j} P_{j,g'}^{G'} R_{c,g\leftarrow G',l,j}^s \\
&\qquad = \sum_{l=0}^{N_l} \frac{2l+1}{2} P_l(\mu_a) \sum_{G'=1}^{N_G} \sum_{j=0}^{N_j} \sum_{g=1}^{N_g^G} P_{i,g}^G R_{c,g\leftarrow G',l,j}^s \sum_{g'=1}^{N_g^{G'}} P_{j,g'}^{G'} .
\end{aligned} \tag{2.17}$$

By examining the (blue) term $\sum_{g'=1}^{N_g^{G'}} P_{j,g'}^{G'}$ at the end of the last line of Eq. (2.17), we can see that if the basis is defined such that all basis functions higher than zeroth order integrate to zero (equivalent to requiring the zeroth-order function be the flat function), only the $j = 0$ scattering term is non-zero. In other words, higher-order scattering terms (within a coarse group) are decoupled from all but the zeroth-order term (in that coarse group), which helps to simplify the final DGM equations as will be shown below. Recall that for simplicity, we assume that the basis is normalized, though this is not a general restriction of the method. With the use of such a basis and the definitions in Eqs. (2.15)–(2.16), the scattering term can be further simplified, or

$$\begin{aligned}
&\sum_{l=0}^{N_l} \frac{2l+1}{2} P_l(\mu_a) \sum_{g=1}^{N_g^G} P_{i,g}^G \sum_{G'=1}^{N_G} \sum_{g'=1}^{N_g^{G'}} \Sigma_{c,g\leftarrow g',l}^s \phi_{c,g',l} \\
&\qquad = \sum_{l=0}^{N_l} \frac{2l+1}{2} P_l(\mu_a) \sum_{G'=1}^{N_G} \sum_{g=1}^{N_g^G} P_{i,g}^G R_{c,g\leftarrow G',l,0}^s \\
&\qquad = \sum_{l=0}^{N_l} \frac{2l+1}{2} P_l(\mu_a) \sum_{G'=1}^{N_G} \sum_{g=1}^{N_g^G} P_{i,g}^G \sum_{g'=1}^{N_g^{G'}} P_{0,g'}^{G'} \Sigma_{c,g\leftarrow g',l}^s \phi_{c,g',l} \\
&\qquad = \sum_{l=0}^{N_l} \frac{2l+1}{2} P_l(\mu_a) \sum_{G'=1}^{N_G} \sum_{g'=1}^{N_g^{G'}} P_{0,g'}^{G'} \phi_{c,g',l} \sum_{g=1}^{N_g^G} P_{i,g}^G \Sigma_{c,g\leftarrow g',l}^s \\
&\qquad = \sum_{l=0}^{N_l} \frac{2l+1}{2} P_l(\mu_a) \sum_{G'=1}^{N_G} \Sigma_{c,G\leftarrow G',l,i}^s \phi_{c,G,l,0} ,
\end{aligned} \tag{2.18}$$

where

$$\Sigma^s_{c,G\leftarrow G',l,i} = \frac{\sum_{g'=1}^{N_g^{G'}} P^{G'}_{0,g'}\phi_{c,g',l} \sum_{g=1}^{N_g^{G}} P^{G}_{i,g}\Sigma^s_{c,g\leftarrow g',l}}{\phi_{c,G,l,0}} \,. \tag{2.19}$$

Equation (2.18) is inserted into Eq. (2.14) to yield

$$\begin{aligned} &\mu_a \frac{\partial}{\partial x}\psi_{c,a,G,i} + \Sigma^t_{c,G}\psi_{c,a,G,i} + \delta_{c,a,G,i}\psi_{c,a,G,0} \\ &\qquad = \sum_{l=0}^{N_l} \frac{2l+1}{2} P_l(\mu_a) \sum_{G'=1}^{N_G} \Sigma^s_{c,G\leftarrow G',l,i}\phi_{c,G',l,0} \\ &\qquad + \frac{\chi_{c,G,i}}{2k} \sum_{G'=1}^{N_G}\sum_{g'=1}^{N_g^{G'}} \nu\Sigma^f_{c,g'}\phi_{c,g',0} \,. \end{aligned} \tag{2.20}$$

2.1.3 Treating the fission term

Finally, we treat the fission term using a reaction rate expansion similar to the scattering term, i.e., defining

$$R^f_{c,g'} = \nu\Sigma^f_{c,g'}\phi_{c,g',0} = \sum_{j=0}^{N_j} P^{G'}_{j,g'} R^f_{c,G',j} \,, \tag{2.21}$$

where

$$R^f_{c,G',j} = \sum_{g'=1}^{N_g^{G'}} P^{G'}_{j,g'} R^f_{c,g'} \,. \tag{2.22}$$

Using Eqs. (2.21) and (2.22), the fission term in Eq. (2.20) may be rearranged as

$$\begin{aligned} \frac{\chi_{c,G,i}}{2k} \sum_{G'=1}^{N_G}\sum_{g'=1}^{N_g^{G'}} \nu\Sigma^f_{c,g'}\phi_{c,g',0} &= \frac{\chi_{c,G,i}}{2k} \sum_{G'=1}^{N_G}\sum_{g'=1}^{N_g^{G'}}\sum_{j=0}^{N_j} P^{G'}_{j,g'} R^f_{c,G',j} \\ &= \frac{\chi_{c,G,i}}{2k} \sum_{G'=1}^{N_G}\sum_{j=0}^{N_j} R^f_{c,G',j} \sum_{g'=1}^{N_g^{G'}} P^{G'}_{j,g'} \,. \end{aligned} \tag{2.23}$$

Again, only the $j = 0$ terms are non-zero due to the blue summation over energy. These terms vanish when the zeroth-order basis vector is the normalized, flat function, which leads

to

$$\begin{aligned}\frac{\chi_{c,G,i}}{2k}\sum_{G'=1}^{N_G}\sum_{g'=1}^{N_g^{G'}}\nu\Sigma^f_{c,g'}\phi_{c,g',0} &= \frac{\chi_{c,G,i}}{2k}\sum_{G'=1}^{N_G}\sum_{j=0}^{N_j}R^f_{c,G',j}\sum_{g'=1}^{N_g^{G'}}P^{G'}_{j,g'} \\ &= \frac{\chi_{c,G,i}}{2k}\sum_{G'=1}^{N_G}R^f_{c,G',0} \\ &= \frac{\chi_{c,G,i}}{2k}\sum_{G'=1}^{N_G}\sum_{g'=1}^{N_g^{G'}}P^{G'}_{0,g'}\nu\Sigma^f_{c,g'}\phi_{c,g',0} \\ &= \frac{\chi_{c,G,i}}{2k}\sum_{G'=1}^{N_G}\nu\Sigma^f_{c,G'}\phi_{c,G',0,0}\,,\end{aligned} \tag{2.24}$$

where

$$\nu\Sigma^f_{c,G'} = \frac{\sum_{g'=1}^{N_g^{G'}}P^{G'}_{0,g'}\nu\Sigma^f_{c,g'}\phi_{c,g',0}}{\phi_{c,G',0,0}}\,. \tag{2.25}$$

Substituting Eq. (2.25) into Eq. (2.20) leads to

$$\begin{aligned}&\mu_a\frac{\partial}{\partial x}\psi_{c,a,G,i} + \Sigma^t_{c,G}\psi_{c,a,G,i} + \delta_{c,a,G,i}\psi_{c,a,G,0} \\ &\qquad = \sum_{l=0}^{N_l}\frac{2l+1}{2}P_l(\mu_a)\sum_{G'=1}^{N_G}\Sigma^s_{c,G\leftarrow G',l,i}\phi_{c,G',l,0} + \frac{\chi_{c,G,i}}{2k}\sum_{G'=1}^{N_G}\nu\Sigma^f_{c,G'}\phi_{c,G',0,0}\,,\end{aligned} \tag{2.26}$$

which are the set of DGM equations. Note that the zeroth-order solution ($i = 0$) is nearly equivalent to the standard multigroup approximation, in which cross sections are collapsed via the conventional, flux-weighting procedure, with the exception being the δ term. Also note that this derivation has assumed an orthonormal basis with unity weights, and the rest of this work will only consider basis sets of this type. This assumption is not a general restriction of the method, but it makes both the presentation and implementation somewhat more concise.

Finally, note that the higher-order equations ($i > 0$) are dependent on the solution to only the zeroth ($i = 0$) equation for a particular value of G. As discussed previously, the decoupling is accomplished by requiring that all higher-order basis function ($i > 0$) integrate to zero or, equivalently, that the zeroth-order ($i = 0$) basis function is the flat function.

Decoupling the moments serves to simplify the solution of the higher-order equations by converting them to purely-absorbing, fixed-source problems, which are a much easier class of problems to solve numerically than those with scattering. Further, the decoupling also improves the stability of the method by preventing higher-moment flux values (which may be arbitrarily small or negative) from appearing in any denominators (e.g., in Eq. (2.13)).

2.2 Iterative Solution of the DGM Equations

The DGM equations (i.e., Eq. (2.26)) can be solved iteratively as depicted by Algorithm 1. We begin the method by assuming a starting flux vector. The closer this vector is to the true fine-group solution, the faster the method will converge.

Since $\chi_{c,G,i}$ does not depend on the fine-group flux, it is computed once at the beginning of the method. Then, (1) the fine-group flux is collapsed into coarse-group moments using Eqs. (2.5) and (2.6). Next, (2) coarse-group cross section moments are computed using Eq. (2.11), Eq. (2.13), Eq. (2.19), and Eq. (2.25). Now, (3) Eq. (2.26) is solved with $i = 0$ as an eigen equation leading to updated zeroth-order, coarse-group moments as well as the eigenvalue. Then, (4) each higher-order moment ($i > 0$) is found by solving Eq. (2.26). Next, (5) reconstruct the fine-group flux from the updated coarse-group moments. This new fine-group flux is a more accurate approximation as compared to the initial, assumed flux vector, and thus (6) return to step (1) until the method converges. The iteration between successive fine-group collapses is the recondensation method discussed in Section 1.3.

Although straightforward in principle, the DGM equations as defined by Eq. (2.26) and their solution by Algorithm 1 exhibit several drawbacks that limit practicality. Due to the definition for $\delta_{c,a,G,i}$ in Eq. (2.13), the fine-group angular flux must be stored, which can lead to significant storage requirements. Additionally, because the coarse-group cross section moments depend on the cell-wise fine-group fluxes, the coarse-group cross section moments become cell-wise quantities even if the underlying fine-group cross sections are not spatially dependent. Again, this can lead to large storage requirements. Ways to address these concerns are the topic of Chapter 5.

Input: cell and material properties, basis vectors
Compute χ moments
Guess the initial, fine-group flux
while *not converged* **do**
    Compute flux moments
    Compute cross-section moments
    Solve zeroth-order equations ($i = 0$)
    Update the eigenvalue
    for *all moments* $i > 0$ **do**
        Solve ith-order equation
    end
    Reconstruct fine-group flux
end

Algorithm 1: Iterative procedure for solving DGM

The DGM method is also prone to instabilities, i.e., the method may be divergent in some cases as discussed in detail by Gibson and Forget[22]. As presented in Algorithm 1, the DGM method is an example of fixed-point iteration. This class of problems continually applies an operator onto a vector until either the method converges to a fixed-point or it diverges. The simplest form of fixed-point iteration is Picard iteration, which is a problem of the form

$$\phi^{\mathrm{k+1}} = \mathcal{F}(\phi^{\mathrm{k}})\,, \tag{2.27}$$

where $\mathcal{F}$ is some operator acting upon the vector ϕ.

For the case of DGM, stability can be improved by adding a relaxation coefficient $\lambda \in (0, 1]$ into Picard iteration, i.e.,

$$\phi^{\mathrm{k+1}} = \lambda\mathcal{F}(\phi^{\mathrm{k}}) + (1 - \lambda)\phi^{\mathrm{k}}\,, \tag{2.28}$$

which is known as Krasnoselskii iteration. Note that if $\lambda = 1.0$, this method reduces to Picard iteration. For divergent problems, a smaller value of λ may be used to improve stability and convergence at the cost of additional iterations. For highly stable problems, λ may be set above unity, which would increase the convergence rate using over-relaxation.

2.3 Precomputing the Coarse Moments

As discussed in the previous sections, the DGM method relies on an iterative approach to find the fine-group solution. Each recondensation iteration begins with the fine-group flux (or an approximation), which is used to produce coarse-group cross section moments. These moments are then used to update the coarse-group flux moments, which leads to an improved fine-group flux. Using the definitions for the coarse-group cross section moments (Eq. (2.11), Eq. (2.13), Eq. (2.19), and Eq. (2.25)), fine-group cross sections data as well as fine-group flux must be stored and used at every iteration. Ideally, DGM can be cast in such a way as to partially precompute these quantities and remove the dependence on fine-group data after the initial computation. A change of this nature would greatly improve the DGM method in terms of both computational and memory costs.

This kind of improvement was first suggested by Everson and Forget [23] for reducing the cost of storing $\delta_{c,a,G,i}$. The goal for this section is to not affect the solution of Eq. (2.26), but rather to increase solution efficiency. We begin by examining the total cross section moments defined in Eq. (2.11) utilizing the definition of the flux moments from Eq. (2.7) as

$$\begin{aligned}
\Sigma^t_{c,G} &= \frac{\sum_{g=1}^{N_g^G} P^G_{0,g}\Sigma^t_{c,g}\phi_{c,g,0}}{\phi_{c,G,0,0}} \\
&= \frac{\sum_{g=1}^{N_g^G} P^G_{0,g}\Sigma^t_{c,g}\sum_{j=0}^{N_j} P^G_{j,g}\phi_{c,G,0,j}}{\phi_{c,G,0,0}} \\
&= \frac{\sum_{j=0}^{N_j} \phi_{c,G,0,j}\sum_{g=1}^{N_g^G} P^G_{0,g}\Sigma^t_{c,g}P^G_{j,g}}{\phi_{c,G,0,0}} \\
&= \frac{\sum_{j=0}^{N_j} \phi_{c,G,0,j}\Sigma^{t*}_{c,G,0,j}}{\phi_{c,G,0,0}} ,
\end{aligned} \tag{2.29}$$

where

$$\Sigma^{t*}_{c,G,i,j} = \sum_{g=1}^{N_g^G} P^G_{i,g}\Sigma^t_{c,g}P^G_{j,g} . \tag{2.30}$$

$\Sigma^{t*}_{c,G,i,j}$ is the total cross section mass matrix and N_j is the number of moments in the expansion. With this definition, the total cross section moments no longer depend on the fine-group data, and may instead be updated using only coarse-group information. Note that these savings are offset by now requiring all coarse-group flux moments to be stored. This final point will receive further discussion at the end of the section.

Next, we perform a similar reformulation for the δ term as

$$\begin{aligned}
\delta_{c,a,G,i} &= \frac{\sum_{g=1}^{N_g^G} P^G_{i,g}\left(\Sigma^t_{c,g} - \Sigma^t_{c,G}\right)\psi_{c,a,g}}{\psi_{c,a,G,0}} \\
&= \frac{\sum_{g=1}^{N_g^G} P^G_{i,g}\left(\Sigma^t_{c,g} - \Sigma^t_{c,G}\right)\sum_{j=0}^{N_j} P^G_{j,g}\psi_{c,a,G,j}}{\psi_{c,a,G,0}} \\
&= \frac{\sum_{j=0}^{N_j}\psi_{c,a,G,j}\sum_{g=1}^{N_g^G} P^G_{i,g}\left(\Sigma^t_{c,g} - \Sigma^t_{c,G}\right)P^G_{j,g}}{\psi_{c,a,G,0}} \\
&= \frac{\sum_{j=0}^{N_j}\psi_{c,a,G,j}\left(\sum_{g=1}^{N_g^G} P^G_{i,g}\Sigma^t_{c,g}P^G_{j,g} - \sum_{g=1}^{N_g^G} P^G_{i,g}\Sigma^t_{c,G,0}P^G_{j,g}\right)}{\psi_{c,a,G,0}} \\
&= \frac{\sum_{j=0}^{N_j}\psi_{c,a,G,j}\sum_{g=1}^{N_g^G} P^G_{i,g}\Sigma^t_{c,g}P^G_{j,g} - \Sigma^t_{c,G}\sum_{g=1}^{N_g^G} P^G_{i,g}\sum_{j=0}^{N_j}\psi_{c,a,G,j}P^G_{j,g}}{\psi_{c,a,G,0}} \\
&= \frac{\sum_{j=0}^{N_j}\psi_{c,a,G,j}\Sigma^{t*}_{c,G,i,j}}{\psi_{c,a,G,0}} - \Sigma^t_{c,G}\frac{\psi_{c,a,G,i}}{\psi_{c,a,G,0}},
\end{aligned} \tag{2.31}$$

using the definitions in Eqs. (2.6) and (2.7). Next, the scattering term is redefined from

Eq. (2.19) as

$$\begin{aligned}\Sigma^{s}_{c,G\leftarrow G',l,i} &= \frac{\sum_{g=1}^{N_g^G} P^G_{i,g} \sum_{g'=1}^{N_g^{G'}} \Sigma^s_{c,g\leftarrow g',l}\phi_{c,g',l}}{\phi_{c,G',l,0}} \\ &= \frac{\sum_{g=1}^{N_g^G} P^G_{i,g} \sum_{g'=1}^{N_g^{G'}} \Sigma^s_{c,g\leftarrow g',l} \sum_{j=0}^{N_j} P^{G'}_{j,g'}\phi_{c,G',l,j}}{\phi_{c,G',l,0}} \\ &= \frac{\sum_{j=0}^{N_j} \phi_{c,G',l,j} \sum_{g=1}^{N_g^G} P^G_{i,g} \sum_{g'=1}^{N_g^{G'}} \Sigma^s_{c,g\leftarrow g',l} P^{G'}_{j,g'}}{\phi_{c,G',l,0}} \\ &= \frac{\sum_{j=0}^{N_j} \phi_{c,G',l,j}\Sigma^{s*}_{c,G\leftarrow G',l,i,j}}{\phi_{c,G',l,0}}\,,\end{aligned} \tag{2.32}$$

where

$$\Sigma^{s*}_{c,G\leftarrow G',l,i,j} = \sum_{g=1}^{N_g^G} P^G_{i,g} \sum_{g'=1}^{N_g^{G'}} \Sigma^s_{c,g\leftarrow g',l} P^{G'}_{j,g'}\,. \tag{2.33}$$

Finally, the same treatment is applied to the fission cross section moments beginning with the Eq. (2.25) as

$$\begin{aligned}\nu\Sigma^{f}_{c,G'} &= \frac{\sum_{g'=1}^{N_g^{G'}} P^{G'}_{0,g'} \nu\Sigma^f_{c,g'}\phi_{c,g',0}}{\phi_{c,G',0,0}} \\ &= \frac{\sum_{g'=1}^{N_g^{G'}} P^{G'}_{0,g'} \nu\Sigma^f_{c,g'} \sum_{j=0}^{N_j} P^{G'}_{j,g'}\phi_{c,G',0,j}}{\phi_{c,G',0,0}} \\ &= \frac{\sum_{j=0}^{N_j} \phi_{c,G',0,j} \sum_{g'=1}^{N_g^{G'}} P^{G'}_{0,g'} \nu\Sigma^f_{c,g'} P^{G'}_{j,g'}}{\phi_{c,G',0,0}} \\ &= \frac{\sum_{j=0}^{N_j} \phi_{c,G',0,j}\nu\Sigma^{f,*}_{c,G',j}}{\phi_{c,G',0,0}}\,,\end{aligned} \tag{2.34}$$

where

$$\nu\Sigma^{f,*}_{c,G',j} = \sum_{g'=1}^{N_g^{G'}} P^{G'}_{0,g'} \nu\Sigma^f_{c,g'} P^{G'}_{j,g'}\,. \tag{2.35}$$

Using these reformed definitions, Algorithm 1 can be rearranged slightly, as shown in Algorithm 2. Now, the mass matrices are computed *before* the DGM iteration, which means that neither fine-group data nor the fine-group solution is needed until the end of the algorithm (and that is only if a the fine-group solution is required in addition to the coarse-group solution). The method retains the previous property of decoupling the higher-order

Input: cell and material properties, basis vectors
Compute χ moments Compute mass matrices
Guess the initial, fine-group flux
Compute flux moments
while *not converged* **do**
    Compute coarse-group cross-section moments
    Solve zeroth-order equation ($i = 0$)
    Update the eigenvalue
    for *all moments* $i > 0$ **do**
        Solve ith-order equation
    end
end
Reconstruct fine-group flux

Algorithm 2: Reformulated iterative procedure for solving DGM

moments provided that the zeroth basis is the flat function. Further, the reformulation makes no approximations except those used for the base DGM derivation. Thus, with the use of this reformulation, DGM may be significantly accelerated by avoiding several fine-group expansions during the recondensation iteration due to reduced computational complexity and smaller memory footprint. However, storage requirements are unchanged in the case of a complete basis set, since the total number of stored moments is equal to the number of fine groups.

2.4 Basis Sets for DGM

2.4.1 Basis Limitations

As derived in Section 2.1, the DGM method relies on an orthogonal basis, and full recovery of the fine-group flux requires that the basis be complete. The derivation assumed that the

basis had unity weights and that the basis was normalized. The last statement is not a requirement of the method but was assumed for a cleaner presentation.

One requirement of the basis is that the zeroth-order function must be the flat function or equivalently that all basis functions except the zeroth must integrate to zero. This feature decouples the solution of the higher-order DGM equations found in Eq. (2.26) from all but the zeroth equation. The zeroth-order equation is consistent with the standard multigroup approximation described in Section 1.2, and that the higher-order equations serve to correct fine-group information. Note that the eigenvalue is preserved by the zeroth-order equation, which allows the higher-order equations to be solved as fixed source problems. In other words, the expense of the eigenvalue solution is necessary only for the zeroth-order equation.

2.4.2 Previous work

As mentioned in the derivation of the DGM method in Section 2.1, an energy-dependent, orthonormal basis set $P_{i,g}^G$ is needed to collapse the energy space from fine group to coarse group. Historically, this basis consisted of the well known, Legendre polynomials, the first several of which are shown in Fig. 2.1. The Legendre polynomials are continuous and orthogonal in the range from -1 to 1. The basis set is defined by setting the zeroth-order function to the flat function, i.e. $P_0(x) = 1$, and the first-order function to $P_1(x) = x$. Then, the nth order function is formed by orthogonalizing $P_n(x) = x^n$ against all lower-order basis functions. Using such a basis, an infinite number of basis functions are needed to perfectly reconstruct a continuous function, e.g., the fine-group flux.

While early work[12;13] related to DGM used continuous polynomials, several difficulties quickly arose. The primary concern was that many Legendre functions are needed to approximate a step function, which is the general shape of the flux after the multigroup approximation is applied. Furthermore, the Legendre polynomials create oscillatory behavior in the reconstructed function, which has the potential for unphysical, negative flux values.

More recent developments in the DGM method have explored the use of the discrete Legendre polynomials (DLPs)[43] shown in Fig. 2.2. The discrete versions of the Legendre

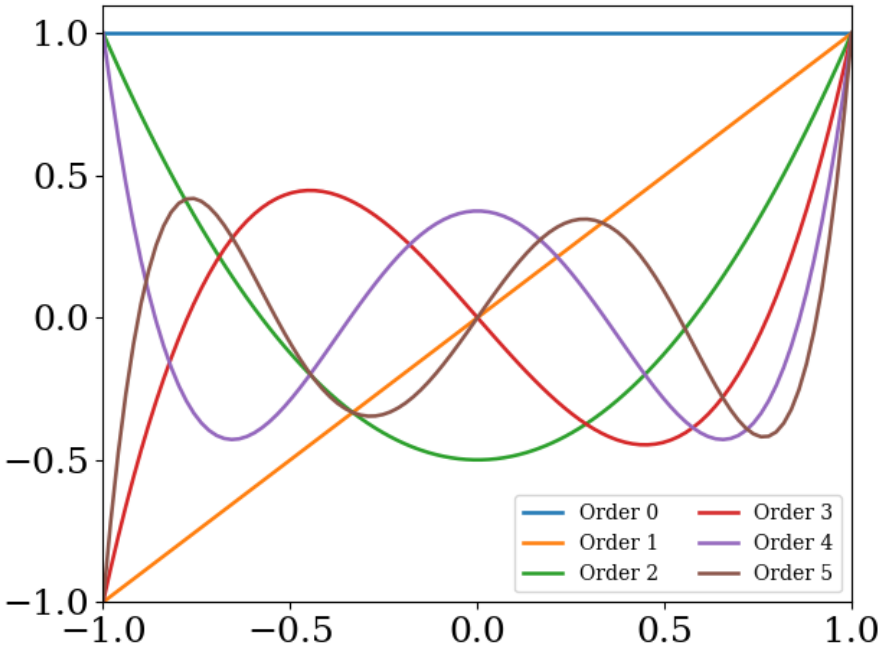

Figure 2.1: Legendre polynomials through order 5

polynomials are formed similarly to the continuous version except that the functions are evaluated at a finite number of discrete points. The DLPs are a more natural fit for approximating discrete data points due to the discrete nature of the basis. For example, N data points may be exactly reproduced using at most N DLPs vectors (i.e., through order $N-1$). In Fig. 2.2, 50 points were used, and the basis has been normalized so each vector is unity when measured with the euclidean norm.

Note that the DGM method breaks the energy space into a number of coarse-group regions. Each of these regions uses a basis that is orthonormal over the coarse group. As an example, say a 44-group spectrum was broken into four coarse-group regions with 26 fine groups in the highest energy coarse group, 15 in the next highest, 2 in the penultimate, and 1 group in the lowest coarse group. The DLP basis sets used for such a structure are shown in Fig. 2.3, where the vertical bars show the boundaries between the coarse groups. In general, the basis for each coarse group will contain a number of degrees of freedom equal to the number of energy groups within a coarse group. Thus, for our example, the highest energy group contains 26 orthogonal DLP functions that are each of length 26. The lowest energy

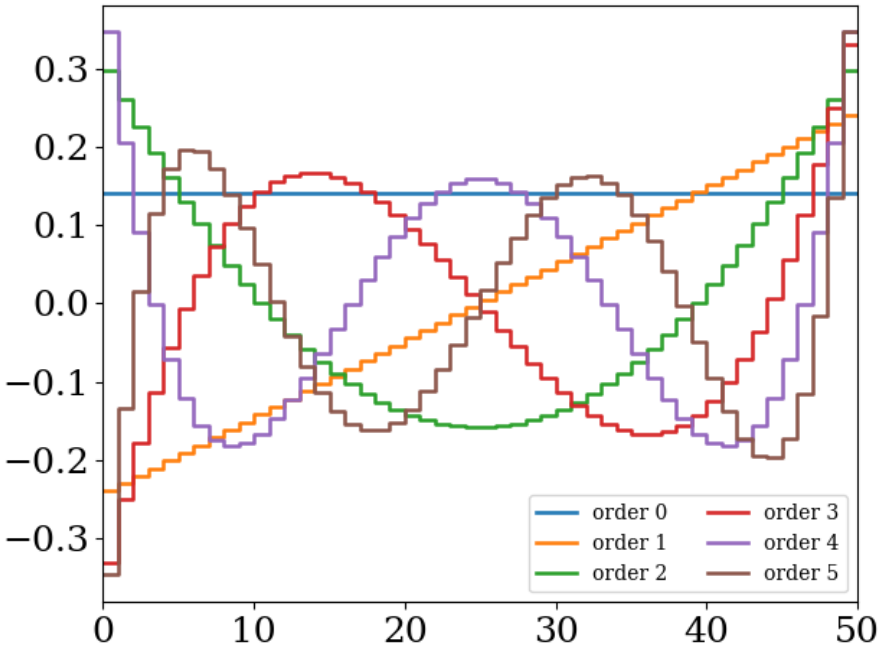

Figure 2.2: discrete Legendre polynomials through order 5

group contains only a single vector, which is equal to unity with a length of one since only one fine group is in the coarse group.

While an improvement for eliminating the oscillatory flux behavior, high-order DLP vectors ($n > 50$) can lose orthogonality due to numerical roundoff. To combat this issue, an alternative discrete basis was explored in the DGM method[23], which used the Fourier transform. In particular, the discrete cosine transform (DCT) can produce a basis set with all necessary properties for DGM. The basis utilizes a flat zeroth vector, while each of the higher vectors is a cosign function with different frequencies, evaluated at a number of discrete points. The DCT basis avoids orthogonality troubles because each function can be defined directly as opposed to the recurrence relationship used to define the DLPs.

Until this point, all considered basis sets were complete, i.e., that an arbitrary vector could be reproduced exactly using that basis. The remainder of this manuscript is focused on the consequences of using an incomplete basis, i.e., a truncated basis. In other words, functions cannot be reproduced exactly, but rather approximately, by using only the low-order basis vectors. A truncated basis performs the best when the low-order basis vectors have

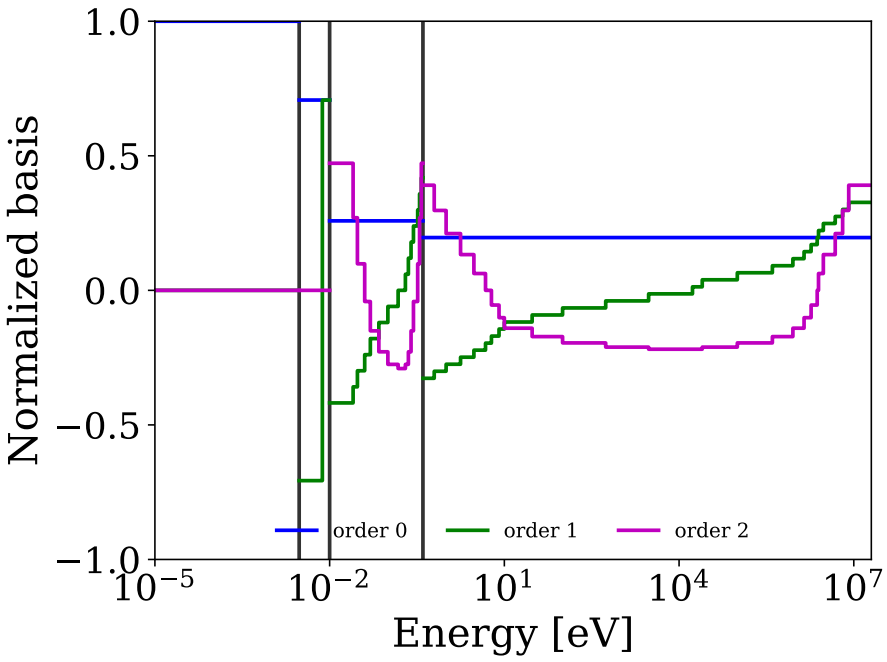

Figure 2.3: DLP vectors applied to a 44-group spectrum. Vertical bars show the boundaries between the coarse groups. The basis is orthogonalized over each coarse group.

approximately the same shape as the expanded function. However, the energy-dependent neutron flux is not well represented by the low-order functions of either the DLPs or the DCTs. Thus, neither basis set performs well under truncation. In Chapter 3, we will explore a different discrete basis, which incorporates physical shapes into the underlying basis to improve the low-order expansions.

Chapter 3

DGM with Truncation in Energy

This chapter will introduce the idea of an incomplete basis set into the discrete generalized multigroup (DGM) equations from Section 2.1. Until this point, the DGM equations have been used as a way to collapse a fine-group problem over energy to coarse-group moments. The DGM approach promises to provide a way to reduce the group structure from a highly-coupled relationship to a coarse-group calculation, which may be refined using relatively low-cost, higher-order moments. A coarse-group problem is much quicker to solve, but recovery of the exact fine-group solution using DGM requires more computational effort than a direct fine-group solution. Only through the means of appropriate approximations (some discussed in this chapter) will DGM uphold its promise. The work in this chapter follows the same basic structure of DGM, but now, the fine-group solution will not be recovered exactly. Instead, the DGM equations will be used to approximate the fine-group solution.

As discussed at the end of Chapter 2, a truncated basis will be used, which will decrease the number of degrees of freedom for the energy variable. This truncation introduces error into the basis expansion, the extent of which is determined by the basis. A basis set based on the SVD is introduced in Section 3.1, which is constructed to provide accurate reconstructions using a small number of degrees of freedom. The basis discussed in Section 3.1 relies on snapshots, which resemble the fine-group flux. This basis is used throughout the remainder of this work, and details about snapshot selection are presented in Chapter 4 for each test

problem. Details regarding the solver and code are presented in Section 3.2.

3.1 Derivation of the POD Basis

The primary objective of this work is to use the DGM method as a way to collapse the energy-space of a problem to prepare cross sections for downstream use. In other words, the number of degrees of freedom (DOF) for the energy space must be reduced, ideally to minimize the resulting error. To this end, we explore the proper orthogonal decomposition (POD) for generating a basis for DGM.

The POD extracts the fundamental modes of a system. The method presented here goes by several names including the Karhunen-Loève transform (KLT) and Principal Component Analysis (PCA)[44]. POD has been used in a variety of applications including image compression[44], fluid dynamics[45], and reactor eigenvalue problems[46]. Additionally, the method was used to approximate the boundaries between regions in the response matrix method[47;48]. Fundamentally, the method is related to the singular value decomposition (SVD).

In a basis expansion, a discrete or continuous function $\boldsymbol{f}(x)$ is represented by a summation of moments in the selected basis, i.e.,

$$\tilde{\boldsymbol{f}}(x) \approx \sum_{i=0}^{k} a_i P_i(x)\,, \tag{3.1}$$

where the ith moment a_i of the function $\boldsymbol{f}(x)$ in the basis $P(x)$ is defined as

$$a_i = \sum_x \boldsymbol{f}(x) P_i(x) \quad \text{for} \quad i \in [0, 1 \ldots, k]\,, \tag{3.2}$$

where $\tilde{\boldsymbol{f}}(x)$ is the reconstructed (approximated) function, and k is the order of the expansion. If the basis is *complete*, $\boldsymbol{f}(x)$ can be reproduced exactly. For an arbitrary, discrete vector x containing N points, N orthogonal basis functions are required for a complete expansion of $\boldsymbol{f}(x)$ in the general case. Similarly, a continuous function would require an infinite number of orthogonal functions for completeness.

To reduce the DOF of the energy space, a truncated (*incomplete*) basis is necessary, and $\boldsymbol{f}(x)$ is approximated. If the basis functions are similar to $\boldsymbol{f}(x)$, a low-order expansion can reproduce the function with high accuracy. For example, although $\boldsymbol{f}(x) = x^2$ is a continuous expansion, a second-order expansion in the continuous Legendre polynomials is an exact representation. Thus, if the basis $P_i(x)$ can be formed as to be similar to $\boldsymbol{f}(x)$, a truncated basis will introduce minimal error into the expansion.

Indeed, the central goal of POD is to represent a function $\boldsymbol{f}(x)$ such that a kth-order expansion provides the smallest possible error in the euclidean norm for the reconstructed function $\tilde{\boldsymbol{f}}(x)$. The method of snapshots[45] is used to construct the basis. This method forms a set of vectors, which closely resemble the function $\boldsymbol{f}(x)$. For example, the energy-dependent, scalar flux for a spatial cell in a reactor assembly closely resembles that of neighboring spatial cells. Snapshot selection is discussed for each of the test problems in Chapter 4.

We begin by assuming that we have a number of snapshots N, each of which is a vector with length M. These vectors are formed into the data matrix $\boldsymbol{D} \in \mathbb{R}^{M\times N}$, where $\boldsymbol{d}_n$ is the nth column of $\boldsymbol{D}$ and the nth snapshot, i.e. $\boldsymbol{D} = [\boldsymbol{d}_1, \boldsymbol{d}_2, \ldots, \boldsymbol{d}_N]$. The SVD of $\boldsymbol{D}$ is

$$\boldsymbol{D} = \boldsymbol{U}_D \boldsymbol{\Sigma}_D \boldsymbol{V}_D^\intercal \,, \tag{3.3}$$

where $\boldsymbol{U}_D \in \mathbb{R}^{M\times M}$ and $\boldsymbol{V}_D \in \mathbb{R}^{N\times N}$ are orthonormal matrices containing the left and right singular vectors of $\boldsymbol{D}$, respectively, and $\boldsymbol{\Sigma}_D \in \mathbb{R}^{M\times N}$ is a diagonal matrix containing the singular values of $\boldsymbol{D}$. Calculations proceed more easily using a semi-positive definite matrix, and thus, we define

$$\boldsymbol{B} \equiv \boldsymbol{D}^\intercal \boldsymbol{D} \,, \tag{3.4}$$

where $\boldsymbol{B} \in \mathbb{R}^{N\times N}$ is semi-positive definite. The SVD of $\boldsymbol{B}$ is

$$\boldsymbol{B} = \boldsymbol{U}_B \boldsymbol{\Sigma}_B \boldsymbol{V}_B^\intercal = \boldsymbol{D}^\intercal \boldsymbol{D} = \boldsymbol{V}_D \boldsymbol{\Sigma}_D \boldsymbol{U}_D^\intercal \boldsymbol{U}_D \boldsymbol{\Sigma}_D \boldsymbol{V}_D^\intercal = \boldsymbol{V}_D \boldsymbol{\Sigma}_D^2 \boldsymbol{V}_D^\intercal = \boldsymbol{Q}\boldsymbol{\Lambda}\boldsymbol{Q}^{-1} \,, \tag{3.5}$$

where $\boldsymbol{U}_B = \boldsymbol{V}_B = \boldsymbol{V}_D = \boldsymbol{Q} \in \mathbb{R}^{N\times N}$ are the right singular vectors of $\boldsymbol{D}$, and $\boldsymbol{\Sigma}_B = \boldsymbol{\Sigma}_D^2 = \boldsymbol{\Lambda} \in \mathbb{R}^{N\times N}$ contain the square of the singular values of $\boldsymbol{D}$. Note that the SVD of $\boldsymbol{B}$ is

equivalent to the eigenvalue decomposition of $\boldsymbol{D}$, i.e., $\boldsymbol{Q}$ and $\boldsymbol{\Lambda}$ contain the eigenvectors and eigenvalues of $\boldsymbol{D}$, respectively. A semi-positive matrix guarantees that the singular values in $\boldsymbol{\Sigma}_B$ are non-negative, and we sort the values in decreasing order, i.e., $\sigma_1 \geq \sigma_2 \geq \ldots \sigma_M \geq 0$, where

$$\boldsymbol{\Sigma} = \begin{bmatrix} \sigma_1 & 0 & \ldots & 0 \\ 0 & \sigma_2 & \ldots & 0 \\ \vdots & \vdots & \ddots & \vdots \\ 0 & 0 & \ldots & \sigma_M \end{bmatrix} . \tag{3.6}$$

This sorting ensures that the decomposition is unique up to degenerate singular values and that the vectors contained in $\boldsymbol{Q}$ are sorted in order of importance, i.e., the zeroth-order vector $\boldsymbol{q}_1$ is the fundamental mode of $\boldsymbol{D}$. The basis $\boldsymbol{P} \in \mathbb{R}^{M \times N}$ is now formed by projecting these modes back onto the snapshots, i.e.,

$$\boldsymbol{p}_i = \boldsymbol{D}\boldsymbol{q}_i \quad \text{for} \quad i \in [0, 1, \ldots, M] \,, \tag{3.7}$$

or

$$\boldsymbol{P} = \boldsymbol{D}\boldsymbol{Q} \,, \tag{3.8}$$

where $\boldsymbol{q}_i$ is the ith column of $\boldsymbol{Q}$ and $\boldsymbol{p}_i$ is the ith POD basis vector and ith column of $\boldsymbol{P}$. Finally, the matrix $\boldsymbol{P}$ is orthonormalized to construct the basis. This method provides N basis vectors of length M, which closely approximate the snapshots of length M contained in $\boldsymbol{D}$. A complete basis is formed by the first M basis vectors if $N \geq M$, and, thus, any vector of length M can be represented exactly using the first M vectors in $\boldsymbol{P}$.

For most applications, creating the basis is complete at this step, but the DGM method requires that the zeroth vector is flat. Thus a vector of ones is inserted as the first column of $\boldsymbol{P}$ changing the size to $\boldsymbol{P} \in \mathbb{R}^{M \times N+1}$. The basis is reorthonormalized, and the resulting vectors are ready for use with the DGM method.

As an example, consider the set of vectors presented graphically in Fig. 3.1. The energy space of a 44-group structure has been divided into four coarse-group regions as indicated by

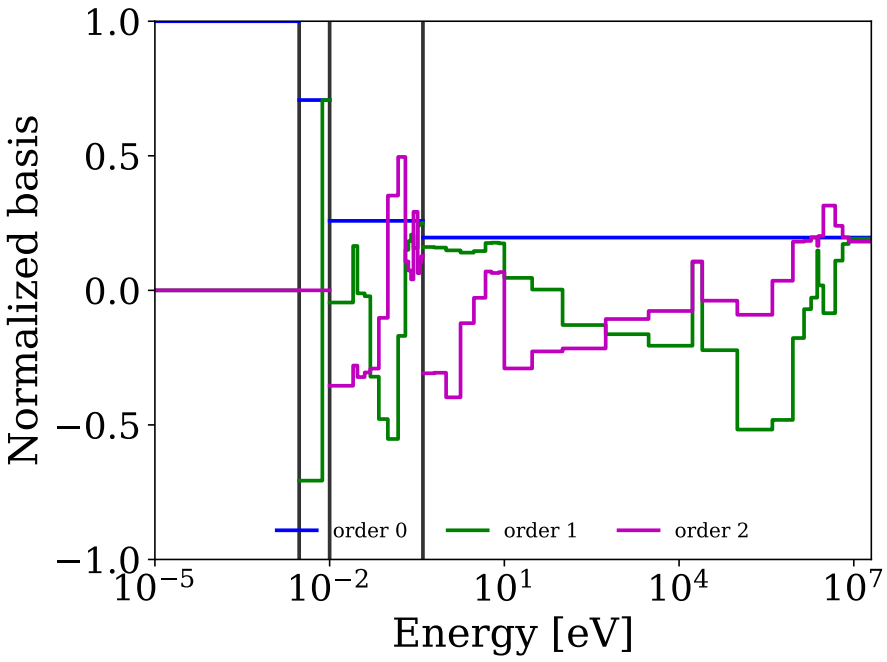

Figure 3.1: POD vectors applied to a 44-group spectrum. Vertical bars show the boundaries between the coarse groups. The basis is orthogonalized over each coarse group.

the vertical bars in the figure. In order of decreasing energy, these coarse groups contain 26, 15, 2, and 1 fine groups. Notice that each group structure uses a different orthogonal basis except for the zeroth, which is the normalized flat function in each case. The figure shows the so-called POD_combine basis, which is described in Chapter 4.

During basis creation, the POD method also creates a matrix holding the singular values, which is $\mathbf{\Sigma}_D$ from Eq. (3.3). Each of these values provides a measure of the significance of the corresponding singular vector. By plotting these values, one may gain insight into how much information is lost due to truncation. For the vectors shown in Fig. 3.1, the corresponding singular values are presented in Fig. 3.2. In the figure, CG=0 corresponds to the highest energy coarse group, and the singular values for all four coarse groups are presented in decreasing order. When a basis is truncated to a given order, information is lost, and the extent of the information loss is related to the magnitudes of the singular values. This work did not seek to predict the performance of a basis from the singular values, but such a prediction could provide a means to further refine a successful basis.

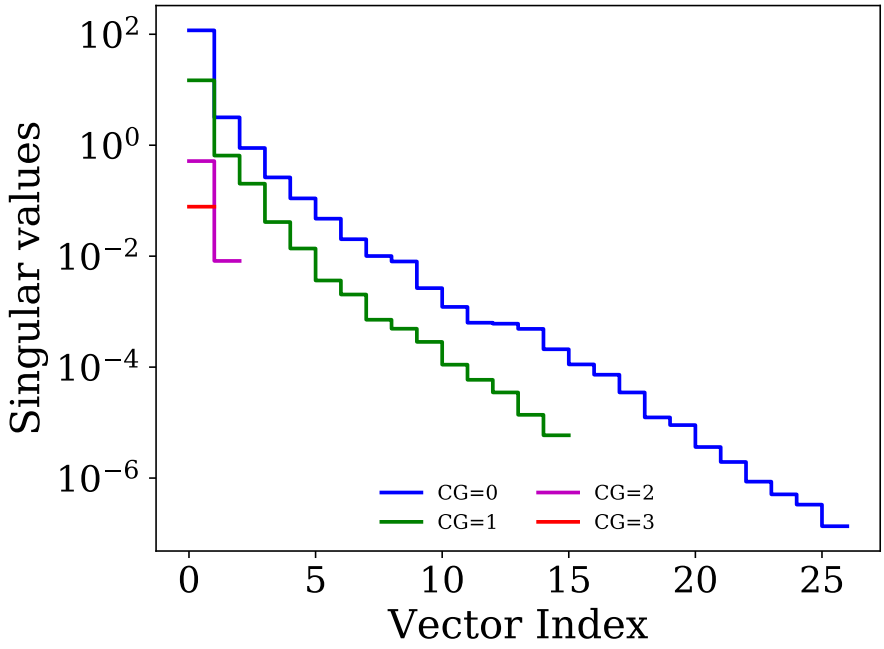

Figure 3.2: Singular values of the POD vectors applied to a 44-group spectrum. These are the singular values corresponding to the vectors shown in Fig. 3.1. CG=0 corresponds to the highest energy coarse group.

3.2 Unotran

To test the performance of a new basis for the DGM method, a one-dimensional (1-D) transport code using the discrete-ordinates solver was developed. The discrete-ordinates solver was not accelerated and written in the FORTRAN language. The underlying routines were wrapped with Python using the `f2py` package, and, thus, the solver can be called in a Python script. The source code is available in an open-source repository[49].

In the discrete-ordinates solver, a 16-angle Gauss Legendre quadrature and the diamond difference spatial discretization were used. It was previously shown that the DGM method is not exact for high-order, spatial discretization methods (e.g., diamond difference)[23]; however, the induced error was found to be much smaller than the error introduced by truncating the basis for the tested problems in this manuscript, i.e., the spatial-discretization error does not impact the results.

Isotropic scattering was assumed in the test problems, though the solver was implemented

to handle anisotropic scattering expanded using a Legendre representation. As described in Appendix B, anisotropic scattering reduced the stability of the DGM method for the selected test problems, and, thus, was not pursued further in this work.

Finally, the Scale 44, Scale 238, and the ECCO 1968 group structures were used in this work. These group structures were incorporated into Serpent[6] to generate cross sections. The cross sections generated using these group structures are described in Appendix A.

Chapter 4

Energy Truncation Results

The discrete generalized multigroup method as discussed in Chapter 2 has previously been implemented using the Legendre polynomials (both discrete and continuous versions) and similar, traditional bases. When the energy variable is represented with a complete (full order) basis, the choice of basis has little impact on the resulting flux vector and reaction rates. However, when truncated, the resulting vector can be quite different depending on how much information the basis can preserve in the lowest orders. A basis constructed using proper orthogonal decomposition, which was the topic of Chapter 3, is designed to preserve much more information in the low orders as compared to Legendre polynomials. While DGM with a truncated basis will contain some amount of error in the flux vector and reaction rates relative to a reference, DGM using a POD basis should have less error than the DLP basis.

This chapter explores how the DGM method performs with a truncated basis set. In particular, several different POD bases are constructed using different sets of snapshots. The performance of these POD bases is compared against the DLP basis as a function of truncation to determine both what information provides a good basis for DGM as well as if the method is viable with a truncated basis.

Several test problems were defined, and each test problem was explored using several, distinct basis sets. The first problem studied, presented in Section 4.1, is an infinite medium problem. This problem was used to ensure that DGM can be used with a truncated basis

in the absence of spatial effects. The second problem studied is a 1-D, 10-pin "slab reactor" and is presented in Section 4.2. This spectrally challenging problem serves to illustrate the performance of truncated DGM in the presence of rather extreme coupled space-energy heterogeneities. Additional, 1-D test problems were defined based loosely on a BWR core design, and are presented in Section 4.3. These BWR problems are more challenging than the other 1-D problems in this chapter, and the results provide some insight into how performance is expected to change as spatial heterogeneity increases. Finally, a preliminary application of truncated DGM to 2-D models was made with the use of a multi-assembly reactor that represents a simplified version of the C5G7 benchmark. These results are shown in Section 4.4. This problem extends the method to two spatial dimensions, which serves as further validation of the method. The chapter concludes in Section 4.5 with a summary of the general behavior of truncated basis sets.

To evaluate the success of a truncated basis, each test problem was solved using a truncated basis at varying order. After converging to the tolerance, the DGM solution was compared to a reference solution computed using the standard, multigroup, discrete-ordinates method. For any truncated basis, some information is lost, which introduces error into the solution. This chapter seeks to quantify this error and its dependence on the choice of basis.

The metric used in this chapter for describing the degree of truncation is the (number of energy) degrees of freedom (DOF). To compute the DOF for the tested cases, we first need a coarse-group structure, which is generated as discussed in Section 3.2. As an example, assume that a 44-group structure is to be collapsed into 3 coarse groups, which contain 37, 6, and 1 fine groups, respectively. The zeroth-order case uses a single degree of freedom per coarse group, which results in three DOF. The first-order case uses two degrees of freedom per coarse group, but the final group is already full order; thus, five DOF are used. This process continues until 43rd-order, which is full order, and the DGM solution is no longer truncated. Each test problem was analyzed using a different group structure (based on the cross sections for that problem); each structure is described in the corresponding section.

4.1 Infinite Medium

4.1.1 Problem Description

The first problem is an infinite medium containing UO_2, which was modeled in 1-D, slab geometry as five cells subject to reflective boundary conditions. Each cell has a length of 1 cm, which gives the total problem a length of 5 cm. This problem was chosen to prove that a truncated basis can be used successfully with DGM. Although spatially trivial, the infinite medium problem is energy dependent and the DGM method is fundamentally a method for treating the energy variable. Thus, this problem is the first step in testing the DGM method with truncated basis sets.

Two POD-driven basis sets were applied to this infinite-medium problem. Snapshots for the first basis were generated from a single UO_2 pin model with reflective conditions, and this basis set is called POD_uo2. Note that this model has *spatial dependence* and, hence, no snapshot from this model represents the true, infinite-medium spectrum. The second basis is called POD_inf and uses snapshots from the infinite medium problem, i.e., the application problem of interest. In both cases, snapshots of the spatially-dependent scalar flux are used as described in Chapter 3. In the latter case, spatial variation only arises from convergence tolerances; in principle, the snapshots would *not* vary in space.

The POD basis sets are compared to the traditional discrete Legendre polynomials. It is expected that POD_inf will perform the best as snapshots of the actual solution are used. Since there is no spatial variation, the error in the DGM solution is expected to be equal to the error tolerance using 2 degrees of freedom per coarse group. Note that the POD_uo2 basis is using heterogeneous snapshots to predict the homogeneous test problem, which provides some insight into how successful imperfect snapshots can perform.

For this problem, the fine-group structure is collapsed into a number of coarse groups for use with DGM. The method for doing so is detailed in Appendix B, but the resulting structures are presented in Table 4.1. From the table, the 44-group structure was collapsed to three coarse groups, whereas the 238-group structure was collapsed to 16 coarse groups.

Table 4.1: Coarse-group (CG) structures for the infinite medium problem. The numbers represent the fine groups included within each coarse group.

	44-group	238-group
CG 1	1-37	1-56
CG 2	38-43	57-78
CG 3	44	79-107
CG 4		108-109
CG 5		110-118
CG 6		119-120
CG 7		121-128
CG 8		129-136
CG 9		137
CG 10		138-166
CG 11		167-226
CG 12		227-231
CG 13		232-234
CG 14		235-236
CG 15		237
CG 16		238

4.1.2 Results

For the infinite medium problem, POD is largely unnecessary because no spatial variation is present. As such, the system can be captured with a single snapshot, which is observed in Fig. 4.1. In Fig. 4.1a, one can see the error in the k-eigenvalue as a function of truncation for various basis sets using the 44-group structure. The error is relative to the reference eigenvalue from a discrete ordinates solution of the test problem. Figure 4.1b shows the error for the scalar flux as a band of errors ranging from the minimum to the maximum errors as a function of space.

As observed in both figures, the choice of basis greatly impacts the truncation error. When a basis vector is the solution (as in POD_inf), the method is equivalent to the reference within numerical precision. A basis composed of similar snapshots (as in POD_uo2) performs better than the discrete Legendre polynomials (DLP). The DLP vectors are dissimilar to the scalar flux, and thus, require many DOF to accurately represent the solution in the DGM method.

Figure 4.2 shows the errors for the 238-group structure. Notice that the relative success

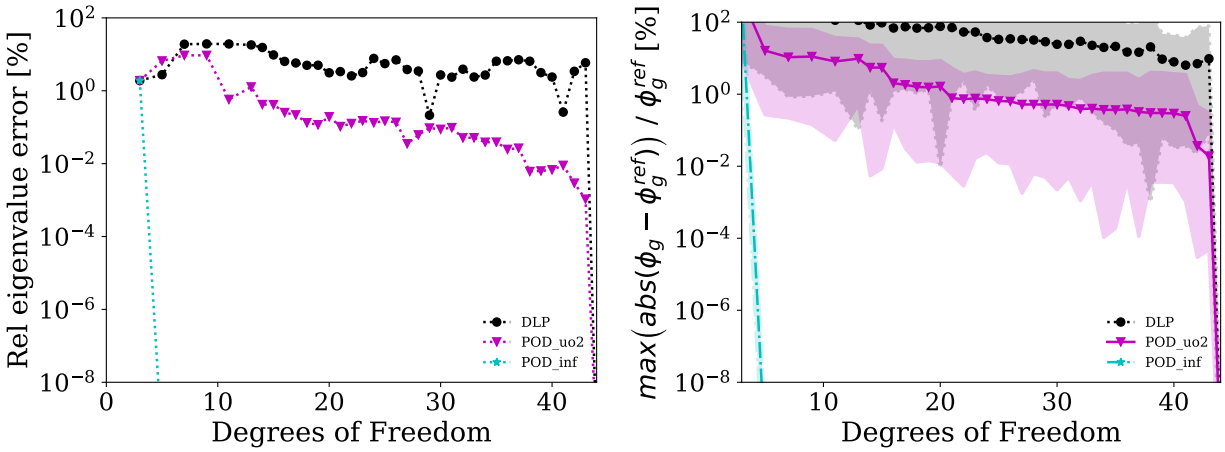

(a) Eigenvalue error

(b) Scalar flux error

Figure 4.1: 44-group infinite medium problem

of a basis set is similar to that of the 44-group structure. Also, note that all basis sets used for DGM require that the zeroth-order basis function be the flat function. Thus, all basis sets share the same error for zeroth order as they are equivalent.

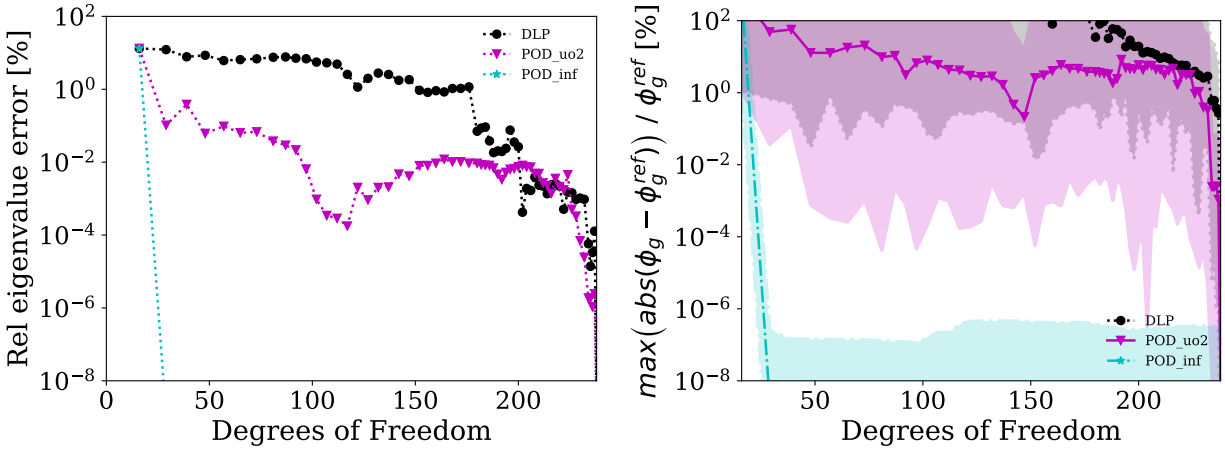

(a) Eigenvalue error

(b) Scalar flux error

Figure 4.2: 238-group infinite medium problem

4.2 10-pin Results

4.2.1 Problem Description

The next test problem selected for this work is a simple 1-D model of the material junction between two assemblies as shown in Fig. 4.3, which is adapted from previous work[50]. The geometry consists of five UO_2 pincells adjacent to five mixed oxide (MOX) pincells. The boundary condition on either side of the model was reflective. This problem serves as a small jump in difficulty from the infinite medium problem. The 10-pin problem contains multiple materials that have different, cross-section resonances, and, hence, serves as a useful test case for the coarse-group selection technique (as discussed in Appendix B) needed by the DGM method. Moreover, because the problem is quick to solve, it provides a useful vehicle for determining the ideal snapshot information required for a successful, truncated basis.

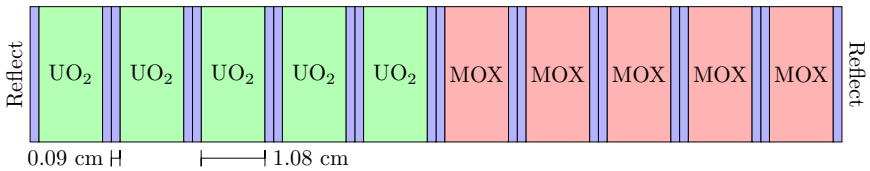

Figure 4.3: Configuration for the 10-pin Test Problem

Fuel regions were 1.08 cm thick with 0.09 cm of the moderator on each side. Each fuel section (UO_2/MOX) was meshed using 22 cells, and each moderator section (blue) was meshed using 3 cells, and, thus, the model had a total of 280 spatial cells. The UO_2 fuel was selected to be approximately 2.2% enriched as discussed in Appendix A, where the methods to generate cross sections and the material compositions are presented.

For this test problem, five POD basis sets were created. The first two utilized snapshots from either a single UO_2 pin or a single MOX pin and are called POD_uo2 and POD_mox, respectively. These basis sets are expected to perform relatively poorly as snapshot information is missing from half of the problem. The next basis set combines snapshots from both of the single pin solutions to form the POD_pins basis.

Next, snapshots were taken from a problem with a UO_2 pin adjacent to a MOX pin with reflective conditions (i.e., a 2-pin problem). These snapshots were combined with those from

the two individual pins to form the POD_combine basis set. The final basis set was formed using snapshots from the true solution, which is called POD_full. Note that POD_full is highly impractical as the solution is required to approximate the solution. However, this basis provides insight into the potential best performance of a POD basis.

The coarse-group structures used for this problem are presented in Table 4.2. From the table, the 44-group structure was collapsed to four coarse groups, the 238-group structure was collapsed to 29 coarse groups, and the 1968-group structure was collapsed to 68 coarse groups.

Table 4.2: Coarse-group (CG) structures for the 10-pin problem. The numbers represent the fine groups included within each coarse group. The number in parenthesis (e.g., (+20)) is the number to add to the coarse group to get the proper index, i.e., CG 1 for column (+20) is actually CG 21.

	44-group	238-group		1968-group			
add'l. #	(+0)	(+0)	(+20)	(+0)	(+20)	(+40)	(+60)
CG 1	1-26	1-56	206-209	1-60	1201-1260	1656	1898
CG 2	27-41	57-107	210-225	61-120	1261-1320	1657	1899
CG 3	42-43	108-109	226-228	121-180	1321-1380	1658	1900
CG 4	44	110-118	229-231	181-240	1381	1659-1668	1901-1929
CG 5		119-120	232-233	241-300	1382-1391	1669-1728	1930-1935
CG 6		121-136	234-235	301-360	1392	1729-1788	1936-1964
CG 7		137	236	361-420	1393-1449	1789-1791	1965-1967
CG 8		138-172	237	421-480	1450	1792	1968
CG 9		173-177	238	481-540	1451-1465	1793	
CG 10		178-179		541-600	1466	1794	
CG 11		180		601-660	1467-1517	1795	
CG 12		181		661-720	1518	1796	
CG 13		182		721-780	1519	1797-1830	
CG 14		183-185		781-840	1520-1527	1831-1890	
CG 15		186		841-900	1528-1587	1891-1892	
CG 16		187		901-960	1588	1893	
CG 17		188		961-1020	1589	1894	
CG 18		189		1021-1080	1590	1895	
CG 19		190		1081-1140	1591-1595	1896	
CG 20		191-205		1141-1200	1596-1655	1897	

4.2.2 Results

The results for the 44-group, 10-pin problem begin with Fig. 4.4 in which the errors as a function of DOF for both the k-eigenvalue and the spatial-cell fission density are shown. Similarly to the infinite medium problem, the k-eigenvalue error results in Fig. 4.4a show that a successful basis utilizes snapshots that are similar to the application, i.e., the 10-pin core. In this case, the POD_uo2 and POD_mox performed similarly to the DLPs, which is to say, poorly under truncation. However, POD_pins and POD_combine performed nearly as well as POD_full despite containing snapshots from simplified problems. The junction information in POD_combine seems to provide little benefit when the basis is compared to POD_pins. The two basis sets performed quite similarly, yet POD_pins used a smaller set of snapshots.

Figure 4.4b shows the maximum error for the fission density among the 220 fuel cells relative to the 10-pin reference solution. The truncated DGM method produces fission density errors of about two orders of magnitude larger than k-eigenvalue errors. However, the relative performance of the basis sets is quite similar. Note that at full order (i.e., the right-most point on the figures) that the solution is no longer truncated and the DGM solution matches the reference fine-group solution to within the convergence tolerance.

Figure 4.5 contains the errors for the 44-group, scalar flux relative to the reference solution. To compute the data, the maximum relative error was found for each energy group, which results in a spatially-dependent error for each DOF. The data points shown are the average over space, which is a shaded region representing the range of spatial errors. On average the POD_combine basis set slightly outperforms POD_pins for all except the most truncated solutions. As observed previously, the DLPs do not perform well under truncation for this problem.

Figure 4.6 contains the k-eigenvalue and fission density errors for the 238-group structure, while Fig. 4.7 contains the scalar flux errors. As compared to the 44-group results, 238-group basis sets perform as expected. The relative errors are approximately equal for the same expansion order (number of points from the left side of the figures). Additionally, the relative performance of the basis sets was quite similar to the 44-group results.

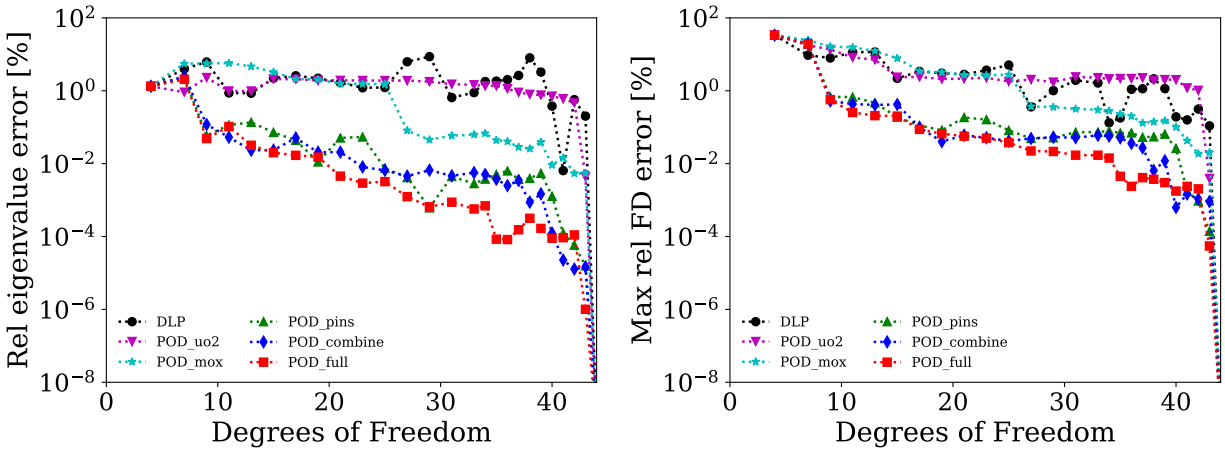

(a) Eigenvalue error

(b) Fission density error

Figure 4.4: 44-group 10-pin problem

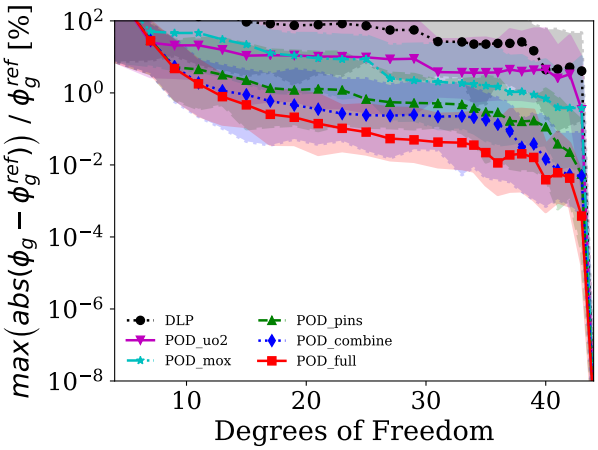

Figure 4.5: Scalar flux error for 44-group, 10-pin problem

The 1968-group structure results are presented in Fig. 4.8 and Fig. 4.9. Overall, the relative performance of the basis sets is similar to the 44-group and 238-group results. The majority of the accuracy is gained in the first few degrees of freedom for each basis set, which is expected due to the construction of the POD basis. In particular, a 0.1% error in the fission density is found using only 4 DOF per coarse group and the POD_combine basis.

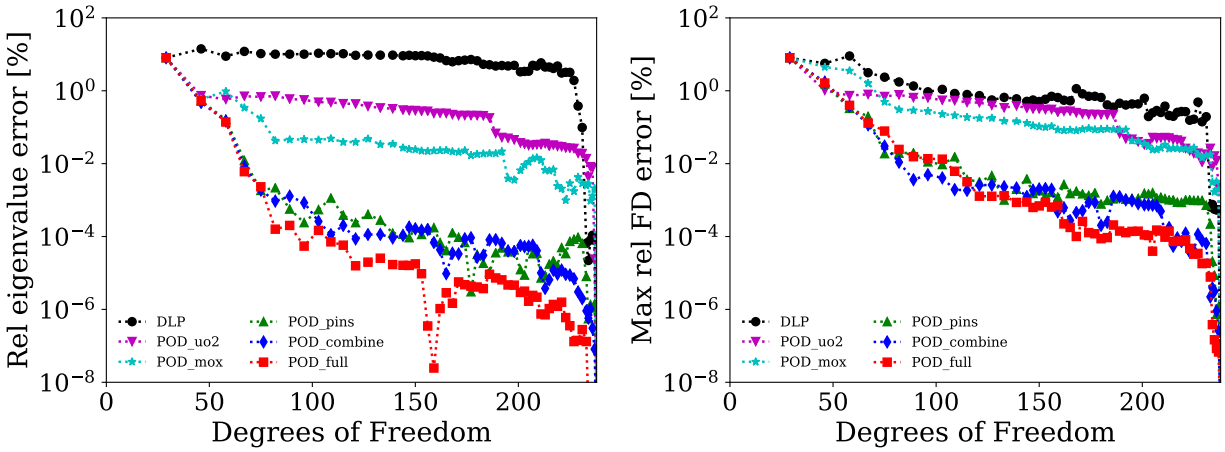

(a) Eigenvalue error

(b) Fission density error

Figure 4.6: 238-group 10-pin problem

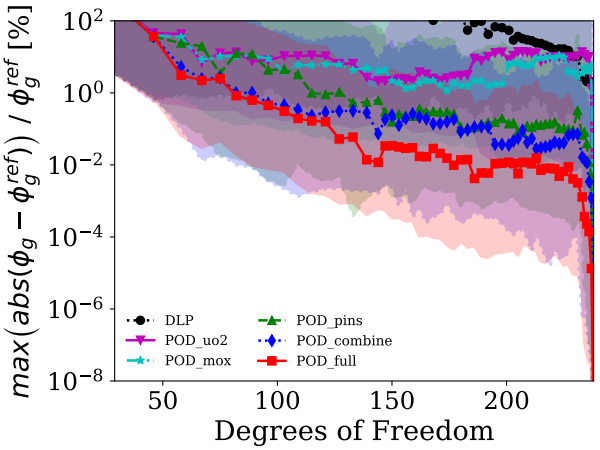

Figure 4.7: Scalar flux error for 238-group, 10-pin problem

4.3 BWR Results

4.3.1 Problem Description

Another set of test problems was designed to represent a heterogeneous bundle of fuel akin to a boiling water reactor (BWR). The 1-D core designs of these two problems are presented in Fig. 4.10, which are adapted from previous work[22]. Each core design is comprised of seven assemblies, and each assembly consists of 6 material regions, which are four 3.2512 cm fuel regions surrounded by 1.1176 cm of water. In this work, configuration one means the design

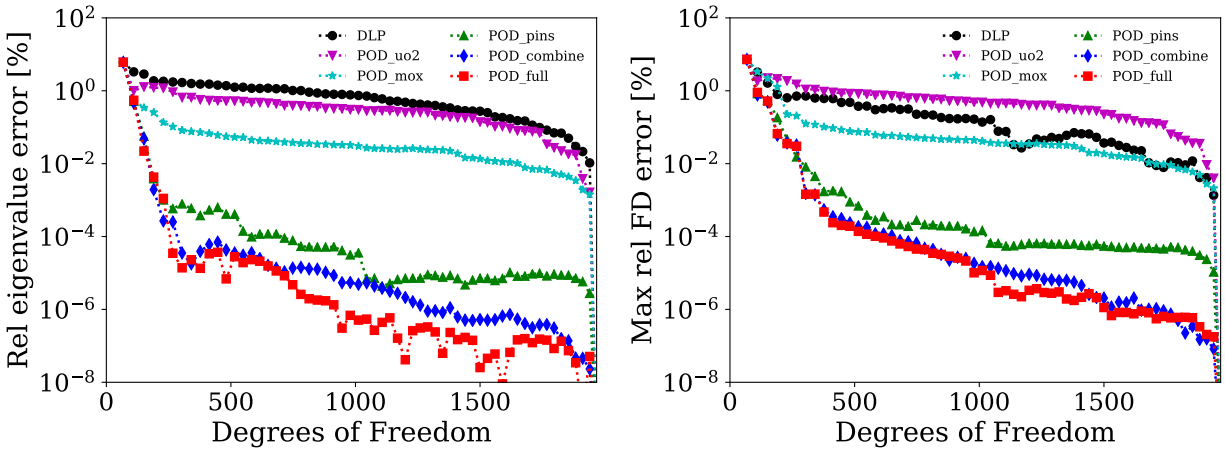

(a) Eigenvalue error

(b) Fission density error

Figure 4.8: 1968-group 10-pin problem

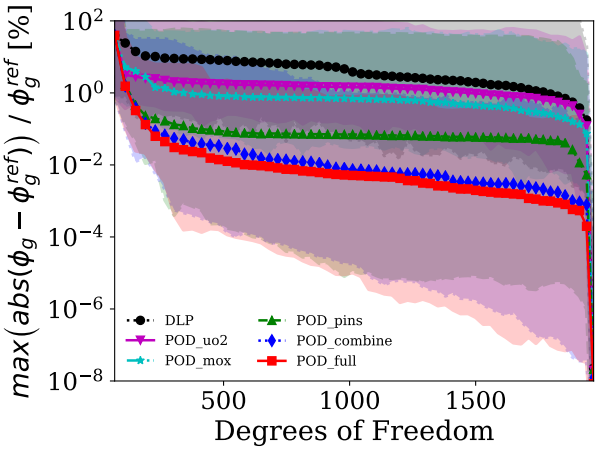

Figure 4.9: Scalar flux error for 1968-group, 10-pin problem

including the UO_2-Gd fuel, whereas configuration two means the design using MOX fuel.

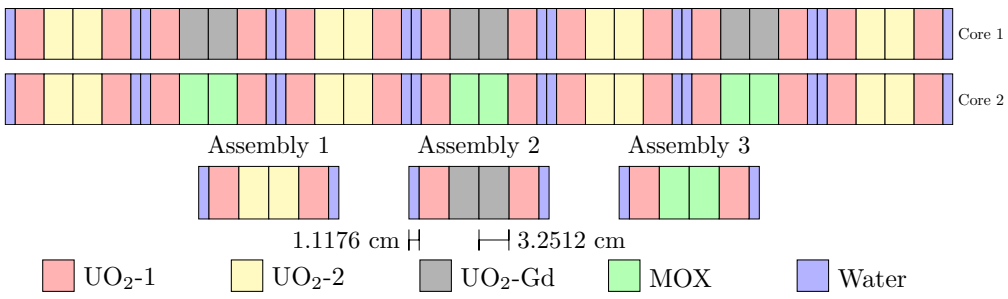

Figure 4.10: Configuration for the BWR Test Problem

Three different types of assemblies were created, which feature different fuel materials on

the interior. The model for configuration one is comprised of assemblies one and two, while configuration two is comprised of assemblies one and three. Each assembly was modeled with two water regions on the sides and four fuel regions in the middle. The water regions were 1.1176 cm long and used six spatial cells each, whereas each fuel region was 3.2512 cm long and used 18 spatial cells. Thus, each assembly measured 15.24 cm and used 84 spatial cells. The total length of the seven assemblies in a core model was 106.68 cm and was modeled using 588 spatial cells.

Three UO_2 fuels were used for the BWR type problems. The first was approximately 2.2% enriched, which was called UO_2-1. The second was approximately 3.6% enriched, which was named UO_2-2. The final UO_2 variant was approximately 4.0% enriched and also contained the poison gadolinium, which was named UO_2-Gd. The MOX fuel contained approximately 3.6% enriched UO_2 mixed with isotopes of neptunium, plutonium, and americium. The material compositions are detailed in Appendix A.

As in the previous problems, the fine-group structures are collapsed into a number of coarse groups for use with DGM. The method for doing so is detailed in Appendix B, but the resulting structures are presented in Table 4.3 for configuration one and Table 4.4 for configuration two. All three group structures (44-group, 238-group, and 1968-group) were used for both configurations. For configuration one, the 44-group structure was collapsed to 12 coarse groups, the 238-group structure was collapsed to 34 coarse groups, and the 1968-group structure was collapsed to 72 coarse groups. Structures for configuration two were collapsed to 4, 29, 68 coarse groups for the 44-group, 238-group, and 1968-group structures, respectively.

The POD basis types used for the two configurations are quite similar. Each problem used four POD basis sets in addition to the DLP basis. The first POD basis was formed similarly to POD_pins from the 10-pin problem, but the snapshots come from pins using the materials in the BWR problem (i.e., configuration one used snapshots from a UO_2-1 pin, a UO_2-2 pin, and a UO_2-Gd pin). For simplicity, the basis will remain named POD_pins, but note that the basis is different for each test problem.

The next POD basis is constructed from snapshots extracted from assembly models.

Table 4.3: Coarse-group (CG) structures for the BWR problem configuration one. The numbers represent the fine groups included within each coarse group. The number in parenthesis (e.g., (+20)) is the number to add to the coarse group to get the proper index, i.e., CG 1 for column (+20) is actually CG 21.

	44-group	238-group		1968-group			
add'l. #	(+0)	(+0)	(+20)	(+0)	(+20)	(+40)	(+60)
CG 1	1-11	1-56	225	1-60	1201-1260	1656	1957
CG 2	12-34	57-78	226	61-120	1261-1320	1657	1958
CG 3	35	79-107	227	121-180	1321-1380	1658	1959
CG 4	36	108-109	228	181-240	1381	1659-1668	1960
CG 5	37	110-118	229	241-300	1382-1391	1669-1728	1961
CG 6	38	119-120	230	301-360	1392	1729-1788	1962
CG 7	39	121-128	231	361-420	1393-1449	1789-1791	1963
CG 8	40	129-136	232	421-480	1450	1792	1964
CG 9	41	137	233	481-540	1451-1465	1793	1965
CG 10	42	138-140	234	541-600	1466	1794	1966
CG 11	43	141-200	235	601-660	1467-1516	1795	1967
CG 12	44	201-214	236	661-720	1517-1518	1796	1968
CG 13		215-216	237	721-780	1519	1797-1820	
CG 14		217-218	238	781-840	1520-1527	1821-1880	
CG 15		219		841-900	1528-1587	1881-1940	
CG 16		220		901-960	1588	1941-1949	
CG 17		221		961-1020	1589	1950-1951	
CG 18		222		1021-1080	1590	1952-1953	
CG 19		223		1081-1140	1591-1595	1954-1955	
CG 20		224		1141-1200	1596-1655	1956	

All three assemblies from Fig. 4.10 were modeled with reflective conditions, and scalar flux snapshots were used to construct the next two basis sets. For configuration one, POD_assay_12 was formed using snapshots from both assembly types used in the model (assembly 1 and assembly 2). Similarly, configuration two uses a basis called POD_assay_13. Additionally, both configurations use the basis called POD_assay_all, which uses snapshots from all three models, thus including snapshots, which are dissimilar to those in the configuration.

The final basis is POD_core#, where # is replaced by the configuration number for the respective test problem. This basis is constructed using snapshots of the test problem itself, i.e., the solution was used to form the basis to approximate the solution. Although this basis is impractical for any real application, it again serves as a useful comparison as to the best possible performance of a POD basis.

Table 4.4: Coarse-group (CG) structures for the BWR problem configuration two. The numbers represent the fine groups included within each coarse group. The number in parenthesis (e.g., (+20)) is the number to add to the coarse group to get the proper index, i.e., CG 1 for column (+20) is actually CG 21.

	44-group	238-group		1968-group			
add'l. #	(+0)	(+0)	(+20)	(+0)	(+20)	(+40)	(+60)
CG 1	1-26	1-56	206-209	1-60	1201-1260	1656	1898
CG 2	27-41	57-107	210-225	61-120	1261-1320	1657	1899
CG 3	42-43	108-109	226-228	121-180	1321-1380	1658	1900
CG 4	44	110-118	229-231	181-240	1381	1659-1668	1901-1929
CG 5		119-120	232-233	241-300	1382-1391	1669-1728	1930-1935
CG 6		121-136	234-235	301-360	1392	1729-1788	1936-1964
CG 7		137	236	361-420	1393-1449	1789-1791	1965-1967
CG 8		138-172	237	421-480	1450	1792	1968
CG 9		173-177	238	481-540	1451-1465	1793	
CG 10		178-179		541-600	1466	1794	
CG 11		180		601-660	1467-1517	1795	
CG 12		181		661-720	1518	1796	
CG 13		182		721-780	1519	1797-1830	
CG 14		183-185		781-840	1520-1527	1831-1890	
CG 15		186		841-900	1528-1587	1891-1892	
CG 16		187		901-960	1588	1893	
CG 17		188		961-1020	1589	1894	
CG 18		189		1021-1080	1590	1895	
CG 19		190		1081-1140	1591-1595	1896	
CG 20		191-205		1141-1200	1596-1655	1897	

4.3.2 Results

The following results are divided into separate sections for each of the two configurations. The first section will showcase results from configuration one, which used the fuel that contained gadolinium. The results from configuration two, which used MOX fuel, will follow.

4.3.3 Configuration 1

The results for the 44-group, configuration one test problem are presented in Fig. 4.11 and Fig. 4.12. Similarly to the 10-pin test problem, the eigenvalue errors in Fig. 4.11a are smaller than those for the fission density (Fig. 4.11b) and the scalar flux (Fig. 4.12) by nearly two orders of magnitude. Again the errors are compared against the degrees of freedom used in

the truncated DGM problem. Also, note that at full order (DOF=44), basis sets are complete (i.e., no truncation) and the DGM results match the reference discrete ordinance solution to the convergence tolerance.

From these figures, we can see that all POD basis sets perform similarly for the first few orders within a coarse group. At higher orders, POD_core1 is the best performing, which is expected as it is formed from the solution snapshots. POD_assay_12 performs nearly as well as POD_core1, whereas POD_assay_all performs slightly worse. This shows that including POD snapshots for assemblies that are not present in the actual test problem can decrease performance. We also see that POD_pins, the worst performing POD basis tested, still greatly outperforms DLP.

Similar trends are observed for the 238-group structure. The k-eigenvalue errors are located in Fig. 4.13a, and the fission density errors are presented in Fig. 4.13b. Scalar flux errors are presented in Fig. 4.14. Again, we can observe that the majority of the gains from a POD basis are located in the low orders. For example, a 0.01% error in the fission density can be represented by approximately 75 degrees of freedom using the POD_assay_12 basis, which is approximately 6 DOF per coarse group.

Once again, we can observe similar relative performance between the basis sets for the 1968-group structure. Figure 4.15 showcases the eigenvalue and fission density errors, while Fig. 4.16 contains the scalar flux errors. From Fig. 4.15b, a 0.01% error in the fission density can be achieved using approximately 300 DOF in the POD_assay_12 basis, which is approximately 8 DOF per coarse group.

4.3.4 Configuration 2

The second configuration, which included MOX fuel instead of gadolinium poisoned UO_2, was found to be slightly easier to capture using DGM as compared to configuration one. This manifests in slightly reduced errors for a constant DOF. Again, results are shown for all three group structures (44-group, 238-group, and 1968-group) in the form of k-eigenvalue, fission density, and scalar flux errors. All errors are relative to a discrete ordinates reference using

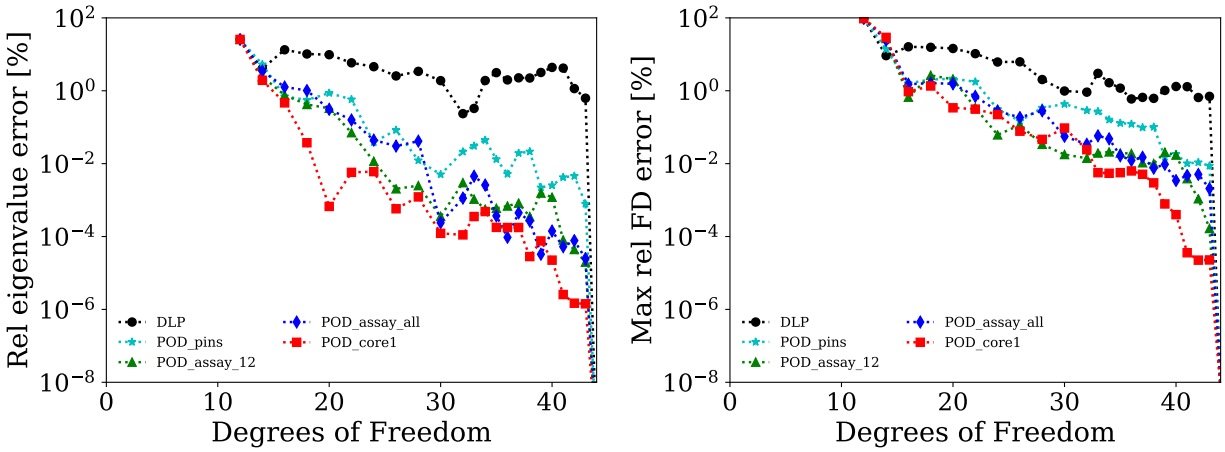

(a) Eigenvalue error

(b) Fission density error

Figure 4.11: 44-group BWR-1 problem

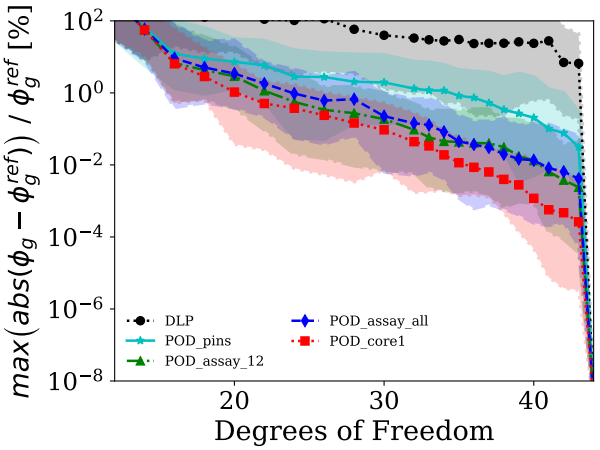

Figure 4.12: Scalar flux error for 44-group, BWR-1 problem

the same fine-group structure as the respective DGM problem.

Figure 4.17 contains the 44-group results for the k-eigenvalue and fission density errors, while Fig. 4.18 presents the scalar flux errors as a function of degrees of freedom. As in the other test problems, the relative performance of the basis sets was similar to prediction. The POD_core2 basis performed the best but is impractical as it requires the correct solution *a priori*. POD_assay_13 performed nearly as well as the core basis despite losing the assembly interaction snapshots. POD_assay_all performed nearly the same as POD_assay_13, which suggests that the extra snapshots from the gadolinium fuel did not strongly affect the solution. Finally, POD_pins performed surprisingly well despite missing snapshots of any material

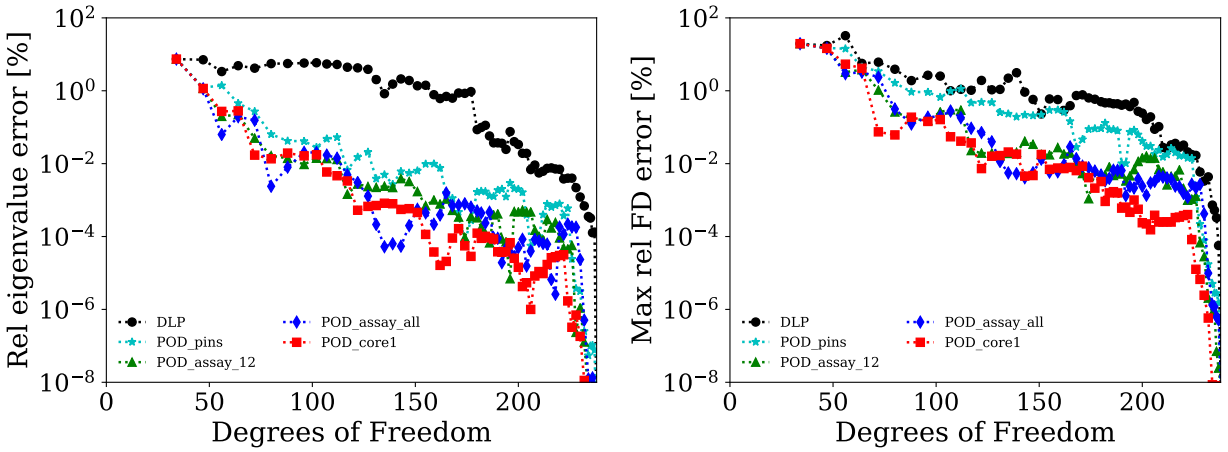

(a) Eigenvalue error

(b) Fission density error

Figure 4.13: 238-group BWR-1 problem

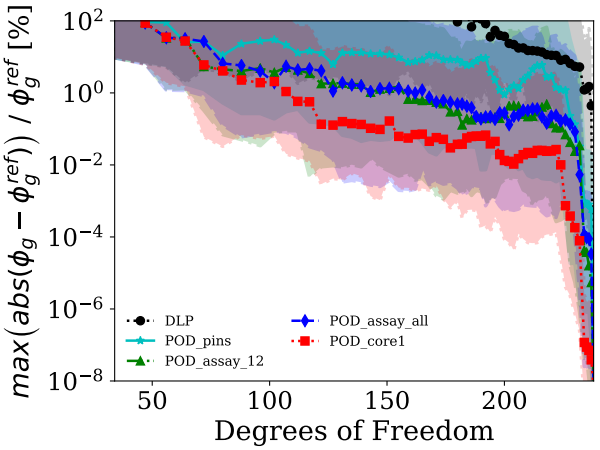

Figure 4.14: Scalar flux error for 238-group, BWR-1 problem

interactions.

The 238-group results for the k-eigenvalue are presented in Fig. 4.19a, and the fission density errors are located in Fig. 4.19b. Scalar flux errors are shown in Fig. 4.20. Again, we see similar relative performance between the different basis sets, and every POD basis outperformed the DLP basis. Note once again that DGM requires a flat basis function as the zeroth basis, so all basis sets perform identically at one DOF per coarse group, which is the left-most point on each of the figures. For the 238-group structure, approximately 6 DOF are required per coarse group (about 75 total DOF) to achieve 0.01% error in the fission density.

Finally, the 1968-group results for the k-eigenvalue and fission densities are shown in

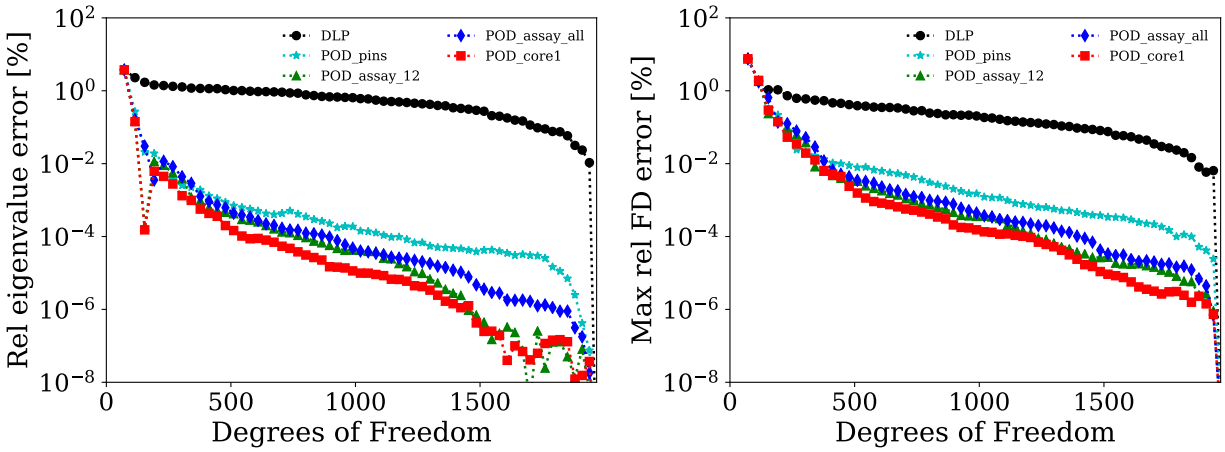

(a) Eigenvalue error

(b) Fission density error

Figure 4.15: 1968-group BWR-1 problem

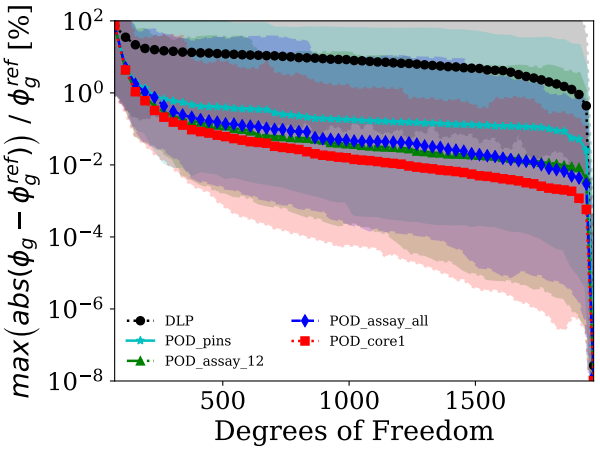

Figure 4.16: Scalar flux error for 1968-group, BWR-1 problem

Fig. 4.21, and the scalar flux errors are located in Fig. 4.22. Once again, similar relative performance is observed for the POD basis sets, and the k-eigenvalue error is approximately two orders of magnitude lower than the fission density error for a constant DOF. A 0.01% error in the fission density can be achieved using approximately 7 DOF per coarse group (approximately 275 DOF total) and the POD_assay_13 basis.

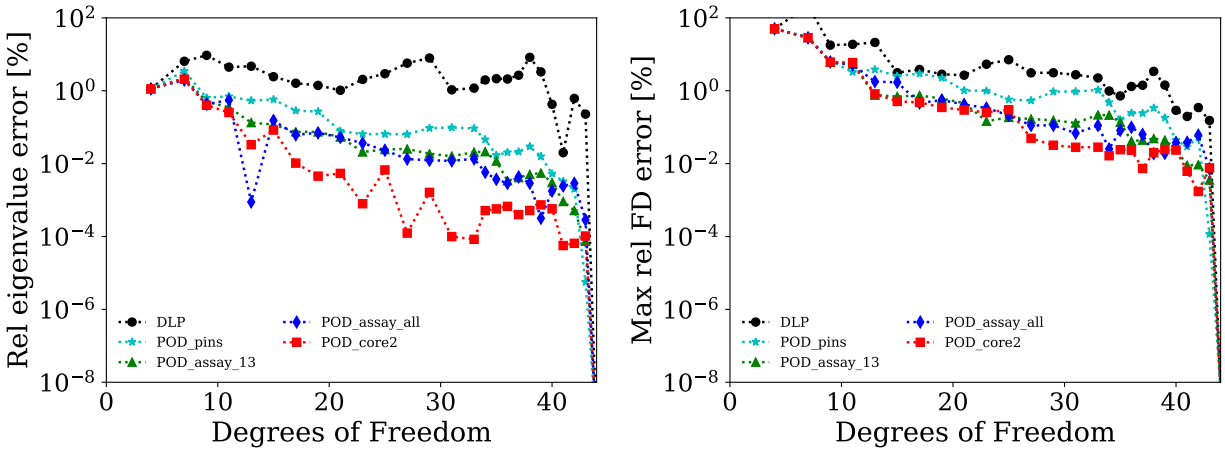

(a) Eigenvalue error

(b) Fission density error

Figure 4.17: 44-group BWR-2 problem

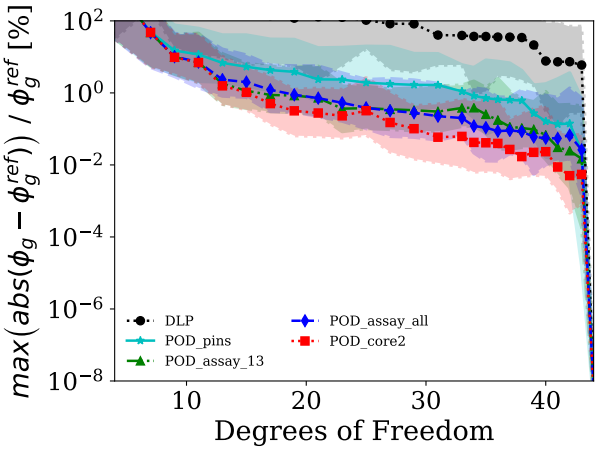

Figure 4.18: Scalar flux error for 44-group, BWR-2 problem

4.4 2-D Results

4.4.1 Problem Description

The final test problem is a two-dimensional structure, which uses the same materials as the 10-pin problem discussed in Section 4.2. A diagram of the geometry is presented in Fig. 4.23, where the colors refer to the same materials as in the 10-pin problem. Each pincell is divided into 64 spatial cells as shown in Fig. 4.24, which gives a total of 46656 spatial cells in the problem. Each pincell has a pitch of 1.26 cm, and the boundaries for the divisions are

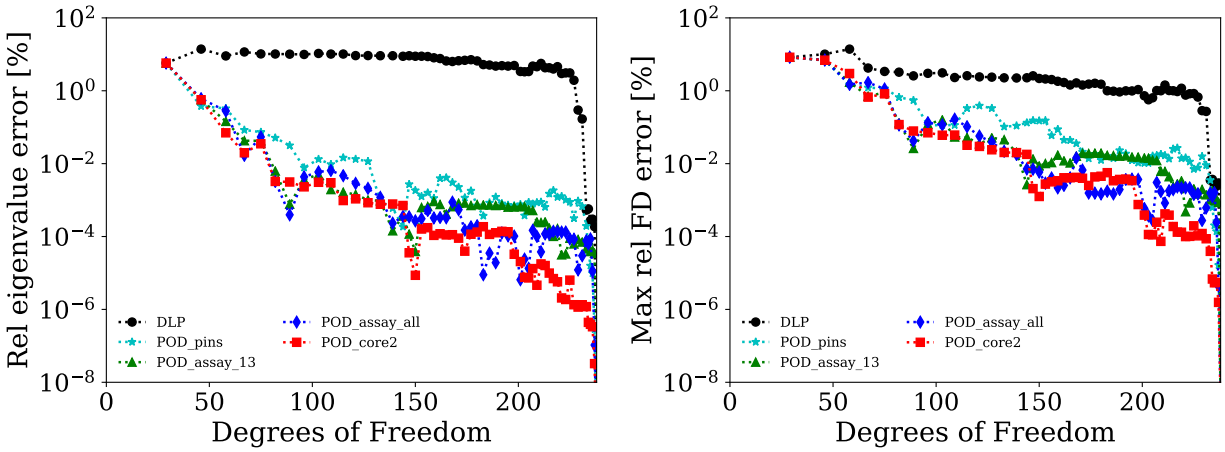

(a) Eigenvalue error

(b) Fission density error

Figure 4.19: 238-group BWR-2 problem

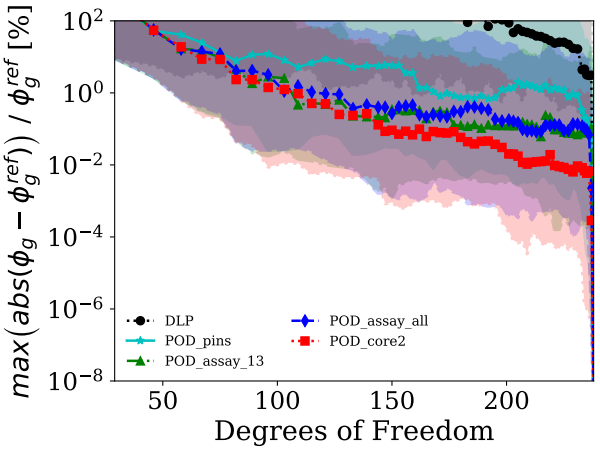

Figure 4.20: Scalar flux error for 238-group, BWR-2 problem

at 0.1015 cm, 0.1967 cm, 0.43133 cm, 0.639015 cm, 0.8467 cm, 1.0633 cm, and 1.1585 cm. Boundary conditions for the problem were vacuum on the bottom and right sides of Fig. 4.23 and reflective on the top and left sides.

For this test problem, four POD basis sets were created. The first utilized snapshots from pincells of either UO_2 MOX and was called POD_2D_pins. The second POD basis modeled a 9x9 pin assembly with reflective conditions for both UO_2 and MOX fuels and combined the snapshots to form the POD_2D_assays basis.

The next basis set was formed using snapshots from the true solution, which is called POD_2D_full. Note that POD_2D_full is highly impractical as the solution is required to

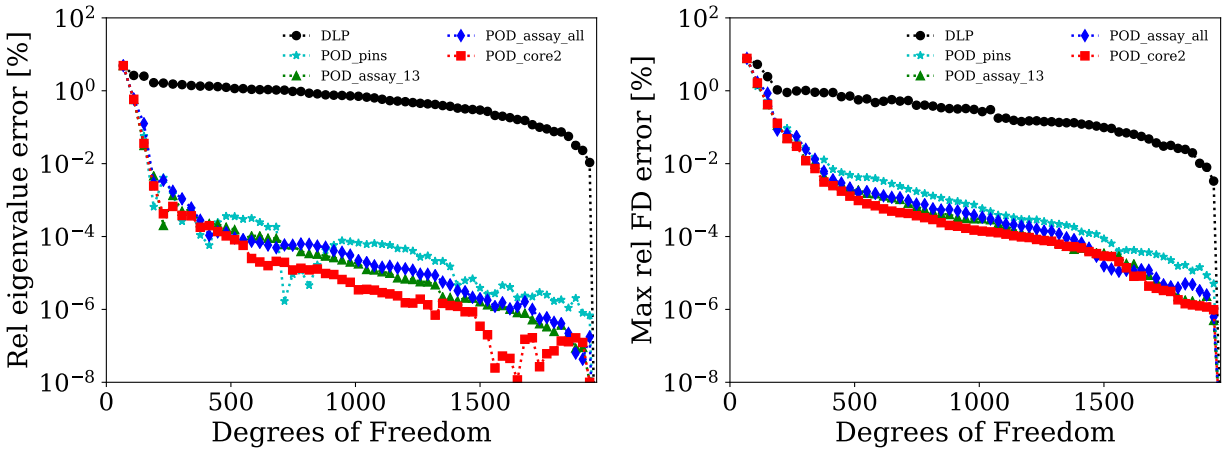

(a) Eigenvalue error

(b) Fission density error

Figure 4.21: 1968-group BWR-2 problem

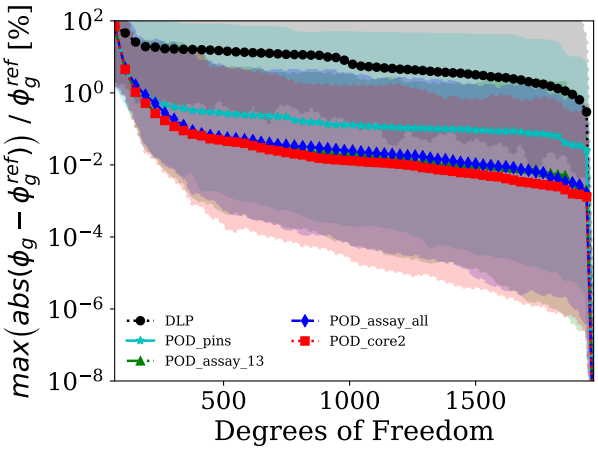

Figure 4.22: Scalar flux error for 1968-group, BWR-2 problem

approximate the solution. However, this basis provides insight into the best performance of a POD basis.

The final basis set was the basis POD_1D which formed from the same snapshots as POD_pins from the 1-D, 10-pin problem. This basis was inexpensive and contained much of the same information as the more expensive 2-D models. Due to computational cost, only the 44-group structure was used for the 2-D problem, and the corresponding coarse-group structure is presented in Table 4.5. From the table, the 44-group structure was collapsed to six coarse groups. Also due to computational costs, each order is only converged to 1×10^{-6}, which should be enough to see the relative performance of the basis sets, but could contribute

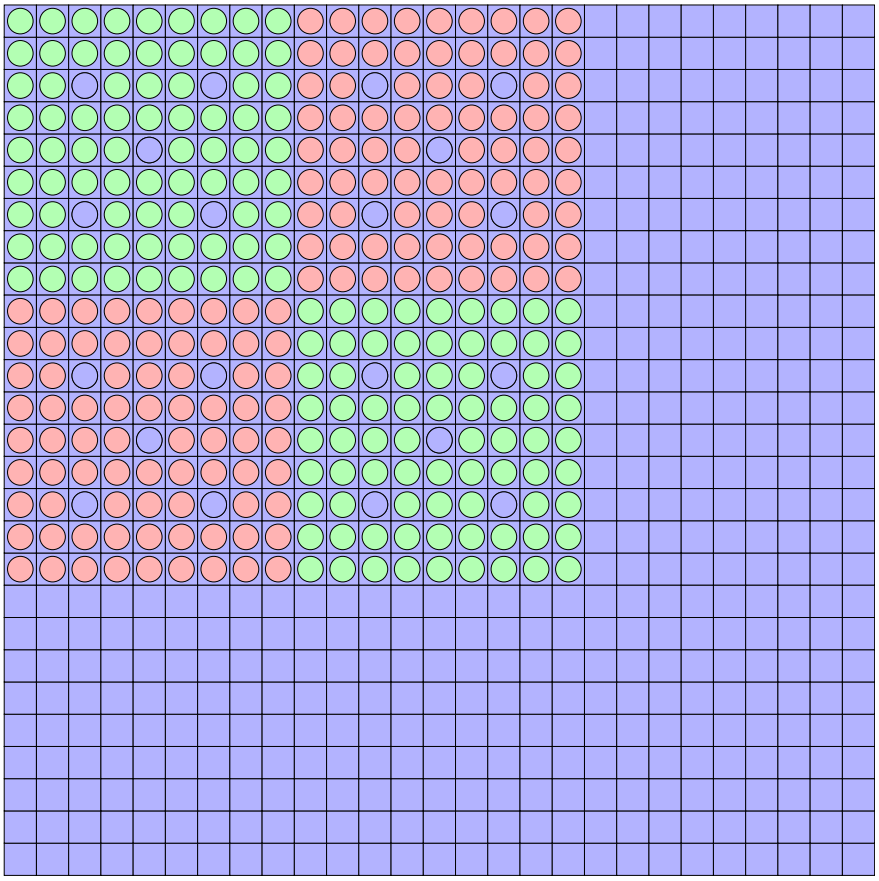

Figure 4.23: Configuration for the 2-D Test Problem

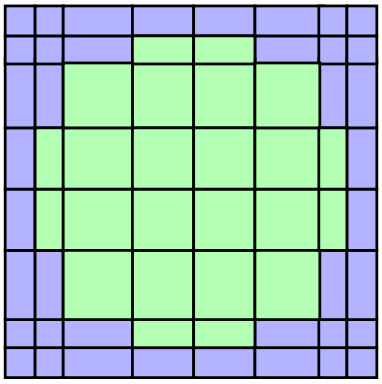

Figure 4.24: Spatial mesh for each pincell in the 2-D Test Problem

to a systematic bias in the results. Note that the test code described in Section 3.2 was unaccelerated, which means that this 2-D problem requires far more computational resources than the 1-D problems in this chapter.

Table 4.5: Coarse-group (CG) structures for the 2-D problem. The numbers represent the fine groups included within each coarse group.

coarse group	group bounds
CG 1	1-11
CG 2	12-28
CG 3	29-30
CG 4	31-41
CG 5	42-43
CG 6	44

4.4.2 Results

The results for the 44-group, 2-D problem begin with Fig. 4.25 wherein the errors as a function of DOF for both the k-eigenvalue and the spatial-cell fission density are shown. The 2-D problem was considerably more unstable than the 1-D problems and required a Krasnoselskii coefficient of less than 0.1 for convergence. Additionally, the errors are larger than the 1-D cases, which suggests that this problem was harder for DGM to capture details. All errors are relative to a discrete ordinates reference using the same fine-group structure as the respective DGM problem.

Figure 4.25 contains the 44-group results for the k-eigenvalue and fission density errors, while Fig. 4.26 presents the scalar flux errors as a function of degrees of freedom. The POD_2D_full basis performed the best but is impractical as it requires the correct solution *a priori*. POD_2D_assays performed nearly as well as the full basis despite losing the assembly interaction snapshots. Finally, POD_2D_pins performed about the same as POD_1D;

Figure 4.5 contains the errors for the 44-group, scalar flux relative to the reference solution. To compute the data, the maximum relative error was found for each energy group, which results in a spatially-dependent error for each DOF. The data points shown are the average over space, which is a shaded region representing the range of spatial errors. On average POD_2D_assays performed nearly as well as POD_2D_full. As observed previously, the DLPs do not perform well under truncation when used with DGM.

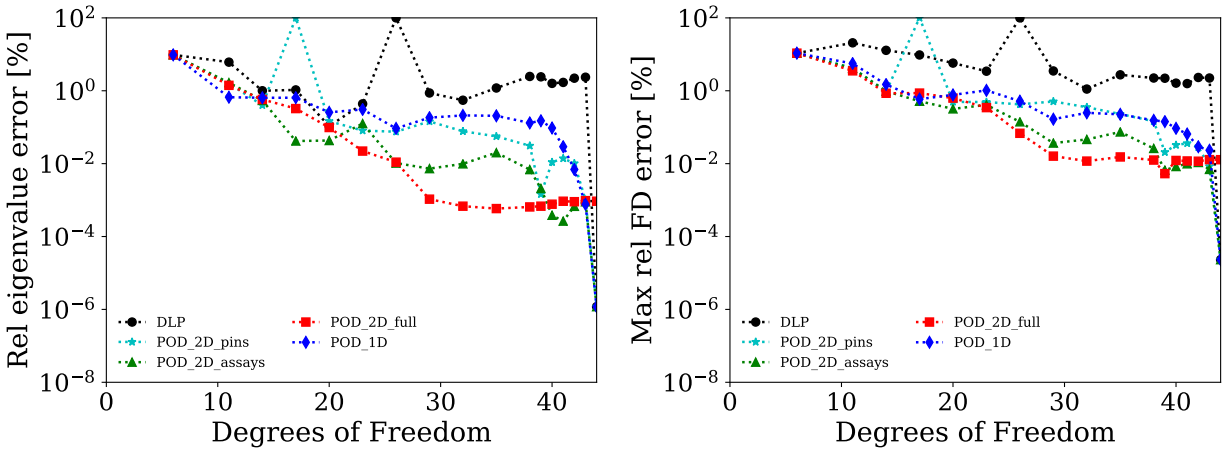

(a) Eigenvalue error

(b) Fission density error

Figure 4.25: 44-group 2-D problem

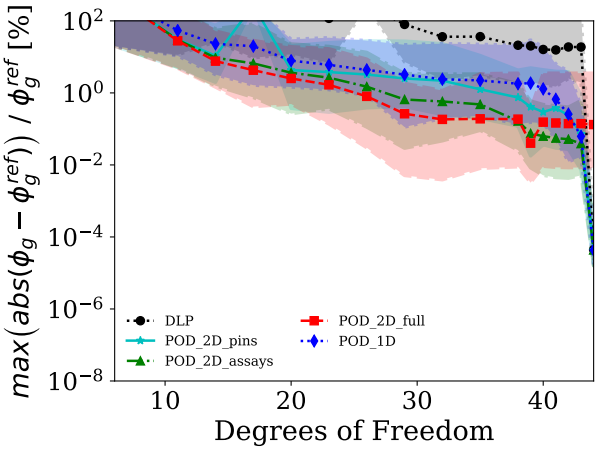

Figure 4.26: Scalar flux error for 44-group, 2-D problem

4.5 Conclusions

From these test problems, it is clear that a properly constructed POD basis is far superior to DLP for reducing errors in a truncated DGM solution. Without truncation, all basis sets provide the same solution, which is identical to that of the reference discrete ordinates solution within convergence tolerance. However, with truncation, the DGM method will disregard the higher-order moments of cross sections and fluxes, which result in lost information. A good basis set allows capturing the shape of the cross sections and fluxes in few orders, which can be easily achieved using a POD basis.

A POD basis is formed from snapshots, which are attained by solving small models, which are similar to the test problem. In other words, we can solve several pincell models to create a basis, which will approximate a full core. The results in this chapter show that a successful POD basis for use in DGM contains snapshots of all fuel types. For the 10-pin problem, the POD_pins model outperformed POD_uo2 and POD_mox, which shows that all fuel types should be represented in the snapshots.

Additionally, material junction snapshots help reduce the error. For example, POD_pins (no pin junction) was compared against POD_combine (pin junction) in the 10-pin problem, and POD_combine was found to be superior. This trend continues for the BWR test problems when comparing POD_pins to POD_assay. If the test problem contains heterogeneous core models, which include material junctions, snapshots should be included that capture the junction. The best performing, practical basis for the 10-pin problem was tied for POD_pins and POD_combine, which achieved less than a 0.1% error in the fission density with three DOF per coarse group for the 44-group structure. The same basis sets achieved less than 0.01% error when using four DOF per coarse group for both the 238- and 1968-group structures.

Including snapshots of materials that are not present in the test problem can hurt performance, e.g., POD_assay_12 compared to POD_assay_all for BWR configuration one. When forming the POD basis, the low-order basis functions form an average of the snapshots, so non-present material can shift the functional shape. However, if the extra material snapshots are similar to other materials in the problem (i.e., the UO_2 fuel containing gadolinium, which is similar to non-poisoned UO_2), the functional shape of the low-order basis is not drastically shifted. As an example, POD_assay_13 and POD_assay_all used in BWR configuration two performed quite similarly, which is due to the extra material snapshots being similar to the other snapshots, thus the basis was not drastically altered. For the first configuration, POD_assay_12 was the best performing, practical basis, which achieved 1% error in the fission density with three DOF per coarse group. The 238- and 1968- group structures for the same basis achieved less than 0.1% error in the fission density for the first configuration. Errors for the second configuration were similar to the first configuration.

Using DGM for a 2-D problem proved to be challenging due to instabilities and computa-

tional costs. Since only the 44-group structure was able to be computed in a reasonable time, conclusions for 2-D, higher-group structures must be foregone. However, it seems that as a problem increases in complexity, the truncated DGM method has a harder time capturing the information in low orders, which manifests in larger overall errors compared to the 1-D test problems. It is possible that introducing advanced solution techniques such as GMRES will increase the stability of the method, which would greatly improve the solution speed and potentially the accuracy.

Finally, it seems that for these test problems, approximately the same number of DOF are required per coarse group to achieve a similar error. For most cases, approximately 8 degrees of freedom are needed per coarse group to achieve an error of 0.01% in the fission density relative to the reference solution. This trend seems to persist for the various group structures. Thus, although the required total DOF to achieve an error goal will change for different group structures (as more coarse groups are used), the number of DOF per coarse group is relatively consistent.

Note that the results in this chapter utilized POD bases constructed from snapshots of the scalar flux ϕ, but additional information could be included in the snapshots before computing the POD basis. Preliminary exploration has tested the inclusion of snapshots for the net neutron current as well as snapshots of the total cross sections. These findings can be found in Appendix C, but the summary is that the inclusion of the types of snapshots does not help the performance of the basis at low orders. The inclusion of the new neutron current does seem to improve higher-order expansions, which is consistent with previous work[48] that included snapshots of the neutron current in POD basis sets for applications in the response matrix method.

Chapter 5

Improvements and Approximations for the Discrete Generalized Multigroup Method

As originally implemented, the DGM method is impractical. One of the problems is a large memory footprint due to requiring that the angular flux be stored. Additionally, the cross section moments are dependent on the spatially-dependent scalar flux, and, therefore, the cross section moments are spatially-dependent even if the cross sections themselves are not. This chapter explores a method for reducing these requirements and assesses the error introduced via approximation. In Section 5.1, we introduce several homogenization methods, which are aimed at reducing the memory footprint of the DGM method. The methods are tested on several test problems, which were the same problems described in Chapter 4. Results from the applications are presented in Section 5.2. The chapter concludes with Section 5.3, which includes a summary of the results as well as potential areas of future study.

5.1 Approximations of the cross section moments

The approximations explored in this chapter can be broken into two categories. The first is approximating the spatial dependence of the cross section moments, which is discussed in Section 5.1.1. The second is approximating the angular dependence of the angular flux, which is discussed in Section 5.1.2.

5.1.1 Spatial Homogenization

As discussed briefly in Section 1.5, spatial homogenization is traditionally used in the preparation of cross sections. In particular, it is common to apply a fine-group structure on a detailed, but small, spatial domain (e.g., a pincell) and subsequently to homogenize over that domain to create averaged or "effective" cross sections in a coarser-group structure. These homogenized cross sections are then used for models with larger spatial domains (e.g., assembly or full-core models). The DGM method already collapses the fine-group structure to a coarse-group structure but does not perform any spatial homogenization. The goal of this section is to use spatial homogenization as a way to reduce the memory footprint of DGM and assess the impact of this approximation on error.

We begin by examining the total cross section moments, which were defined in Eq. (2.11) as

$$\Sigma^t_{c,G} = \frac{\sum_{j=0}^{N_j} \phi_{c,G,0,j} \Sigma^{t*}_{c,G,0,j}}{\phi_{c,G,0,0}}, \qquad \text{(2.11 revisited)}$$

where all terms were defined in Chapter 2. The total cross section moments are spatially dependent, and we use traditional flux weighting to average the moments over a spatial region as

$$\Sigma^t_{r,G} = \frac{\sum_{c\in r} \Sigma^t_{c,G} \phi_{c,G,0,0} V_c}{\sum_{c\in r} \phi_{c,G,0,0} V_c} = \frac{\sum_{c\in r} \sum_{j=0}^{N_j} \phi_{c,G,0,j} \Sigma^{t*}_{c,G,0,j} V_c}{\sum_{c\in r} \phi_{c,G,0,0} V_c}, \tag{5.1}$$

where r is a region of space containing spatial cells c, and V_c is the volume of cell c (length in 1-D or area in 2-D). With this definition, a total reaction rate over a region r and coarse

group G is preserved for a known flux. A similar definition can be formed for the scattering and fission terms. Though several approaches exist to homogenize δ in space, it was decided to implement the conventional flux-weighted scheme, i.e,

$$\delta_{r,a,G,i} = \frac{\sum_{c \in r} \delta_{c,a,G,i} \phi_{c,G,0,0} V_c}{\sum_{c \in r} \phi_{c,G,0,0} V_c} \,. \tag{5.2}$$

While many choices for spatial homogenization are available, this work explored two, which were chosen to minimize the deviation from the underlying problem. The first was to homogenize over adjacent spatial cells with the same material, thus instead of a set of cross sections for each fine-mesh cell, the number of material moments was reduced to the number of coarse-mesh cells. Of the two methods, this choice was expected to have a smaller impact with regards to error.

The second choice was to homogenize over all cells with the same material, thus instead of a set of cross section moments for each fine-mesh cell, the number of material moments was reduced to the initial number of materials. This choice provided the best reduction in memory use but was expected to introduce significant error into the DGM method.

5.1.2 Approximating the Angular flux

In addition to storing spatially-dependent cross section moments, the term $\delta_{c,a,G,i}$ is also angular dependent, and, hence, the angular flux must be stored as discussed in Chapter 2. As a reminder, $\delta_{c,a,G,i}$ was defined in Eq. (2.31) as

$$\delta_{c,a,G,i} = \frac{\sum_{j=0}^{N_j} \psi_{c,a,G,j} \Sigma^{t*}_{c,G,i,j}}{\psi_{c,a,G,0}} - \Sigma^t_{c,G} \frac{\psi_{c,a,G,i}}{\psi_{c,a,G,0}} \,. \tag{2.31 revisited}$$

Typically, the angular flux is not stored in practice due to the large memory requirements and the fact that only flux moments are needed for computing reaction rates. Consequently, we explore a method for approximating the angular flux. Assume that angular flux moments

(computed using spherical harmonics) through order L are computed in place of the full angular flux, i.e.,

$$\psi_{c,a,G,i} \approx \sum_{l=0}^{L} \frac{2l+1}{4\pi} \sum_{m=-l}^{l} \phi^{m}_{c,G,i,l} R^{m}_{a,l} \,, \tag{5.3}$$

where $R^{m}_{a,l}$ is the harmonic for degree l and order m evaluated at angle a, and $\phi^{m}_{c,G,l,i}$ is the corresponding flux moment. Using this approximation for ψ, Eq. (2.31) can be approximated using moments of the coarse-group scalar flux instead. For testing this approximation, both a flat approximation ($L = 0$) and a linear ($L = 1$) were used. An alternative definition that should be explored in future work is the direct expansion of the product $\delta_{c,a,G,i}\psi_{c,a,G,0}$ in spherical harmonics for inclusion as a traditional scattering term.

5.2 Approximation Results

In this section, we apply the aforementioned approximations to three different test problems, which were previously used in Chapter 4. Each of these problems was tested using the 44-, 238-, and 1968-group structures, which were discussed in Section 3.2. The coarse-group structures corresponding to each fine-group structure are discussed in the description for each problem in Chapter 4. To test the approximations, several cases were developed. These cases are summarized in Table 5.1. The first is the 10-pin problem, which is presented in Section 5.2.1. The BWR configuration 1 and 2 are presented in Section 5.2.2 and Section 5.2.3, respectively. Finally, the approximations are applied to the 2-D problem in Section 5.2.4.

The first case is the use of the flat approximation of ψ. The second case is to use a linear approximation for ψ. The spatial approximations begin in the third case, where cross section moments were homogenized over adjacent cells of the same material. The fourth case homogenized the cross section moments over all spatial cells sharing a material type. The fifth and final case used both a linear approximation for ψ and homogenized the cross section moments over all similar spatial cells (i.e., combined the second and fourth cases). All five of these cases were explored in the DGM method using a full-order (complete basis) as well as a truncated basis.

Table 5.1: Summary of the test cases used for evaluating the spatial and angular approximations.

Short Name	Description
Full-(1)	Flat approximation of ψ using a complete basis
Full-(2)	Linear approximation of ψ using a complete basis
Full-(3)	Spatial homogenization over coarse-mesh region using a complete basis
Full-(4)	Spatial homogenization over material type using a complete basis
Full-(5)	Both Full-(2) and Full-(4)
Trun.-(1)	Flat approximation of ψ using a truncated basis
Trun.-(2)	Linear approximation of ψ using a truncated basis
Trun.-(3)	Spatial homogenization over coarse-mesh region using a truncated basis
Trun.-(4)	Spatial homogenization over material type using a truncated basis
Trun.-(5)	Both Trun.-(2) and Trun.-(4)
Full-Ref	Reference solution computed using discrete ordinates
Trun.-Ref	Reference DGM solution using a truncated basis but no approximations

For the truncated cases, the basis used a maximum of three degrees of freedom per coarse group, which corresponds to the third point from the left in the figures in Chapter 4. At this point, the truncation error was approximately the same order of magnitude as the approximation cases explored in this chapter. Note that the values presented in this chapter are the power peaking factors for each pincell, which is computed by dividing the fission density within a pincell by the average pincell fission density for the problem. Since the power peaking factors are averaged quantities for the pincell, the errors for this chapter are expected to be smaller than those presented in Chapter 4. All of the cases are compared against a reference, fine-group solution for the same problem.

To compare the homogenization methods, the eigenvalue and power peaking factors are computed for each case as well as the reference for each test problem and group structure. The results are tabulated in the next sections, which present the reference values along with the error of each case relative to that reference.

5.2.1 10-pin results

The first test problem is the 10-pin problem, which is described in Section 4.2. The problem used 280 total spatial cells, which were divided evenly between the 10 pincells. Results using

the 44-group structure are presented in Table 5.2. These results are from using the POD_pins basis.

Table 5.2: 44-group, 10-pin test problem comparison of DGM with and without spatial homogenization and expanded δ. The column "Full-Ref" contains the reference values for k and the power peaking factors. The remaining columns are the percent errors relative to the reference. The Trun cases each used 9 degrees of freedom for the DGM expansion.

	Full-Ref	Full-(1)	Full-(2)	Full-(3)	Full-(4)	Full-(5)
k_{eff}	1.07	-0.30	-0.12	-0.14	-0.72	-0.44
Pin 1	0.95	-2.57	-1.57	-0.13	-11.06	-12.06
Pin 2	0.93	-2.60	-1.57	-0.18	-10.64	-11.49
Pin 3	0.88	-2.61	-1.53	-0.28	-9.47	-10.14
Pin 4	0.78	-2.49	-1.40	-0.40	-7.14	-7.60
Pin 5	0.60	-2.03	-1.10	-0.51	-3.43	-3.67
Pin 6	1.74	0.15	0.13	0.54	-1.67	-1.90
Pin 7	1.14	2.49	1.48	0.10	6.17	6.33
Pin 8	1.02	2.69	1.55	0.07	10.21	10.84
Pin 9	0.99	2.39	1.37	0.02	11.20	12.26
Pin 10	0.98	2.17	1.25	0.00	11.08	12.50

	Full-Ref	Trun.-Ref	Trun.-(1)	Trun.-(2)	Trun.-(3)	Trun.-(4)	Trun.-(5)
k_{eff}	1.07	-0.12	-0.37	-0.22	-0.24	-0.70	-0.47
Pin 1	0.95	-0.28	-2.98	-1.92	-0.38	-10.73	-11.43
Pin 2	0.93	-0.17	-2.89	-1.81	-0.33	-10.27	-10.88
Pin 3	0.88	0.04	-2.69	-1.57	-0.22	-9.06	-9.55
Pin 4	0.78	0.29	-2.29	-1.18	-0.11	-6.72	-7.09
Pin 5	0.60	0.35	-1.70	-0.79	-0.14	-3.10	-3.33
Pin 6	1.74	0.13	0.19	0.17	0.59	-1.32	-1.51
Pin 7	1.14	-0.26	2.32	1.27	-0.15	5.75	5.87
Pin 8	1.02	0.02	2.84	1.68	0.08	9.61	10.07
Pin 9	0.99	0.04	2.59	1.53	0.08	10.64	11.42
Pin 10	0.98	-0.03	2.34	1.35	0.01	10.57	11.64

For this problem, we see that angular approximations (cases 1 and 2) introduced approximately a 1% error into the pin powers, and approximately 0.1% error into the eigenvalue. As shown in Table 5.2, the truncated basis introduced approximately a 0.1% error into the solution when using 9 degrees of freedom. Truncated, angular approximations are slightly less favorable than the complete basis but introduce the same magnitude of error.

The spatial homogenization over coarse-mesh regions (case 3) introduced approximately 0.1% error into both the pin powers and eigenvalue for both the complete and truncated

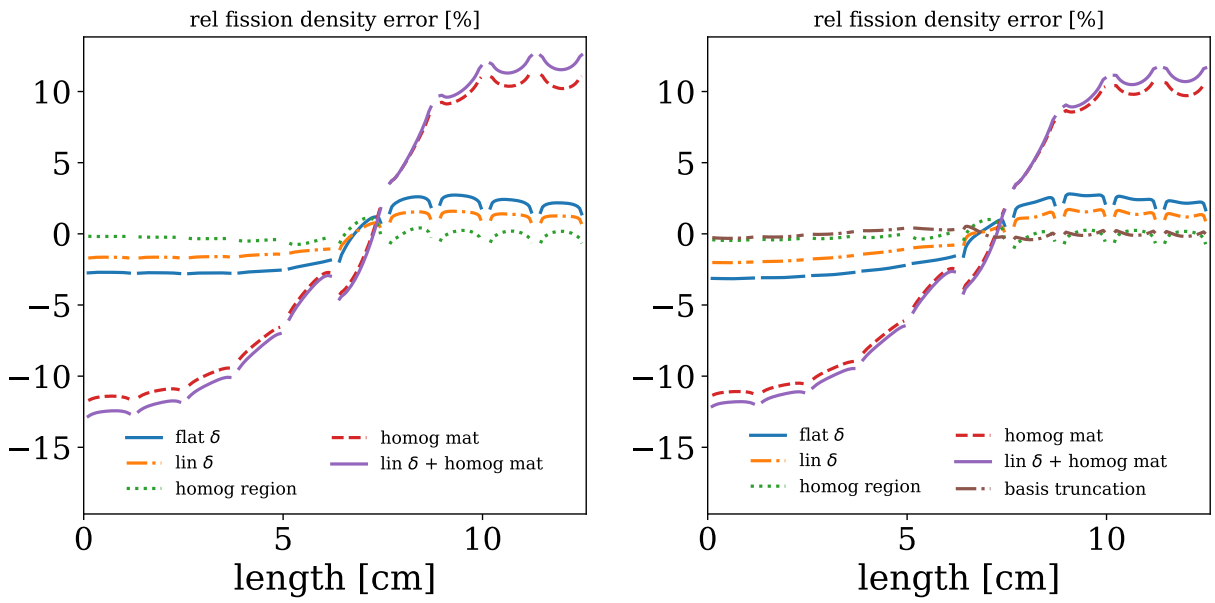

(a) Complete basis

(b) Truncated basis

Figure 5.1: Spatially dependent, relative fission density errors for the 44g, 10-pin problem

basis sets. Apparently favorable error cancellation means that the cost to accuracy is small for using this scheme with a truncated basis. Spatial homogenization over materials (case 4), however, introduced approximately a 10% error into the solution, particularly at the problem boundaries. Adding a linear angular approximation (case 5) slightly increased all errors, but shows that the largest savings to memory came at a cost of approximately a 10% error for the 44-group case.

The spatial dependence of the error is shown in Fig. 5.1, which includes curves for both a complete and a truncated basis used with DGM. Note that the errors presented in the figure are cell fission densities; thus, the figure results show a different quantity than the data presented in Table 5.2 that has been averaged over a spatial region. The errors introduced by truncation are small compared to those in the approximations for the 44-group structure.

Results from the 10-pin problem using the 238-group structure are presented in Table 5.3. Angular approximations (cases 1 and 2) introduced approximately 0.3% error for the power peaking factors and approximately 0.03% error into the eigenvalue. Truncating the basis to 58 DOF introduced approximately 0.1% error. Homogenizing over coarse-mesh regions

Table 5.3: 238-group, 10-pin test problem comparison of DGM with and without spatial homogenization and expanded δ. The column "Full-Ref" contains the reference values for k and the power peaking factors. The remaining columns are the percent errors relative to the reference. The Trun cases each used 58 degrees of freedom for the DGM expansion.

	Full-Ref	Full-(1)	Full-(2)	Full-(3)	Full-(4)	Full-(5)
k_{eff}	1.12	-0.05	0.02	-0.05	-0.25	-0.03
Pin 1	0.94	-0.56	-0.33	-0.06	-1.11	-1.01
Pin 2	0.92	-0.52	-0.30	-0.06	-0.91	-0.89
Pin 3	0.87	-0.44	-0.24	-0.06	-0.68	-0.69
Pin 4	0.77	-0.36	-0.18	-0.06	-0.35	-0.39
Pin 5	0.60	-0.37	-0.19	-0.07	-0.03	-0.08
Pin 6	1.74	-0.06	-0.01	0.15	-0.32	-0.43
Pin 7	1.15	0.31	0.18	-0.07	0.36	0.31
Pin 8	1.03	0.47	0.25	0.02	0.87	0.91
Pin 9	1.00	0.56	0.29	0.02	1.00	1.08
Pin 10	0.99	0.59	0.31	0.02	1.01	1.10

	Full-Ref	Trun.-Ref	Trun.-(1)	Trun.-(2)	Trun.-(3)	Trun.-(4)	Trun.-(5)
k_{eff}	1.12	-0.15	-0.17	-0.14	-0.18	-0.32	-0.16
Pin 1	0.94	0.03	-0.47	-0.28	-0.02	-0.92	-0.89
Pin 2	0.92	0.03	-0.44	-0.26	-0.02	-0.79	-0.81
Pin 3	0.87	0.02	-0.39	-0.22	-0.03	-0.63	-0.66
Pin 4	0.77	-0.02	-0.36	-0.21	-0.07	-0.37	-0.41
Pin 5	0.60	-0.12	-0.44	-0.31	-0.18	-0.14	-0.18
Pin 6	1.74	0.25	0.17	0.20	0.36	0.02	-0.06
Pin 7	1.15	-0.16	0.13	0.02	-0.18	0.28	0.26
Pin 8	1.03	-0.14	0.31	0.13	-0.12	0.65	0.69
Pin 9	1.00	-0.06	0.45	0.25	-0.05	0.75	0.83
Pin 10	0.99	-0.04	0.51	0.29	-0.02	0.73	0.84

(case 3) introduced approximately 0.1% error, whereas homogenizing over material (case 4) introduced approximately 1% error. The largest memory savings (Trunc.-(5)) introduced less than a 1% error for the 238-group case, which is approximately an order of magnitude less than the same case for the 44-group structure.

The spatial dependence of the error is shown in Fig. 5.2, which includes curves for both a complete and a truncated basis used with DGM. Note that the errors presented in the figure are on cell fission densities, thus will not compare directly with the data presented in Table 5.3. From Fig. 5.2, we see that truncating the energy variable seems to provide favorable cancellation of errors, which manifests in slightly reduced errors for the truncated

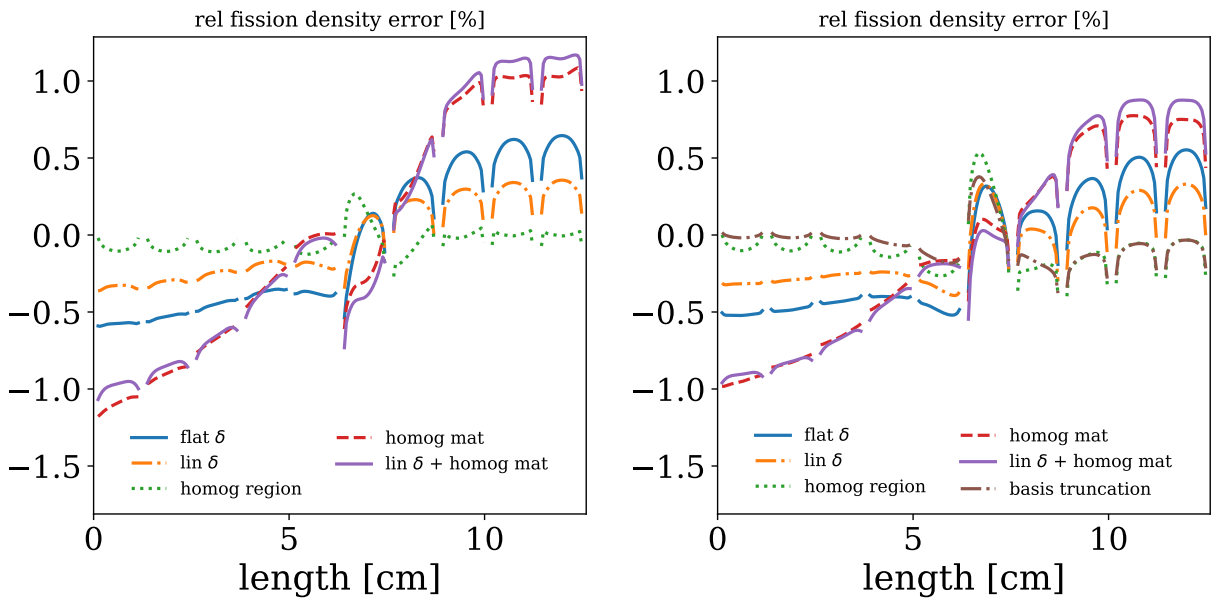

(a) Complete basis

(b) Truncated basis

Figure 5.2: Spatially dependent, relative fission density errors for the 238g, 10-pin problem

basis vs the complete basis.

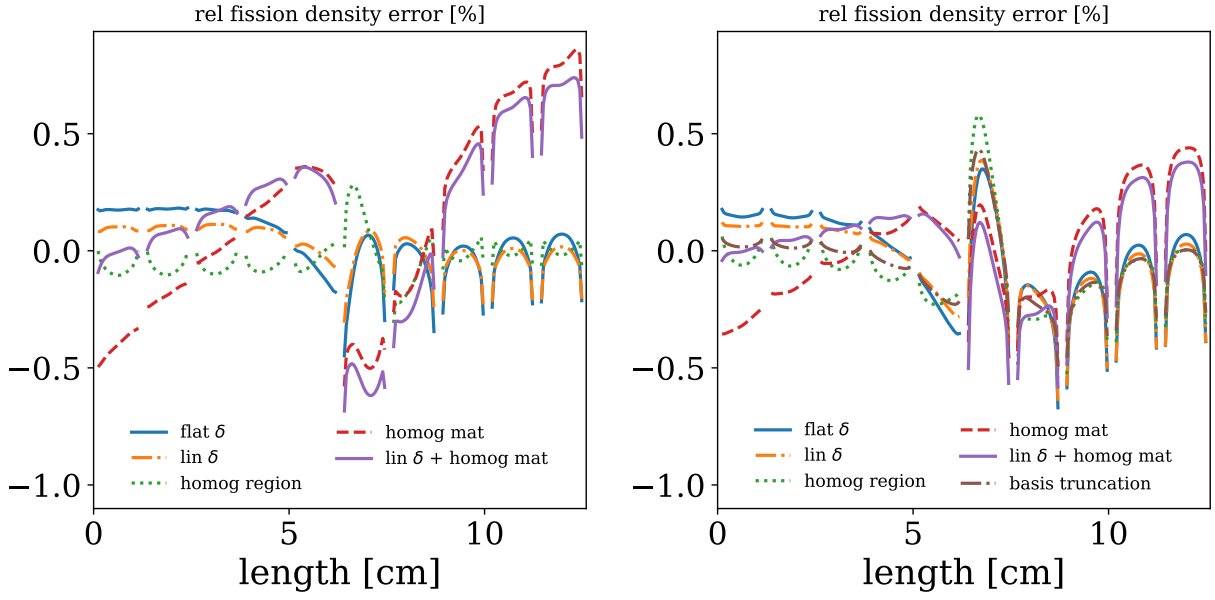

(a) Complete basis

(b) Truncated basis

Figure 5.3: Spatially dependent, relative fission density errors for the 1968g, 10-pin problem

Results from the 10-pin problem using the 1968-group structure are presented in Table 5.4.

Table 5.4: 1968-group, 10-pin test problem comparison of DGM with and without spatial homogenization and expanded δ. The column "Full-Ref" contains the reference values for k and the power peaking factors. The remaining columns are the percent errors relative to the reference. The Trun cases each used 151 degrees of freedom for the DGM expansion.

	Full-Ref	Full-(1)	Full-(2)	Full-(3)	Full-(4)	Full-(5)
k_{eff}	1.15	-0.03	0.00	0.01	-0.04	0.01
Pin 1	0.94	0.15	0.08	-0.05	-0.48	-0.11
Pin 2	0.92	0.15	0.09	-0.05	-0.26	-0.03
Pin 3	0.87	0.15	0.09	-0.05	-0.07	0.06
Pin 4	0.77	0.09	0.07	-0.04	0.13	0.18
Pin 5	0.60	-0.10	-0.02	-0.02	0.27	0.22
Pin 6	1.74	-0.12	-0.05	0.14	-0.53	-0.65
Pin 7	1.15	-0.07	-0.02	-0.10	-0.18	-0.31
Pin 8	1.03	-0.07	-0.06	0.01	0.32	0.22
Pin 9	1.00	-0.04	-0.06	0.02	0.58	0.49
Pin 10	0.99	-0.02	-0.05	0.02	0.71	0.59

	Full-Ref	Trun.-Ref	Trun.-(1)	Trun.-(2)	Trun.-(3)	Trun.-(4)	Trun.-(5)
k_{eff}	1.15	-0.05	-0.07	-0.05	-0.04	-0.07	-0.03
Pin 1	0.94	0.06	0.16	0.13	0.02	-0.32	-0.03
Pin 2	0.92	0.06	0.16	0.13	0.02	-0.17	0.02
Pin 3	0.87	0.04	0.13	0.11	0.00	-0.04	0.07
Pin 4	0.77	-0.02	0.03	0.03	-0.05	0.08	0.11
Pin 5	0.60	-0.15	-0.22	-0.17	-0.16	0.11	0.07
Pin 6	1.74	0.26	0.13	0.19	0.35	-0.02	-0.12
Pin 7	1.15	-0.22	-0.23	-0.22	-0.27	-0.23	-0.33
Pin 8	1.03	-0.17	-0.18	-0.19	-0.16	0.05	-0.03
Pin 9	1.00	-0.06	-0.07	-0.09	-0.05	0.26	0.18
Pin 10	0.99	-0.02	-0.02	-0.04	-0.00	0.35	0.26

Angular approximations (cases 1 and 2) introduced approximately 0.1% error for the power peaking factors and approximately 0.01% error into the eigenvalue. Truncating the basis to 151 DOF introduced approximately 0.1% error. Homogenizing over coarse-mesh regions (case 3) introduced approximately 0.05% error, whereas homogenizing over material (case 4) introduced approximately 0.5% error. The largest memory savings (Trunc.-(5)) introduced less than a 0.2% error for the 1968-group case, which is approximately a third of the error for the same case for the 238-group structure.

The spatial dependence of the error is shown in Fig. 5.3, which includes curves for both a complete and a truncated basis used with DGM. Note that the errors presented in the

figure are for cell fission densities, thus will not compare directly with the data presented in Table 5.4. Again, it seems that truncating the energy variable provides favorable cancellation of errors, which manifests in slightly reduced errors for the truncated basis vs the complete basis.

From these results, the impact of spatial and angular approximations appears to be inversely proportional to the number of energy groups. For the 1968-group structure, the approximations used with a truncated basis introduced approximately the same error as using the truncated basis alone, which is likely due to favorable cancellation of errors.

5.2.2 BWR - Configuration 1 results

This section contains the results from the first BWR configuration, which is described in Section 4.3. The problem used a total of 588 spatial cells divided evenly between seven assemblies. For the results in this section, power peaking factors were computed for each assembly, i.e., the ratio of each assembly fission density to the average assembly fission density was computed. As was the case for the 10-pin problem, the results provided in this section for the assembly powers are expected to be better than those in Chapter 4 as the values are for an entire assembly instead of for individual spatial cell. The results obtained for the truncated case are based on the POD_pins, which is different than the POD_pins basis used for the 10-pin problem as discussed in Section 4.3.

Results from the BWR problem for configuration 1 using the 44-group structure are presented in Table 5.5. Angular approximations (cases 1 and 2) introduced approximately 2% error for the power peaking factors and approximately 0.6% error into the eigenvalue. Truncating the basis to 16 DOF added approximately 0.5% error. Homogenizing over coarse-mesh regions (case 3) introduced approximately 2% error, whereas homogenizing over material (case 4) introduced approximately 5% error. The largest memory savings (Trunc.-(5)) introduced approximately 5% error for the 44-group case, which is approximately half of the error from the 44-group, 10-pin problem.

The spatial dependence of the error is shown in Fig. 5.4, which includes curves for both

a complete and a truncated basis used with DGM. Note that the errors presented in the figure are for cell fission densities, thus will not compare directly with the data presented in Table 5.5. We can see that the largest errors occur near the boundaries, which are vacuum for this problem.

Table 5.5: 44-group, BWR-configuration 1 test problem comparison of DGM with and without spatial homogenization and expanded δ. The column "Full-Ref" contains the reference values for k and the power peaking factors. The remaining columns are the percent errors relative to the reference. The Trun cases each used 16 degrees of freedom for the DGM expansion.

	Full-Ref	Full-(1)	Full-(2)	Full-(3)	Full-(4)	Full-(5)
k_{eff}	0.92	0.62	0.65	-0.04	-0.79	0.59
Assay 1	0.39	-8.45	-4.68	-1.37	-6.91	-6.44
Assay 2	0.54	-2.73	-1.32	-2.45	-6.29	-5.28
Assay 3	2.12	2.44	1.35	1.32	3.82	3.29
Assay 4	0.90	-0.81	-0.67	-2.08	-4.40	-3.52
Assay 5	2.12	2.44	1.35	1.32	3.82	3.29
Assay 6	0.54	-2.73	-1.32	-2.45	-6.29	-5.28
Assay 7	0.39	-8.45	-4.68	-1.37	-6.91	-6.44

	Full-Ref	Trun.-Ref	Trun.-(1)	Trun.-(2)	Trun.-(3)	Trun.-(4)	Trun.-(5)
k_{eff}	0.92	-0.70	-0.14	-0.09	-0.82	-1.40	-0.29
Assay 1	0.39	1.11	-7.98	-4.46	-0.08	-6.83	-6.17
Assay 2	0.54	0.02	-2.61	-1.33	-2.18	-5.64	-4.66
Assay 3	2.12	-0.16	2.32	1.31	1.02	3.51	2.96
Assay 4	0.90	-0.24	-0.77	-0.67	-2.11	-3.79	-2.97
Assay 5	2.12	-0.16	2.32	1.31	1.02	3.51	2.96
Assay 6	0.54	0.02	-2.61	-1.33	-2.18	-5.64	-4.66
Assay 7	0.39	1.11	-7.98	-4.46	-0.08	-6.83	-6.17

Results from the BWR problem for configuration 1 using the 238-group structure are presented in Table 5.6. Angular approximations (cases 1 and 2) introduced approximately 2% error for the power peaking factors, where the majority of the error was at the boundary. The eigenvalue has approximately 1.3% error relative to the reference problem. Truncating the basis to 56 DOF added approximately 4% error. Homogenizing over coarse-mesh regions (case 3) introduced approximately 0.5% error, whereas homogenizing over material (case 4) introduced approximately 5% error. The largest memory savings (Trunc.-(5)) introduced approximately 5% error for the 238-group case, which is approximately the same as the 44-group results.

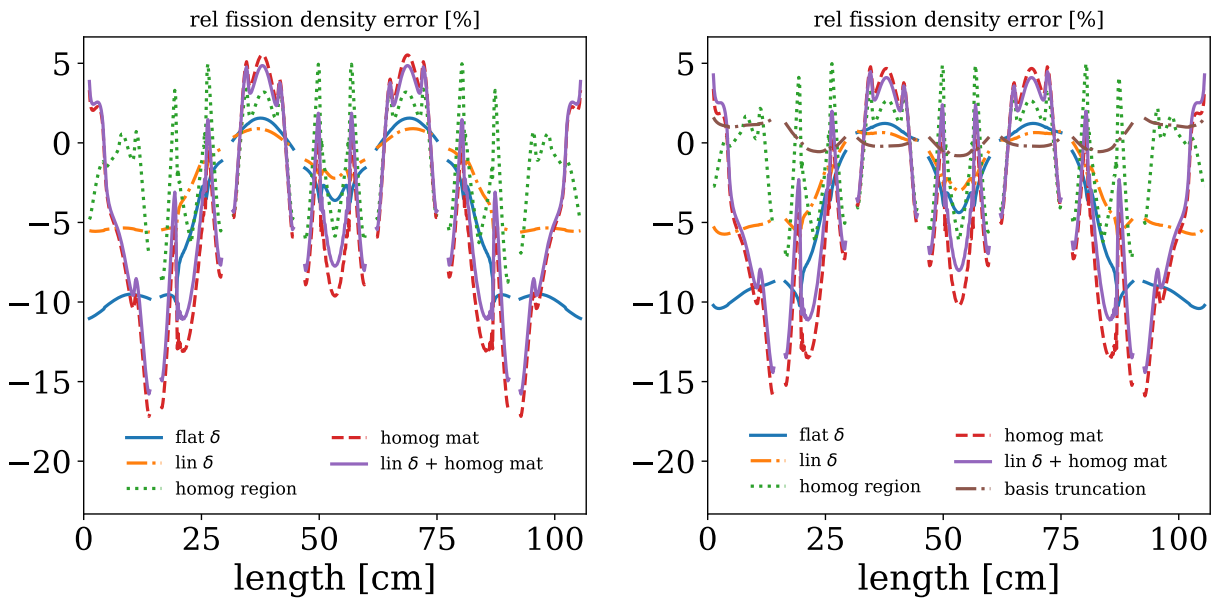

(a) Complete basis

(b) Truncated basis

Figure 5.4: Spatially dependent, relative fission density errors for the 44g BWR-1 problem

The spatial dependence of the error is shown in Fig. 5.5, which includes curves for both a complete and a truncated basis used with DGM. Note that the errors presented in the figure are for cell fission densities, thus will not compare directly with the data presented in Table 5.6. For this case, we see that the errors for the truncated basis are dominated by the truncation, which manifests as all of the curves appearing similar.

Results from the BWR problem for configuration 1 using the 1968-group structure are presented in Table 5.7. Angular approximations (cases 1 and 2) introduced approximately 0.2% error for the power peaking factors, where the largest errors were at the boundary. The eigenvalue had approximately 0.03% error relative to the reference problem. Truncating the basis to 164 DOF added approximately 0.1% error. Homogenizing over coarse-mesh regions (case 3) introduced approximately 0.02% error, whereas homogenizing over material (case 4) introduced approximately 0.3% error. The largest memory savings (Trunc.-(5)) introduced approximately 0.3% error for the 1968-group case, which is approximately an order of magnitude less than the 238-group results.

The spatial dependence of the error is shown in Fig. 5.6, which includes curves for both

Table 5.6: 238-group, BWR-configuration 1 test problem comparison of DGM with and without spatial homogenization and expanded δ. The column "Full-Ref" contains the reference values for k and the power peaking factors. The remaining columns are the percent errors relative to the reference. The Trun cases each used 56 degrees of freedom for the DGM expansion.

	Full-Ref	Full-(1)	Full-(2)	Full-(3)	Full-(4)	Full-(5)
k_{eff}	0.96	1.32	1.34	-0.26	-1.70	1.10
Assay 1	0.40	-13.46	-7.27	-0.67	-13.23	-12.57
Assay 2	0.53	-4.24	-1.95	-0.06	-5.89	-4.25
Assay 3	2.12	3.86	2.08	0.13	4.57	3.73
Assay 4	0.89	-1.30	-1.09	0.07	-2.91	-1.43
Assay 5	2.12	3.86	2.08	0.13	4.57	3.73
Assay 6	0.53	-4.24	-1.95	-0.06	-5.89	-4.25
Assay 7	0.40	-13.46	-7.27	-0.67	-13.23	-12.57

	Full-Ref	Trun.-Ref	Trun.-(1)	Trun.-(2)	Trun.-(3)	Trun.-(4)	Trun.-(5)
k_{eff}	0.96	1.39	1.47	1.48	1.38	1.21	1.45
Assay 1	0.40	-10.08	-11.22	-10.63	-10.20	-10.91	-10.92
Assay 2	0.53	-3.81	-4.35	-4.11	-3.81	-4.28	-4.23
Assay 3	2.12	3.16	3.58	3.39	3.18	3.50	3.47
Assay 4	0.89	-1.49	-1.80	-1.75	-1.46	-1.77	-1.71
Assay 5	2.12	3.16	3.58	3.39	3.18	3.50	3.47
Assay 6	0.53	-3.81	-4.35	-4.11	-3.81	-4.28	-4.23
Assay 7	0.40	-10.08	-11.22	-10.63	-10.20	-10.91	-10.92

a complete and a truncated basis used with DGM. Note that the errors presented in the figure are for cell fission densities, thus will not compare directly with the data presented in Table 5.7. Here, we again see the favorable cancellation for the truncated basis.

Overall, we can see a similar trend to the results from the 10-pin problem, which is that more energy groups seems to lead to a smaller impact for spatial and angular approximations. The largest errors were at the boundary for nearly all cases. Overall, for a 1968-group structure, approximating the spatial and angular dependence causes errors, which are approximately the same order of magnitude as a truncated basis. This suggests that for a truncated DGM solution, approximations for space and angle may have a negligible cost to eigenvalue or assembly power errors.

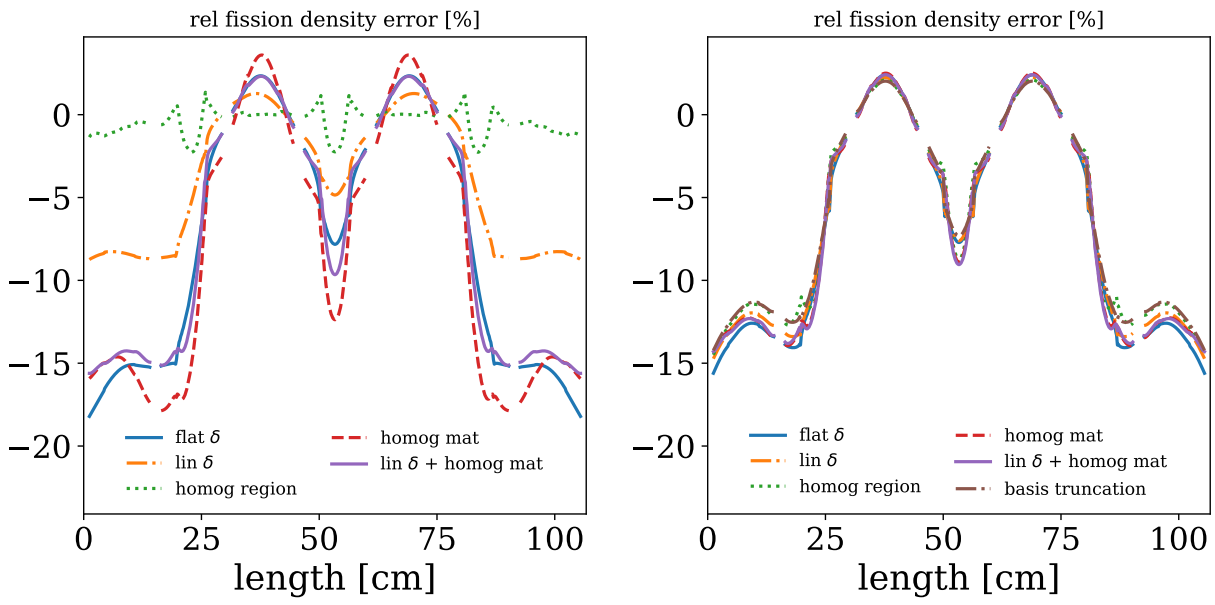

(a) Complete basis

(b) Truncated basis

Figure 5.5: Spatially dependent, relative fission density errors for the 238g BWR-1 problem

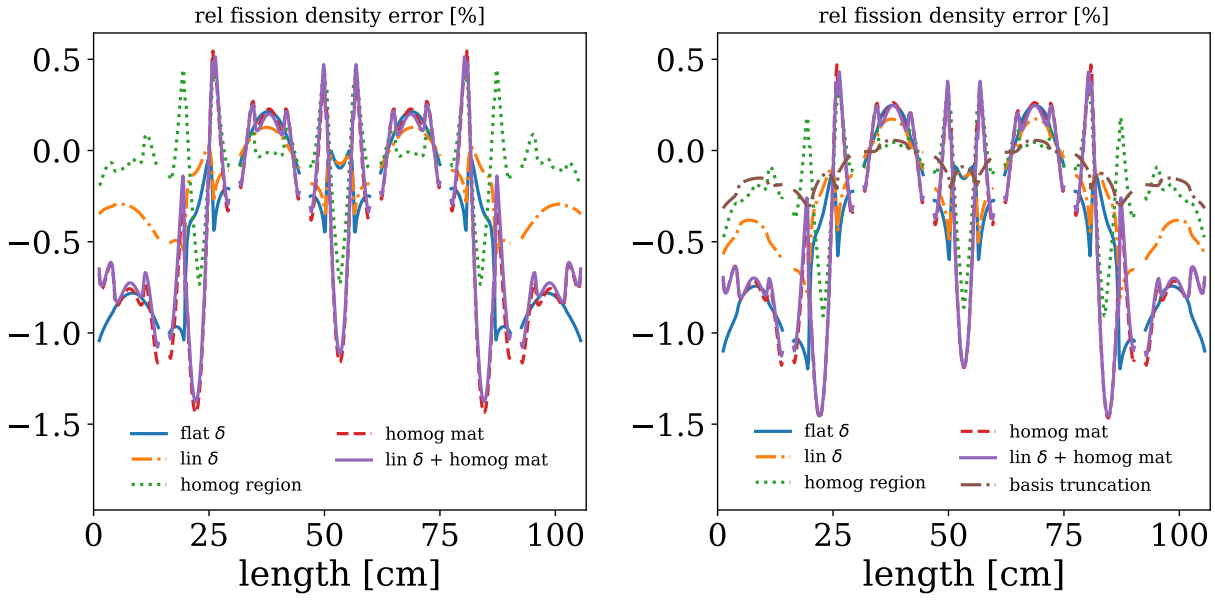

(a) Complete basis

(b) Truncated basis

Figure 5.6: Spatially dependent, relative fission density errors for the 1968g BWR-1 problem

Table 5.7: 1968-group, BWR-configuration 1 test problem comparison of DGM with and without spatial homogenization and expanded δ. The column "Full-Ref" contains the reference values for k and the power peaking factors. The remaining columns are the percent errors relative to the reference. The Trun cases each used 164 degrees of freedom for the DGM expansion.

	Full-Ref	Full-(1)	Full-(2)	Full-(3)	Full-(4)	Full-(5)
k_{eff}	0.98	0.03	0.03	0.00	-0.07	0.04
Assay 1	0.40	-0.72	-0.30	-0.05	-0.73	-0.69
Assay 2	0.53	-0.29	-0.15	0.01	-0.25	-0.21
Assay 3	2.13	0.23	0.12	0.00	0.22	0.19
Assay 4	0.89	-0.12	-0.12	0.02	-0.08	-0.05
Assay 5	2.13	0.23	0.12	0.00	0.22	0.19
Assay 6	0.53	-0.29	-0.15	0.01	-0.25	-0.21
Assay 7	0.40	-0.72	-0.30	-0.05	-0.73	-0.69

	Full-Ref	Trun.-Ref	Trun.-(1)	Trun.-(2)	Trun.-(3)	Trun.-(4)	Trun.-(5)
k_{eff}	0.98	-0.02	-0.01	-0.00	-0.02	-0.07	0.01
Assay 1	0.40	-0.15	-0.70	-0.38	-0.19	-0.71	-0.69
Assay 2	0.53	-0.09	-0.35	-0.23	-0.07	-0.29	-0.27
Assay 3	2.13	0.06	0.25	0.16	0.06	0.23	0.22
Assay 4	0.89	-0.04	-0.17	-0.16	-0.02	-0.11	-0.10
Assay 5	2.13	0.06	0.25	0.16	0.06	0.23	0.22
Assay 6	0.53	-0.09	-0.35	-0.23	-0.07	-0.29	-0.27
Assay 7	0.40	-0.15	-0.70	-0.38	-0.19	-0.71	-0.69

5.2.3 BWR - Configuration 2 results

A second BWR configuration was developed, which used mixed oxide (MOX) fuel in place of gadolinium-uranium fuel. This configuration is fully described in Section 4.3. Once again the 588 total spatial cells were divided into seven assemblies, and power peaking factors were computed for each. These results are from utilizing the POD_pins basis.

Results from the BWR problem for configuration 2 using the 44-group structure are presented in Table 5.8. Angular approximations (cases 1 and 2) introduced approximately 1% error for the power peaking factors and approximately 0.6% error into the eigenvalue. Truncating the basis to 9 DOF added approximately 1% error. Homogenizing over coarse-mesh regions (case 3) introduced approximately 0.5% error, whereas homogenizing over material (case 4) introduced approximately 3% error. The largest memory savings (Trunc.-(5)) introduced approximately 4% error for the 44-group case, which is approximately half of

Table 5.8: 44-group, BWR-configuration 2 test problem comparison of DGM with and without spatial homogenization and expanded δ. The column "Full-Ref" contains the reference values for k and the power peaking factors. The remaining columns are the percent errors relative to the reference. The Trun cases each used 9 degrees of freedom for the DGM expansion.

	Full-Ref	Full-(1)	Full-(2)	Full-(3)	Full-(4)	Full-(5)
k_{eff}	1.10	0.20	0.66	-0.45	-3.00	-0.15
Assay 1	0.39	-7.05	-1.09	-1.38	-5.99	-6.14
Assay 2	0.94	-0.96	0.15	-0.15	1.45	1.30
Assay 3	1.43	1.83	0.28	0.31	-0.97	-0.79
Assay 4	1.47	1.41	-0.16	0.32	3.20	3.12
Assay 5	1.43	1.83	0.28	0.31	-0.97	-0.79
Assay 6	0.94	-0.96	0.15	-0.15	1.45	1.30
Assay 7	0.39	-7.05	-1.09	-1.38	-5.99	-6.14

	Full-Ref	Trun.-Ref	Trun.-(1)	Trun.-(2)	Trun.-(3)	Trun.-(4)	Trun.-(5)
k_{eff}	1.10	-0.64	-0.79	-0.46	-0.94	-2.71	-1.03
Assay 1	0.39	-3.71	-6.58	-3.11	-4.57	-6.40	-6.44
Assay 2	0.94	-0.53	-0.65	-0.14	-0.51	1.62	1.56
Assay 3	1.43	0.88	1.43	0.61	0.96	-1.09	-1.01
Assay 4	1.47	0.93	1.54	0.64	1.21	3.44	3.40
Assay 5	1.43	0.88	1.43	0.61	0.96	-1.09	-1.01
Assay 6	0.94	-0.53	-0.65	-0.14	-0.51	1.62	1.56
Assay 7	0.39	-3.71	-6.58	-3.11	-4.57	-6.40	-6.44

the error from the 44-group, 10-pin problem.

The spatial dependence of the error is shown in Fig. 5.7, which includes curves for both a complete and a truncated basis used with DGM. Note that the errors presented in the figure are for cell fission densities, thus will not compare directly with the data presented in Table 5.8. For this case, the errors are highest at the center of the MOX fuel regions.

Results from the BWR problem for configuration 2 using the 238-group structure are presented in Table 5.9. Angular approximations (cases 1 and 2) introduced approximately 0.4% error for the power peaking factors and approximately 0.5% error into the eigenvalue. Truncating the basis to 58 DOF added approximately 0.3% error. Homogenizing over coarse-mesh regions (case 3) introduced approximately 0.5% error, whereas homogenizing over material (case 4) introduced approximately 1.5% error. The largest memory savings (Trunc.-(5)) introduced approximately 1% error for the 44-group case, which is smaller than the results using a 44-group structure.

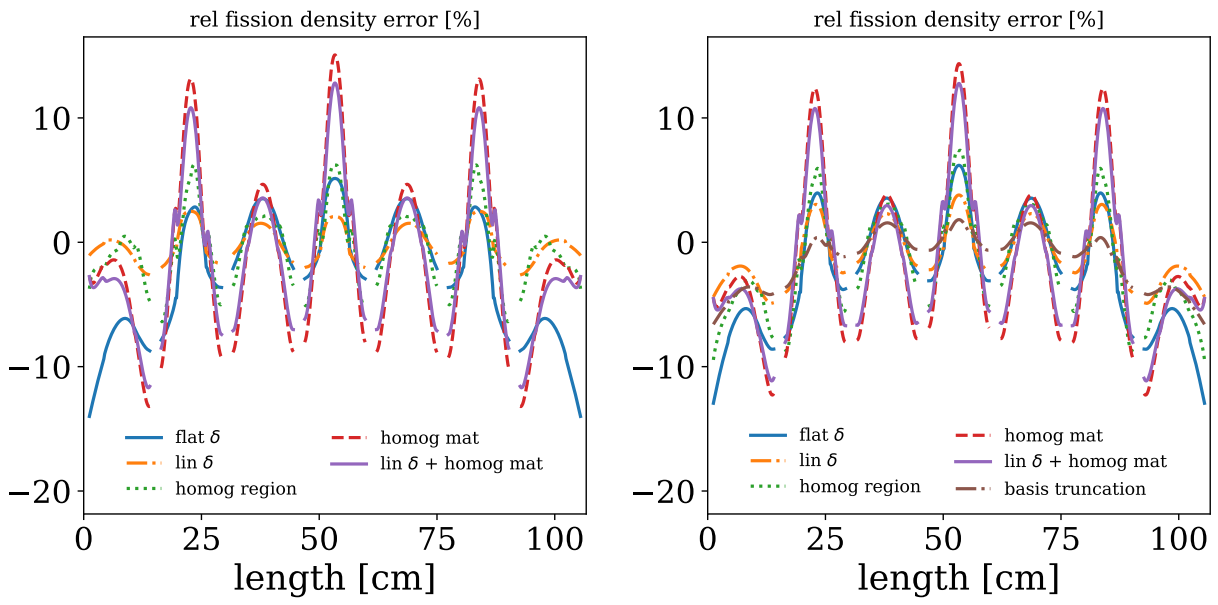

(a) Complete basis

(b) Truncated basis

Figure 5.7: Spatially dependent, relative fission density errors for the 44g BWR-2 problem

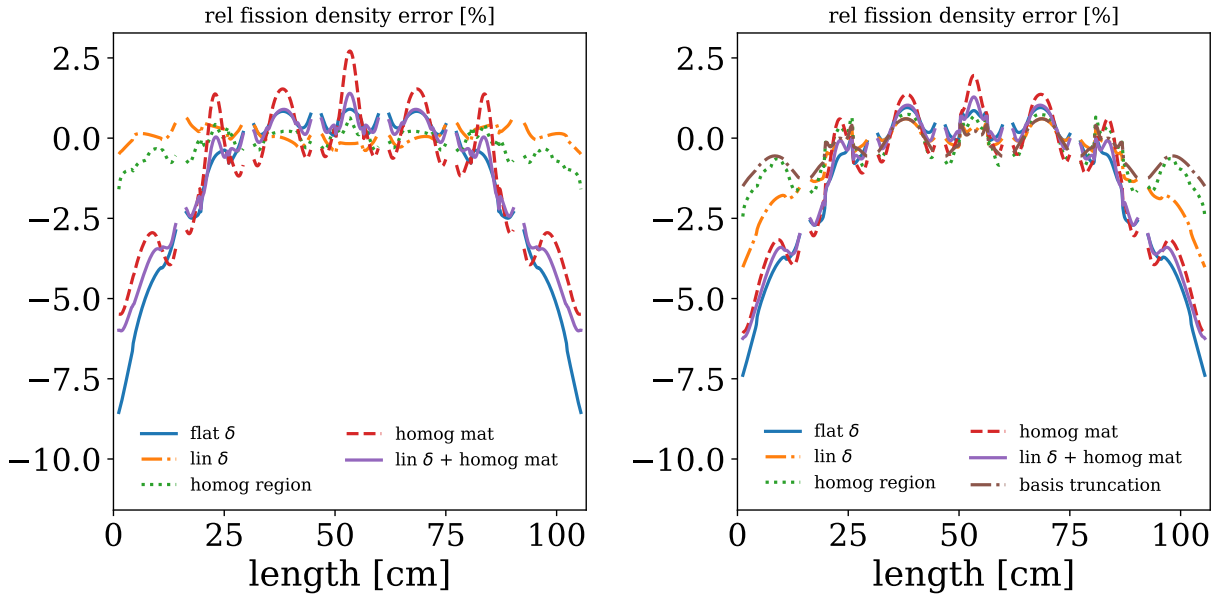

(a) Complete basis

(b) Truncated basis

Figure 5.8: Spatially dependent, relative fission density errors for the 238g BWR-2 problem

The spatial dependence of the error is shown in Fig. 5.8, which includes curves for both a complete and a truncated basis used with DGM. Note that the errors presented in the figure are for cell fission densities, thus will not compare directly with the data presented in

Table 5.9: 238-group, BWR-configuration 2 test problem comparison of DGM with and without spatial homogenization and expanded δ. The column "Full-Ref" contains the reference values for k and the power peaking factors. The remaining columns are the percent errors relative to the reference. The Trun cases each used 58 degrees of freedom for the DGM expansion.

	Full-Ref	Full-(1)	Full-(2)	Full-(3)	Full-(4)	Full-(5)
k_{eff}	1.15	0.31	0.51	-0.25	-2.08	0.11
Assay 1	0.39	-4.11	0.04	-0.55	-3.32	-3.47
Assay 2	0.95	-0.52	0.25	-0.03	-0.38	-0.48
Assay 3	1.42	0.98	-0.06	0.08	0.68	0.82
Assay 4	1.48	0.96	-0.22	0.17	0.93	0.88
Assay 5	1.42	0.98	-0.06	0.08	0.68	0.82
Assay 6	0.95	-0.52	0.25	-0.03	-0.38	-0.48
Assay 7	0.39	-4.11	0.04	-0.55	-3.32	-3.47

	Full-Ref	Trun.-Ref	Trun.-(1)	Trun.-(2)	Trun.-(3)	Trun.-(4)	Trun.-(5)
k_{eff}	1.15	-0.33	-0.07	0.04	-0.46	-1.23	-0.17
Assay 1	0.39	-0.74	-3.73	-1.85	-1.03	-3.44	-3.50
Assay 2	0.95	-0.17	-0.54	-0.16	-0.16	-0.42	-0.47
Assay 3	1.42	0.28	0.93	0.45	0.29	0.74	0.82
Assay 4	1.48	0.07	0.89	0.31	0.19	0.92	0.89
Assay 5	1.42	0.28	0.93	0.45	0.29	0.74	0.82
Assay 6	0.95	-0.17	-0.54	-0.16	-0.16	-0.42	-0.47
Assay 7	0.39	-0.74	-3.73	-1.85	-1.03	-3.44	-3.50

Table 5.9. For this case, the largest source of error is from the boundaries.

Results from the BWR problem for configuration 2 using the 1968-group structure are presented in Table 5.10. Angular approximations (cases 1 and 2) introduced approximately 0.05% error for the power peaking factors and approximately 0.1% error into the eigenvalue. Truncating the basis to 151 DOF added approximately 0.1% error. Homogenizing over coarse-mesh regions (case 3) introduced approximately 0.05% error, whereas homogenizing over material (case 4) introduced approximately 0.1% error. The largest memory savings (Trunc.-(5)) introduced approximately 0.2% error for the 1968-group case, which is approximately an order of magnitude smaller than the results from the 238-group structure.

The spatial dependence of the error is shown in Fig. 5.9, which includes curves for both a complete and a truncated basis used with DGM. Note that the errors presented in the figure are for cell fission densities, thus will not compare directly with the data presented

Table 5.10: 1968-group, BWR-configuration 2 test problem comparison of DGM with and without spatial homogenization and expanded δ. The column "Full-Ref" contains the reference values for k and the power peaking factors. The remaining columns are the percent errors relative to the reference. The Trun cases each used 151 degrees of freedom for the DGM expansion.

	Full-Ref	Full-(1)	Full-(2)	Full-(3)	Full-(4)	Full-(5)
k_{eff}	1.17	-0.04	0.10	-0.04	-0.69	-0.09
Assay 1	0.39	-0.22	0.05	-0.07	-0.03	-0.13
Assay 2	0.95	-0.11	0.03	0.06	-0.15	-0.11
Assay 3	1.42	0.14	-0.03	-0.06	0.15	0.12
Assay 4	1.48	-0.00	-0.02	0.07	-0.08	-0.03
Assay 5	1.42	0.14	-0.03	-0.06	0.15	0.12
Assay 6	0.95	-0.11	0.03	0.06	-0.15	-0.11
Assay 7	0.39	-0.22	0.05	-0.07	-0.03	-0.13

	Full-Ref	Trun.-Ref	Trun.-(1)	Trun.-(2)	Trun.-(3)	Trun.-(4)	Trun.-(5)
k_{eff}	1.17	-0.06	-0.09	0.02	-0.10	-0.59	-0.13
Assay 1	0.39	-0.01	-0.19	0.04	-0.06	-0.06	-0.12
Assay 2	0.95	-0.09	-0.18	-0.07	-0.04	-0.17	-0.17
Assay 3	1.42	0.09	0.20	0.08	0.04	0.17	0.19
Assay 4	1.48	-0.06	-0.06	-0.08	0.00	-0.09	-0.08
Assay 5	1.42	0.09	0.20	0.08	0.04	0.17	0.19
Assay 6	0.95	-0.09	-0.18	-0.07	-0.04	-0.17	-0.17
Assay 7	0.39	-0.01	-0.19	0.04	-0.06	-0.06	-0.12

in Table 5.10. For the 1968-group structure, the magnitudes of the errors are considerably smaller than the 238-group structure, and all cases perform similarly.

Once again the impact of spatial and angular approximations is inversely proportional to the number of energy groups. For the 1968-group structure, the approximations used with a truncated basis introduced approximately the same error as using the truncated basis alone, which is likely due to favorable cancellation of errors.

5.2.4 2-D results

A 2-D problem was designed to test how the spatial homogenization and angular approximation schemes extend to higher spatial orders. The 2-D problem used 44 energy groups and modeled 304 pincells, which were each divided into 64 spatial cells. With these and the moderator cells, a total of 46656 were used. The problem is fully defined in Section 4.4. The 238 and

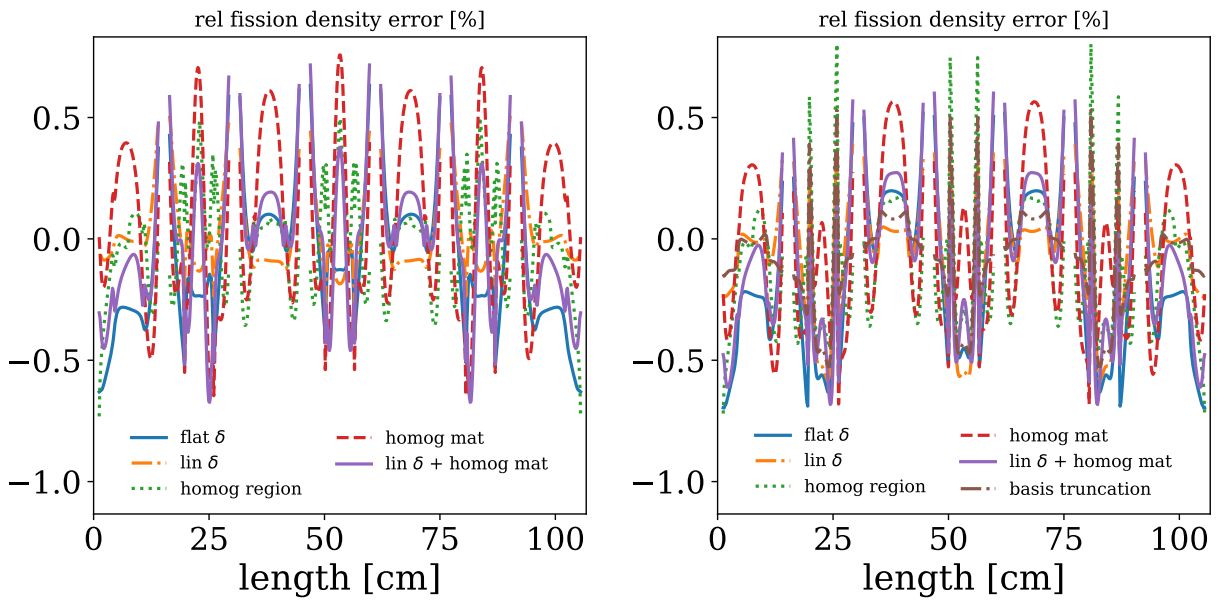

(a) Complete basis

(b) Truncated basis

Figure 5.9: Spatially dependent, relative fission density errors for the 1968g BWR-2 problem

1968 group structures were prohibitively expensive for this problem. This section presents the results from using the POD_2D_pins basis, which was described in Section 4.4. Note that for the 2-D problem, homogenization over coarse-mesh region provided relatively little memory savings as each pincell was homogenized as shown in Fig. 5.10, where each unique number is a homogenized region. The 64 spatial cells of Fig. 4.24 are reduced to 49 spatial cells when case 3 is implemented.

1	2	3	4	4	5	6	7
8	9	10	11	11	12	13	14
15	16	17	18	18	19	20	21
22	23	24	25	25	26	27	28
22	23	24	25	25	26	27	28
29	30	31	32	32	33	34	35
36	37	38	39	39	40	41	42
43	44	45	46	46	47	48	49

Figure 5.10: Homogenized cells for each pincell in the 2-D problem. The 64 spatial cells from Fig. 4.24 are reduced to 49 spatial cells for case 3, regional spatial homogenization.

Figure 5.11 presents the results from the non-truncated DGM solution to the 2-D problem.

The figure shows several cells, which each represent a pincell. The highest value in each cell of the figure is the power peaking factors for the pincell computed from the reference solution (Full-Ref), while the remaining numbers are percent errors relative to the reference. The power peaking factors were computed by dividing the pincell fission density for a cell by the fission density averaged over non-moderator cells. The pincell fission density was computed by summing the fission density from each of the 64 spatial cells in a pincell.

For the errors, the first column is Full-(1) (flat approximation of ψ) then Full-(2) (linear approximation of ψ), while the second column is Full-(3) (spatial homogenization over region) then Full-(4) (spatial homogenization over material) then Full-(5) (both case 2 and case 4). The yellow highlighted values are the maximum for that homogenization scheme over the assembly, while the blue highlighting is the minimum. The top and the diagonal are reflective surfaces while the right face is adjacent water. For convenience, Fig. 5.12, Fig. 5.13, and Fig. 5.14 are zoomed in plots of the same data as Fig. 5.11.

The results from the truncated problem are presented in Fig. 5.15, which follows a similar layout to the non-truncated figures. For these results, the basis was truncated to 9 DOF. The top value in each cell is the power peaking factor for the (non-truncated) reference solution, while the other values are percent errors relative to the reference. The first column of the errors is Trun.-Ref then Trun.-(1) then Trun.-(2), while the second column is Trun.-(3) then Trun.-(4) then Trun.-(5). The yellow highlighted values are the maximum for that homogenization scheme over the assembly, while the blue highlighting is the minimum. The top and the diagonal are reflective surfaces while the right face is adjacent water. For convenience, zoomed in versions for Fig. 5.15 are available in Fig. 5.16, Fig. 5.17, and Fig. 5.18.

Note that the errors from homogenizing over material type (case 4) are listed as N/A in Fig. 5.11 and Fig. 5.15. The method of spatially homogenizing over material type caused the problem to be exceedingly unstable, which prevented a solution for a Krasnoselskii parameter greater than 0.01. We can also see that the linear approximation of ψ (case 2) performed nearly two orders of magnitude worse than the flat approximation of ψ (case 1). Since the 1-D tests suggest the opposite trend (i.e. linear approximation is better than a flat approximation), an error may be present in the 2-D implementation related to the angular

approximation. This would also impact the results for case 5, which combines the results of cases 2 and 4. Also note that although case 4 was unstable, combining this method with case 2 resulted in a reduced error as compared to case (2) alone, which is likely due to favorable cancellation once again.

5.3 Conclusions

Overall, spatial homogenization and angular approximations appear to be relatively successful for use in the discrete generalized multigroup method. In all 1-D cases, the linear approximation (case 2) for the angular flux performed better than the flat approximation (case 1), especially in problems with a large angular variation, which was entirely expected. For most cases, a linear approximation introduced approximately a maximum of 1% error into the solution, and the higher-group structures (238- and 1968-group) typically saw errors smaller than that.

Spatial homogenization for the 1-D problems provided a similar story, where the method of homogenizing over coarse region (case 3) performed far better than homogenizing over material (case 4), which was expected. However, for large group structures, the impact of case 4 was often less than 0.1% error in the pin powers, which was approximately the same error introduced by truncating the basis.

It seems that for problems with a large group structure, spatial and angular approximations can be used with nearly negligible additional cost to error if a truncated basis is to be used for DGM. Essentially, large problems are both where a researcher would want the most approximations to minimize the computation time and also where these approximations have the smallest impact. More research is needed to show that this holds in general instead of just to the test problems in this chapter. Additionally, more research effort will be required to explain why this trend holds, but a likely explanation is simply that more degrees of freedom were used for the problem, thus removing information from the space and angle dimensions had a proportionally smaller impact.

For the 2-D problem, the flat approximation (case 1) was more successful than the linear

approximation (case 2) though this may be due to an error in the angular approximation. The flat approximation introduced a maximum of 3.24% error in the power peaking factors for the 2-D problem for the non-truncated case and 0.51% error for the truncated case. This maximum error occurred at the reflective boundary adjacent to the junction of the MOX assembly with the moderator. Case 3 (regional homogenization) introduced relatively little error, but as previously mentioned was not over large regions. Thus case 3 also provided only a small benefit to computational costs. More efforts are required to test the impact of homogenizing over larger regions such as entire pincells. Overall, the 2-D results suggest that the homogenization schemes can be successful, but more efforts are needed to verify these findings.

Finally, more efforts are required to quantify the memory saving from these approximations. In this work, the impact on error was assessed, but direct measurement of the memory use could provide additional support for the use of these approximations. Further, the spatial homogenization approximation was applied in two rather limited ways. It would be interesting to spatially average over natural, homogenization regions such as a pincell and assess the impact for the DGM approach.

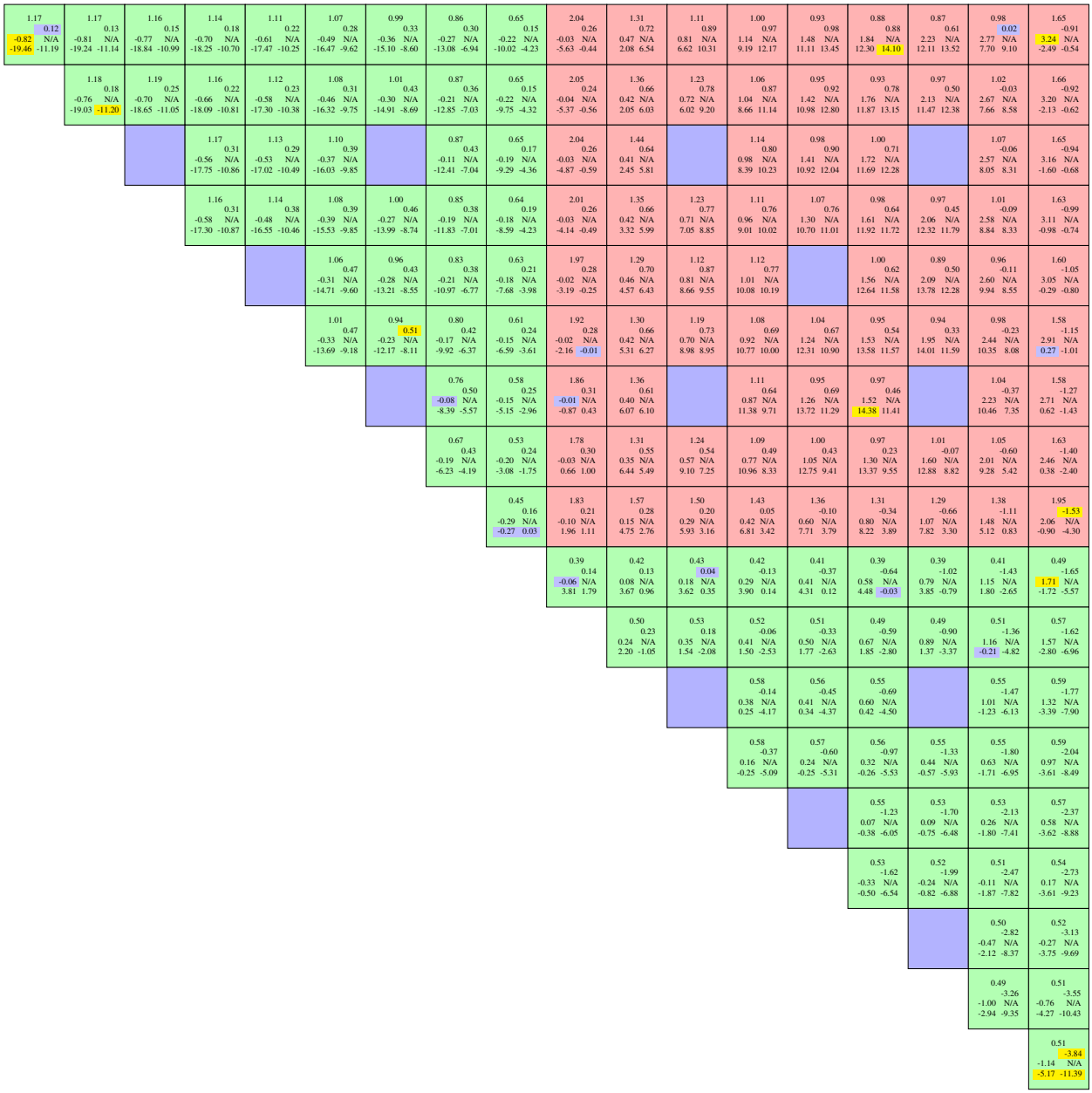

Figure 5.11: 44-group 2-D test problem comparison of non-truncated DGM with and without spatial homogenization and expanded δ. The top value in each cell is the reference power peaking factor, while the other values are percent errors relative to the reference. Of the percent errors the first column is Full-(1) then Full-(2), while the second column is Full-(3) then Full-(4) then Full-(5). The yellow highlighted values are the maximum for that homogenization scheme over the assembly, while the blue highlighting is the minimum. The top and the diagonal are reflective surfaces while the right face is adjacent water.

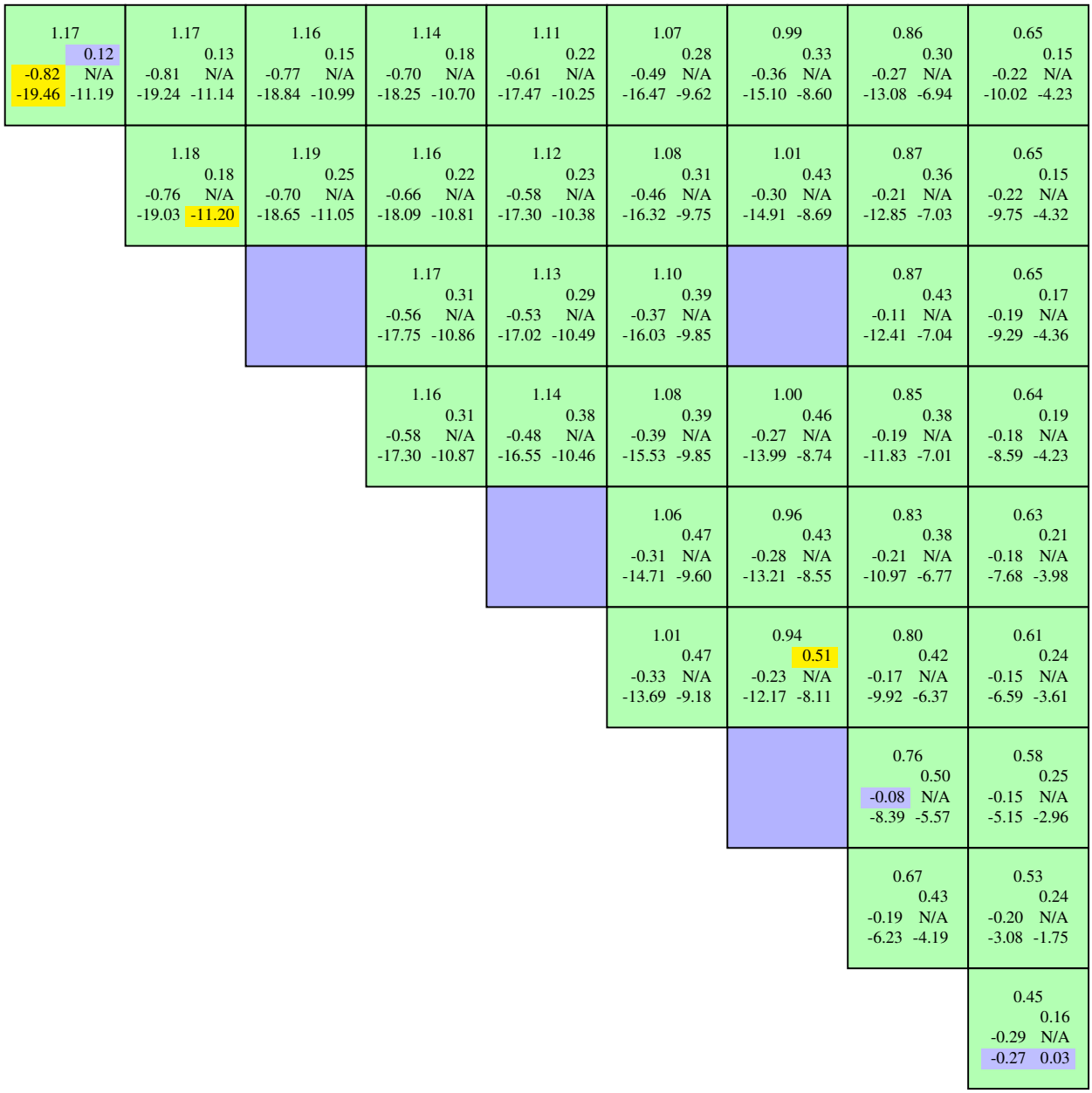

Figure 5.12: Top left assembly of Fig. 5.11

2.04 0.26 -0.03 N/A -5.63 -0.44	1.31 0.72 0.47 N/A 2.08 6.54	1.11 0.89 0.81 N/A 6.62 10.31	1.00 0.97 1.14 N/A 9.19 12.17	0.93 0.98 1.48 N/A 11.11 13.45	0.88 0.88 1.84 N/A 12.30 14.10	0.87 0.61 2.23 N/A 12.11 13.52	0.98 0.02 2.77 N/A 7.70 9.10	1.65 -0.91 3.24 N/A -2.49 -0.54
2.05 0.24 -0.04 N/A -5.37 -0.56	1.36 0.66 0.42 N/A 2.05 6.03	1.23 0.78 0.72 N/A 6.02 9.20	1.06 0.87 1.04 N/A 8.66 11.14	0.95 0.92 1.42 N/A 10.98 12.80	0.93 0.78 1.76 N/A 11.87 13.15	0.97 0.50 2.13 N/A 11.47 12.38	1.02 -0.03 2.67 N/A 7.66 8.58	1.66 -0.92 3.20 N/A -2.13 -0.62
2.04 0.26 -0.03 N/A -4.87 -0.59	1.44 0.64 0.41 N/A 2.45 5.81		1.14 0.80 0.98 N/A 8.39 10.23	0.98 0.90 1.41 N/A 10.92 12.04	1.00 0.71 1.72 N/A 11.69 12.28		1.07 -0.06 2.57 N/A 8.05 8.31	1.65 -0.94 3.16 N/A -1.60 -0.68
2.01 0.26 -0.03 N/A -4.14 -0.49	1.35 0.66 0.42 N/A 3.32 5.99	1.23 0.77 0.71 N/A 7.05 8.85	1.11 0.76 0.96 N/A 9.01 10.02	1.07 0.76 1.30 N/A 10.70 11.01	0.98 0.64 1.61 N/A 11.92 11.72	0.97 0.45 2.06 N/A 12.32 11.79	1.01 -0.09 2.58 N/A 8.84 8.33	1.63 -0.99 3.11 N/A -0.98 -0.74
1.97 0.28 -0.02 N/A -3.19 -0.25	1.29 0.70 0.46 N/A 4.57 6.43	1.12 0.87 0.81 N/A 8.66 9.55	1.12 0.77 1.01 N/A 10.08 10.19		1.00 0.62 1.56 N/A 12.64 11.58	0.89 0.50 2.09 N/A 13.78 12.28	0.96 -0.11 2.60 N/A 9.94 8.55	1.60 -1.05 3.05 N/A -0.29 -0.80
1.92 0.28 -0.02 N/A -2.16 -0.01	1.30 0.66 0.42 N/A 5.31 6.27	1.19 0.73 0.70 N/A 8.98 8.95	1.08 0.69 0.92 N/A 10.77 10.00	1.04 0.67 1.24 N/A 12.31 10.90	0.95 0.54 1.53 N/A 13.58 11.57	0.94 0.33 1.95 N/A 14.01 11.59	0.98 -0.23 2.44 N/A 10.35 8.08	1.58 -1.15 2.91 N/A 0.27 -1.01
1.86 0.31 -0.01 N/A -0.87 0.43	1.36 0.61 0.40 N/A 6.07 6.10		1.11 0.64 0.87 N/A 11.38 9.71	0.95 0.69 1.26 N/A 13.72 11.29	0.97 0.46 1.52 N/A 14.38 11.41		1.04 -0.37 2.23 N/A 10.46 7.35	1.58 -1.27 2.71 N/A 0.62 -1.43
1.78 0.30 -0.03 N/A 0.66 1.00	1.31 0.55 0.35 N/A 6.44 5.49	1.24 0.54 0.57 N/A 9.10 7.25	1.09 0.49 0.77 N/A 10.96 8.33	1.00 0.43 1.05 N/A 12.75 9.41	0.97 0.23 1.30 N/A 13.37 9.55	1.01 -0.07 1.60 N/A 12.88 8.82	1.05 -0.60 2.01 N/A 9.28 5.42	1.63 -1.40 2.46 N/A 0.38 -2.40
1.83 0.21 -0.10 N/A 1.96 1.11	1.57 0.28 0.15 N/A 4.75 2.76	1.50 0.20 0.29 N/A 5.93 3.16	1.43 0.05 0.42 N/A 6.81 3.42	1.36 -0.10 0.60 N/A 7.71 3.79	1.31 -0.34 0.80 N/A 8.22 3.89	1.29 -0.66 1.07 N/A 7.82 3.30	1.38 -1.11 1.48 N/A 5.12 0.83	1.95 -1.53 2.06 N/A -0.90 -4.30

Figure 5.13: Top right assembly of Fig. 5.11

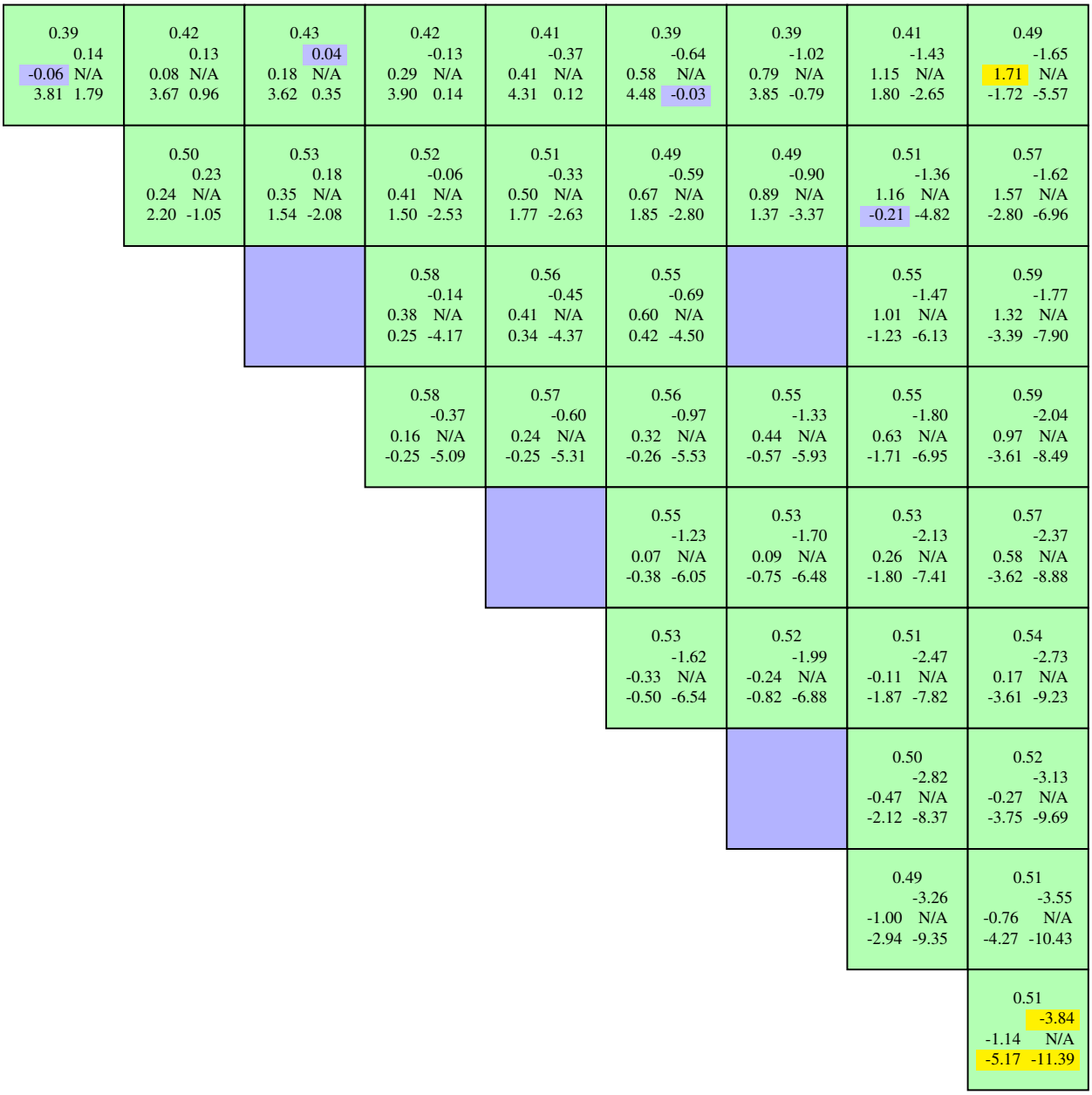

Figure 5.14: bottom right assembly of Fig. 5.11

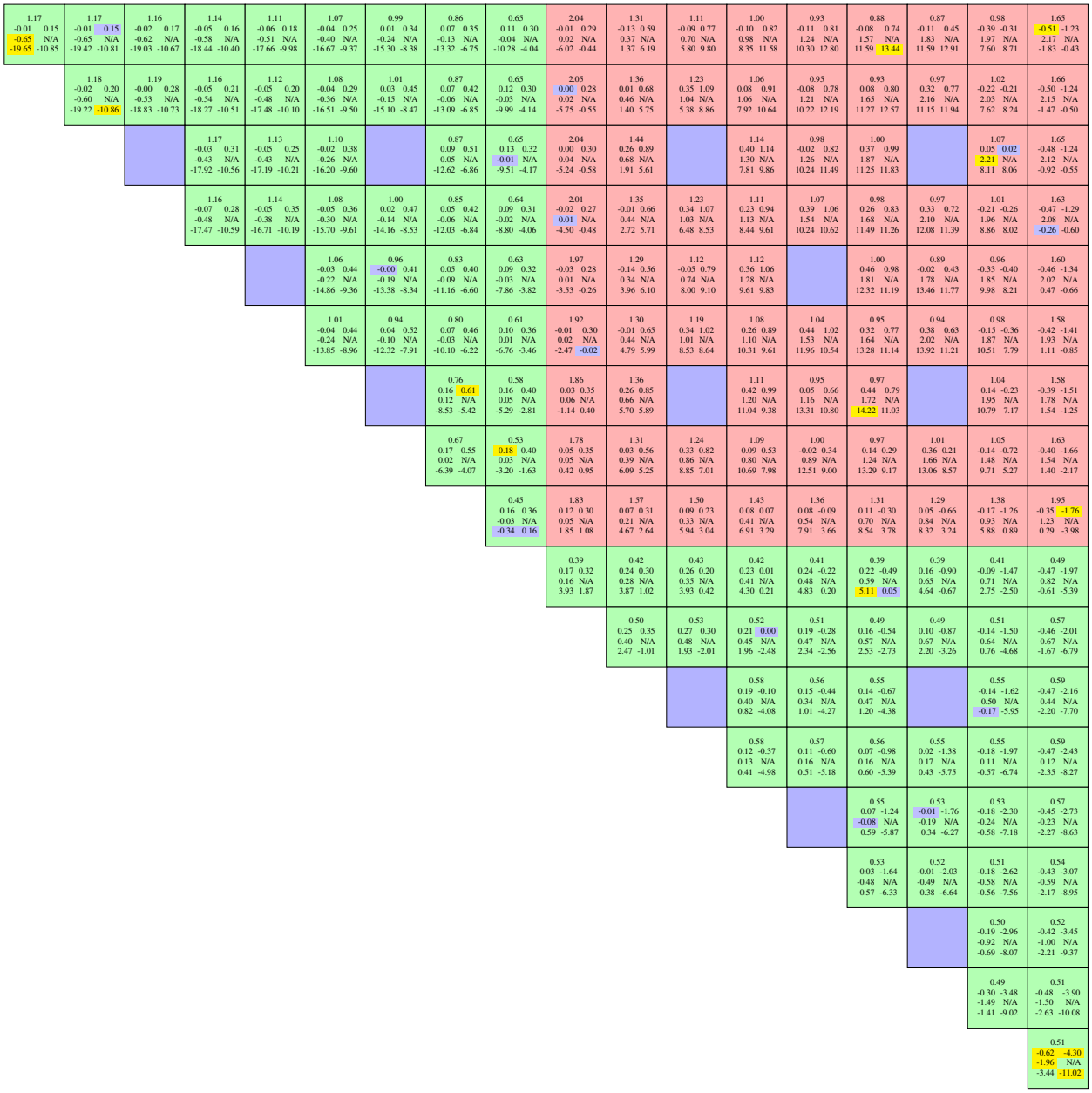

Figure 5.15: 44-group 2-D test problem comparison of truncated DGM with and without spatial homogenization and expanded δ. The top value in each cell is the power peaking factor, while the other values are percent errors relative to the reference. Of the percent errors the first column is Trun.-Ref then Trun.-(1) then Trun.-(2), while the second column is Trun.-(3) then Trun.-(4) then Trun.-(5). The yellow highlighted values are the maximum for that homogenization scheme over the assembly, while the blue highlighting is the minimum. The top and the diagonal are reflective surfaces while the right face is adjacent water.

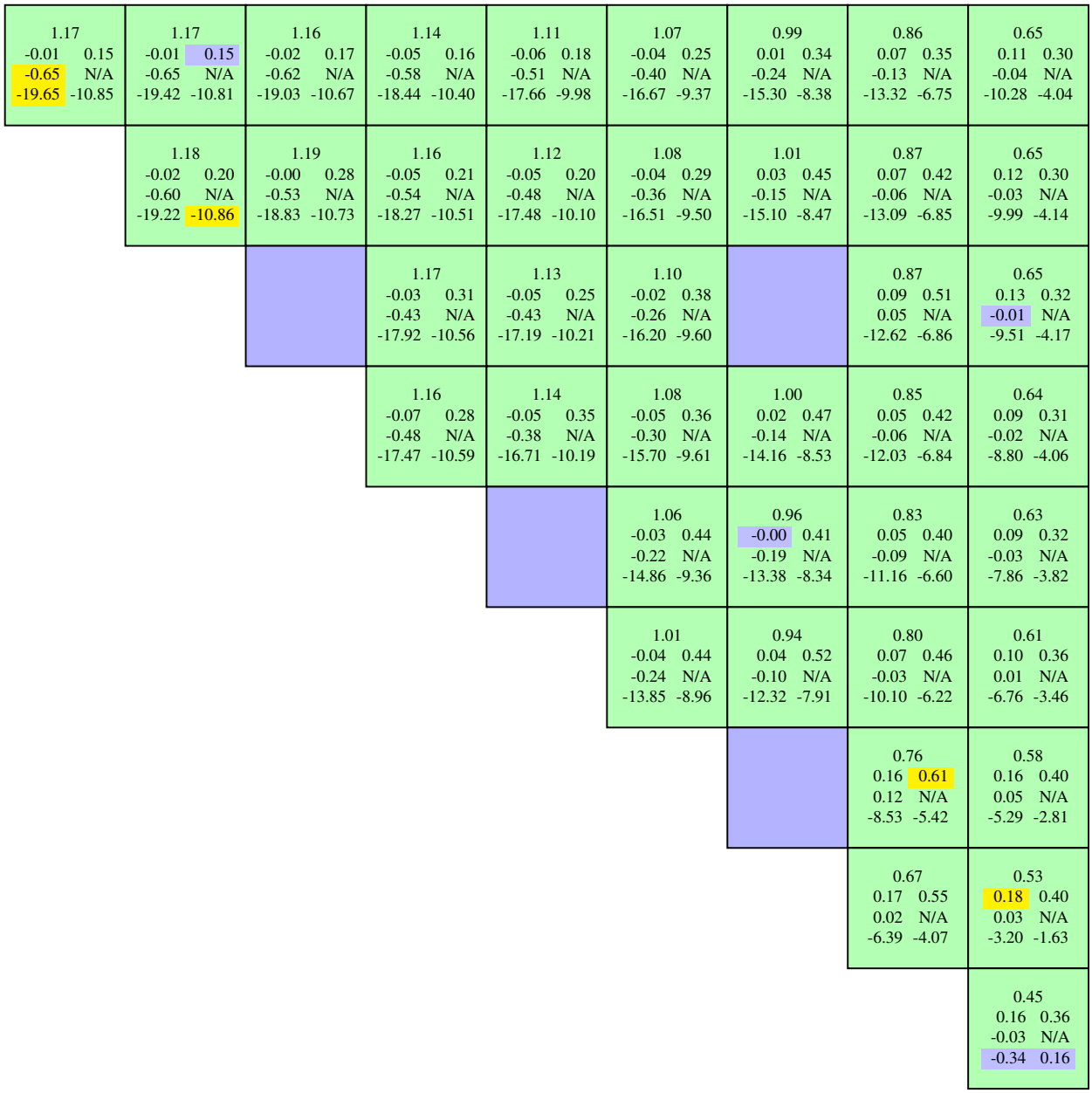

Figure 5.16: Top left assembly of Fig. 5.15

2.04 -0.01 0.29 0.02 N/A -6.02 -0.44	1.31 -0.13 0.59 0.37 N/A 1.37 6.19	1.11 -0.09 0.77 0.70 N/A 5.80 9.80	1.00 -0.10 0.82 0.98 N/A 8.35 11.58	0.93 -0.11 0.81 1.24 N/A 10.30 12.80	0.88 -0.08 0.74 1.57 N/A 11.59 13.44	0.87 -0.11 0.45 1.83 N/A 11.59 12.91	0.98 -0.39 -0.31 1.97 N/A 7.60 8.71	1.65 -0.51 -1.23 2.17 N/A -1.83 -0.43
2.05 0.00 0.28 0.02 N/A -5.75 -0.55	1.36 0.01 0.68 0.46 N/A 1.40 5.75	1.23 0.35 1.09 1.04 N/A 5.38 8.86	1.06 0.08 0.91 1.06 N/A 7.92 10.64	0.95 -0.08 0.78 1.21 N/A 10.22 12.19	0.93 0.08 0.80 1.65 N/A 11.27 12.57	0.97 0.32 0.77 2.16 N/A 11.15 11.94	1.02 -0.22 -0.21 2.03 N/A 7.62 8.24	1.66 -0.50 -1.24 2.15 N/A -1.47 -0.50
2.04 0.00 0.30 0.04 N/A -5.24 -0.58	1.44 0.26 0.89 0.68 N/A 1.91 5.61		1.14 0.40 1.14 1.30 N/A 7.81 9.86	0.98 -0.02 0.82 1.26 N/A 10.24 11.49	1.00 0.37 0.99 1.87 N/A 11.25 11.83		1.07 0.05 0.02 2.21 N/A 8.11 8.06	1.65 -0.48 -1.24 2.12 N/A -0.92 -0.55
2.01 -0.02 0.27 0.01 N/A -4.50 -0.48	1.35 -0.01 0.66 0.44 N/A 2.72 5.71	1.23 0.34 1.07 1.03 N/A 6.48 8.53	1.11 0.23 0.94 1.13 N/A 8.44 9.61	1.07 0.39 1.06 1.54 N/A 10.24 10.62	0.98 0.26 0.83 1.68 N/A 11.49 11.26	0.97 0.33 0.72 2.10 N/A 12.08 11.39	1.01 -0.21 -0.26 1.96 N/A 8.86 8.02	1.63 -0.47 -1.29 2.08 N/A -0.26 -0.60
1.97 -0.03 0.28 0.01 N/A -3.53 -0.26	1.29 -0.14 0.56 0.34 N/A 3.96 6.10	1.12 -0.05 0.79 0.74 N/A 8.00 9.10	1.12 0.36 1.06 1.28 N/A 9.61 9.83		1.00 0.46 0.98 1.81 N/A 12.32 11.19	0.89 -0.02 0.43 1.78 N/A 13.46 11.77	0.96 -0.33 -0.40 1.85 N/A 9.98 8.21	1.60 -0.46 -1.34 2.02 N/A 0.47 -0.66
1.92 -0.01 0.30 0.02 N/A -2.47 -0.02	1.30 -0.01 0.65 0.44 N/A 4.79 5.99	1.19 0.34 1.02 1.01 N/A 8.53 8.64	1.08 0.26 0.89 1.10 N/A 10.31 9.61	1.04 0.44 1.02 1.53 N/A 11.96 10.54	0.95 0.32 0.77 1.64 N/A 13.28 11.14	0.94 0.38 0.63 2.02 N/A 13.92 11.21	0.98 -0.15 -0.36 1.87 N/A 10.51 7.79	1.58 -0.42 -1.41 1.93 N/A 1.11 -0.85
1.86 0.03 0.35 0.06 N/A -1.14 0.40	1.36 0.26 0.85 0.66 N/A 5.70 5.89		1.11 0.42 0.99 1.20 N/A 11.04 9.38	0.95 0.05 0.66 1.16 N/A 13.31 10.80	0.97 0.44 0.79 1.72 N/A 14.22 11.03		1.04 0.14 -0.23 1.95 N/A 10.79 7.17	1.58 -0.39 -1.51 1.78 N/A 1.54 -1.25
1.78 0.05 0.35 0.05 N/A 0.42 0.95	1.31 0.03 0.56 0.39 N/A 6.09 5.25	1.24 0.33 0.82 0.86 N/A 8.85 7.01	1.09 0.09 0.53 0.80 N/A 10.69 7.98	1.00 -0.02 0.34 0.89 N/A 12.51 9.00	0.97 0.14 0.29 1.24 N/A 13.29 9.17	1.01 0.36 0.21 1.66 N/A 13.06 8.57	1.05 -0.14 -0.72 1.48 N/A 9.71 5.27	1.63 -0.40 -1.66 1.54 N/A 1.40 -2.17
1.83 0.12 0.30 0.05 N/A 1.85 1.08	1.57 0.07 0.31 0.21 N/A 4.67 2.64	1.50 0.09 0.23 0.33 N/A 5.94 3.04	1.43 0.08 0.07 0.41 N/A 6.91 3.29	1.36 0.08 -0.09 0.54 N/A 7.91 3.66	1.31 0.11 -0.30 0.70 N/A 8.54 3.78	1.29 0.05 -0.66 0.84 N/A 8.32 3.24	1.38 -0.17 -1.26 0.93 N/A 5.88 0.89	1.95 -0.35 -1.76 1.23 N/A 0.29 -3.98

Figure 5.17: Top right assembly of Fig. 5.15

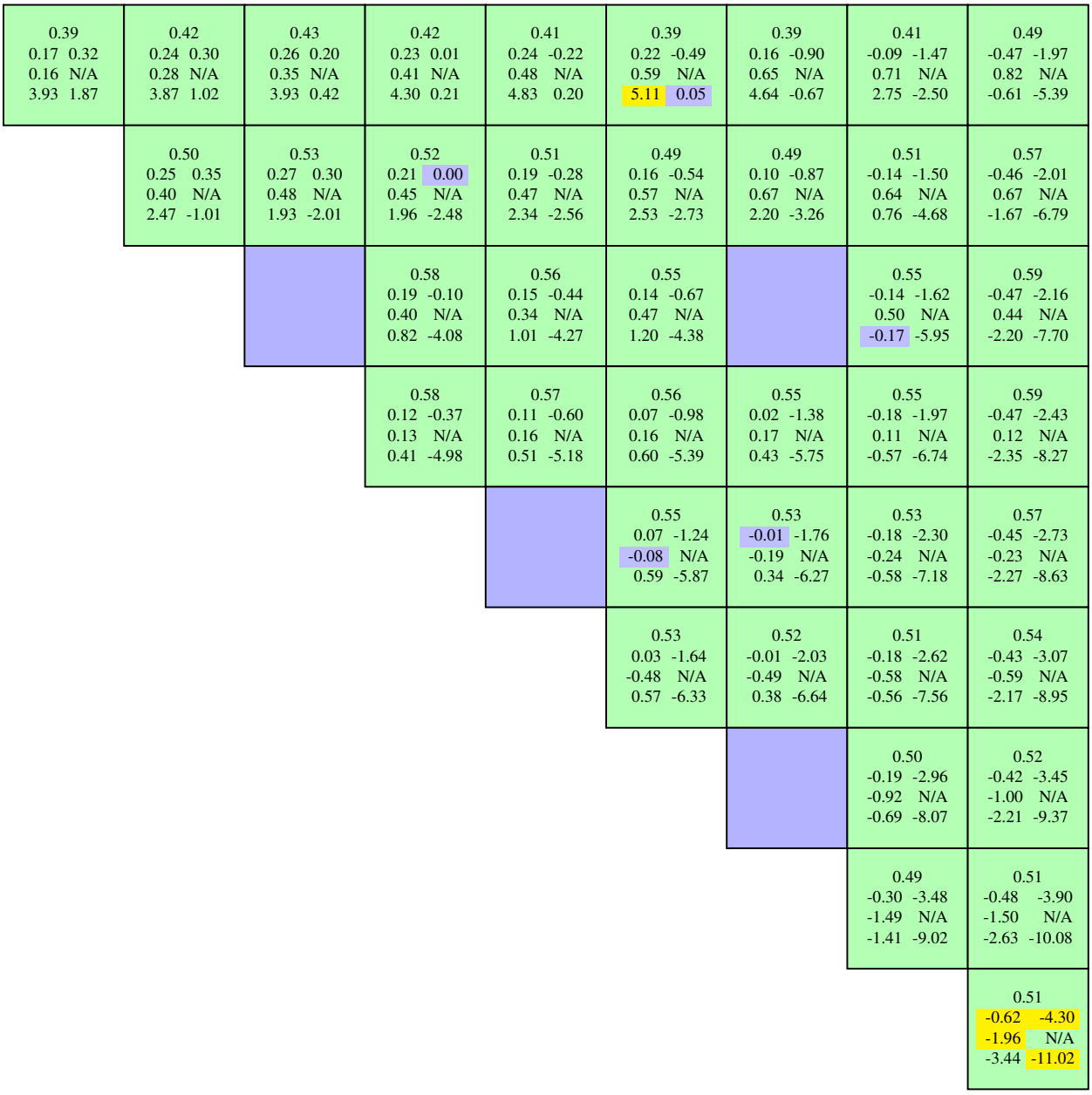

Figure 5.18: bottom right assembly of Fig. 5.15

Chapter 6

Incorporating SPH into DGM

In this chapter, we discuss the possibility of using the discrete generalized multigroup method to produce cross sections for downstream use. As mentioned in Chapter 1, the computation of SPH factors is one method for correcting cross sections after spatial or energy homogenization. In Section 6.1, the standard derivation of SPH factors is presented. Following that, Section 6.2 derives a form of the SPH factors for use in DGM. We then present three test problems to evaluate the use of DGM-SPH factors in Section 6.3. The results from the test problems are presented in Section 6.4. The chapter concludes in Section 6.5 with a summary of general observations as well as suggestions for future research areas.

6.1 SPH Factors

The use of SPH factors as discussed in Chapter 1 provides a way to ensure that reaction rates are preserved while applying homogenization techniques. To review their derivation, first, consider a general reaction rate as

$$R_{c,g} = \Sigma_{c,g}\phi_{c,g} \,, \tag{6.1}$$

where c is a spatial cell, and g is a energy group from the fine-group structure. We desire to homogenize this information over a number of spatial cells in region r as

$$\bar{R}_{r,g} = \frac{\sum\limits_{c\in r} R_{c,g} V_c}{\sum\limits_{c\in r} V_c} = \frac{\sum\limits_{c\in r} \Sigma_{c,g}\phi_{c,g} V_c}{\sum\limits_{c\in r} V_c} \,, \tag{6.2}$$

where V_c is the volume for spatial cell c. Let's assume that we can find a spatially-averaged cross section for a region, which is multiplied into a spatially-averaged flux as

$$\bar{R}_{r,g} = \bar{\Sigma}_{r,g}\bar{\phi}_{r,g} \,, \tag{6.3}$$

where the spatially-averaged flux $\bar{\phi}_{r,g}$ is defined as

$$\bar{\phi}_{r,g} = \frac{\sum\limits_{c\in r} \phi_{c,g} V_c}{\sum\limits_{c\in r} V_c} \,, \tag{6.4}$$

which leads to the definition for the spatially-averaged cross section $\bar{\Sigma}_{r,g}$ as

$$\bar{\Sigma}_{r,g} = \frac{\sum\limits_{c\in r} \Sigma_{c,g}\phi_{c,g} V_c}{\sum\limits_{c\in r} \phi_{c,g} V_c} \,. \tag{6.5}$$

Defined in this way, the reaction rate should be preserved; however, in practice this is not always true because the flux found by solving the transport equation with homogenized cross sections is not the same as that found by Eq. (6.4).

To eliminate (or, at least, to minimize) this error, we seek a correction factor, which is applied to the cross sections directly to force preservation of reaction rates. We first assume that the reference problem has been solved, which results in the spatially-fine scalar flux and corresponding reaction rates. In other words, $\phi^{\text{ref}}_{c,g}$ has been found by solving the transport equation using $\Sigma_{c,g}$. Using this reference flux in Eqs. (6.3) and (6.5) leads to a reference, homogenized cross section $\bar{\Sigma}^{\text{ref}}_{r,g}$ and corresponding reaction rate $\bar{R}^{\text{ref}}_{r,g}$.

The transport equation is then solved again using the homogenized cross sections $\bar{\Sigma}^{\text{ref}}_{r,g}$,

which results in $\bar{\phi}^{\text{homog}}_{c,g}$. Then, this flux vector is spatially averaged over a region using Eq. (6.4) to find $\bar{\phi}^{\text{homog}}_{r,g}$. The spatially-homogenized reaction rate can be written as

$$\bar{R}^{\text{homog}}_{r,g} = \bar{\Sigma}^{\text{homog}}_{r,g} \bar{\phi}^{\text{homog}}_{r,g} \,, \tag{6.6}$$

where $\bar{\Sigma}^{\text{homog}}_{r,g}$ is the homogenized cross section. We require that the reaction rate is unchanged by the spatial homogenization, and, thus, we set the reference and homogenized reaction rates equal, or

$$\bar{\Sigma}^{\text{ref}}_{r,g} \bar{\phi}^{\text{ref}}_{r,g} = \bar{R}^{\text{ref}}_{r,g} = \bar{R}^{\text{homog}}_{r,g} = \bar{\Sigma}^{\text{homog}}_{r,g} \bar{\phi}^{\text{homog}}_{r,g} \,, \tag{6.7}$$

which suggests that the spatially-homogenized cross section be defined as

$$\bar{\Sigma}^{\text{homog}}_{r,g} = \bar{\Sigma}^{\text{ref}}_{r,g} \frac{\bar{\phi}^{\text{ref}}_{r,g}}{\bar{\phi}^{\text{homog}}_{r,g}} = \omega_{r,g} \bar{\Sigma}^{\text{ref}}_{r,g} \,, \tag{6.8}$$

where $\omega_{r,g}$ is the SPH factor for region r and group g, i.e., the correction factor sought. Notice that the SPH factor depends on the homogenized flux $\bar{\phi}^{\text{homog}}_{r,g}$, which in turn depends on the SPH factor. Thus, the homogeneous problem is iteratively solved until convergence of the SPH factors, at which time, the reaction rate is preserved for the region.

Note that as presented here, an infinite number of SPH factors can be defined that preserve the reaction rates. Therefore, it is common to normalize the flux levels as

$$\frac{\sum\limits_{r} V_r \phi^{\text{homog}}_{r,g}}{\sum\limits_{r} V_r} = \frac{\sum\limits_{c} V_c \phi^{\text{ref}}_{c,g}}{\sum\limits_{c} V_c} \,, \tag{6.9}$$

where $V_r = \sum\limits_{c \in r} V_c$, which ensures that a unique set of SPH factors is determined. Once the SPH factors are determined for each group and region, the reaction rates are preserved over the homogenized region, and the homogenized cross sections are ready downstream use in core models.

Thus far, these equations assume that only spatial homogenization is performed. However, SPH factors can also preserve reaction rates when homogenizing over energy with the

modification that Eq. (6.4) becomes

$$\bar{\phi}_{r,G} = \frac{\sum_{g\in G}\sum_{c\in r}\phi_{c,g}V_cE_g}{\sum_{g\in G}\sum_{c\in r}V_cE_g}\,, \tag{6.10}$$

and Eq. (6.5) becomes

$$\bar{\Sigma}_{r,G} = \frac{\sum_{g\in G}\sum_{c\in r}\Sigma_{c,g}\phi_{c,g}V_cE_g}{\sum_{g\in G}\sum_{c\in r}\phi_{c,g}V_cE_g}\,, \tag{6.11}$$

where E_g is the width of energy group g. In many transport calculations, it is convenient to solve using $E_g = 1$ for all g, which means that the solution vector is actually $\phi_{c,g}E_g$. If desired, the actual flux may be easily recovered after solving the transport equation. For several illustrative examples of the 1-group calculation of SPH factors, the work of Yamamoto et al.[39] is an excellent resource.

6.2 Derivation of DGM-SPH

In this section, we seek a way to correct the coarse-group moments produced by DGM using an approach similar to SPH. However, we desire a form of the SPH factors that do not require reformation of the fine-group flux or cross sections from the coarse-group moments. In other words, we seek SPH factors that can be used to correct the mass matrices of Section 2.3, where the SPH factors are computed using moments of the flux vectors. However, we first must have a relationship for spatial homogenization of the mass matrices. In the following derivation, we will assume that any treatment of the energy variable is done by the DGM method such that only spatial homogenization is required.

We begin with the definition of the total mass matrix defined in Section 2.3 as

$$\bar{\Sigma}^{t*}_{r,G,i,j} = \sum_{g=1}^{N_g^G} P^G_{i,g}\bar{\Sigma}^t_{r,g}P^G_{j,g}\,. \tag{6.12}$$

where the mass matrix has been formed directly from the spatially-averaged, fine-group data

$\bar{\Sigma}^t_{r,g}$. Over the next few steps, we will find a definition for the homogenized mass matrix $\bar{\Sigma}^{t*}_{r,G,i,j}$ that is a function of the spatially-dependent mass matrices $\Sigma^{t*}_{c,G,i,j}$. The spatially-averaged, fine-group cross sections are also defined as

$$\bar{\Sigma}^t_{r,g} = \frac{\sum_i P_{i,g} \bar{\Sigma}^t_{r,G,i} \bar{\phi}_{r,G,0}}{\bar{\phi}_{r,g}} , \tag{6.13}$$

where $P_{i,g}$ is an element of an orthogonal basis as discussed in Chapter 2. This definition is substituted into Eq. (6.12) to find

$$\bar{\Sigma}^{t*}_{r,G,i,j} = \sum_{g \in G} P_{i,g} \frac{\sum_k P_{k,g} \bar{\Sigma}^t_{r,G,k} \bar{\phi}_{r,G,0}}{\bar{\phi}_{r,g}} P_{j,g} . \tag{6.14}$$

A cross section moment may be spatially homogenized as

$$\bar{\Sigma}_{r,G,i} = \frac{\sum_{c \in r} \Sigma_{c,G,i} \phi_{c,G,0} V_c}{\sum_{c \in r} \phi_{c,G,0} V_c} , \tag{6.15}$$

which is inserted into Eq. (6.14) to yield

$$\bar{\Sigma}^{t*}_{r,G,i,j} = \sum_{g \in G} P_{i,g} \frac{\sum_k P_{k,g} \frac{\sum_{c \in r} \Sigma_{c,G,k} \phi_{c,G,0} V_c}{\sum_{c \in r} \phi_{c,G,0} V_c} \bar{\phi}_{r,G,0}}{\bar{\phi}_{r,g}} P_{j,g} . \tag{6.16}$$

We now rearrange Eq. (6.16) to find

$$\bar{\Sigma}^{t*}_{r,G,i,j} = \sum_{g \in G} \frac{P_{i,g} P_{j,g}}{\bar{\phi}_{r,g}} \sum_k P_{k,g} \frac{\sum_{c \in r} \Sigma_{c,G,k} \phi_{c,G,0} V_c}{\sum_{c \in r} \phi_{c,G,0} V_c} \bar{\phi}_{r,G,0} . \tag{6.17}$$

The spatially-averaged flux moments are defined as

$$\bar{\phi}_{r,G,0} = \frac{\sum_{c \in r} \phi_{c,G,0} V_c}{\sum_{c \in r} V_c} , \tag{6.18}$$

which is substituted into Eq. (6.17) to find

$$\bar{\Sigma}^{t*}_{r,G,i,j} = \sum_{g\in G} \frac{P_{i,g}P_{j,g}}{\bar{\phi}_{r,g}} \sum_k P_{k,g} \frac{\sum\limits_{c\in r} \Sigma_{c,G,k}\phi_{c,G,0}V_c}{\sum\limits_{c\in r} V_c} \,. \tag{6.19}$$

We now switch the order of summation and rearrange to yield

$$\bar{\Sigma}^{t*}_{r,G,i,j} = \sum_{c\in r} \frac{V_c}{L} \sum_{g\in G} \frac{P_{i,g}P_{j,g}}{\bar{\phi}_{r,g}} \sum_k P_{k,g}\Sigma_{c,G,k}\phi_{c,G,0} \,, \tag{6.20}$$

where $L = \sum\limits_{c\in r} V_c$. The total reaction rate moments are defined as

$$R^t_{c,G,i} = \Sigma^t_{c,G,i}\phi_{c,G,0} = \sum_j \phi_{c,G,j}\Sigma^{t*}_{c,G,i,j} \,, \tag{6.21}$$

which is substituted into Eq. (6.20), to yield

$$\bar{\Sigma}^{t*}_{r,G,i,j} = \sum_{c\in r} \frac{V_c}{L} \sum_{g\in G} \frac{P_{i,g}P_{j,g}}{\bar{\phi}_{r,g}} \sum_k P_{k,g} \sum_l \phi_{c,G,l}\Sigma^{t*}_{c,G,k,l} \,. \tag{6.22}$$

After once again changing the order of summation and rearranging, we arrive at

$$\bar{\Sigma}^{t*}_{r,G,i,j} = \sum_{c\in r} \frac{V_c}{L} \sum_l \phi_{c,G,l} \sum_k \Sigma^{t*}_{c,G,k,l} \sum_{g\in G} \frac{P_{i,g}P_{j,g}P_{k,g}}{\bar{\phi}_{r,g}} \,. \tag{6.23}$$

Equation (6.23) provides a relationship that will spatially homogenize the total mass matrix without requiring access to the fine-group cross section. Note that the fine-group flux does appear in the relationship, which is easily computed as $\bar{\phi}_{r,g} = \sum\limits_i P_{i,g}\bar{\phi}_{r,G,i}$ as discussed in Chapter 2 with Eq. (2.7).

Similar steps as above may be followed to arrive at relationships for spatially homogenizing the scattering and fission cross sections as

$$\bar{\Sigma}^{s}_{r,G\leftarrow G',i,j} = \sum_{c\in r} \frac{V_c}{L} \sum_k \phi_{c,G',k} \sum_l \Sigma^{s}_{c,G\leftarrow G',i,l} \sum_{g'\in G'} \frac{P_{j,g'}P_{k,g'}P_{l,g'}}{\bar{\phi}_{r,g'}} \,, \tag{6.24}$$

and

$$\bar{\Sigma}^{f}_{r,G',j} = \sum_{c\in r} \frac{V_c}{L} \sum_{k} \phi_{c,G',k} \sum_{l} \Sigma^{f}_{c,G',l} \sum_{g'\in G'} \frac{P_{j,g'} P_{k,g'} P_{l,g'}}{\bar{\phi}_{r,g'}} \,, \tag{6.25}$$

respectively. The spatially-averaged chi moment for a region is given by

$$\bar{\chi}_{r,G,i} = \frac{\sum_{c\in r} \chi_{c,G,i} V_c}{\sum_{c\in r} V_c} \,. \tag{6.26}$$

With these relationships defined, we are now in a position to find the SPH factors to correct the homogenized mass matrices. The total reaction rate moments are defined as

$$\bar{R}^{t}_{r,G,i} = \bar{\Sigma}^{t}_{r,G,i} \bar{\phi}_{r,G,0} = \sum_{j} \bar{\phi}_{r,G,j} \bar{\Sigma}^{t}_{r,G,i,j} \,, \tag{6.27}$$

which can be used to form a relationship similar to Eq. (6.7), as

$$\bar{\Sigma}^{\text{ref}}_{r,G,i} \bar{\phi}^{\text{ref}}_{r,G,0} = \bar{R}^{\text{ref}}_{r,G,i} = \bar{R}^{\text{homog}}_{r,G,i} = \bar{\Sigma}^{\text{homog}}_{r,G,i} \bar{\phi}^{\text{homog}}_{r,G,0} = \sum_{j} \bar{\phi}^{\text{homog}}_{r,G,j} \bar{\Sigma}^{\text{homog}}_{r,G,i,j} \,. \tag{6.28}$$

If we followed a similar path as Eq. (6.8), we could define

$$\bar{\Sigma}^{\text{homog}}_{r,G,i} = \bar{\Sigma}^{\text{ref}}_{r,G,i} \frac{\bar{\phi}^{\text{ref}}_{r,G,0}}{\bar{\phi}^{\text{homog}}_{r,G,0}} = \omega_{r,G} \bar{\Sigma}^{\text{ref}}_{r,G,i} \,. \tag{6.29}$$

However, this provides a correction factor for the coarse-group moments and not for the mass matrices! Thus, Eq. (6.29) cannot be our path forward.

We would like to define

$$\sum_{j} \bar{\phi}^{\text{ref}}_{r,G,j} \bar{\Sigma}^{\text{ref}}_{r,G,i,j} = \sum_{j} \bar{\phi}^{\text{homog}}_{r,G,j} \bar{\Sigma}^{\text{homog}}_{r,G,i,j} \,, \tag{6.30}$$

and set each of the terms equal, i.e.,

$$\bar{\Sigma}^{\text{homog}}_{r,G,i,j} = \frac{\bar{\phi}^{\text{ref}}_{r,G,j}}{\bar{\phi}^{\text{homog}}_{r,G,j}} \bar{\Sigma}^{\text{ref}}_{r,G,i,j} = \omega_{r,G,j} \bar{\Sigma}^{\text{ref}}_{r,G,i,j} \,, \tag{6.31}$$

but this leaves the higher-order flux moments $\bar{\phi}^{\text{homog}}_{r,G,j}$ in the denominator. This quickly leads to instabilities as $\bar{\phi}^{\text{homog}}_{r,G,j}$ may be arbitrarily small for $J > 0$ as discussed in Chapter 2. Thus, once again, Eq. (6.31) cannot be our path forward.

Instead, we define

$$r^k_{r,G} = \frac{\bar{R}^{\text{ref}}_{r,G,0}}{\bar{R}^{\text{k, homog}}_{r,G,0}}\,, \tag{6.32}$$

which is the ratio of the zeroth-order, reference reaction rate and the zeroth-order, homogenized reaction rate for the kth iteration of the SPH algorithm. We can then define the SPH factors for the kth iteration as

$$\omega^k_{r,G} = \omega^{k-1}_{r,G} r^k_{r,G}\,. \tag{6.33}$$

Defined in this way, the SPH factors will converge in tandem with the homogenized reaction rates. The SPH factors $\omega_{r,G}$ are then applied to the mass matrices as

$$\bar{\Sigma}^{\text{homog}}_{r,G,i,j} = \bar{\Sigma}^{\text{ref}}_{r,G,i,j}\omega_{r,G}\,. \tag{6.34}$$

Since the DGM method is designed to preserve the bulk reaction rates in the zeroth-order terms, an alternative method is to only apply the SPH factors to the zeroth-order terms in the mass matrices, i.e.,

$$\bar{\Sigma}^{\text{homog}}_{r,G,0,0} = \bar{\Sigma}^{\text{ref}}_{r,G,0,0}\omega_{r,G}\,. \tag{6.35}$$

These ideas manifested in four different methods to test, which result from the two sets of two choices. The first choice is to compute the reaction rate ratios with either the zeroth-order, total reaction rates or with the fission reaction rates. The second choice is to apply the SPH factors to all orders of the mass matrices or just the zeroth-order moments.

Additionally, the success of using the ratio of fluxes was measured as well and the resulting SPH factors could be applied to all orders of just the zeroth order of the mass matrices. The final method to test uses the SPH corrected cross sections from the non-DGM case, i.e., Eq. (6.8), then computes homogenized mass matrices directly from the fine-group data. These methods are summarized in Table 6.1, which names each method and summarizes the

method for computing the SPH factors.

Table 6.1: Methods for computing the SPH factors for use with DGM

Method	Description
R_t - ω_0	Total reaction rates and applied to 0th-order mass matrices
R_f - ω_0	Fission reaction rates and applied to 0th-order mass matrices
R_t - ω	Total reaction rates and applied to all mass matrices
R_f - ω	Fission reaction rates and applied to all mass matrices
ϕ - ω_0	0th scalar flux moments applied to 0th-order mass matrices
ϕ - ω	0th scalar flux moments applied to all mass matrices
ω_g	DGM with SPH corrected fine-group cross sections
SPH corrected	Non-DGM solution that corrects cross sections with SPH factors
Non-SPH corrected	Non-DGM solution with no SPH correction

These DGM-SPH methods were compared against the standard approach of using SPH factors as discussed in Section 6.1, which is to say homogenizing the cross sections without using DGM. Finally, we compare these methods to the performance of homogenizing cross sections without the use of correction with SPH factors. In Table 6.1, these test cases appear at the end and are called "SPH corrected" and "Non-SPH corrected", respectively. Both of these non-DGM cases are tested by creating coarse-group structures for homogenization that use the same number of degrees of freedom as a DGM expansion of order i. For example, if a DGM coarse group contains 15 fine groups and uses a third-order expansion, then three degrees of freedom are utilized of the 15 possible DOF. The non-DGM cases would divide the 15 fine groups into three sub-regions, thus forming three coarse groups for homogenization resulting in three DOF, which can be compared to the DGM cases.

6.3 Test Problem for DGM with SPH

To test the DGM method with SPH, we returned to the 10-pin problem discussed in Section 4.2. In practice, however, we need two types of problems for testing SPH correction. The first of these will be used to generate homogenized cross sections and will be the smaller of the two. This problem will be called the "generation" problem in this chapter. The second is used to test the success of the cross sections and will be called the "test" problem in this chapter. In

this section, we test three different choices of generating problem and apply all three sets of corrected cross sections to the same test problem.

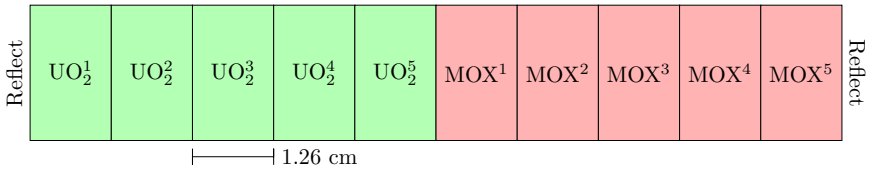

Figure 6.1: Configuration for the test problem, where materials are generated by homogenizing over each pincell

As mentioned, the test problem will be the 10-pin problem, which is homogenized over each of the 10 pincells to produce 10 unique materials with associated cross sections as shown in Fig. 6.1. The 44-group structure was used for this purpose, which was collapsed into four coarse groups as described in Table 4.2. The first generating problem used the same geometry and materials as the test problem, i.e., we expect traditional SPH correction to preserve the reaction rates exactly.

The second generating problem is presented in Fig. 6.2 and uses a reduced number of pins and will be called the 2-pin problem. The 2-pin problem used the same materials and the same number of mesh cells per pin as the 10-pin problem from Section 4.2, but with the geometry shown in Fig. 6.2. The 2-pin problem was homogenized over each of the two pincells in Fig. 6.2 to produce a homogenized UO_2 material and a homogenized MOX material, which was used as the corresponding materials in the test problem shown in Fig. 6.3. As this problem is different than the test problem, SPH factors are not expected to reproduce reaction rates exactly because the method is correcting the rates to the "wrong" values, i.e., to different than the test problem.

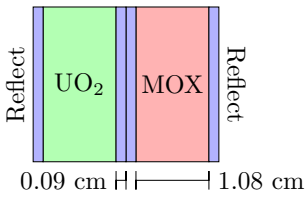

Figure 6.2: Configuration for the 2-pin, generating problem

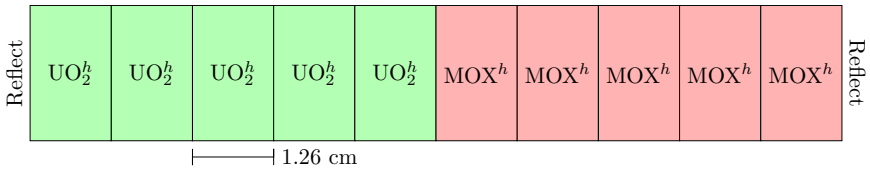

Figure 6.3: Test geometry for the generating problems that produce a reduced number of materials

The final generating problem uses the same geometry as the 10-pin, test problem, but homogenizes over all of the pins for a given material, thus forming a homogenized UO_2 material and a homogenized MOX material as shown in Fig. 6.4. This final generating problem will be called the 5-pin problem. These materials are tested using the geometry shown in Fig. 6.3. Once again, the SPH method is correcting the cross sections to the "wrong" values, and are not expected to correctly reproduce the reaction rates.

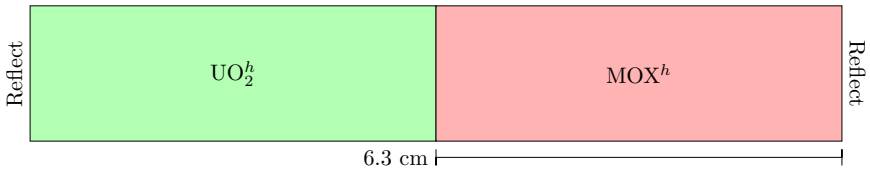

Figure 6.4: Configuration for the test problem, where materials are generated by homogenizing over each pincell

These three problems were used to study the performance of the SPH method both with and without DGM. For the standard (non-DGM) solution, energy homogenization was used to collapse the 44-group solution to a structure using the same degrees of freedom as the corresponding DGM solution.

The steps for testing the standard SPH method are as follows

1. Solve the generating problem with standard (fine-group) cross sections
2. Homogenize the standard cross sections using the reference scalar flux
3. Solve the generating problem with the homogenized cross sections
4. Solve for the SPH factors
5. Correct the homogenized cross sections with the SPH factors

6. Return to step (3) until SPH factors (and cross sections) have converged
7. Solve the test problem with standard (fine-group) cross sections
8. Solve the test problem with SPH-corrected, homogenized cross sections
9. Compare the solutions to the test problem

A DGM solution truncated to zeroth order is comparable to the standard SPH approach since reaction rates are preserved by the zeroth-order DGM equation. Thus, the goal for this section is to embed more information in the cross section moments than a traditional downstream scheme would allow for a given number of degrees of freedom. As such, the SPH-corrected mass matrices will be corrected with a full-order DGM solution, but the resulting mass matrices will be used with a truncated basis. This will allow comparisons of the success as a function of order, which should be dependent on the orthogonal basis chosen. For this work, four basis sets are selected, which include the discrete Legendre polynomials (DLPs), then three POD-driven basis sets. The POD basis sets are POD_full, POD_combine, and POD_pins, which are described in Section 4.2. The steps for testing the SPH method for use with DGM are

1. Solve the generating problem with standard mass matrices using full-order DGM
2. Homogenize the standard mass matrices using the reference scalar flux moments
3. Solve the generating problem with the homogenized mass matrices using full-order DGM
4. Solve for the SPH factors using the chosen method from Table 6.1
5. Correct the homogenized mass matrices with the DGM-SPH factors
6. Return to step (3) until SPH factors (and mass matrices) have converged
7. Solve the test problem with standard (fine-group) cross sections (not using DGM)

8. Solve the test problem with SPH-corrected, homogenized mass matrices using oth-order DGM

9. Compare the solutions to the test problem

6.4 Results

In this section, each of the methods presented in Table 6.1 is compared against the standard approach to homogenizing using SPH. This is done for all three of the generating problems discussed in the preceding section. To compare each of the methods, a reference solution of the test problem is computed, which is used to compute reference pincell, fission densities. Then, the steps in Section 6.3 are used to produce pincell fission densities for each of the methods including the non-DGM case.

In Fig. 6.5, a comparison of the methods is presented for the first generating problem. Figure 6.5a presents the DGM methods utilizing the DLPs, whereas Fig. 6.5b uses the POD_combine basis set for DGM calculations. The SPH corrected curve that represents a non-DGM solution is not present because this method had no error for this generating problem as mentioned previously since the generating problem matches the test problem. The Non-SPH corrected curve from the figures corresponds to using a non-DGM solution to homogenize over both space and energy that is not corrected via SPH. All data points in the figure are the maximum error in the pincell fission density relative to the reference test problem. Spatially dependent results are tabulated in Table 6.2.

Some of the methods discussed in Table 6.1 are more successful than others. In particular, the ratio of reaction rates (either fission or total) appears to perform the best when applied to all orders of the mass matrix. The ratio of fission reaction rates (R_f - ω) seems to perform better than the ratio of total reaction rates (R_t - ω) for the POD basis, but the two methods perform similarly for the DLP basis. For the POD basis, both of these methods have less than a 1% error after using three degrees of freedom per coarse group.

Note that correcting the fine-group cross sections with SPH before computing the mass

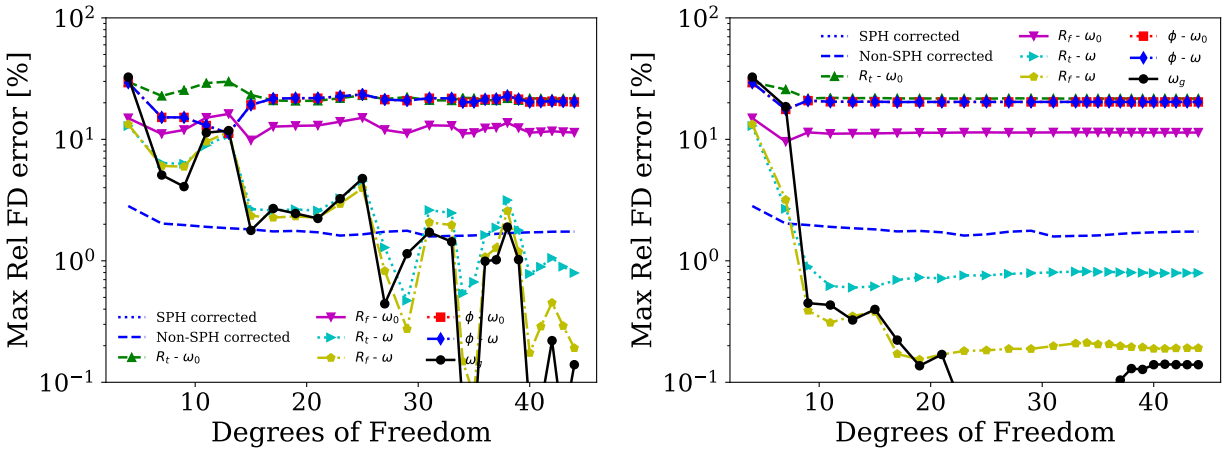

(a) Using the DLP basis for DGM

(b) Using the POD_combine basis for DGM

Figure 6.5: Comparison of the DGM-SPH methods when solving the test problem with cross sections generated by the 10-pin problem. All errors are computed relative to a non-homogenized, fine-group solution of the test problem, and present the maximum error as a function of space for a pincell fission density as a function of degrees of freedom in the energy variable.

Note that the SPH corrected curve is at an error of 0.0 for this problem as the generating problem matches the test problem.

matrices (ω_g) is the most successful method at the high orders. All three of these methods are more accurate than the uncorrected cross sections (Non-SPH corrected) once 3 degrees of freedom are used per coarse group for the POD basis. Also note that although three different POD basis sets were tested, the performance was nearly identical, and thus, only the POD_combine basis is presented in this section.

Results from the second generating problem are presented in Fig. 6.6 which again includes the performance of the DLP basis in Fig. 6.6a and performance of the POD_combine basis in Fig. 6.6b. The spatially dependent results are tabulated in Table 6.3. For this problem, the SPH method is correcting the reaction rates to the wrong value since the generating problem does not match the test problem. Thus, the performance of the SPH corrected curve is quite poor until many degrees of freedom are used. However, the performance of the DGM-SPH methods is nearly the same as compared to the first generating problem.

Again we see that the ratio of the fluxes (ϕ - ω) is not a viable method, but the ratio of reaction rates is relatively successful. In particular, the best performing method is the ratio

Table 6.2: Errors in normalized fission densities for each pincell in the test problem using cross sections from the first generating problem relative to the reference. All columns are in percent error except for the Ref column, which is the normalized fission density for each pincell. SPH-X refers to Non-DGM, SPH-corrected, results, and NON-X refers to Non-DGM, Non-SPH results, where X=0 is one DOF per coarse group, X=2 is three DOF per coarse group, and X=Full is full order in all coarse groups. The DGM-SPH methods are provided for three DOF per coarse group utilizing the POD_combine basis.

Pin	Ref	SPH-0	SPH-2	SPH-Full	NON-0	NON-2	NON-Full
0	0.290	0.000	0.000	0.000	2.669	0.687	0.302
1	0.283	0.000	0.000	0.000	2.653	0.731	0.353
2	0.267	0.000	0.000	0.000	2.622	0.844	0.483
3	0.237	0.000	0.000	0.000	2.598	1.106	0.776
4	0.184	0.000	0.000	0.000	2.825	1.971	1.741
5	0.529	0.000	0.000	0.000	0.774	0.634	0.629
6	0.347	0.000	0.000	0.000	1.689	0.525	0.277
7	0.310	0.000	0.000	0.000	1.665	0.312	0.001
8	0.300	0.000	0.000	0.000	1.544	0.204	0.097
9	0.297	0.000	0.000	0.000	1.476	0.164	0.126

Pin	Ref	R_t - ω_0	R_f - ω_0	R_t - ω	R_f - ω	ϕ - ω_0	ϕ - ω	ω_g
0	0.290	21.723	5.849	0.608	0.020	12.119	12.102	0.065
1	0.283	2.651	0.520	0.674	0.090	14.748	14.739	0.034
2	0.267	18.047	7.163	0.805	0.229	19.176	19.174	0.222
3	0.237	18.761	11.412	0.894	0.389	20.824	20.850	0.440
4	0.184	7.531	8.000	0.640	0.319	9.571	9.579	0.449
5	0.529	2.702	0.270	0.691	0.165	11.734	11.753	0.028
6	0.347	1.517	2.997	0.609	0.079	8.472	8.478	0.314
7	0.310	1.388	2.260	0.021	0.147	5.953	5.941	0.064
8	0.300	1.689	1.891	0.182	0.011	5.113	5.088	0.066
9	0.297	1.628	1.796	0.135	0.174	4.831	4.799	0.125

of the total reaction rate that is applied to only the zeroth-order mass matrices (R_f - ω_0). However, this method was not viable for the first generating problem. Taking the ratio of total reaction rates and applying to all orders (R_t - ω) performs quite well and was consistent with the performance of the first generating problem. Again, forming the mass matrices from SPH corrected, fine-group data performs quite well. Note once again, that the DGM-SPH methods are closer to the reference solution than the Non-DGM cases once three degrees of freedom are used per coarse group for the POD_combine basis.

Finally, the performance of the third generating problem are presented in Fig. 6.7 with

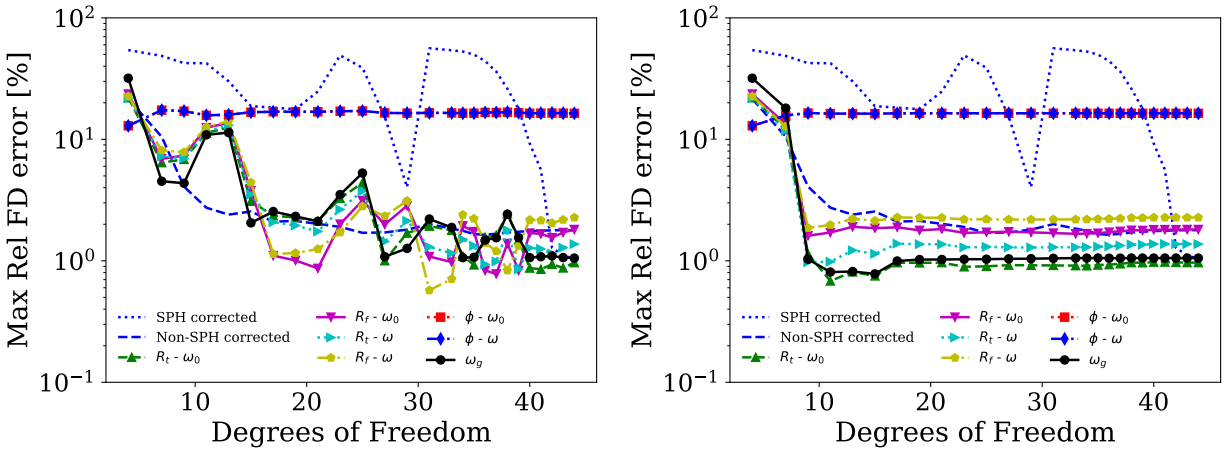

(a) Using the DLP basis for DGM

(b) Using the POD_combine basis for DGM

Figure 6.6: Comparison of the DGM-SPH methods when solving the test problem with cross sections generated by the 2-pin problem. All errors are computed relative to a non-homogenized, fine-group solution of the test problem, and present the maximum error as a function of space for a pincell fission density as a function of degrees of freedom in the energy variable.

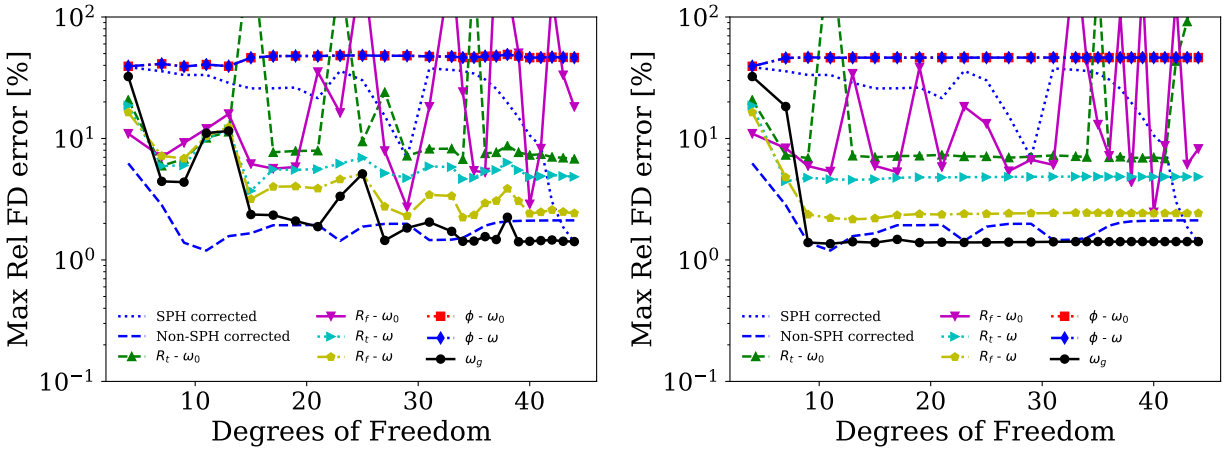

(a) Using the DLP basis for DGM

(b) Using the POD_combine basis for DGM

Figure 6.7: Comparison of the DGM-SPH methods when solving the test problem with cross sections generated by the 5-pin problem. All errors are computed relative to a non-homogenized, fine-group solution of the test problem, and present the maximum error as a function of space for a pincell fission density as a function of degrees of freedom in the energy variable.

the DLP basis results in Fig. 6.7a and the POD_combine results in Fig. 6.7b. The results are tabulated in Table 6.4. This problem leads to considerably more instabilities for the DGM methods, which manifested in spikes in the error where some of the methods failed

Table 6.3: Errors in normalized fission densities for each pincell in the test problem using cross sections from the second generating problem relative to the reference. All columns are in percent error except for the Ref column, which is the normalized fission density for each pincell. SPH-X refers to Non-DGM, SPH-corrected, results, and NON-X refers to Non-DGM, Non-SPH results, where X=0 is one DOF per coarse group, X=2 is three DOF per coarse group, and X=Full is full order in all coarse groups. The DGM-SPH methods are provided for three DOF per coarse group utilizing the POD_combine basis.

Pin	Ref	SPH-0	SPH-2	SPH-Full	NON-0	NON-2	NON-Full
0	0.290	54.323	42.434	0.507	21.566	4.083	0.233
1	0.283	53.374	41.883	0.525	20.952	4.056	0.280
2	0.267	50.937	40.239	0.526	19.520	3.954	0.404
3	0.237	45.383	35.914	0.392	16.801	3.701	0.699
4	0.184	31.113	23.865	0.607	12.240	3.586	1.788
5	0.529	17.210	13.198	1.037	1.413	0.597	0.641
6	0.347	23.875	23.261	0.556	9.517	2.375	0.059
7	0.310	37.528	32.468	0.474	14.835	2.898	0.030
8	0.300	41.108	33.156	0.318	16.749	2.893	0.072
9	0.297	41.936	32.603	0.257	17.332	2.816	0.086

Pin	Ref	R_t - ω_0	R_f - ω_0	R_t - ω	R_f - ω	ϕ - ω_0	ϕ - ω	ω_g
0	0.290	0.522	1.610	0.867	1.864	6.253	6.257	0.455
1	0.283	0.205	1.331	0.594	1.589	7.239	7.242	0.573
2	0.267	0.418	0.777	0.070	1.062	9.244	9.246	0.763
3	0.237	1.142	0.121	0.538	0.442	11.978	11.977	0.845
4	0.184	0.279	0.865	0.122	0.816	12.851	12.849	0.161
5	0.529	0.302	0.276	0.445	0.399	16.475	16.473	1.031
6	0.347	0.838	0.201	0.188	0.409	1.282	1.282	0.273
7	0.310	0.351	0.891	0.673	1.476	4.081	4.078	0.404
8	0.300	0.615	1.101	0.952	1.810	3.808	3.803	0.246
9	0.297	0.585	1.047	0.975	1.843	3.450	3.445	0.129

to converge. Outside of these artifacts, computing the mass matrices from SPH-corrected, fine-group data (ω_g) performs the best. The second best performing method utilized the ratio of fission reaction rates with SPH factors applied to all orders of the mass matrices (R_f - ω). Both of these methods are closer to the reference result as compared to the traditional SPH correction, and are around a 1% error in the relative fission density error when using the POD_combine basis truncated to three DOF per coarse group.

For each of the tested generating problems, the DGM-SPH methods seem to be more problem independent than the traditional SPH correction. This is likely because the DGM

Table 6.4: Errors in normalized fission densities for each pincell in the test problem using cross sections from the third generating problem relative to the reference. All columns are in percent error except for the Ref column, which is the normalized fission density for each pincell. SPH-X refers to Non-DGM, SPH-corrected, results, and NON-X refers to Non-DGM, Non-SPH results, where X=0 is one DOF per coarse group, X=2 is three DOF per coarse group, and X=Full is full order in all coarse groups. The DGM-SPH methods are provided for three DOF per coarse group utilizing the POD_combine basis.

Pin	Ref	SPH-0	SPH-2	SPH-Full	NON-0	NON-2	NON-Full
0	0.290	10.339	8.268	0.346	6.238	1.387	0.335
1	0.283	8.287	6.656	0.345	5.701	1.310	0.394
2	0.267	3.072	2.416	0.314	4.467	1.129	0.544
3	0.237	8.688	7.519	0.158	2.266	0.851	0.895
4	0.184	38.662	33.336	0.741	0.317	1.115	2.117
5	0.529	30.712	29.898	1.399	0.061	0.427	0.906
6	0.347	5.218	5.476	1.316	1.524	0.476	0.018
7	0.310	17.843	17.535	0.914	3.690	0.749	0.104
8	0.300	21.532	20.860	0.510	4.554	0.780	0.145
9	0.297	22.538	21.693	0.356	4.777	0.742	0.158

Pin	Ref	R_t - ω_0	R_f - ω_0	R_t - ω	R_f - ω	ϕ - ω_0	ϕ - ω	ω_g
0	0.290	0.484	0.395	0.566	0.956	11.470	11.467	0.238
1	0.283	0.018	0.972	0.154	0.506	13.542	13.539	0.337
2	0.267	0.928	2.206	0.674	0.403	18.507	18.504	0.498
3	0.237	2.054	4.013	1.780	1.649	28.276	28.274	0.565
4	0.184	0.093	3.749	1.981	2.072	46.512	46.511	0.326
5	0.529	2.964	5.928	2.889	0.673	35.895	35.894	1.392
6	0.347	6.892	0.038	4.749	2.368	5.634	5.633	1.068
7	0.310	1.142	3.255	2.354	0.458	3.833	3.835	0.879
8	0.300	0.292	3.694	1.240	0.277	5.999	6.002	0.485
9	0.297	0.468	3.528	0.950	0.447	6.376	6.378	0.282

method provides a way to retain spectral information into the cross section moment my way of the basis collapse using an orthogonal basis. In other words, the DGM method better maintains the material interactions than traditional SPH correction for these problems.

It seems that the DGM-SPH methods can allow for a variable amount of error, which is a function of the number of degrees of freedom. However, the choice of basis is still important for this method as the errors in the DGM-SPH methods using the POD_combine basis plateau at approximately three degrees of freedom per coarse group. The errors resulting from the DLP basis do not plateau until nearly a full order expansion. This is because the errors from

a POD expansion fall below that of the SPH correction at few DOF for a POD basis, but require many more DOF for the DLP basis.

Prior research[39] has shown that SPH factors do not correctly account for the neutron leakage. The selected problems include a junction between two different fuel types, which causes a non-zero leakage from the homogenized regions. However, the DGM-SPH approach seems to better preserve the leakage, which results in improved SPH performance as compared to the non-DGM approach for general problems.

6.5 Conclusions

As presented in Section 6.4, many of the various DGM-SPH methods perform better than the standard approach for SPH in terms of the relative error in the fission density. The method R_f - ω performed consistently well, which computed the SPH factors from the ratio of the reference fission reaction rate to the homogenized fission reaction rate and applied the SPH factors to all moments of the mass matrices. The methods that utilized the ratio of scalar fluxes did not perform well for any of the generating problems.

While promising, the methods in this chapter do not represent an ideal solution yet. The methods described in Section 6.2 describe a method to use SPH factors that preserve the zeroth-order reaction rate moments. However, the higher-order moments are not preserved with respect to the reference except for the case of ω_g, which uses the SPH-corrected, fine-group data that we are trying to avoid. More work is needed to find a method to compute DGM-SPH factors that are capable of preserving the higher-order moments, which will further improve the performance.

Furthermore, this method must be validated against other problems to ensure the general performance of the DGM-SPH methods is consistent. In particular, this work should be applied to larger group structures, e.g., the scale 238-group or the ECCO 1968-group structures. Additionally, this method should be tested on larger problems as well as problems with more challenging spectral features.

Further, the methods in this section have used a naive approach to computing the SPH

factors, which is unable to preserve neutron leakage. Another path forward for the DGM method is to explore correction factors that can preserve the leakage such as the generalized equivalence theory first mentioned in Section 1.5.

Chapter 7

Conclusions

7.1 Concluding Remarks

The overarching goal for this work was to seek improvements to the discrete generalized multigroup (DGM) method, which would ultimately lead to homogenized cross sections for downstream use. This work can be divided into three major thrusts, which correspond to Chapter 4, Chapter 5, and Chapter 6, respectively. In the following pages, we will summarize the major findings of this research, and then end with outlining avenues for continuing this research.

The DGM method provides a way to model the energy variable within a transport calculation that expands the fluxes and cross sections using an orthogonal basis. In theory, the DGM method maps a fine-group, energy structure to a number of coarse energy groups. A transport problem can be solved on the coarse energy grid, and then the fine-group fluxes may be reconstructed. However, as originally designed, the DGM method suffered from several drawbacks, which include:

- a potential for negative fluxes or instabilities
- a requirement to store the angular flux
- spatially dependent cross section moments even if the cross sections themselves are not

- high computational expense compared to standard multigroup treatment of the energy variable

This work sought to find improvements for the method that would bring DGM closer to practicality.

In Chapter 4, we explored a new way to define bases for DGM that has the capability of embedding information about the physics into the basis vectors. This technique constructs a basis using the proper orthogonal decomposition (POD) and the method of snapshots. The resulting POD basis made possible the use of DGM with a truncated basis. Historically, the DGM method was used with the Legendre polynomials, which do not accurately approximate the shape of the fluxes with low-order expansions. Using POD instead allows an accurate representation of the fluxes in the DGM method even at low-order expansions. Thus, with the introduction of a small truncation error, the method can be performed with computational savings.

To test the truncated basis, the infinite medium problem, three 1-D problems, and one 2-D problem were tested with a variety of POD basis sets. These tests showed that the best POD basis sets utilized snapshots from all material types as well as junctions of material types. A decrease in performance was observed for basis sets that included snapshots of extra materials, though the effect was much smaller than the absence of material information. For these problems, most practical POD basis sets achieved less than 0.1% error in the fission density utilizing three degrees of freedom (DOF) per coarse group for the 1-D problems. This finding was nearly independent of group structure, though more work is required to determine if this trend holds for more difficult problems. To achieve an error of 0.01% in the fission density, approximately eight degrees of freedom per coarse group were required.

This work continued in Chapter 5 by exploring reformulations of the DGM equations as well as approximations for the cross section moments. First, many computational savings are found by precomputing so-called "mass matrices," which are partially-computed, cross section moments. This improvement was at no cost to accuracy, and it provided more than an order of magnitude improvement to the computational speed. The other experiments explored

in Chapter 5 did introduce error but were designed to address some of the aforementioned drawbacks.

First, the angular flux is required for the DGM method for one particular term that stores the total angular reaction rate. This work sought to approximate this angular dependence using a low-order Legendre expansion, which removes the need to store the angular flux. Linear expansion of the scalar flux was found to introduce approximately a 1% error in the fission densities whereas flat approximation resulted in roughly double the errors. When used in conjunction with a basis truncated to three DOF per coarse group, the errors are only slightly increased.

The second approximation was designed to address the cross-section moment storage requirements. Since the cross-section moments are functions of the spatially-dependent fluxes, the moments will be spatially dependent even if the cross sections are not. To reduce the storage, this work explored two homogenization options for the cross-section moments. The first would homogenize the cross-section moments over a certain spatial region, e.g. a pincell. The second option would homogenize the moments over all cells sharing a material type.

The greatest storage savings were from the second option, but the smallest impact to errors was from the first option. Homogenizing over region introduced approximately 0.5% error into the fission densities, while homogenizing over material had errors of approximately 10% in the fission densities for the 44-group problem. Material homogenization performed better over an order of magnitude better for the larger group structures. When used with a basis truncated to three DOF per coarse group, the first option errors increased very slightly. The errors for the truncated second option were slightly smaller than the non-truncated case, which was likely due to favorable cancellation. Overall, a truncated DGM solution that utilized spatial homogenization over regions and linear expansion of the angular flux would have approximately the same error as the truncated solution without approximation. Thus, the memory requirements for a truncated DGM solution can be greatly reduced by no longer requiring the angular flux and reducing the spatial dependence of the moments.

The final exploration for this work explored the use of spatial homogenization factors (SPH factors) that are designed to preserve reaction rates when homogenizing cross sections.

SPH factors are designed to work for both spatial and energy homogenization to prepare cross sections for downstream use. Chapter 6 explored ways to use SPH factors with the DGM method. In particular, we desired a method that collapsed the fine-group cross sections to mass matrices for use with DGM and directly homogenized the mass matrices without reconstructing the fine-group data. The method for deriving SPH factors for DGM is not as simple as that of the non-DGM derivation, but an effective method was found. The performance of the SPH corrected mass matrices was dependent on the basis, but the performance was improved as compared to traditional homogenization schemes for a test problem.

In particular, the use of SPH with DGM seemed to be more problem independent than traditional SPH calculations. The DGM moments were able to retain some of the material interactions in the higher-order terms, which greatly improved the performance relative to traditional methods for general problems. While SPH factors can preserve reaction rates for a specific problem, if those corrected cross sections are used for a different problem, reaction rates are no longer preserved and can perform worse than the uncorrected cross sections. However, SPH-corrected, DGM moments resulted in approximately 1% error in the pincell fission densities when using a POD basis truncated to three DOF per coarse group.

7.2 Future Work

The DGM method is still far from a replacement for standard methods such as the discrete ordinates method. When used as a method for solving the transport equation, the DGM method finds a solution using both more memory and more computational time. Further, the DGM method suffers from instabilities, which can only be somewhat mitigated by the use of Krasnoselskii iteration. This work explored the DGM method using an unaccelerated, discrete ordinates solver. However, it is possible that advanced solvers such as GMRES would improve the performance or stability of the DGM method. Using acceleration schemes is likely to be the best way to test the performance of the DGM method for larger problems.

The most promising area for this work was the creation of homogenized cross sections. A

lingering task is to compute these cross sections using the various approximations discussed in Chapter 5. SPH correction may be enough to correct for the error introduced by the approximations. Further, only simple problems were tested for homogenizing the cross sections, thus future exploration should be done on more difficult and realistic problems.

Additionally, the stability of the DGM method greatly impacts the success of future research. One avenue for assessing stability is by creating idealized cross sections and perturbing the structure to determine the cause of the instabilities. Such an approach may lead to strategies for mitigating the unstable behavior, which would greatly increase the tractability of the DGM approach.

Although the DGM method is not yet ready to be the industry standard for lattice physics calculations, it provides much potential. Standard multigroup solutions assume that the shape of the flux is flat within a coarse group, which discards much of the dependence. The DGM method provides a way to recapture the higher-order dependence, and future research may lead to ways to do so more efficiently.

Bibliography

[1] Elmer Eugene Lewis and Warren F Miller. Computational methods of neutron transport. 1984.

[2] E. P. Wigner, E. Creutz, H. Jupnik, and T. Snyder. Resonance absorption of neutrons by spheres. *Journal of Applied Physics*, 26(3):260–270, 1955.

[3] Rubin Goldstein and E. Richard Cohen. Theory of resonance absorption of neutrons. *Nuclear Science and Engineering*, 13(2):132–140, 1962.

[4] N. M. Greene, J. L. Lucius, L. M. Petrie, W. E. Ford III, J. E. White, and R. Q. Wright. Ampx: A modular code system for generating coupled multigroup neutron-gamma libraries from endf/b. Technical report, Oak Ridge National Lab., Tenn.(USA), 1976.

[5] Robert Macfarlane, Douglas W Muir, RM Boicourt, Albert Comstock Kahler III, and Jeremy Lloyd Conlin. The njoy nuclear data processing system, version 2016. Technical report, Los Alamos National Lab.(LANL), Los Alamos, NM (United States), 2017.

[6] Jaakko Leppänen, Maria Pusa, Tuomas Viitanen, Ville Valtavirta, and Toni Kaltiaisenaho. The serpent monte carlo code: Status, development and applications in 2013. In *SNA+ MC 2013-Joint International Conference on Supercomputing in Nuclear Applications+ Monte Carlo*, page 06021. EDP Sciences, 2014.

[7] Dan Gabriel Cacuci. *Handbook of Nuclear Engineering: Vol. 1: Nuclear Engineering Fundamentals; Vol. 2: Reactor Design; Vol. 3: Reactor Analysis; Vol. 4: Reactors of Generations III and IV; Vol. 5: Fuel Cycles, Decommissioning, Waste Disposal and Safeguards*, volume 3. Springer Science & Business Media, 2010.

[8] Alain Hébert. A review of legacy and advanced self-shielding models for lattice calculations. *Nuclear science and engineering*, 155(2):310–320, 2007.

[9] Alain Hébert. *Applied reactor physics*. Presses inter Polytechnique, 2009.

[10] Matthew Eklund, Miltiadis Alamaniotis, Hermilo Hernandez, and Tatjana Jevremovic. Method of characteristics–a review with applications to science and nuclear engineering computation. *Progress in Nuclear Energy*, 85:548–567, 2015.

[11] Alain Hébert. The ribon extended self-shielding model. *Nuclear science and engineering*, 151(1):1–24, 2005.

[12] Benoit Forget and Farzad Rahnema. A spectral unfolding method. *Transactions of the American Nuclear Society*, 96:669–671, 2007.

[13] Farzad Rahnema, Steven Douglass, and Benoit Forget. Generalized energy condensation theory. *Nuclear Science and Engineering*, 160(1):41–58, 2008.

[14] Lei Zhu and Benoit Forget. A discrete generalized multigroup energy expansion theory. *Nuclear Science and Engineering*, 166(3):239–253, 2010.

[15] Lei Zhu and Benoit Forget. Transport methods: General-a nonlinear energy acceleration method. *Transactions of the American Nuclear Society*, 104:317, 2011.

[16] B. Forget and L. Zhu. Mixed energy reactor simulations using the discrete generalized multigroup method-275. 2010.

[17] Lei Zhu and Benoit Forget. An energy recondensation method using the discrete generalized multigroup energy expansion theory. *Annals of Nuclear Energy*, 38(8): 1718–1727, 2011.

[18] Steven Douglass and Farzad Rahnema. Cross section recondensation method via generalized energy condensation theory. *Annals of Nuclear Energy*, 38(9):2105–2110, 2011.

[19] Steven Douglass and Farzad Rahnema. Consistent generalized energy condensation theory. *Annals of Nuclear Energy*, 40(1):200–214, 2012.

[20] Nathan A. Gibson and Benoit Forget. Application of the discrete generalized multigroup method to ultra-fine energy mesh in infinite medium calculations. 2012.

[21] Nathan A. Gibson and Benoit Forget. Eliminating flux updates from the discrete generalized multigroup method. *Transactions of the American Nuclear Society*, 107:1132, 2012.

[22] Nathan A. Gibson and Benoit Forget. On the stability of the discrete generalized multigroup method. *Annals of Nuclear Energy*, 65:421–432, 2014.

[23] Matthew S. Everson and Benoit Forget. Spatial recondensation using the discrete generalized multigroup method. *Annals of Nuclear Energy*, 62:487–498, 2013.

[24] Matthew S. Everson and Benoit Forget. The source equivalence acceleration method. *Annals of Nuclear Energy*, 76:177–192, 2015.

[25] Steven Douglass and Farzad Rahnema. Subgroup decomposition method. *Annals of Nuclear Energy*, 48:84–101, 2012.

[26] M. Gamarino, A. DallOsso, D. Lathouwers, and J. L. Kloosterman. Spectral rehomogenization of nodal cross-sections via proper orthogonal decomposition. In *Proc. Int. Conf. Mathematics and Computational Methods Applied to Nuclear Science and Engineering (M&C 2017)*, pages 16–20, 2017.

[27] Matteo Gamarino, Aldo DallOsso, Danny Lathouwers, and Jan Leen Kloosterman. Rehomogenization of nodal cross sections via modal synthesis of neutron spectrum changes. *Nuclear Science and Engineering*, 190(1):1–30, 2018.

[28] Alexander V. Shilkov. Generalized multigroup approximation and lebesgue averaging method in particle transport problems. *Transport Theory and Statistical Physics*, 23(6): 781–814, 1994.

[29] Andrew Till. *Finite Elements with Discontiguous Support for Energy Discretization in Particle Transport*. PhD thesis, 2015.

[30] Andrew T. Till, Jim E. Morel, and Marvin L. Adams. A generalized multigroup method based on finite elements. Technical report, 2015.

[31] Andrew Thomas Till. A generalized multigroup method. Master's thesis, 2014.

[32] Ibrahim Khalil Attieh. *Generalized Multigroup Method*. PhD thesis, 2004.

[33] I. K. Attieh and R. E. Pevey. An adaptive general multigroup method. 2002.

[34] Kord S. Smith. Assembly homogenization techniques for light water reactor analysis. *Progress in Nuclear Energy*, 17(3):303–335, 1986.

[35] Richard Sanchez. Assembly homogenization techniques for core calculations. *Progress in Nuclear Energy*, 51(1):14–31, 2009.

[36] Lulin Yu and Yung-An Chao. A unified generic theory on discontinuity factors in diffusion, sp3 and transport calculations. *Annals of Nuclear Energy*, 75:239–248, 2015.

[37] A. Hébert and A. Kavenoky. Development of the sph homogenization method. Technical report, CEA Centre d'Etudes Nucleaires de Saclay, 1981.

[38] Alain Hebert. A consistent technique for the pin-by-pin homogenization of a pressurized water reactor assembly. *Nuclear Science and Engineering*, 113(3):227–238, 1993.

[39] Akio Yamamoto, Masahiro Tatsumi, Yasunori Kitamura, and Yoshihiro Yamane. Improvement of the sph method for pin-by-pin core calculations. *Journal of nuclear science and technology*, 41(12):1155–1165, 2004.

[40] A. Hébert. A reformulation of the transport-transport sph equivalence technique. In *Proc. 7th Int. Conf. Modelling and Simulation in Nuclear Science and Engineering (7ICMSNSE)*, pages 18–21, 2015.

[41] Bin Zhang, Hongchun Wu, Yunzhao Li, Liangzhi Cao, and Wei Shen. Evaluation of pin-cell homogenization techniques for pwr pin-by-pin calculation. *Nuclear Science and Engineering*, 186(2):134–146, 2017.

[42] Javier Ortensi, Yaqi Wang, Alexandre Laurier, Sebastian Schunert, Alain Hébert, and Mark DeHart. A newton solution for the superhomogenization method: The pjfnk-sph. *Annals of Nuclear Energy*, 111:579–594, 2018.

[43] Charles P. Neuman and Dave I. Schonbach. Discrete (legendre) orthogonal polynomials-a survey. *International Journal for Numerical Methods in Engineering*, 8(4):743–770, 1974.

[44] Kamisetty Ramam Rao and Patrick C. Yip. *The transform and data compression handbook*. CRC press, 2000.

[45] Lawrence Sirovich. Turbulence and the dynamics of coherent structures. i. coherent structures. *Quarterly of applied mathematics*, 45(3):561–571, 1987.

[46] A. G. Buchan, C. C. Pain, F. Fang, and I. M. Navon. A pod reduced-order model for eigenvalue problems with application to reactor physics. *International Journal for Numerical Methods in Engineering*, 95(12):1011–1032, 2013.

[47] Richard L. Reed and Jeremy A. Roberts. An energy basis for response matrix methods based on the karhunen–loéve transform. *Annals of Nuclear Energy*, 78:70–80, 2015.

[48] Richard L. Reed and Jeremy A. Roberts. Application of the karhunen–loève transform to the c5g7 benchmark in the response matrix method. *Annals of Nuclear Energy*, 103: 350–355, 2017.

[49] Richard Reed and Jeremy Roberts. corps-g/unotran: Dissertation version, November 2019. URL https://doi.org/10.5281/zenodo.3541154.

[50] Richard L. Reed and Jeremy A. Roberts. Effectiveness of the discrete generalized multigroup method based on truncated, pod-driven basis sets. *Annals of Nuclear Energy*, 126:253–261, 2019.

Appendix A

Cross Section Generation using Serpent

All cross sections used in this work were generated using Serpent[6]. A relatively simple 2-D, pincell model with reflective conditions was created that used various fuel materials surrounded by water. The geometry is shown in Fig. A.1.

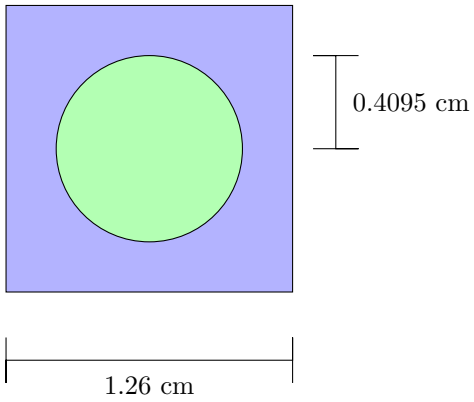

Figure A.1: The pincell model developed in Serpent.

Serpent is a Monte Carlo code, which allows homogenizing cross sections over spatial regions to produce cross sections for a desired group structure. For this work, three group structures were chosen, which were built into Serpent, named scale44 (SCALE 44-group structure), scale238 (SCALE 238-group structure), and nj20 (ECCO 1968-group structure). An example input file for Serpent is presented in Listing A.1.

Table A.1: Atomic compositions in atom/barn.cm

	UO_2-1	UO_2-2	UO_2-Gd	MOX	Water
H-1	2.73×10^{-2}	2.73×10^{-2}	2.73×10^{-2}	2.73×10^{-2}	4.03×10^{-2}
O-16	2.87×10^{-2}	2.87×10^{-2}	2.86×10^{-2}	2.86×10^{-2}	2.02×10^{-2}
Zr (nat)	4.79×10^{-3}	4.79×10^{-3}	4.79×10^{-3}	4.79×10^{-3}	7.86×10^{-3}
U-234	1.50×10^{-6}	2.52×10^{-6}	2.63×10^{-6}	2.32×10^{-6}	
U-235	1.68×10^{-4}	2.75×10^{-4}	2.87×10^{-4}	2.53×10^{-4}	
U-238	7.39×10^{-3}	7.28×10^{-3}	6.88×10^{-3}	6.70×10^{-3}	
Gd-154			9.68×10^{-6}		
Gd-155			6.58×10^{-5}		
Gd-156			9.10×10^{-5}		
Gd-157			6.96×10^{-5}		
Gd-158			1.10×10^{-4}		
Gd-160			9.80×10^{-5}		
Np-237				3.23×10^{-5}	
Pu-238				1.59×10^{-5}	
Pu-239				2.93×10^{-4}	
Pu-240				1.32×10^{-4}	
Pu-241				6.38×10^{-5}	
Pu-242				3.76×10^{-5}	
Am-241				2.04×10^{-5}	
Am-242				1.05×10^{-5}	

This work utilized four different fuel materials. The atomic compositions of each of these materials are presented in Table A.1. The materials include three different varieties of UO_2 as well as a MOX fuel. An input file similar to the example script was generated for each of the four fuels for each of the three group structures for a total of 12 input files. Serpent was used to process each of these files, which leads to an output file that was processed using Python to extract the homogenized cross sections.

The 44-group cross sections produced by Serpent are shown in Fig. A.2, whereas the 238- and 1968-group cross section are in Fig. A.3 and Fig. A.4 respectively. These figures show the total cross section as a function of energy for each of the materials.

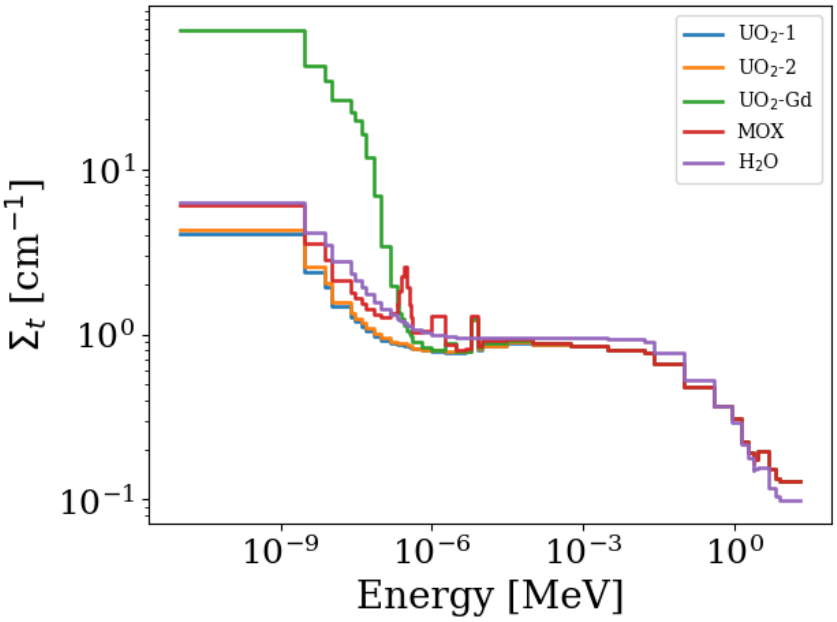

Figure A.2: Cross sections for 44-group structure

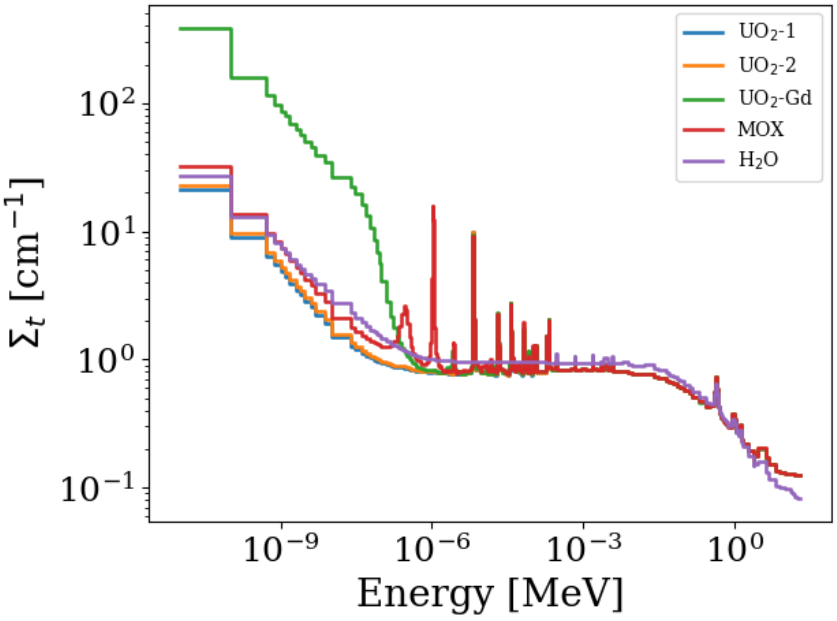

Figure A.3: Cross sections for 238-group structure

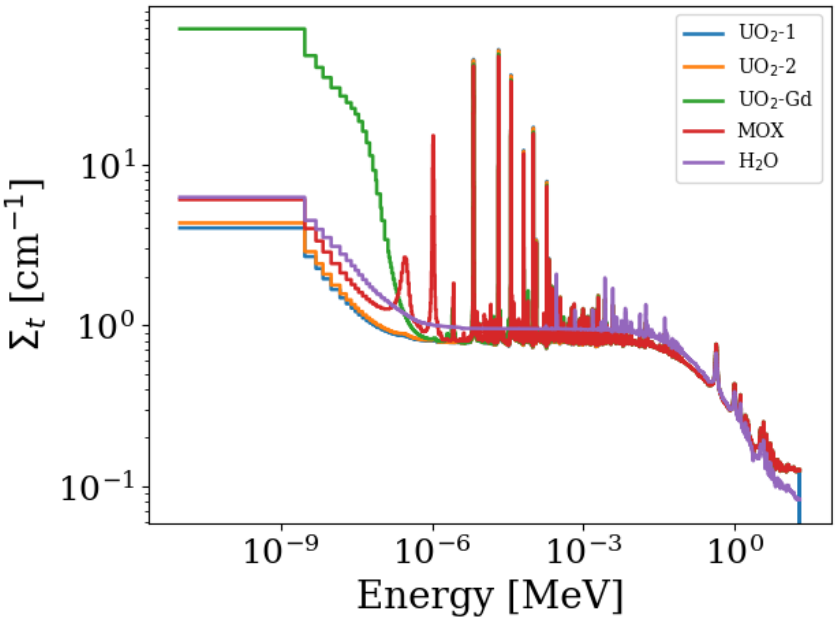

Figure A.4: Cross sections for 1968-group structure

Listing A.1: Example input for serpent cross section generation

```
% ** UO2-2 PINCELL SIMULATION
set title "UO2-2 PINCELL"
% ************************************************************
% ** SURFACE CARDS
  surf   1    sqc   0.0000 0.0000 0.6333     /* outmost SURFACE */
  surf   2    cyl   0.0000 0.0000 0.4095     /* fuel */
% ************************************************************
% ** CELL CARDS
  cell 1    1 fuel     -2        % Fuel
  cell 2    2 water 2  -1        % moderator
  cell 11   0 fill 1 -2
  cell 12   0 fill 2 2 -1
% Reflective boundary
  cell 99 0 outside   1          % Outside world
% ************************************************************
% **MATERIAL CARDS
% ** fuel discretization
mat  fuel       sum    tmp 456
      1001.03c 2.73e-2
      8016.03c 2.87e-2
     40000.03c 4.79e-3
     92234.03c 2.52e-6
     92235.03c 2.75e-4
     92238.03c 7.28e-3
% **  Water
mat   water sum moder lwtr 1001  % Considering the binding effects
      1001.03c      4.03e-2
      8016.03c      2.02e-2
     40000.03c      7.86e-3
% ************************************************************
% **thermal scattering data for light water
therm lwtr lwj3.11t
% ************************************************************
% **reflective boundary condition
set bc 2
set gcu 0 1 2 % homogenious in universe 0
set sym 8 % square symmetry for error reduction
set nfg scale44
set micro scale44
ene grid44 4 scale44
%************************************************************
% ** Neutron population and criticality cycles:
set pop 1000000 100 20 1.00
% ** Decay and fission yield libraries
% ** end ***************************************************
```

Appendix B

Creating a Coarse-Group Structure

In this appendix, the method for selecting a coarse-group structure from a fine-group structure is presented. The method is based on the basic algorithm introduced by Gibson and Forget [22]. Their method incorporated four rules which were:

- limit the ratio of the smallest to the largest cross section in a coarse group
- relax the ratio for groups containing only small cross sections
- cap the number of fine groups per coarse group
- force coarse-group breaks where desired.

Their recommended limits were a smallest to largest ratio of 2, which was suppressed for cross sections below 1.5 cm^{-1} in coarse groups with up to 60 fine groups.

The work presented in the remainder of this manuscript began with these rules but explored several variations in an attempt to find stable configurations. In the work of Gibson and Forget [22], only a single material was used, but for multiple materials, a method was needed to create stable structures for sets of cross sections. The findings for such a method are presented in Section B.1.

A brief study was explored, which would make use of noncontiguous, coarse-group structures, which are akin to the banded methods discussed in Section 1.4. The results of the

study are presented in Section B.2. Ultimately, this work utilized a cross section difference instead of a cross section ratio to select a coarse group as discussed in Section B.3.

Finally, the lessons learned from each of these studies led to a parameter search to select the more stable structures for use in this work. The parameter search is presented in Section B.4, along with the resulting group structures. Finally, the search for stable parameters for linear anisotropic scattering problems is discussed in Section B.5.

For this section, we sought a simple way to assess the stability of a coarse-group structure from the structure alone. One attempt was to explore the diagonal dominance of the mass matrices as computed in Section 2.3. In particular, the mass matrix computed from the total cross section $\Sigma^{t*}_{m,G,i,j}$ was explored. For a particular material m and coarse-group G, the mass matrix was a square matrix that could be checked for diagonal dominance. It was found that strong diagonal dominance was neither sufficient to predict stability nor required for stability. Thus, to assess stability, the 44-group, 10-pin problem as discussed in Section 4.2 was solved for various parameters to find the stable configurations. The basis was chosen to be the POD_combine basis. Though stability can be improved by the use of Krasnoselskii iteration as discussed in Section 2.2, the stability in this section assumes $\lambda = 1.0$.

B.1 Group structures with multiple materials

When using multiple materials, we desire a group structure to be the same for all materials. To this end, several methods for combining the cross sections were explored. The first method preprocessed the cross sections to find the minimum value over material for each energy group. The second method still preprocessed the cross sections, but instead found the maximum value over material for each energy group. The third method took the average over material as the cross section values for each group. The final method limited the ratio in each coarse group of the maximum cross section of all materials to the minimum cross section of all materials.

While each of these methods could produce group structures, some were far more stable consistently. The results are presented in Fig. B.1, where each square represents a complete

solve and identifies the stability. The number on each square is the degrees of freedom used in that problem, while the color assesses the stability. The horizontal axis is the order of the basis expansion. The vertical axis is the ratio of maximum to minimum cross section within a coarse group after the aforementioned preprocessing. The minimum cutoff was set to ignore the ratio if the maximum cross section was below 1.5 cm^{-1}.

We desire a method that is stable for all expansion orders, thus methods that have an entire yellow row. Also, we prefer a low number of coarse groups. The number of coarse groups can be read from the plot as the number on the leftmost column.

The first method performed quite poorly, which is expected as resonance regions were disregarded. The fourth method performed quite well but produced group structures with few fine groups per coarse group for some problems, which limited the success of the DGM method. The second method was chosen as the best option for its simplicity and success.

B.2 Non-contiguous group structures

Non-contiguous group structures were also explored. These structures were similar to the banded methods discussed in Section 1.4. The same four methods of preprocessing the data from Section B.1 were applied. In theory, a noncontiguous group structure would allow for less cross section variation within each coarse group as well as fewer coarse groups. However, as observed in Fig. B.2, the noncontiguous structures are much less stable than the contiguous structures. The structures required very specific ratios for stability, which could not be assessed *a priori*. It is possible that further research could find a fruitful path for success in this direction, but all group structures chosen for this work were contiguous.

B.3 Additive difference vs multiplicative ratio

To simplify the method for selecting group structures, we explored the use of a cross section difference instead of a cross section ratio for each coarse group. In essence, the difference between the largest cross section and the smallest cross section in a coarse group was limited.

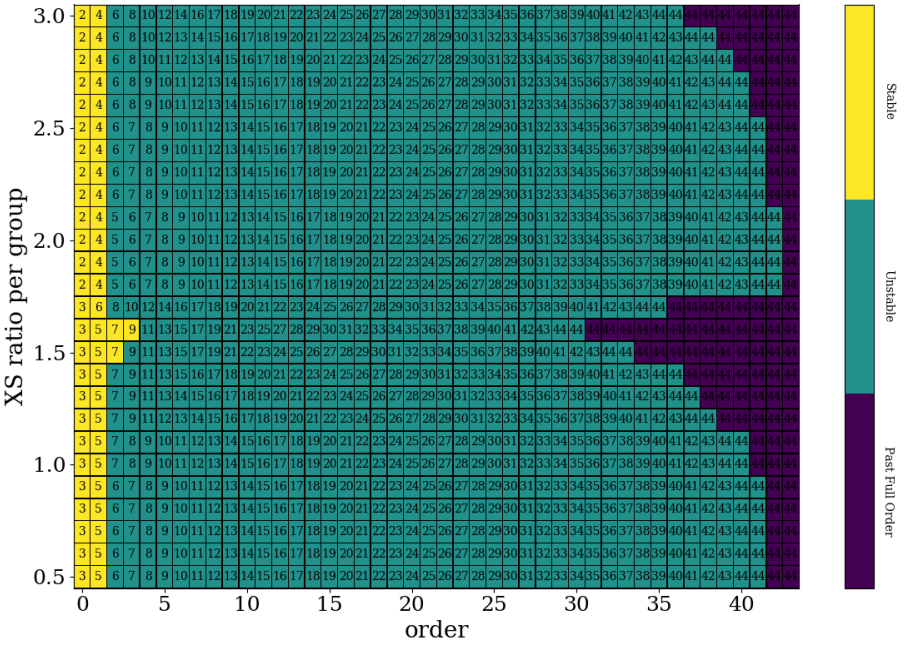

(a) Method 1: compare minimum

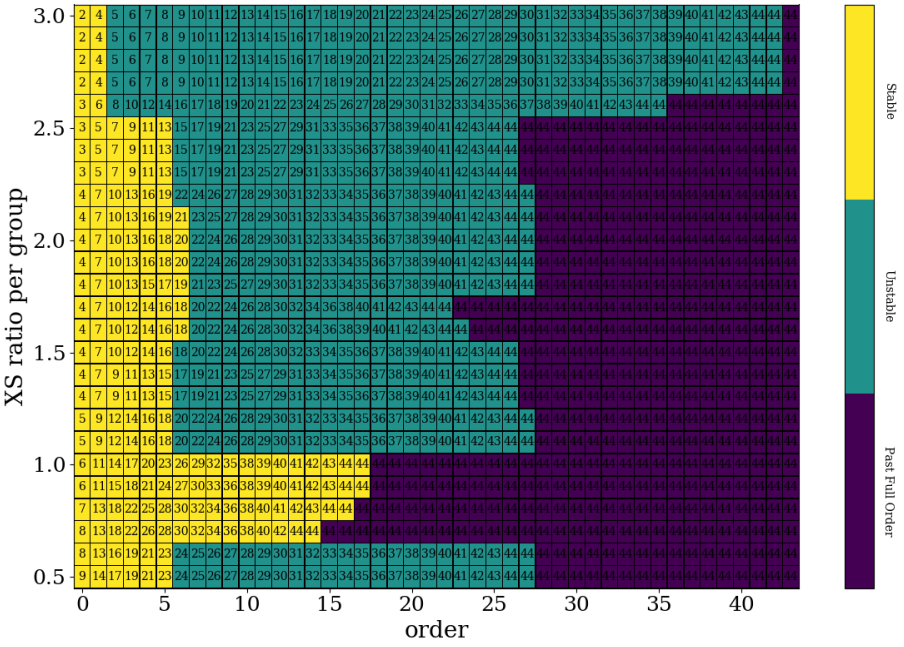

(b) Method 2: compare maximum

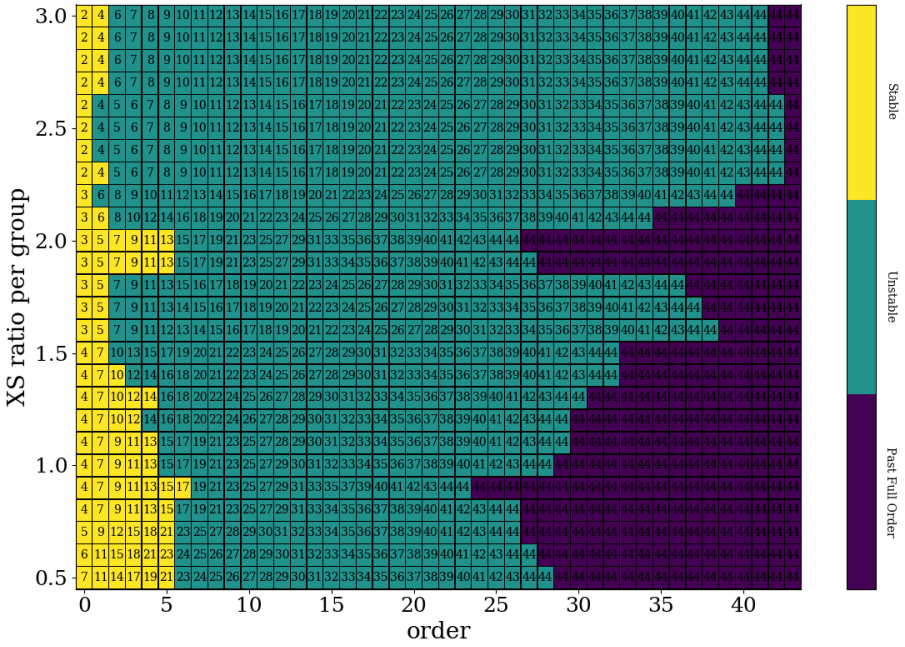

(c) Method 3: compare average

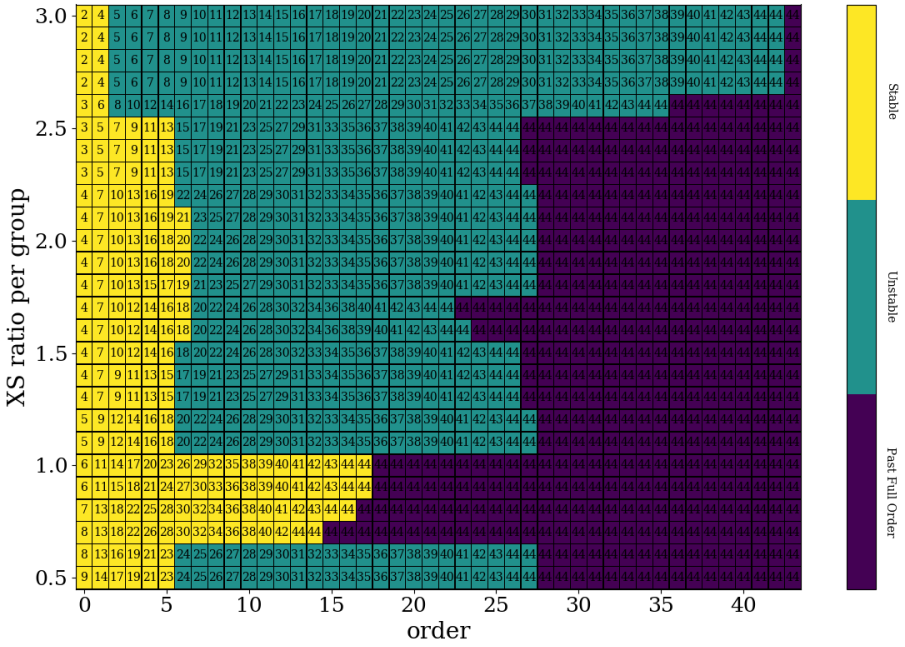

(d) Method 4: compare difference

Figure B.1: Stability of the four methods for selecting the coarse-group structure. Numbers are the degrees of freedom used in the problem. The ordinate is the expansion order, thus the left column utilizes only the flat function, while the right column is a full expansion. The abscissa is the ratio of maximum to minimum cross section in a group. The purple squares are already full order and were not run. Yellow squares represent problems that were stable.

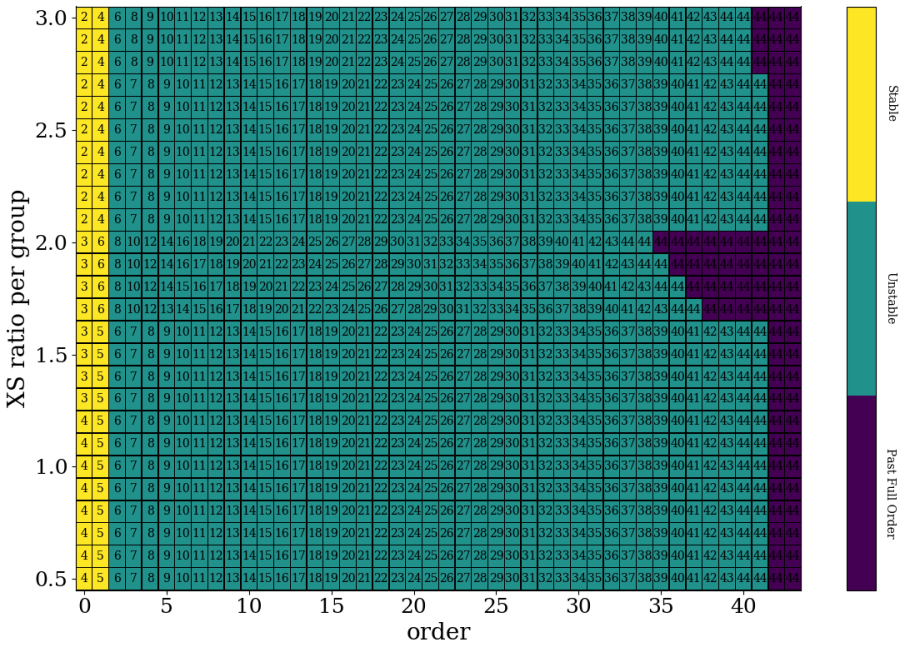

(a) Non-contiguous method 1: compare minimum

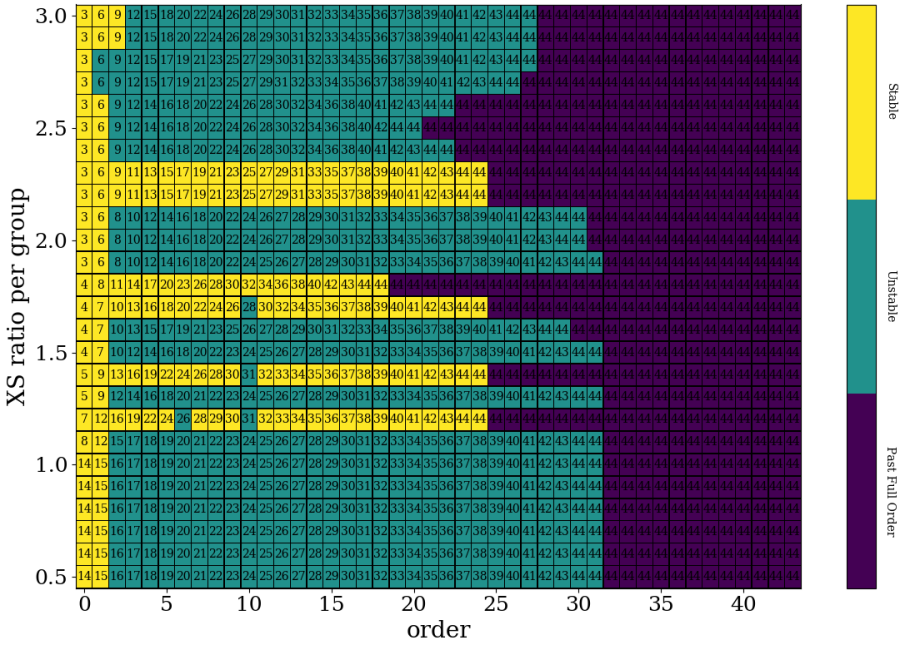

(b) Non-contiguous method 2: compare maximum

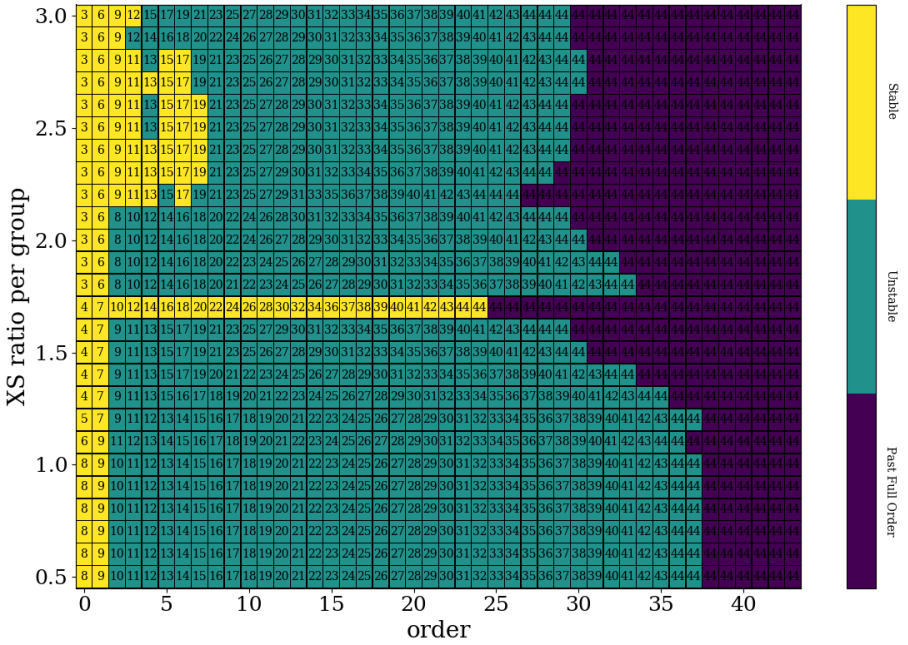

(c) Non-contiguous method 3: compare average

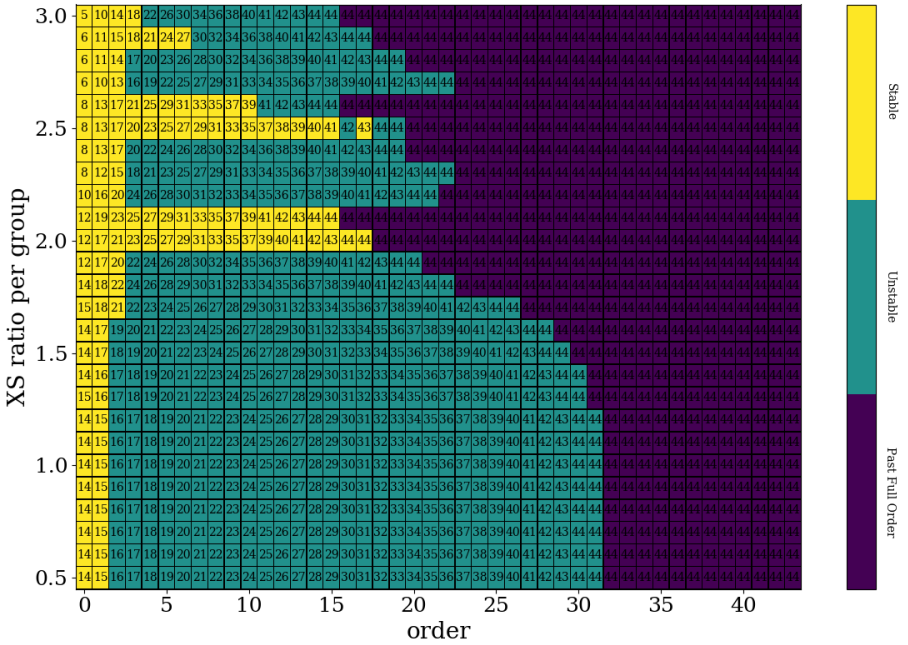

(d) Non-contiguous method 4: compare difference

Figure B.2: Stability of the four methods for selecting the noncontiguous coarse-group structure. Numbers are the degrees of freedom used in the problem. The ordinate is the expansion order, thus the left column utilizes only the flat function, while the right column is a full expansion. The abscissa is the ratio of maximum to minimum cross section in a group. The purple squares are already full order and were not run. Yellow squares represent problems that were stable.

With this small change, there was no need to relax the ratio for small cross sections. To test this method, the same preprocessing steps were applied as presented in Section B.1.

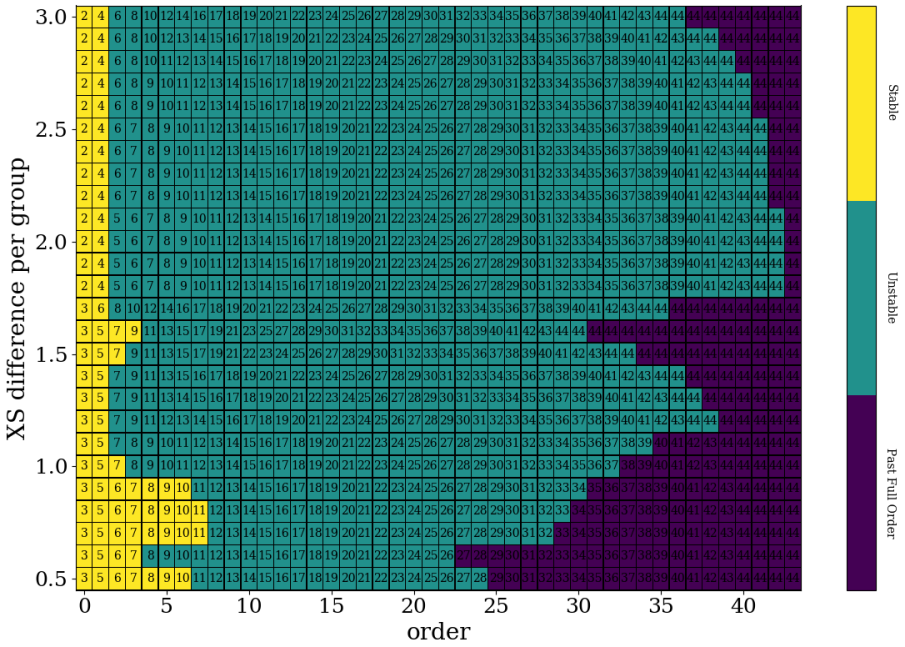

(a) Method 1: compare minimum

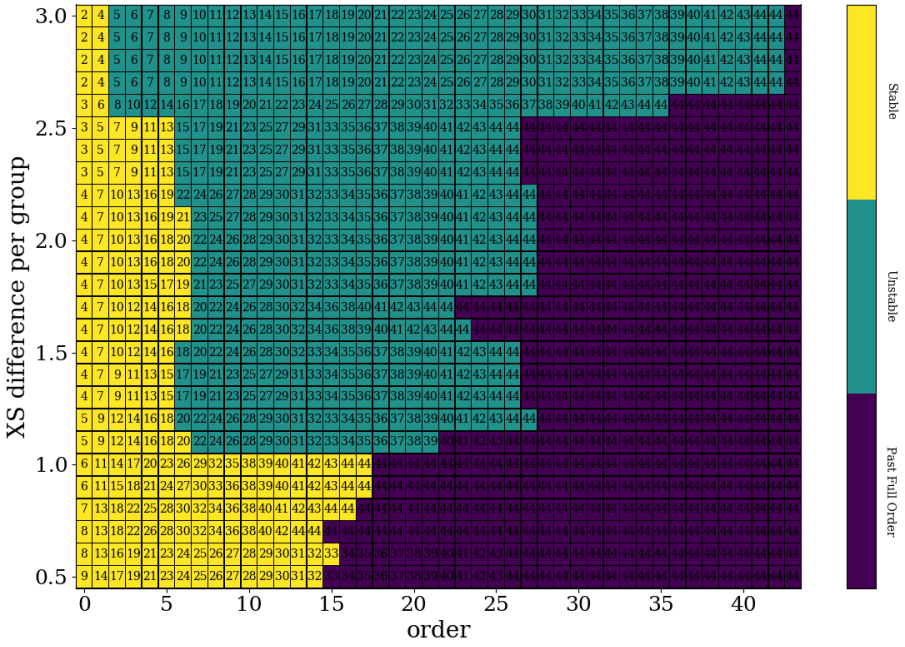

(b) Method 2: compare maximum

The results for the contiguous group structures are presented in Fig. B.3, while the noncontiguous structures are presented in Fig. B.4. From the figures, we can see that more

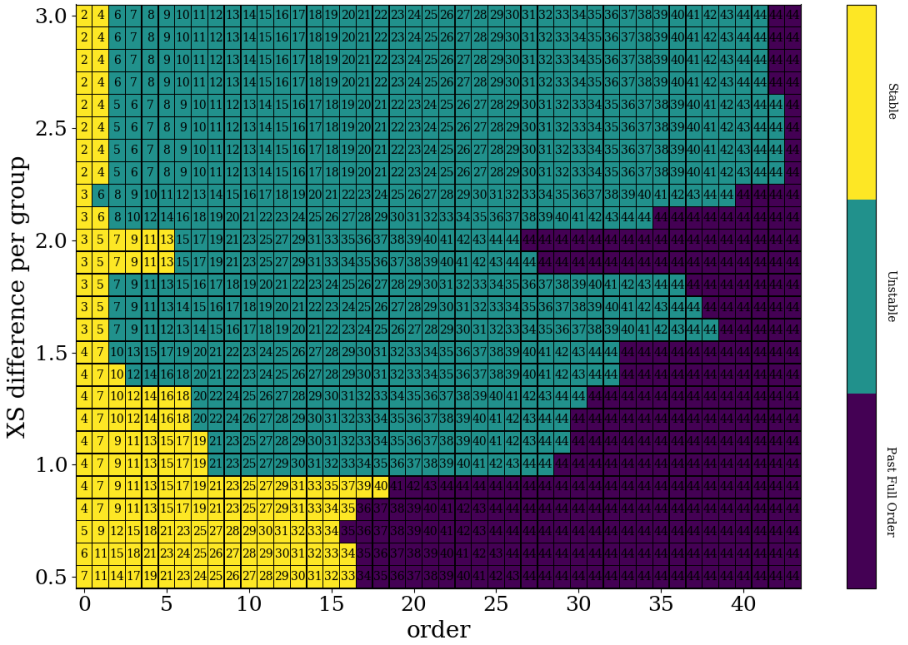

(c) Method 3: compare average

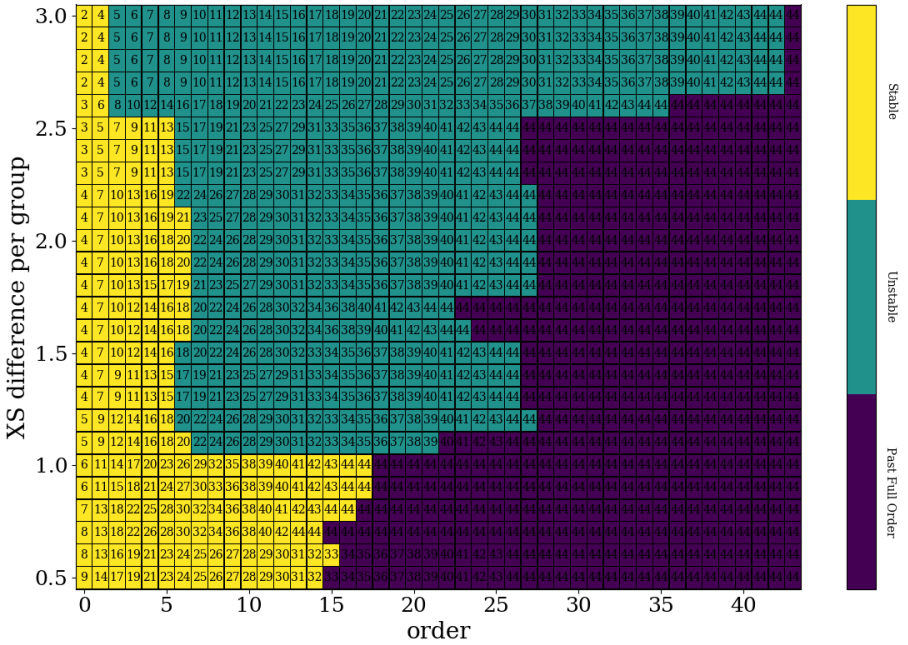

(d) Method 4: compare difference

Figure B.3: Stability of the four methods for selecting the coarse-group structure. Numbers are the degrees of freedom used in the problem. The ordinate is the expansion order, thus the left column utilizes only the flat function, while the right column is a full expansion. The abscissa is the difference of maximum to minimum cross section in a group. The purple squares are already full order and were not run. Yellow squares represent problems that were stable.

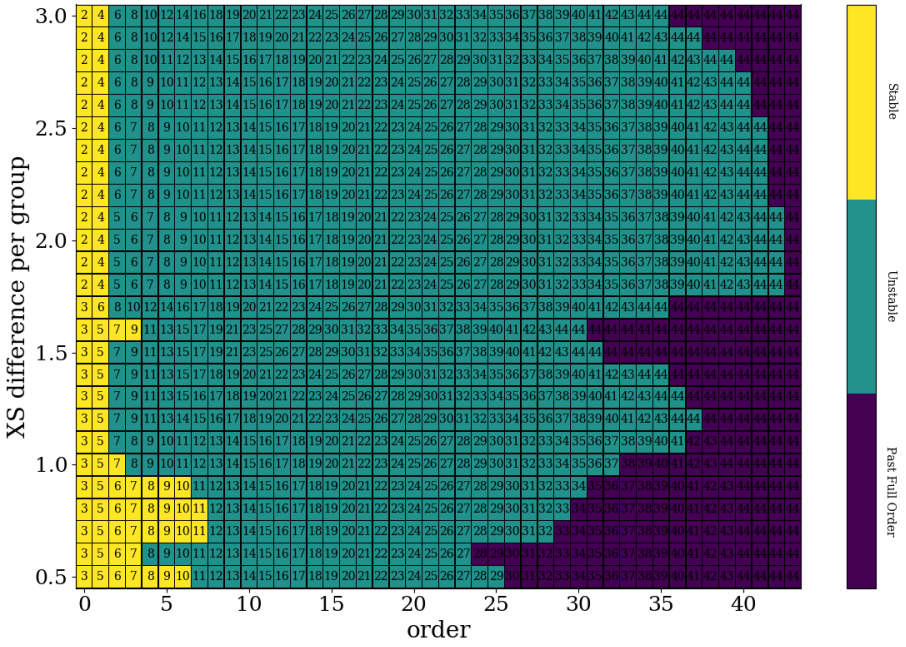

(a) Non-contiguous method 1: compare minimum

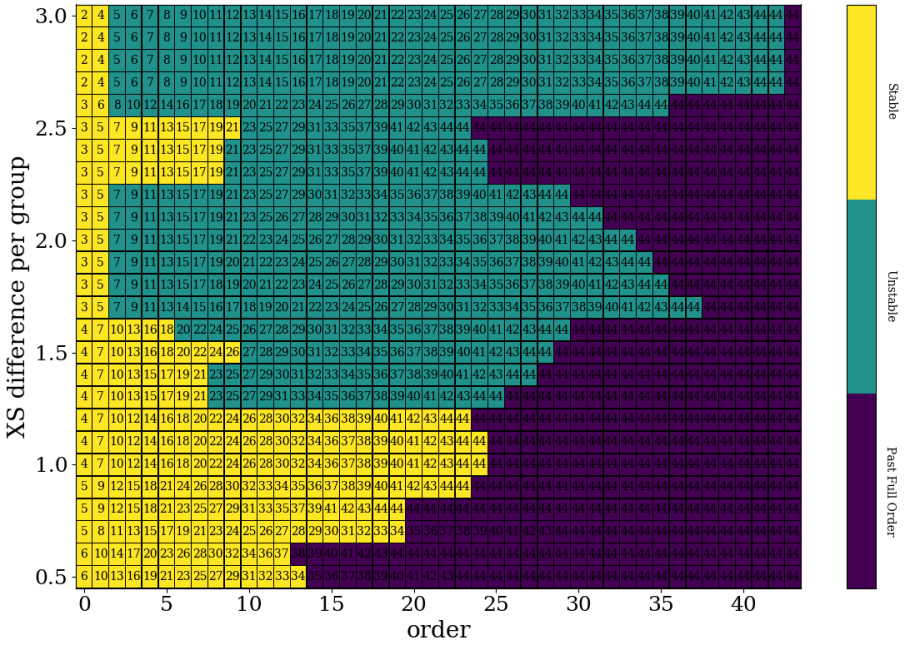

(b) Non-contiguous method 2: compare maximum

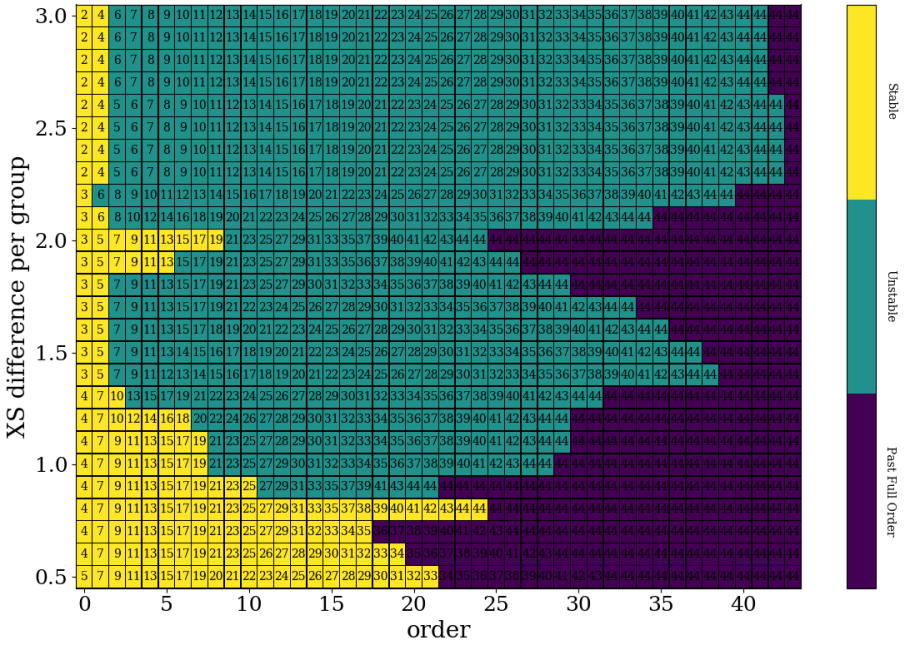

(c) Non-contiguous method 3: compare average

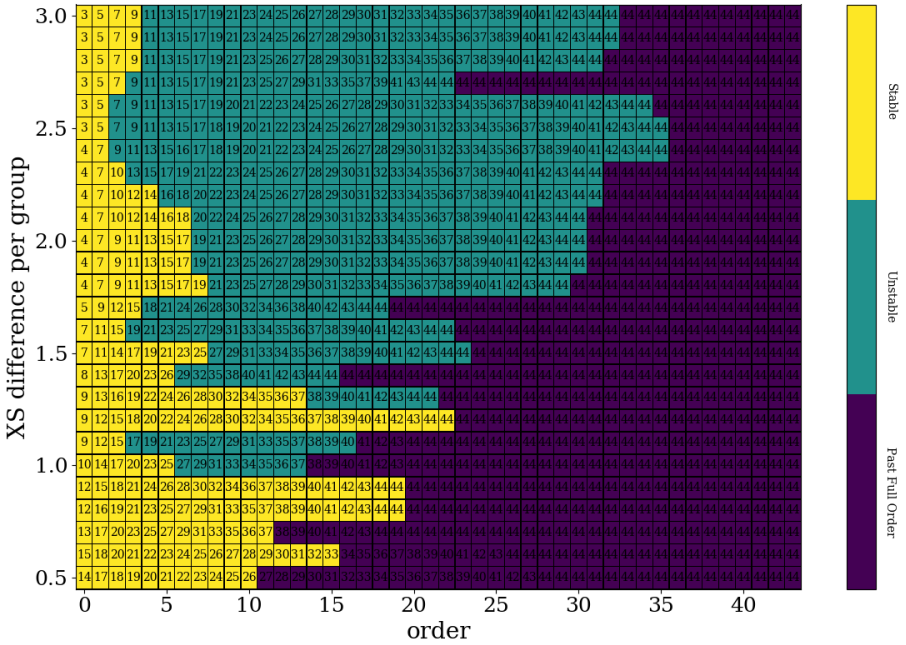

(d) Non-contiguous method 4: compare difference

Figure B.4: Stability of the four methods for selecting the noncontiguous coarse-group structure. Numbers are the degrees of freedom used in the problem. The ordinate is the expansion order, thus the left column utilizes only the flat function, while the right column is a full expansion. The abscissa is the difference of maximum to minimum cross section in a group. The purple squares are already full order and were not run. Yellow squares represent problems that were stable.

configurations are stable. In particular, below a certain threshold cross section difference, all orders are stable, which is highly desired. Overall, using a cross section difference instead of a cross section ratio improved the stability, and this method was chosen for the work in this manuscript.

Note also that the noncontiguous structures are also improved using a cross section difference. In both contiguous and noncontiguous tests, the second method (preprocessing to find the maximum cross section over material) was either outright or tied for the most stable method for coarse-group selection.

The performance of the noncontiguous basis structures are presented in Fig. B.5 and Fig. B.6 for the 44- and 238-group solutions to the 10-pin problem as discussed in Section 4.2, respectively. The group structures are formed following the noncontiguous method 2 with a maximum difference set to 1.3. In the figures, a basis beginning with POD is a continuous group structure, whereas a basis name beginning with NCT is a noncontiguous group structure. From the figures, the noncontiguous basis set tends to provide better performance (lower errors) as compared to the contiguous basis sets. This does come at a cost to stability, which manifests as requiring a slightly smaller value for the Krasnoselskii coefficient. Due to time constraints, the noncontiguous structures were not explored for additional problems, but the performance here is promising.

B.4 Structures used in this manuscript

Plots similar to the rest in this section were produced for each of the test problems to check for stable parameters. It was found that using the following rules produced sufficiently stable group structures for the infinite medium problem (Section 4.1), the 10-pin problem (Section 4.2), and the second configuration of the BWR problem (Section 4.3):

- limit the difference of the smallest to the largest cross section in a coarse group to 1.3 cm^{-1}
- cap the number of fine groups per coarse group to 60.

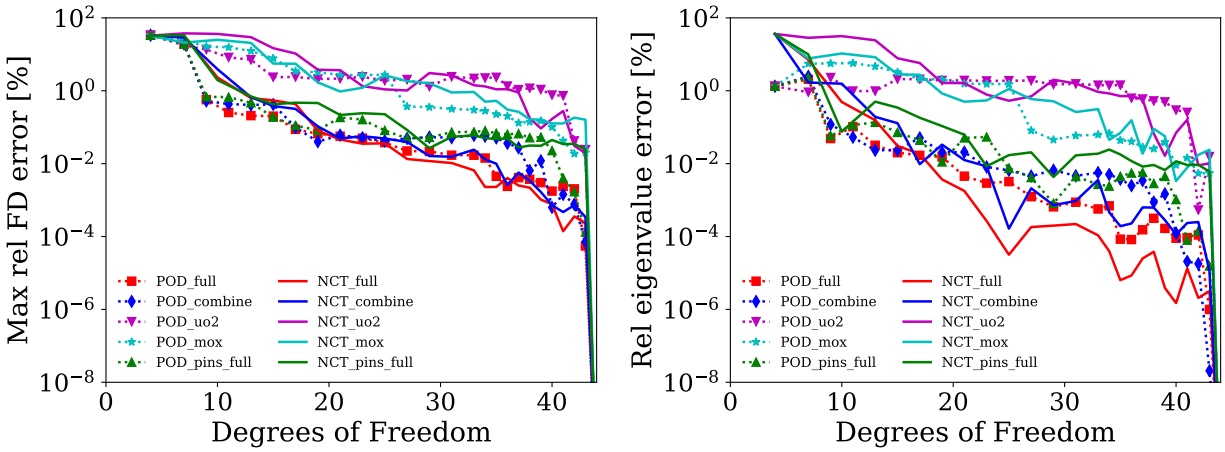

(a) Fission density error

(b) Eigenvalue error

Figure B.5: 44-group comparison of contiguous basis to noncontiguous basis sets formed with the same snapshots. POD_XXX uses a continuous group structure formed with method 2. NCT_XXX uses a noncontiguous group structure formed with method 2. XXX refers to the base snapshot model, which is described in Section 4.2.

For the remaining problems, the following parameters were used:

- limit the difference of the smallest to the largest cross section in a coarse group to 1.0 cm^{-1}
- cap the number of fine groups per coarse group to 60.

This choice of parameters required the Krasnoselskii of less than unity for most problems. However, the structures utilized few coarse groups, which balanced the computational expense of a reduced λ. The required relaxation coefficients are shown in Table B.1 for each test problem and group structure. Each of these parameters was found by beginning at unity and iterating lower until a stable value was found. It is clear that problems with finer-group structures are inherently less stable, thus require lower λ values.

B.5 Legendre Order

Since anisotropic scattering in the form of Legendre moments is supported in Unotran, stable parameters were sought for linear anisotropy. The results of the parameter search for

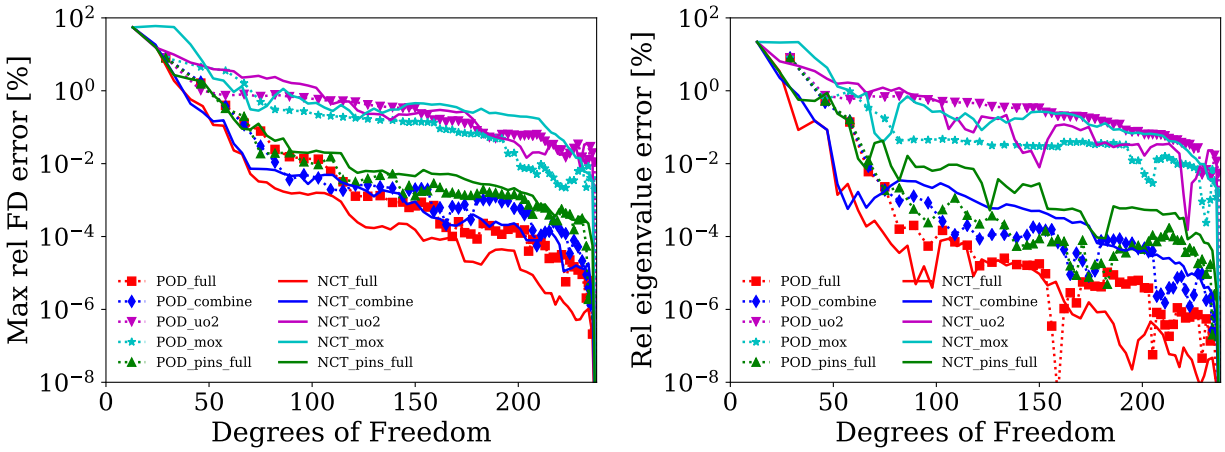

(a) Fission density error

(b) Eigenvalue error

Figure B.6: 238-group comparison of contiguous basis to noncontiguous basis sets formed with the same snapshots. POD_XXX uses a continuous group structure formed with method 2. NCT_XXX uses a noncontiguous group structure formed with method 2. XXX refers to the base snapshot model, which is described in Section 4.2.

Table B.1: Required Krasnoselskii iteration coefficients λ for stability

	44-group	238-group	1968-group
Infinite Medium (Section 4.1)	0.8	0.7	0.4
10-pin (Section 4.2)	0.8	0.5	0.3
BWR-1 (Section 4.3)	0.7	0.6	0.5
BWR-2 (Section 4.3)	0.8	0.4	0.3
2-D (Section 4.4)	0.1	–	–

contiguous group structures are presented in Fig. B.7. Since the stability of the method was severely reduced, only isotropic scattering was considered in the remainder of the manuscript.

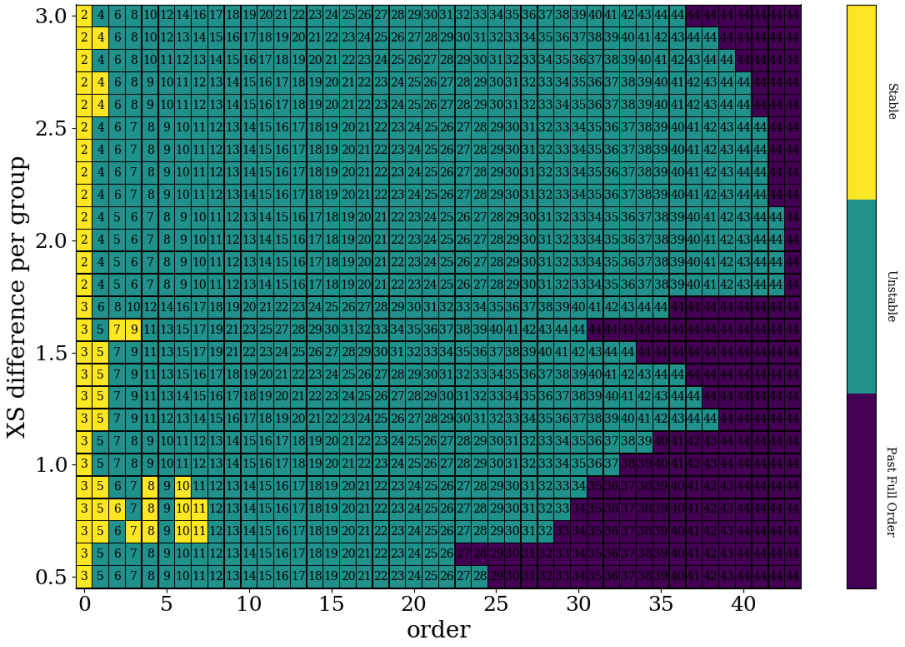

(a) Method 1: compare minimum

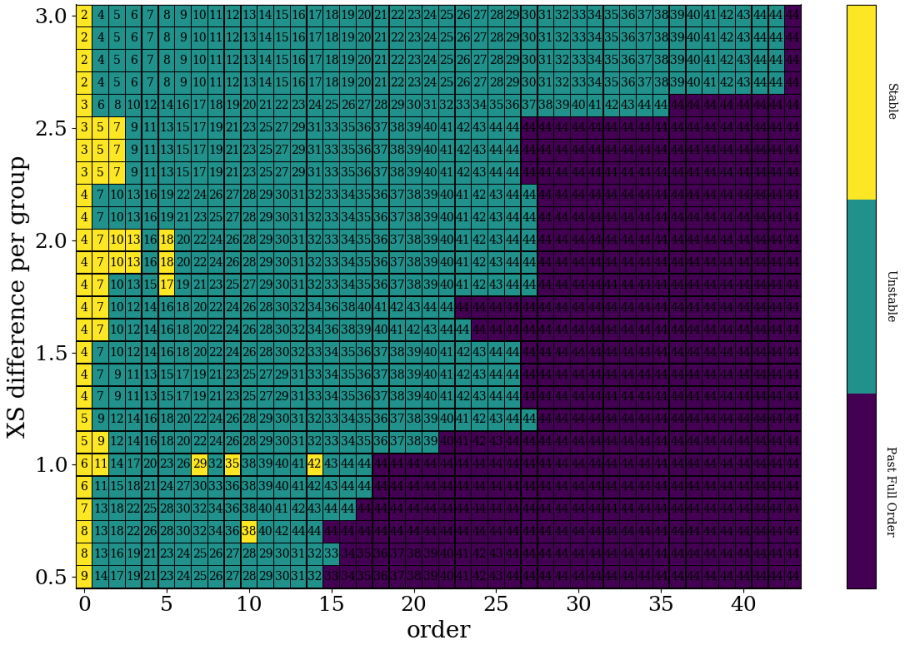

(b) Method 2: compare maximum

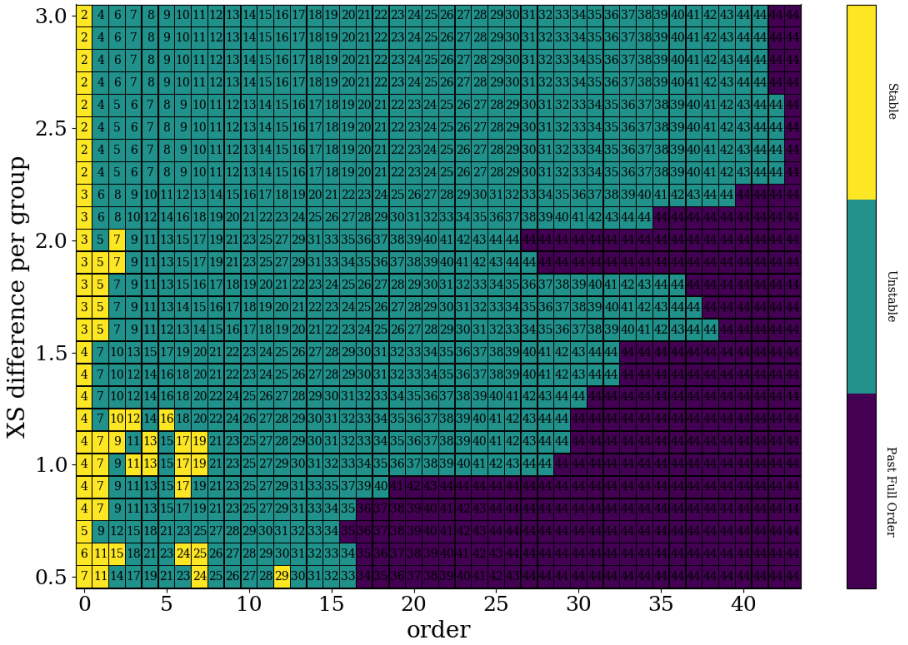

(c) Method 3: compare average

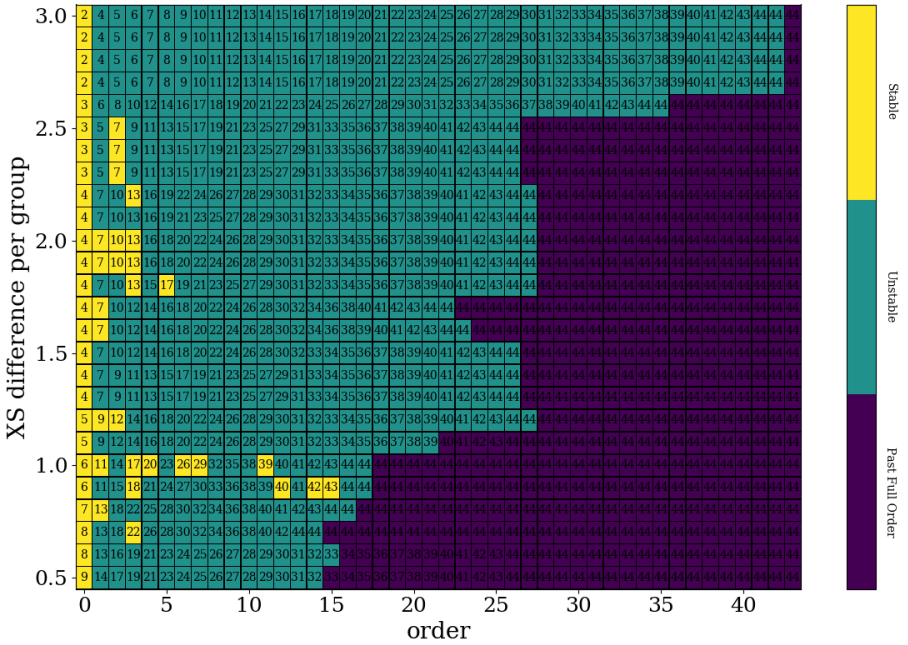

(d) Method 4: compare difference

Figure B.7: Stability of the four methods for selecting the coarse-group structure for anisotropic scattering. Numbers are the degrees of freedom used in the problem. The ordinate is the expansion order, thus the left column utilizes only the flat function, while the right column is a full expansion. The abscissa is the difference of maximum to minimum cross section in a group. The purple squares are already full order and were not run. Yellow squares represent problems that were stable.

Appendix C

Snapshot Selection

This chapter explores what information improves a basis for use in the remainder of this work. In particular, we explore what snapshots provide useful information for use in creating a POD basis, which is the topic of Section 3.1. Several ideas are explored in this appendix, and these are showcased using the 44- and 238-group structures as discussed in Appendix A. Further, these group structures will be used for the 10-pin problem, which is presented in Section 4.2.

For this section, we will use a POD basis constructed from snapshots of the scalar flux extracted from the 10-pin problem as the reference basis. This means that the 10-pin problem is solved, which generates 280 vectors of the group-dependent scalar flux. These snapshots form the POD_full basis as described in Section 4.2. For comparison's sake, several different snapshot models from that same section are presented on these plots.

In Section C.1 we explore the difference between computing the POD basis from snapshots directly then truncating for each coarse group against truncating the snapshots first. Then, Section C.2 explores the effect of adding snapshots of the net neutron current to the scalar flux snapshots. Section C.3 tests how snapshots of the total cross section change the POD basis. Finally, Section C.4 presents the effect of combining the scalar flux, the net neutron current, and the total cross section snapshots.

C.1 Order of POD truncation

As discussed in Section 3.1, a POD basis is formed from a set of snapshots. The SVD is used to extract the most common shapes or modes within the snapshots, and a basis is formed that mimics those modes. This has the result of creating an orthogonal basis that can accurately reproduce a vector with a low-order basis expansion if that vector is similar to the snapshots.

When a basis is used for the DGM method, an orthogonal basis must be used for each of the coarse groups. Thus, for DGM we have two choices for forming the POD basis. The first choice is to truncate each snapshot to only the parts corresponding to the fine groups g within coarse group G, which truncates each snapshot to a length of o. A basis $\boldsymbol{P}^G \in \mathbb{R}^{o \times o}$ is then formed from those snapshots. This process is the subject of Chapter 3, and is used for the remainder of this work.

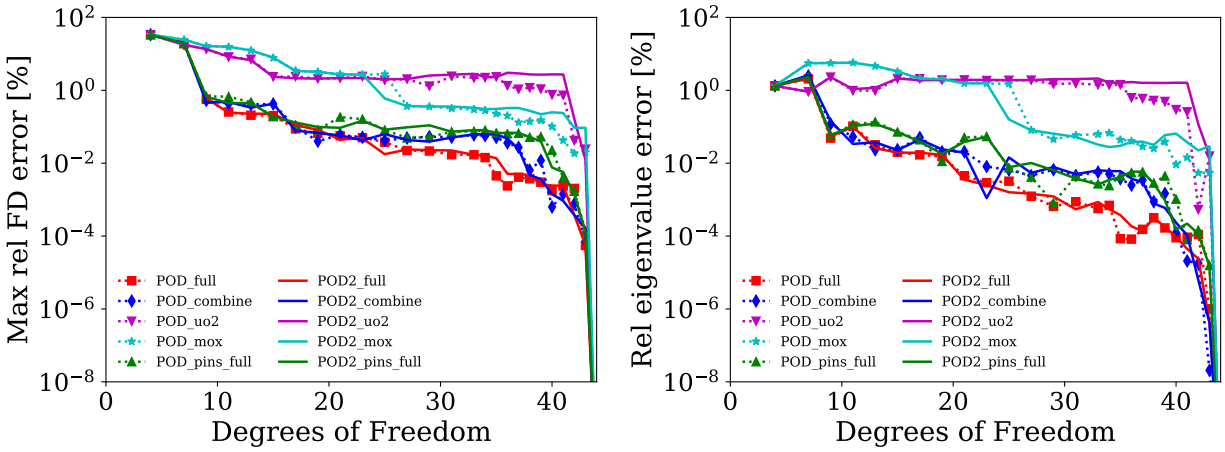

(a) Fission density error

(b) Eigenvalue error

Figure C.1: 44-group comparison of when to truncate the basis. POD_XXX truncates the snapshots then forms the basis for the coarse group. POD2_XXX forms the basis then truncates the basis to the order of the coarse group. XXX refers to the base snapshot model, which is described in Section 4.2.

The second is to form a basis set $\boldsymbol{P} \in \mathbb{R}^{g \times g}$ from the non-truncated snapshots, where g is the number of fine groups. The basis is then truncated to the vectors corresponding to $g \in G$ and reorthogonalized, where G is the coarse group. This process then produces an orthogonal basis $\boldsymbol{P}^G \in \mathbb{R}^{o \times o}$ for each coarse group G, where o is the number of fine groups within coarse group G.

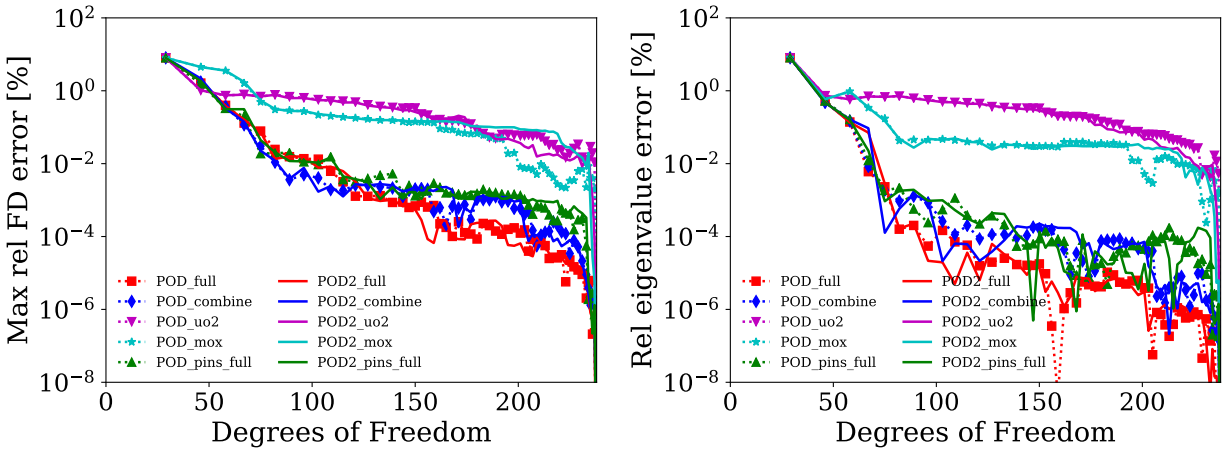

(a) Fission density error

(b) Eigenvalue error

Figure C.2: 44-group comparison of when to truncate the basis. POD_XXX truncates the snapshots then forms the basis for the coarse group. POD2_XXX forms the basis then truncates the basis to the order of the coarse group. XXX refers to the base snapshot model, which is described in Section 4.2.

We demonstrate the impact of this choice in Fig. C.1 and Fig. C.2. In the figures, the first method (truncate snapshots then make basis) is labeled as POD_XXX, where XXX refers to the snapshot model. The second method is labeled as POD2_XXX.

As one can see, this choice has a negligible effect on the performance of the basis. This is expected as the underlying basis vectors are nearly identical between the two methods, which can be observed in Fig. C.3. This suggests that there is not a strong coupling between the coarse groups, which could be problem dependent. It is possible that for a highly scattering problem, a difference could arise, but more work is needed to assess this possibility.

C.2 Snapshots of the current

In this section, we explore the impact of including snapshots of the net neutron current into the POD calculation. All POD basis sets in this section include snapshots of the scalar flux. However, it is possible to include additional snapshots prior to forming the POD basis. Here, we explore if the inclusion of the net neutron current allows a POD basis to better approximate the solution of the DGM method, particularly at the low orders. As shown in

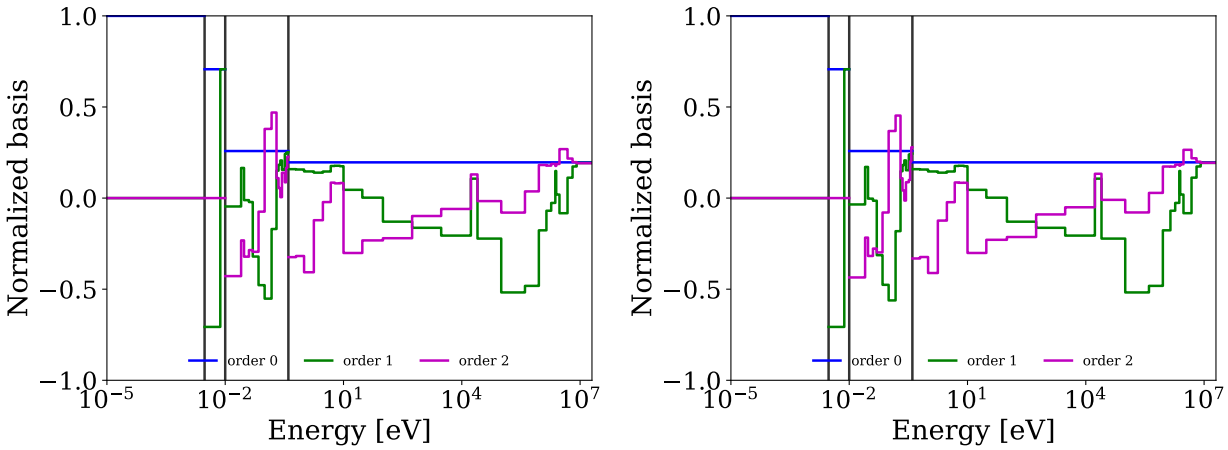

(a) Truncating vectors (Choice 1)

(b) Truncating snapshots (Choice 2)

Figure C.3: 44-group comparison of the resulting POD basis from the two methods when using the 'POD_full' snapshot model. Black vertical bars are the dividing points between the coarse groups.

Fig. C.4, the differences in the resulting vectors are negligible at low orders, thus we expect the impact to be small.

Indeed, we see a small impact on the resulting 44-group fission density and eigenvalue errors in Fig. C.5. It seems that the inclusion of the net current snapshots does improve the basis, but only for the high orders, which is of lesser importance in this work. For the low orders, there is almost no difference between including or disregarding the net current snapshots. The impact on the 238-group results is presented in Fig. C.6, which show the same trends as the 44-group results.

These tests were performed on a test problem with isotropic scattering. It is possible that for anisotropic scattering, including snapshots of the net neutron current could improve the stability of the problem, which was discussed in Section B.5. However, the J snapshots were not required for the success of a low-order, isotropic scattering DGM solution.

C.3 Snapshots of the total cross section

Since the DGM method uses a basis expansion for both fluxes and cross sections, another idea is to determine the effect of inserting snapshots of the total cross section before computing

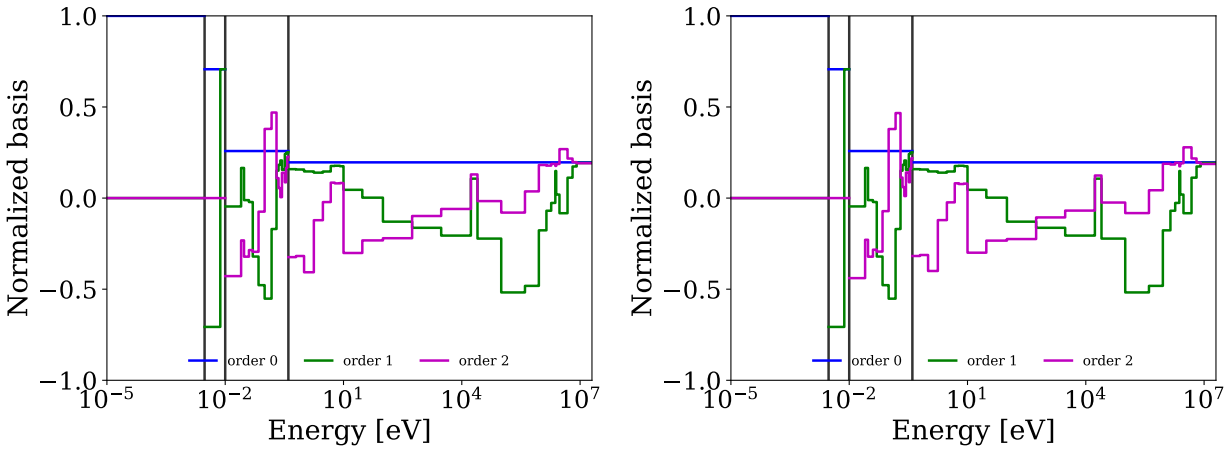

(a) Snapshots of only ϕ

(b) Snapshots of $\phi + J$

Figure C.4: 44-group comparison of the resulting POD basis from including or disregarding snapshots of the net neutron current. Black vertical bars are the dividing points between the coarse groups.

the basis. In theory, this would allow the cross section moments to be better represented at low orders, which could provide better performance and lower errors at the low orders. Figure C.7 presents a comparison of the first three orders of a basis computed with and without the total cross section snapshots.

We can see the performance of the new basis sets in Fig. C.8 for the 44-group problem and in Fig. C.9 for the 238-group problem. The discontinuities in some of the lines are where the solution was unstable and is thus unavailable. These results suggest that adding snapshots of the total cross section does not improve the solution at low orders, and degrades the solution in some cases. At higher orders, some improvement to the errors can be observed in particular for the poorly performing basis sets of XXX_uo2 and XXX_mox. However, the increased performance is accompanied by a cost to stability. Thus, snapshots of the total cross section are not ideal and are not used in the remainder of this work.

C.4 Snapshots of both current and total cross section

For completeness, this section explores the effect of including both snapshots of the net neutron current as well as the total cross section. Since the performance of either choice

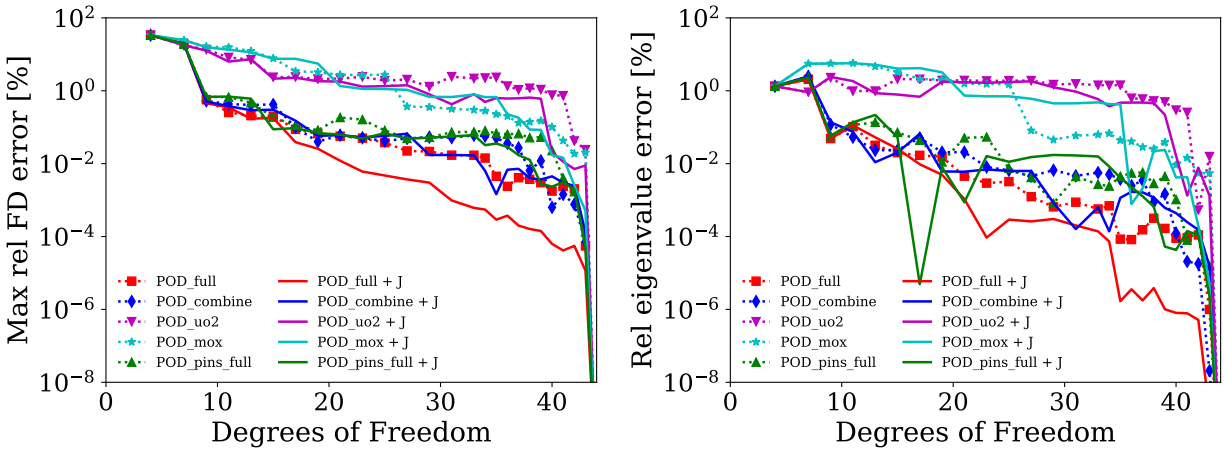

(a) Fission density error

(b) Eigenvalue error

Figure C.5: 44-group comparison of impact of including snapshots of the neutron current J. POD_XXX uses snapshots of only the scalar flux ϕ. POD_XXX + J includes snapshots of ϕ and J. XXX refers to the base snapshot model, which is described in Section 4.2.

was not favorable in the previous sections, it is unlikely that the combination is useful. Nevertheless, Fig. C.10 compares the standard basis formed from scalar flux snapshots against the POD basis computed from including snapshots of the scalar flux, net neutron current, and the total cross section.

In Fig. C.11 and Fig. C.12, the 44- and 238-group results are presented, respectively. As expected, the performance is comparable to the inclusions of either the net current snapshots or the total cross section snapshots in isolation. At the higher orders, better performance (lower errors) can be achieved at the cost of stability, which is manifesting as discontinuities in the curves. At the lower orders, which is of interest to this work, almost no difference can be observed.

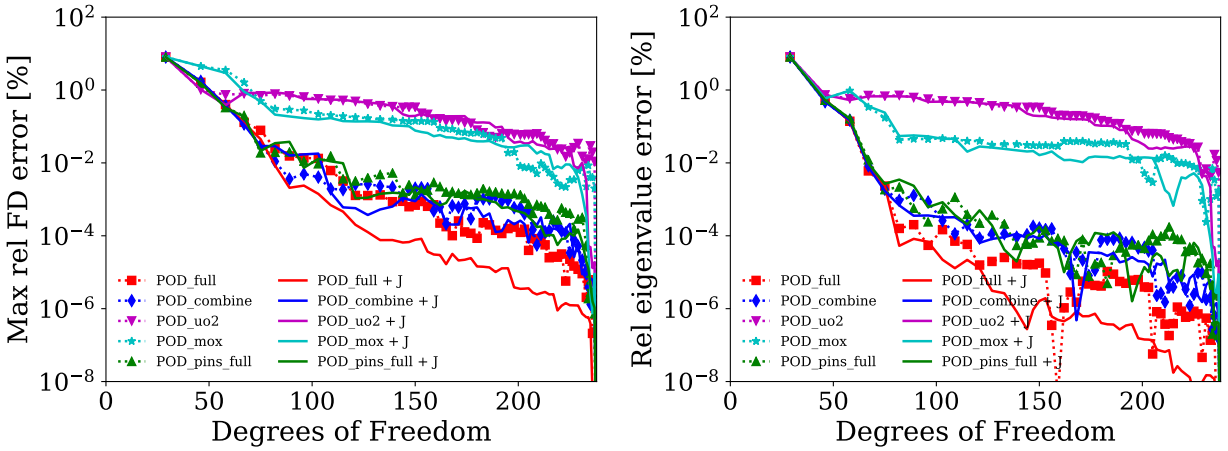

(a) Fission density error

(b) Eigenvalue error

Figure C.6: 238-group comparison of impact of including snapshots of the neutron current J. POD_XXX uses snapshots of only the scalar flux ϕ. POD_XXX + J includes snapshots of ϕ and J. XXX refers to the base snapshot model, which is described in Section 4.2.

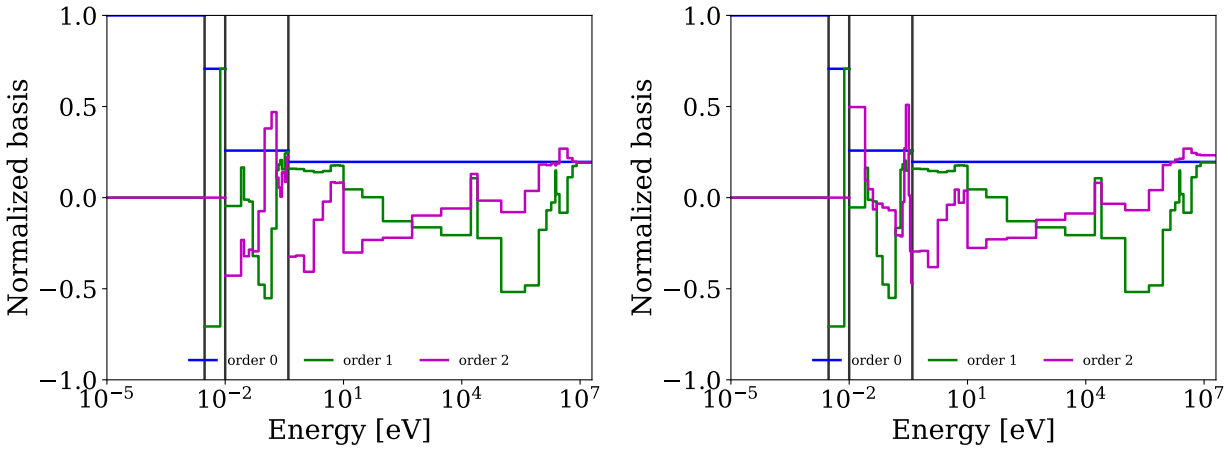

(a) Snapshots of only ϕ

(b) Snapshots of $\phi + \Sigma_t$

Figure C.7: 44-group comparison of the resulting POD basis from including or disregarding snapshots of the total cross section. Black vertical bars are the dividing points between the coarse groups.

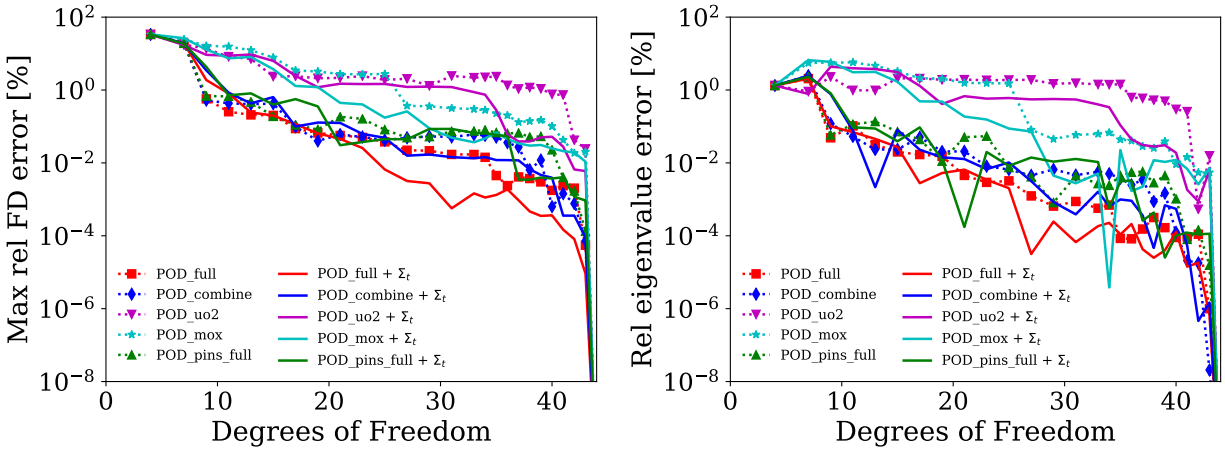

(a) Fission density error

(b) Eigenvalue error

Figure C.8: 44-group comparison of impact of including snapshots of the total cross section Σ_t. POD_XXX uses snapshots of only the scalar flux ϕ. POD_XXX + Σ_t includes snapshots of ϕ and Σ_t. XXX refers to the base snapshot model, which is described in Section 4.2.

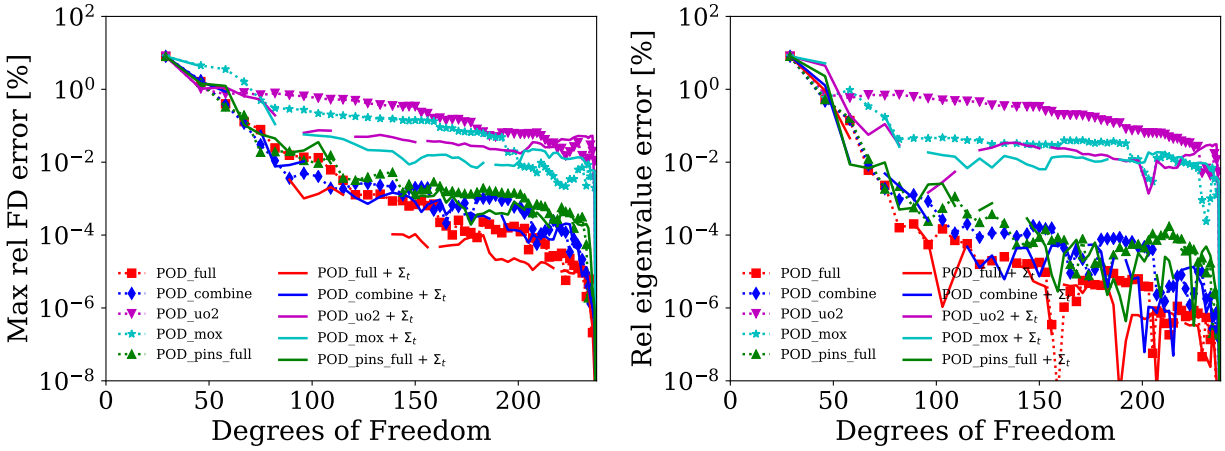

(a) Fission density error

(b) Eigenvalue error

Figure C.9: 238-group comparison of impact of including snapshots of the total cross section Σ_t. POD_XXX uses snapshots of only the scalar flux ϕ. POD_XXX + Σ_t includes snapshots of ϕ and Σ_t. XXX refers to the base snapshot model, which is described in Section 4.2.

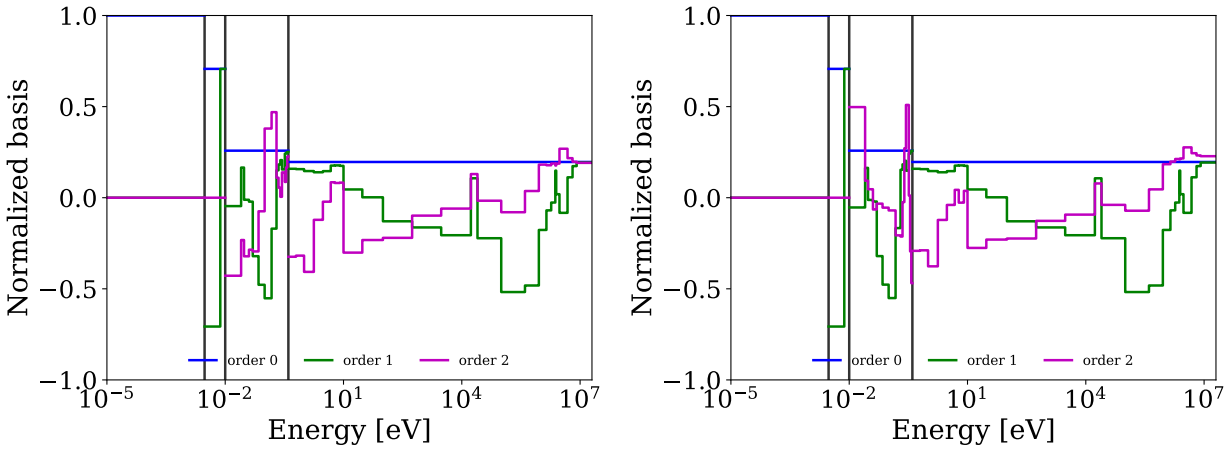

(a) Snapshots of only ϕ

(b) Snapshots of $\phi + \Sigma_t + J$

Figure C.10: 44-group comparison of the resulting POD basis from including or disregarding snapshots of the total cross section. Black vertical bars are the dividing points between the coarse groups.

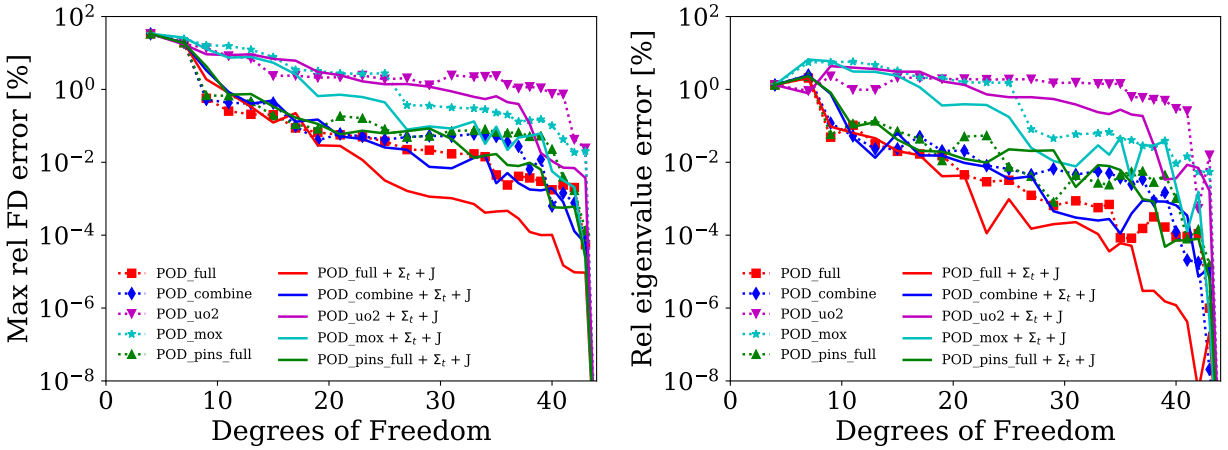

(a) Fission density error

(b) Eigenvalue error

Figure C.11: 44-group comparison of impact of including snapshots of the total cross section Σ_t and the net neutron current J. POD_XXX uses snapshots of only the scalar flux ϕ. POD_XXX + Σ_t + J includes snapshots of ϕ, Σ_t, and J. XXX refers to the base snapshot model, which is described in Section 4.2.

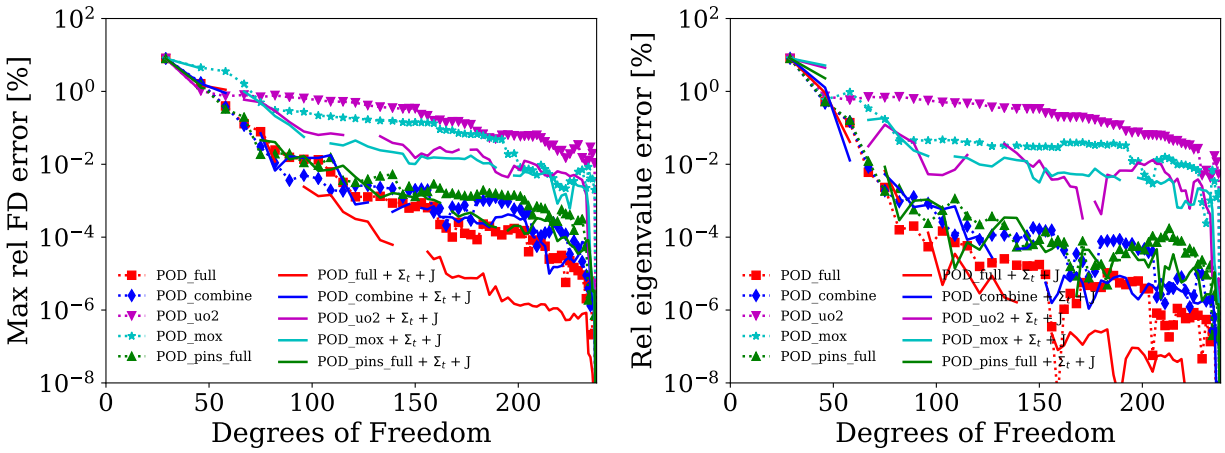

(a) Fission density error

(b) Eigenvalue error

Figure C.12: 238-group comparison of impact of including snapshots of the total cross section Σ_t and the net neutron current J. POD_XXX uses snapshots of only the scalar flux ϕ. POD_XXX + Σ_t + J includes snapshots of ϕ, Σ_t, and J. XXX refers to the base snapshot model, which is described in Section 4.2.